Compact Near-Infrared 3-Dimensional Channel Waveguide Lasers

Rose Mary

A dissertation submitted for the degree of Doctor of Philosophy

Heriot-Watt University

School of Engineering and Physical Sciences

September 2014

Abstract

This thesis presents the development of ultrafast near-infrared (NIR) waveguide laser sources, through the fabrication of waveguides in Yb-doped bismuthate glass using ultrafast laser inscription (ULI). An integrated linear cavity waveguide laser is demonstrated in the glass with output powers of 163 mW and a slope efficiency of 79%. The laser performance is comparable to bulk systems while providing additional advantages in terms of low threshold ~35 mW and system compactness. The simultaneous achievement of low propagation losses and preservation of the fluorescence properties of Yb ions after the ULI process is key to the outstanding laser performance.

Based on the current interest in ultrafast laser development using graphene as a saturable absorber (SA), a systematic study of nonlinear absorption in graphene is presented. The nonlinear optical characterisation of graphene at the wavelengths of 1 μm and 2 μm contributes to the experimental evidence for the wavelength independent absorption saturation in the material.

Ultrashort pulse generation from the Yb-doped bismuthate waveguide laser is investigated using SAs based on semiconductor technology and carbon nanostructures. The quasi-monolithic waveguide laser, employing a graphene SA generated ~485 mW output power with a slope efficiency of 49%. The laser generated ~1 ps pulses in a Q-switched mode-locked regime, with the mode-locked pulses measuring a high repetition rate of 1.5 GHz.

Ultrafast laser development is also investigated based on a novel evanescent-wave mode-locker device, fabricated by ULI. The device consists of an orthogonal waveguide with the right-angle positioned along its angled facet. The substrate is converted into a mode-locker by depositing carbon nanotube SA at the angled facet. Mode-locked operation is demonstrated by incorporating the substrate in an Er-doped ring laser, generating ~800 fs pulses at 26 MHz. Some preliminary work is done to replicate the device design in an active gain medium, namely, Yb-doped bismuthate glass, for the development of compact laser sources.

To my family and friends

Special thanks to Ashleigh Barron for being a great friend throughout and tolerating my music choices. Thanks to Peter Kremer for being a kindred spirit, especially on the topic of food. Thanks to Martin Smith who taught me the beauty of irony. And Nitin, who gives valuable life lessons using puns.

Big thanks to Cristtel Ramirez for being the wonderful friend that she is! I will forever cherish all our experiences over the years, right from the Summer School SUSSP '66, ASSP, Olympics 2012, Korean songs and to whatever the future holds as well. I am always amazed by your boundless enthusiasm about everything. Thanks to all my other friends who has contributed to make my time in Scotland amazing: Ximing, Nabin, Chandra, Ruth, Yingying, Ying Peng, Arun Babu, Tam, Wolf, Diego, Rajiv, Akhil, Hari-mon, Pragati, Hema, Himanshu, to name a few .

Special thanks to Joanne, for her support and friendship throughout the years. The Christmas at your place was a fairy tale come true. Thank you.

Rishad, Shraddha and Anusha, I love you folks! In my mind, we form the equivalent of 'F.R.I.E.N.D.S'. Thanks for all the wonderful times, the musical evenings, food appreciation sessions, the umpteen bouts of craziness, and infinite number of insightful discussions including physics.

Special thanks to my wonderful friend Supta. I'm truly blessed to have you in my life. Thanks to Adi, Supta and Adwita for adopting me as part of their family, and for the many dinners. Thanks to wee Adwita for being my bestie.

Thanks to Swapna maam for her love, care and hospitality.

Thanks to Linda Bruce, for her friendship, and for teaching all about Scotland.

My thanks to my many friends from back home, who remains a vital part of my life: Tanya, Sonia, Priyamvada, Thomas, Jenu, Nishant, Suchand Sandeep, Manthan, Yedhu, Raji, Abhinav and many more.

Thanks to Heriot-Watt University for the opportunities and support in the form of the sports centre, library, the many clubs and most importantly, the Chaplaincy. My thanks

Publications by the Author

Peer reviewed journal articles by the author

1. **R. Mary**, S. J. Beecher, G. Brown, R. R. Thomson, D. Jaque, S. Ohara, and A. K. Kar, "Compact, highly efficient ytterbium doped bismuthate glass waveguide laser," Opt. Lett. **37**, 1691-1693 (2012).

2. **R. Mary**, G. Brown, S. J. Beecher, F. Torrisi, S. Milana, D. Popa, T. Hasan, Z. P. Sun, E. Lidorikis, S. Ohara, A. C. Ferrari, and A. K. Kar, "1.5 GHz picosecond pulse generation from a monolithic waveguide laser with a graphene-film saturable output coupler," Opt. Express **21**, 7943-7950 (2013).

3. **R. Mary**, G. Brown, S. J. Beecher, R. R. Thomson, D. Popa, Z. Sun, F. Torrisi, T. Hasan, S. Milana, F. Bonaccorso, A. C. Ferrari and A. K. Kar, "Evanescent-wave coupled right angled buried waveguide: Applications in carbon nanotube mode-locking," Appl. Phys. Lett. **103**, 221117 (2013).

4. **R. Mary**, D. Choudhury and A. K. Kar, "Applications of fiber lasers for the development of compact photonic devices," IEEE J. Sel. Top. Quant. Electron, **20**, (2014). doi: 10.1109/JSTQE.2014.2301136.

5. Y. Ren, G. Brown, **R. Mary**, G. Demetriou, D. Popa, F. Torrisi, A. C. Ferrari, F. Chen and A. K. Kar, "7.8 GHz graphene-based 2 μm monolithic waveguide laser," IEEE J. Sel. Top. Quant. Electron. doi: 10.1109/JSTQE.2014.2350016.

Conference papers by the author

1. **R. Mary**, S. Beecher, G. Brown, R. R. Thomson and A. K. Kar, "Yb-doped Bismuthate Glass waveguide laser fabricated by Ultrafast Laser Inscription", ASSP - Lasers, Sources, and Related Photonic Devices, OSA Technical Digest (CD) (Optical Society of America, 2012), paper AM4A.14. 30th January 2012.

2. **R. Mary**, S. J. Beecher, G. Brown, S. Ohara, and A. K. Kar, "Passive Q-switched Mode-Locking in a Ytterbium Doped Bismuthate Planar Waveguide Laser," Fibre Optic and Waveguides symposia, Photon 12, Durham, 6th September 2012.

3. **R. Mary**, S. Beecher, G. Brown, Z. Sun, D. Popa, T. Hasan, A. Ferrari, S. Ohara, and A. Kar, "Q-switched modelocking using carbon nanotubes in an ultrafast laser inscribed ytterbium doped bismuthate glass waveguide laser," International Conference on Fibre Optics and Photonics (Photonics 2012, Chennai, India), OSA Technical Digest (online) (Optical Society of America, 2012), Paper T3B.3.

4. **R. Mary**, G. Brown, S. J. Beecher, S. Ohara, and A. K. Kar, "Passive Mode-locking of a Monolithic Waveguide Laser with Simultaneous Q-Switching," CLEO-PR & OECC/PS 2013, Kyoto, Japan (2013). Paper WA4-5.

5. G. Brown, R. R. Thomson, S. J. Beecher, **R. Mary**, D. Popa, Z. Sun, F. Torrisi, T. Hasan, S. Milana, F. Bonaccorso, A. C. Ferrari and A. K. Kar, "Mode-locking Using Right-angle Waveguide Based Nanotube Saturable Absorber,"CLEO-PR&OECC/PS 2013, Kyoto, Japan (2013). Paper WA4-4.

6. **R. Mary**, S. J. Beecher, G. Brown, A. K. Kar, "Ultrafast Waveguide Laser in Ytterbium Doped Bismuthate Glass using Direct Laser Writing," Aston Institute of Photonic Technologies Student Conference 2013, Aston University, Birmingham UK (2013).

Table of Contents

List of abbreviations

ANDi - all-normal-dispersion

CL - coupling loss

CNT- carbon nanotubes

CVD - chemical vapour deposition

CW - continuous–wave

CW-ML - continuous-wave mode-locking

DUT - device under test

Er - Erbium

fs - femtosecond

FTIR - frustrated TIR

FLG - few layer graphene

FWHM - full-width at half-maximum

GaN - Gallium Nitride

InGaN – Indium Gallium Nitride

He-Ne - Helium-Neon

HiPCo - high pressure carbon monoxide

HR - high-reflectivity

IL - insertion loss

KLM - Kerr lens mode-locking

LPE - Liquid Phase Exfoliation

LOC - lab-on-chips

MID-IR - mid-infrared

MM - multimodal

MOPA - master-oscillator power-amplifier fibre

MLG - monolayer graphene

NIR - near-infrared

Nd - Neodymium

PBS - polarising beam splitter

PL - propagation loss

ps - picoseconds

PVA - polyvinyl alcohol

QML - Q-switched mode-locking

RF - Radio frequency

SA - saturable absorber

SAM - SA-mirrors

SA-OC Saturable absorber output coupler

SEM - Scanning electron microscope

SESAM - Semiconductor Saturable Absorber Mirrors

SESOC - Semiconductor Saturable Output Coupler

SM - Single-mode

SPR - surface plasmon resonance

Ti - Titanium

TIR - total internal reflection

TBP - time-bandwidth product

TPA - two-photon absorption

ULI - Ultrafast Laser Inscription

UV - ultraviolet

WDM - wavelength division multiplexer

Yb - Ytterbium

Yb-BG - Ytterbium doped bismuthate glass

0-D - zero-dimensional

1-D - one dimensional

2-D - Two dimensional

3-D - Three-dimensional

List of Figures

Lists of Tables

Chapter 1 - Introduction

1.1   Background

The first laser was demonstrated by Theodore H. Maiman in a ruby crystal in 1960 [1]. More than 50 years hence, lasers find ubiquitous impact in application domains ranging from industry, medicine and basic research, to everyday life. Recent years have witnessed a number of celebrations associated with major anniversaries related to laser technology. The year 2010 marked '50 years of lasers'; with celebrations across the globe acclaiming its social, technological and scientific impact. With subsequent celebrations on the trailing edge such as the 50th anniversary of Nonlinear Optics, to a planned agenda for an 'International Year of Light and Light based Technologies' declared for the year 2015 by the United Nations [2]; the past narrates a brilliant account of sublime innovation, bright ideas to life, and unprecedented development. The present still engages in active research in the field, expanding the application horizons, and the future holds bright promise of scientific breakthroughs and technological progress.

From the first ruby laser which emitted short-lived coherent light at 694 nm in the red spectral region, lasers have come a long way. Tracing back along the historical evolution of lasers, a distinct shift can be noticed in the way that lasers are perceived. While the first decade of laser development focused mainly on possible laser sources with their applications pursued later, the current laser technology is practically dictated by potential applications. As a consequence, even with the tremendous advances over the past 50 years, there is no dearth in the field of laser development. And each laser, with its application-specific features such as operating wavelength, power efficiency, mode of operation and size, is no less significant than any other. Lasers are invaluable tools across a multitude of applications such as industrial manufacturing, medical research and diagnostics and high speed optical communications. Moreover, the extreme versatility of lasers has expanded research into unique applications such as laser-enabled linear particle accelerators [3], laser fusion experiments [4], increased sensitivity for the search of extra-terrestrial life [5] and laboratory built black-holes [6]. Thus, lasers still present an exciting field, producing the same distinct feeling they instilled in researchers at their inception.

One of the broad classifications of lasers is based on the mode of operation. Lasers can function in a continuous–wave (CW) or pulsed regime. In the CW mode, the laser output power remains constant over a period of time. The first CW laser operation was demonstrated in 1960 in a Helium-Neon (He-Ne) laser [7]. While this laser worked at a wavelength of 1153 nm, the visible operation wavelength at 632.8 nm is preferred for many industrial and scientific uses. By virtue of the good beam quality, low-cost and stable CW output, visible He-Ne lasers are used for laboratory demonstrations, integrated bar-code readers, optical disc readers, and for alignment purposes in laser surgery and industry. CW lasers also initiated the important field of laser material processing based on linear absorption processes in materials.

High power CW CO_2 lasers have been extensively used for laser cutting and welding, with lower power lasers used for metal marking [8]. CO_2 lasers are also used for surgical applications by virtue of the water absorption at their operating wavelength of 10.6 µm. The preference for CO_2 lasers has however reduced over the years because of the expensive constituents including the use of Helium in the system.

Another class of CW lasers, namely semiconductor lasers, is prevalent in a wide variety of applications including fibre-optic communication, as pump sources for other laser systems to everyday use such as laser-printers, laser-pointers, hand-held bar-code scanners and compact disk drives. Thus, CW lasers have a major impact in many applications.

However certain fields require high peak power laser operation, thereby leading to advances in pulsed lasers. For example, the high irradiances in pulsed lasers have enabled material processing with sub-micron features by virtue of nonlinear absorption processes. In the pulsed regime, the laser output consists of periodic pulses with the pulse durations ranging from nanoseconds to attoseconds. Pulsed operation in lasers is commonly achieved by either Q-switching or mode-locking, with their pulse durations differing accordingly.

Pulses with durations of the order of nanoseconds (ns) are obtained by the technique of Q-switching, where, the cavity quality factor or Q-factor is modulated by a variable

attenuator to produce pulses with high peak powers. Due to the high instantaneous powers obtained by this process, Q-switching is also termed as 'giant pulsations' [9].

Lasers with their pulse durations of the order of picoseconds (ps) to femtoseconds (fs) and rightly termed as 'ultrafast lasers', are typically achieved by the technique of mode-locking [10]. In this technique, a phase relationship is established between longitudinal modes to produce a train of short pulses. Compared to Q-switching, mode-locked lasers are characterised by higher pulse repetition rates, peak powers and shorter pulse durations. Recent advances in the field of short-pulse generation have led to laser pulses of even shorter durations of the order of attoseconds, which corresponds to 10^{-18} seconds. Short duration pulses allow the study of dynamic processes which occur at a similar time scale, resulting in the field of ultrafast laser spectroscopy. Depending on the duration of the laser pulses, the branch of study varies from ns to attosecond spectroscopy. Attoscience, a burgeoning field only just over a decade old, involves the study of some of the fastest physical events such as those existing in atoms and molecules, by the use of attosecond pulses. Such short duration pulses are obtained by higher harmonic generation, where integer multiples of the incident light frequency are produced by nonlinear processes [11].

Research spanning half-a-century and more has facilitated laser operation in a large number of gain media, with their application dependent operating wavelength, ranging from soft X-rays to the far infrared region of the electromagnetic spectrum. Based on the gain material used, lasers are categorised as gas-lasers, liquid-lasers and solid-state lasers. A broad classification can also be made based on the operating wavelength. Visible lasers, whose wavelengths fall in the 400 nm - 700 nm range, find useful applications in spectroscopy, laser medicine, interferometry, holography, to name but a few. He-Ne lasers, the most commonly used gas laser, fall in this category. The lasers in the lower wavelength end of the visible spectrum are termed as blue lasers. In addition to Helium-Cadmium and Argon-ion lasers, this wavelength region is dominated by semiconductor lasers based on Gallium Nitride (GaN) [12] and Indium Gallium Nitride (InGaN) [13]. These lasers find important uses in colour displays and compact disk memories. The use of the shorter wavelength ~405 nm in Blu-ray discs facilitates greater density data storage.

Another important laser operating in the visible region of the spectrum is the dye laser, which typically incorporates liquid-based fluorescent dyes as the gain medium. Additional features of these lasers include short-pulse generation and wavelength tuneability, facilitated by the broad emission spectra of the fluorescent dyes. In fact, the first sub-100 fs pulses were demonstrated in a Rhodamine-6G dye laser producing 90 fs pulses [14], and subsequently, 27 fs pulses [15]. In the early 1990s, dye lasers were replaced by solid-state lasers by virtue of their compact size, efficient operation and long life. The predominant solid-state laser used Titanium (Ti) doped Sapphire as the gain medium, which was capable of room temperature operation, with a wide tuneability from 650 to 1100 nm and capable of producing sub-6 fs pulses [16]. In addition to Ti: Sapphire lasers, the near-infrared (NIR) region of the electromagnetic spectrum is dominated by other solid-state laser materials, a major example being the Neodymium (Nd) doped YAG laser which works at a wavelength of 1064 nm. Nd: YAG lasers have a compact configuration well-suited for an industrial environment, and find important applications in medicine and manufacturing. With a shorter operation wavelength compared to CO_2 lasers, Nd:YAG lasers offer higher absorption for metals such as copper and aluminium, and are used extensively for large-scale material processing [8]. Nd-doped materials have a four-level laser system, wherein, population inversion can be achieved at low powers unlike three-level lasers. A low operation threshold is possible since the lower laser level in Nd is situated well above the ground state so that it can de-populate quickly by multi-phonon transitions. Further application regimes of NIR solid-state lasers include range-finding, laser target designation, surgery, research and frequency doubling to form visible laser sources.

Laser diodes based on InGaAsP, AlGaInP and AlGaAs semiconductors, which work in the NIR region, are used as pump sources for other laser systems facilitating the development of compact, all-solid-state lasers, suited to industrial environments. In addition, laser diodes and vertical cavity surface emitting lasers, with operating wavelengths in the telecom region ~1550 nm are an integral part of long-haul fibre-optic communication systems.

Fibre lasers, one of the by-products of the telecommunication revolution, and an exemplary example of developments in laser architecture, have also complemented solid-state laser development. An optical fibre is a cylindrical structure consisting of a core region surrounded by a lower index cladding. Transmission of light within the

small cores allows highly stable and rugged laser systems in comparison to bulk laser systems. For instance, in the field of micromachining, fibre lasers have ousted the predominantly used CO_2 lasers by virtue of their superior features of easy beam delivery and stable operation. Fibre lasers have also facilitated development of novel gain media such as Ytterbium (Yb) doped laser systems, which constitutes a three-level laser.

Laser sources in the mid-infrared (MID-IR) region, which find uses in laser spectroscopy and remote sensing, include chromium doped ZnSe and ZnS, and quantum cascade lasers. In the ultraviolet (UV) region of the electromagnetic spectrum, the available laser sources include excimer lasers, which, in spite of its poor beam quality, are used in semiconductor manufacturing and laser surgery. And, corresponding to the far end of the electromagnetic spectrum with the lowest wavelengths possible, we have X-ray lasers, which have applications in dense plasma research, X-ray microscopy, and medical imaging.

In this very broad range of operating wavelengths possible for lasers, the NIR region of the electromagnetic spectrum around 1 μm is an important wavelength for a number of vital applications. This wavelength region corresponds to where water absorption is low (~ 0.17 cm^{-1}) [17], thereby making it an important wavelength for medical diagnostics and biological imaging [18]. Ultrafast lasers operating at a central wavelength around 1 μm find important applications in laser micromachining [19] and biomedicine. In addition, lasers with repetition rates > 1 GHz find important applications for frequency comb generation [20], and optical sampling [21]. Figure 1.1, reproduced from Ref. [22] provides an indication of the wide and overlapping application routes of different laser architectures with their operating wavelength in the NIR region of the electromagnetic spectrum.
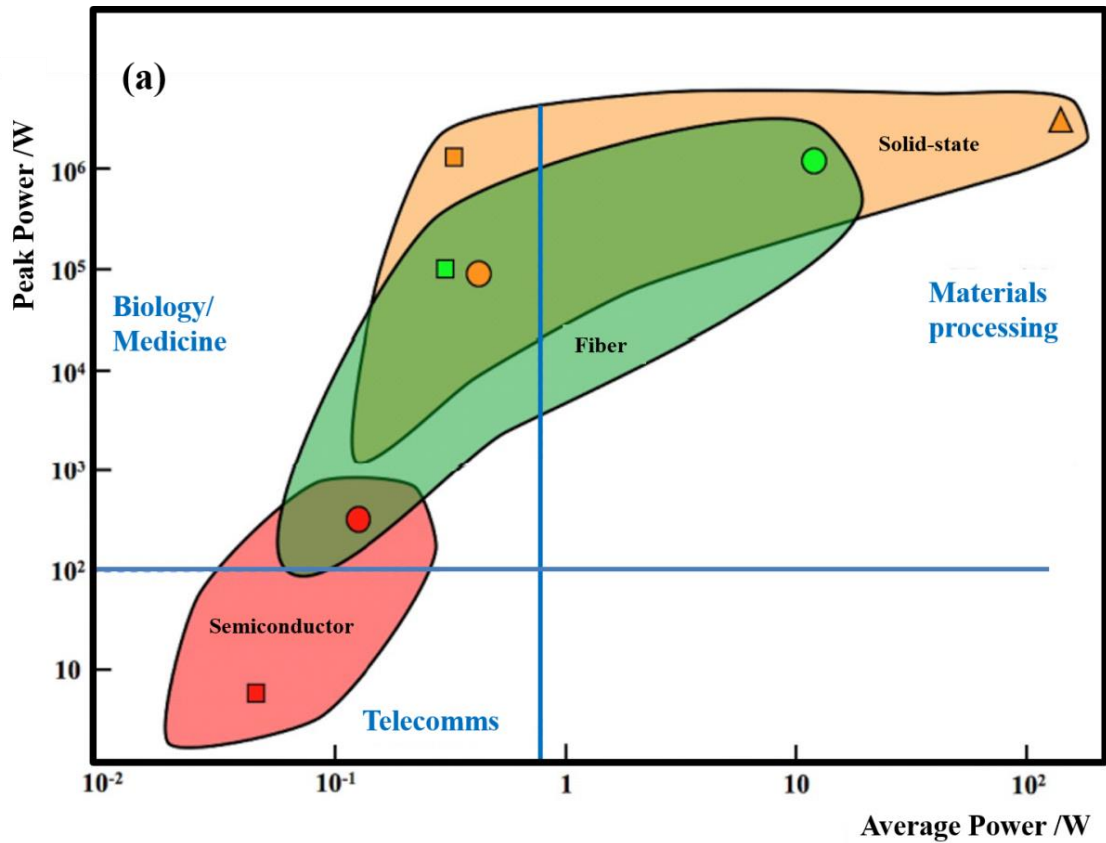
Figure 1. 1. Plot of peak power versus average power for a range of ultrafast laser oscillator technologies. Also included are indicative application areas placed in appropriate regions of laser performance. Table 1.1 shows the performance of the sources indicated. Reproduced from Ref [22].

Table 1. 1 .The key for Figure 1.1 which plots the trend in laser architectures in the NIR region. Reproduced from Ref [22].

Type	Symbol	P_{avg}(W)	P_{peak}(kW)	τ (fs)	PRF(MHz)	λ(nm)
Solid state (typical)	●	0.45	90	60	80	870
Solid state (cavity dumped)	■	0.33	1300	250	1	1040
Solid state (thin disc)	△	141	2800	738	60	1030
Semiconductor (monolithic)	■	0.045	0.006	400	$2x\ 10^4$	1260
Semiconductor (VECSEL)	●	0.125	0.315	300	1×10^3	830
Fiber	■	0.33	100	85	20	1030
Fiber (PCF)	●	12	1200	115	84	1030

With regard to this wide application domain surrounding 1 μm, the wavelength specific laser development has covered long strides, fostered by advances in laser gain media, architectures and mode-locking technologies. The dominant gain media in the early developmental stage include Nd: YAG and Ti: Sapphire systems. Simultaneously, a renewed interest in mode-locking technologies was initiated due to the need for ultrafast lasers for a variety of applications. The short pulse durations possible by mode-locking are a pre-requisite for time resolved spectroscopic studies which provides an understanding of fast dynamic processes, for instance, in photochemistry. In addition, the high peak powers attainable in pulsed lasers support nonlinear processes, and expedite corresponding applications such as laser micromachining, surgical uses and two-photon microscopy [23].

Mode-locking in lasers is achieved by using either external means for intracavity light modulation, termed active mode-locking, or, by incorporating intracavity elements that introduce a self-modulation of light, also called passive mode-locking. Active mode-locking usually employs acousto-optic or electro-optic modulators to introduce a periodic modulation in the cavity which is synchronised with the cavity round-trip time. The resultant pulses have typical durations of the order of ps, limited by the speed of the driving electronics. Passive mode-locking, on the other hand, utilises a saturable absorber (SA) within the laser cavity, with the SAs experiencing a low absorption or attenuation for higher pulse irradiances. The use of SAs is much simpler, with no driving or synchronisation circuits like in active mode-locking. Passive mode-locking allows the generation of fs pulses since the loss modulation by an SA occurs on a much faster timescale compared to electronic modulators, and is therefore preferred over active mode-locking for fs pulse generation.

For the operation wavelength of 1 μm, passive mode-locking was first demonstrated in an Nd: glass laser incorporating a dye SA [24]. However, the mode-locked operation was accompanied by simultaneous Q-switching, where the ultrashort mode-locked pulses have an additional modulation under a Q-switch envelope that occurs at a lower repetition rate, of the order of ~kHz.

A breakthrough in ultrafast laser development occurred with the demonstration of Kerr lens mode-locking (KLM) by Wilson Sibbett's research group at St. Andrews University, in Ti: Sapphire laser to produce 60 fs pulses [25]. KLM works by the

principle of nonlinear self-focusing within the gain medium in order to form an artificial SA. Sub-10 fs mode-locked pulses were possible with this technique soon after [26], with the additional key advantages being high laser stability and system compactness. An alternate passive mode-locking device with a real SA based on semiconductor technologies was developed in 1992 in Bell Labs led by Ursulla Keller. Semiconductor Saturable Absorber Mirrors (SESAMs) [27] comprise of Bragg mirrors on a semiconductor wafer with a wavelength specific quantum well absorber forming the top layer. Bandstructure engineering in SESAMs allows precise control over the SA parameters such as saturation fluence, modulation depth, recovery time and operating wavelength, allowing all-solid-state laser development at high average output powers [28] and laser repetition rates [29].

The development of low propagation loss fibre structures as gain media brought about a new phase in laser development for 1 μm. Optical fibres confine light within small cores preserving light intensities over large distances and thereby allowing laser operation with high efficiency and beam quality. The need for a four-level laser system to facilitate efficient lasing at a low pump threshold was no longer necessary merely by virtue of the fibre geometry. This kindled interest in Yb-doped systems, which have a quasi-three-level laser scheme where the lower laser level corresponds to the ground state. This simple energy level series of Yb precludes any excited state absorption and concentration quenching in the system. Also, the quantum defect, defined as the energy difference between the pump and signal photons, is low (<10%) in Yb-doped lasers [30]. These two points contribute to high efficiency of operation in these systems, and the feature of power scalability. Ultrafast operation in fibre lasers is facilitated by SAs that can be integrated within the fibre systems. In addition to SESAMs, relatively recently, one dimensional (1-D) and two dimensional (2-D) forms of carbon, namely, carbon nanotubes (CNT) [31, 32] and graphene [33, 34] have emerged as novel SAs with sub-ps recovery times, mechanical and environmental robustness, and are well-suited to a range of laser designs especially fibre lasers [35]. Single layer graphene consists of a monolayer of carbon atoms in a 2-D honeycomb lattice. A 1-D rolled up graphene constitutes single-walled CNT [36]. For CNTs, the operation wavelength for saturable absorption is dictated by the tube diameter. In graphene, absorption is wavelength independent by virtue of its linear dispersion relation, dubbing it a 'universal' SA.

1.2   Waveguide Lasers

Currently, research in the field of ultrafast laser development is also focused towards compact, highly efficient systems, made possible by advances in laser architectures. These include thin-disc, fibre and waveguide lasers. In a thin-disc laser, the gain medium is such that its thickness is less than the diameter of the laser mode. A high reflectivity mirror coated onto one face of the disc forms one of the cavity mirrors. This surface is also attached to a heat sink, thereby improving the cooling efficiency of the system. These laser systems are therefore effective in high power operation, reporting an average power more than 25 kW for CW operation [37]. Power scalability is an important feature also in fibre lasers, with achieved CW output power of ~10 kW [38]. Usually, a double-clad fibre structure is used, with the laser signal guided along the core, and the pump guided along a second core surrounding the first.

There is also interest in lasers based on planar and channel waveguides, fuelled by advances in compact photonic devices brought about by the concept of integrated optics [39]. While they cannot compete with the advancements in fibre and thin-disc laser technologies in terms of power scalability, they present an attractive source for low-power laser applications requiring a smaller footprint [40]. Figure 1.2 (a) shows the schematic of a planar waveguide laser, which consists of a planar region of refractive index n_1, sandwiched between regions of refractive indices n_2 and n_3, with $n_1 > n_2, n_3$. In this case, the light is confined in only one direction, indicated by the plane with refractive index n_1. In a channel waveguide, depicted in Figure 1.2 (b), light is confined in two directions as in a fibre by having the guiding region with refractive index n_1 in the form of a channel or a ridge, and $n_1 > n_2, n_3$. The waveguide supports a finite number of allowed modes, each with a distinct distribution of spatial energy.

(a) Planar Waveguide   (b) Channel Waveguide
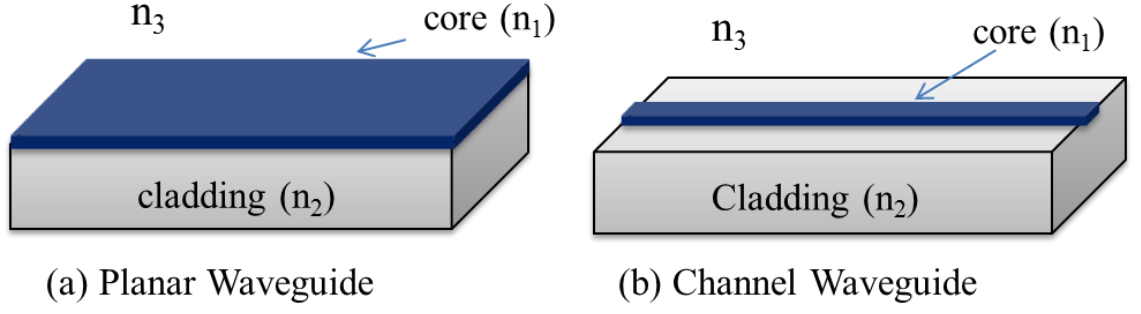
Figure 1. 2. (a)A planar slab waveguide. (b) A channel waveguide. The region with refractive index n_1 forms the guiding region with $n_1 > n_2, n_3$.

The behaviour of electromagnetic waves within the waveguide can be described by the following wave equation, derived from Maxwell's equations in a non-magnetic, non-conducting medium [41].

$$\nabla^2 \boldsymbol{E}(\boldsymbol{r}) = \varepsilon_0 \mu_0 n^2 \frac{\partial^2 \boldsymbol{E}(\boldsymbol{r})}{\partial t^2} \qquad (1.1)$$

where E is the electric field vector, ε_0 is the permittivity of vacuum, μ_0 is the permeability of vacuum and n is the refractive index of the medium. When subject to boundary conditions such as that existing in a waveguide, the solutions to this equation give information about the allowed propagation modes,

$$\boldsymbol{E}(\boldsymbol{r}, \boldsymbol{t}) = \boldsymbol{E_0}(\boldsymbol{r}) \exp(i\beta z - i\omega t) \qquad (1.2)$$

where β is the propagation constant and ω is the angular frequency of the propagating wave. Substituting this equation into equation (1.1) for a Cartesian coordinate system, we obtain:

$$\nabla^2 \boldsymbol{E}(\boldsymbol{x}, \boldsymbol{y}) + [k^2 n^2(x, y) - \beta^2]\boldsymbol{E}(\boldsymbol{x}, \boldsymbol{y}) = 0 \qquad (1.3)$$

where $\beta = n_{eff} k$, where n_{eff} is the effective index of the mode. The solutions to equation 1.3 describes the guided waveguide modes, with a direct relationship between the field distribution of the guided modes *E(x, y)* and the cross-sectional refractive index profile *n(x, y)*. For allowed waveguide modes, the condition $k_0^2 n_1^2 > \beta^2 > k_0^2 n_2^2$ is satisfied, where $k_0 = 2\pi/\lambda$, n_1 and n_2 are the refractive indices of the core and cladding respectively and λ is the wavelength of light.

The nature of the propagating modes is characterised by the physical dimensions of the waveguide. The number of allowed guided modes in a waveguide is governed by the V parameter or normalised frequency given by

$$V = k_0 a \sqrt{n_1^2 - n_2^2} \qquad (1.4)$$

where *a* is the core radius. The waveguide have a cut-off value of V=2.4048, which corresponds to the shortest wavelength for which single mode propagation is allowed in the waveguide.

Waveguide lasers including fibre lasers, for which the gain medium tightly confines the beam within the core, present several advantages over other solid-state laser architectures. The high surface area to volume ratio in waveguides allows high efficiencies and improved cooling in waveguide lasers compared to bulk lasers. Also, the waveguiding nature allows good mode overlap between the pump and signal beams. Diffraction limited beam quality can be achieved by having single mode guidance. In the case of channel waveguides, the possibility of high gain, short cavity systems allows high repetition rate mode-locking. Waveguide systems are predominantly fabricated by thin-film technologies such as flame hydrolysis deposition, chemical vapour deposition and pulsed laser deposition assisted by photo-lithography. Other fabrication techniques include ion-exchange and in-diffusion techniques [42].

In comparison, a flexible waveguide fabrication technology is Ultrafast Laser Inscription (ULI) [43]. In ULI, a fs pulse train is focused within the sample to induce nonlinear absorption processes, which result in energy transfer to the lattice. Under correct inscription conditions, a local permanent refractive index change can be achieved. The attained modification can be extended along an arbitrary path by translating the sample or the beam, with three-dimensional (3-D) flexibility, which is one of the most important characteristics of this technique.

When a positive refractive index change is attained at the focal volume and extended along the sample length, the modified region forms the core of a straight line channel waveguide with the surrounding unmodified region constituting the cladding. The

typical refractive index change possible in a ULI waveguide is of the order of ~0.5% [44] compared to ~3% in optical fibres [45]. This results in poor confinement of the guided mode which is compensated to some extent by increasing the dimension of the waveguide. The low refractive index contrast has an adverse effect on complex photonic circuitry including waveguide bends. The limiting bend radius in ULI waveguides is of the order of ~20 mm, compared to R< 1 mm possible in fibres [45, 46]. In spite of these limitations, ULI has emerged as a stand-alone technology with unique applications. First demonstrated in 1996 [47], waveguide fabrication by ULI is now possible in a wide range of materials [43]. While the initial research focused on passive waveguide devices such as directional couplers and splitters for integrated circuits at the telecom wavelength, the versatility of the technique has been extended in order to develop waveguides in active materials for laser applications [48]. Just over 15 years old, ULI has immense application potential in terms of compact laser source development. The advantages and limitations of various laser gain media and mode-locking technologies studied over the years provide a better understanding of potential merits and demerits for developing new laser technologies.

1.3   Motivation of the thesis

The development of compact, highly efficient, ultrafast waveguide laser systems based on ULI serves as the motivation for the work described in this thesis. The technique of ULI allows low propagation loss waveguide structures in an unprecedented variety of materials including glasses, crystals and ceramics [43]. This key feature, which can be utilised for active and passive device geometries, is at the heart of the work presented in this thesis.

With regard to the large number of applications at 1 μm, which interestingly also includes ULI, the thesis explores a new Yb-doped material composition for ULI-based waveguide laser systems. The possibilities of power scalability and high-repetition rate ultrafast operation are investigated based on existing mode-locking technologies. Finally, the versatility of the ULI method is exploited to fabricate a passive device geometry to improve the functionality and efficiency of existing mode-locking technologies.

1.4 Thesis Outline

The thesis is organised as follows:

Chapter 2 introduces the topics relevant to understand the work presented in this thesis. The technology of ULI is presented including the underlying nonlinear processes and consequent material modification regimes. The laser inscription setup used for the work described in subsequent chapters is also detailed.

Chapter 3 provides a brief review of active photonic devices fabricated by ULI technology. The widely used active rare-earth ions, namely, Nd, Yb and Er, and their unique spectroscopic properties are discussed. Ultrashort pulse generation based on SA technologies, such as SESAM, CNTs and graphene are also presented. The final section provides a concise review of ULI waveguide lasers reported over the years.

Chapter 4 introduces the gain material used for the work, namely, Yb-doped bismuthate glass. The suitability of the glass for ULI waveguides is studied extensively, using a wide range of inscription parameters. The ULI-induced material modification in the glass is analysed using microluminescence studies. A compact, linear cavity waveguide laser is obtained from the corresponding optimal waveguide, with a high slope efficiency close to the quantum defect limit.

Chapter 5 outlines nonlinear optical characterisation of graphene at 1 μm for subsequent passive mode-locking of the Yb-doped bismuthate glass waveguide laser. The saturable absorption in the material is studied in terms of the operation wavelength and number of graphene layers, to derive the key SA parameters of saturation fluence, modulation depth and non-saturable losses.

Chapter 6 investigates the feasibility of passive mode-locking in the linear laser cavity featuring Yb-doped bismuthate glass waveguide as gain element. The compact cavity configuration is maintained by the incorporation of a SA in the Fabry-Perot cavity. The SAs used for the study include semiconductor materials, CNT and graphene. High repetition rate mode-locked pulses are achieved from the cavity, with simultaneous Q-switching. Power scalability from the cavity is also studied.

13

Chapter 7 explores the versatility of ULI to fabricate a novel waveguide geometry for passive mode-locking by evanescent-field interaction of light with a SA. The design comprises orthogonal waveguides in a substrate, with their points of intersection lying along the angled facet of the chip. A suitable SA introduced at this angled facet facilitates effective evanescent-field interaction allowing passive mode-locking in a laser cavity incorporating the chip. The geometry was inscribed in a EAGLE glass substrate coated with CNT and incorporated in an Er-doped fibre ring laser to produce mode-locked pulses. The feasibility of a compact ultrafast waveguide laser in Yb-doped Bismuthate glass is also investigated by replicating this right angled geometry in the active substrate.

Chapter 8 details the conclusions achieved from the discussed work and the proposed future plans. A limitation observed with the linear cavity waveguide laser, namely, fibre-fuse effect is discussed.

1.5   Summary

The work presented in this thesis explores the application of ULI for novel photonic device fabrication. Low-loss waveguide fabrication is investigated in Yb-doped bismuthate glass to be used afterwards in an integrated waveguide laser. The key features of the resultant laser include the inherent compactness, high efficiency and the potential for monolithic device application. High-repetition rate pulsed operation is investigated using SAs based on semiconductor technology and carbon nanostructures. The remaining part of the thesis focuses on the applicability of ULI for a novel right-angled waveguide device with the advanced functionality of efficient CNT mode-locking.

Chapter 2– Ultrafast Laser Inscription

2.1 Introduction

ULI is fast becoming a powerful tool for novel photonic device fabrication, with the possible applications ranging from passive optics and active devices to monolithic lab-on-chips (LOC) having varied functionalities. This chapter introduces the technology of ULI, including the underlying principles and the different structural modification regimes. A description of typical lasers used for ULI is also given, including the one used for the presented work.

ULI was first demonstrated by Davis et al. in 1996 [47]. They reported femtosecond-laser-enabled fabrication of a 3-D optical waveguide in silica glass. The laser-processed material was characterised by a refractive index increment within the substrate, thereby forming the core of the waveguide. Since this first demonstration, ULI has been widely studied in a variety of transparent substrates, for a number of applications [43, 49, 50]. Passive device applications extensively employ fused silica and borosilicate glass, for applications such as power splitters, couplers and fan-out devices [49]. For active devices, glass hosts allowing a higher active ion solubility than silica and borosilicate are preferred. Phosphate glasses and bismuthate glasses doped with Er and Yb:Er, having gain and laser operation in the telecom C-band have been demonstrated [49]. ULI-based waveguide lasers and amplifiers have also been demonstrated in laser crystals and ceramics [51, 52]. Femtosecond laser micromachining of transparent substrates relies on strong nonlinear absorption leading to localised energy deposition within the material. The resultant permanent modification within the material depends on the properties of the incident laser pulse, the substrate under study, and other experimental conditions such as focusing optics and sample translation system. The basic schematic of a ULI rig is given in Figure 2.1. It consists of an ultrafast laser system, with the laser pulses directed through appropriate optics before being focused inside the substrate, which is placed on a high-precision x-y-z translation stage.
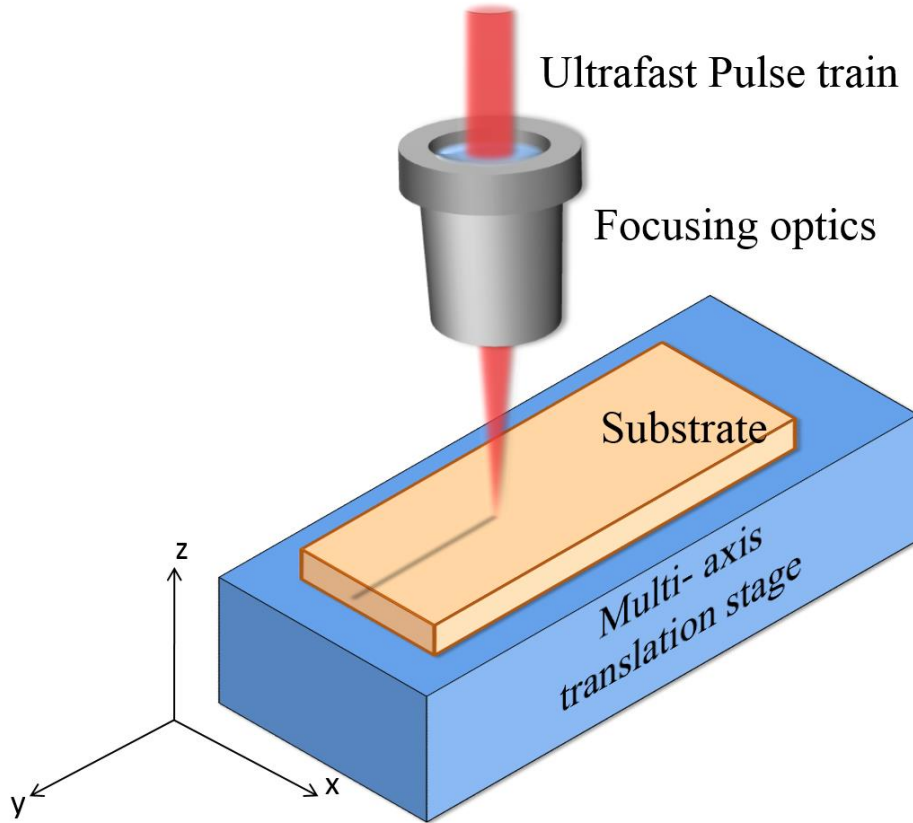
Figure 2. 1. Schematic of a typical ULI rig. The setup consists of an ultrafast laser which is focused within the sample using a microscope objective. The high irradiance achieved at the focus results in material modification by virtue of nonlinear absorption processes. This modification can be extended along any arbitrary 3-D path within the sample using the x-y-z translation stage.

2.2   Introduction to Nonlinear Optics

When an oscillating electromagnetic field is incident on a dielectric, it primarily interacts with the valence band electrons within the material to form electric dipoles. The induced polarisation of the material, defined as the dipole moment per unit volume, is dependent on the electric field of the light falling on it. For low intensity light sources, the electric field, this is weaker than that binding the electrons to the atoms, results in only small perturbations in the atomic electric field. The resultant material polarisation therefore experiences a linear relationship with the electric field of the light. The polarisation of a material in the case of conventional or linear optical regime is given by [53],

$$\vec{P}_{linear}(t) = \varepsilon_0 \chi^{(1)} \vec{E}(t) \tag{2.1}$$

where $\vec{P}_{linear}$ is the polarisation, $\vec{E}(t)$ is the electric field of the incident light, $\chi^{(1)}$ is the linear susceptibility of the medium and ε_0 is the permittivity of free space. $\vec{P}_{linear}$ is responsible for effects such as diffraction, dispersion and refraction. The refractive index (n_0), dielectric constant (ε) and linear susceptibility of the medium are further related by the equation,

$$n_0^2 = \varepsilon = 1 + \chi^{(1)} \tag{2.2}$$

Before the advent of lasers, light-matter interaction was considered to be linear, with the optical properties of the material remaining consistent regardless of the irradiance of the incident light. However lasers allow light irradiances much higher than that achieved before. Thus, with the incident electric field strength now comparable to the atomic fields, the optical properties of material systems were found to depend on the irradiance of the incident light in a nonlinear manner, resulting in the field of nonlinear optics [54]. In nonlinear optics, the expression for the polarisation can be generalised using a Taylor series, given as,

$$\vec{P}_{nonlinear} = P^{(1)} + P^{(2)} + P^{(3)} + \cdots + P^{(n)} \tag{2.3}$$

$$\vec{P}_{nonlinear} = \varepsilon_0 \, \chi^{(1)} \vec{E}(t) + \varepsilon_0 \chi^{(2)} \vec{E}^2(t) + \varepsilon_0 \, \chi^{(3)} \vec{E}^3(t) + \cdots + \varepsilon_0 \, \chi^{(n)} \vec{E}^n(t) \tag{2.4}$$

The quantities $P^{(1)}$, $P^{(2)}$, $P^{(3)}$, and $P^{(n)}$ are known as the first-, second-, third-, and n-th order polarisation terms, respectively. Similarly, $\chi^{(2)}$, $\chi^{(3)}$ and $\chi^{(n)}$ are the second- , third- , and n-th order nonlinear optical susceptibilities. The susceptibility terms are tensors due to the vectorial nature of the fields. When the electric field of the incident light becomes comparable to the inter-atomic electric field, the higher order polarisation terms become important. The contributions from the time-varying polarisation terms appear in the form of various coherent optical frequency mixing effects.

2.2.1   Second-Order Nonlinear Polarisation

Second-order polarisation is the lowest order of nonlinear polarisation possible in a material. It arises from the $\chi^{(2)}$ nonlinearity, which occurs only in crystals with a non-centrosymmetric structure. This can be attributed to the tensor form of $\chi^{(2)}$; where, symmetry conditions dictate the tensor components to be zero in centrosymmetric crystals. The resultant polarisation has a quadratic dependence on the electric field of the incident light and is given by,

$$P^{(2)} = \varepsilon_0 \chi^{(2)} \vec{E}^2(t) \tag{2.5}$$

Second-order polarisation in materials results in nonlinear frequency conversion effects, examples being second harmonic generation, sum and difference frequency generation, optical rectification, parametric amplification and oscillation. In fact, the first nonlinear process to be demonstrated was second harmonic generation, or frequency doubling, in which light with twice the incident frequency was generated [54].

2.2.2   Third-Order Nonlinear Polarisation

Third-order nonlinear polarisation arises as a result of $\chi^{(3)}$ nonlinearity, and occurs in all media. It is given as,

$$P^{(3)} = \varepsilon_0 \chi^{(3)} \vec{E}^3(t) \tag{2.6}$$

The real and imaginary parts of $\chi^{(3)}$ describe nonlinear refraction and nonlinear absorption respectively. Other nonlinear processes that occur as a result of third-order polarisation include the optical Kerr effect, third-harmonic generation, and stimulated scattering effects [53]. The nonlinear processes driving ULI include nonlinear absorption, and will be discussed in the next section.

2.3   Nonlinear Excitation Mechanisms in ULI

In ULI, a permanent material modification is induced inside transparent substrates by focusing ultrafast laser pulses to a desired depth. Since the material under study is transparent to the incident light, it means that a single photon energy is insufficient to promote a valence band electron to the conduction band. Therefore, light absorption

occurs via nonlinear excitation mechanisms, caused by the high irradiances of the focused ultrashort pulses. This is followed by the transfer of the absorbed energy to the surrounding lattice resulting in permanent structural modifications.

There are two proposed routes to nonlinear absorption in transparent materials, namely, photoionisation and avalanche ionisation [55, 56]. The probability of occurrence of each or both to induce material modification depends on the laser parameters as well as the material properties. Deterministic laser parameters include the operating wavelength, irradiance and pulse durations, whereas the vital material parameter is its energy bandgap.

2.3.1   Nonlinear Photoionisation

Nonlinear photoionisation refers to the direct excitation of a valence band electron to the conduction band by nonlinear absorption of the incident laser photons. Depending on the laser irradiance and wavelength, it is of two types.

(a) *Tunnelling ionisation*: This occurs when light with electric field comparable to the inter-atomic field strength is incident on the material. In such a situation, the strong incident field is capable of suppressing the Coulomb potential that binds the valence band electron to its parent atom, such that, the bound electron can now tunnel from the valence band to the conduction band. This is illustrated in Figure 2.2 (a). Tunnelling ionisation occurs for optical frequencies much lower than that required for linear absorption.

(b) *Multiphoton ionisation*: At high optical frequencies, simultaneous absorption of multiple photons can excite an electron from the valence band to the conduction band, as shown in Figure 2.2(b). In this case, the total photon energy must exceed the material bandgap, the condition being given by

$$\boldsymbol{m}h\upsilon \geq E_g \qquad\qquad (2.7)$$

where $\boldsymbol{m}$ denotes the number of photons absorbed, h is the Planck's constant, υ is the incident laser frequency and E_g is the bandgap of the material. Multiphoton ionisation occurs at higher laser frequencies close to the material bandgap since the number of photons required to free a bound electron is less

19

than that needed for lower laser frequencies. Also, the probability of multiphoton ionisation$P(I)_{MPI}$, depends on the light intensity *(I)* by the relation,

$$P(I)_{MPI} = \sigma_m I^m \tag{2.8}$$

where *m* is the number of photons absorbed and σ_m is the multiphoton absorption coefficient. Compared to this, tunnelling ionisation scales more weakly with incident laser intensity.
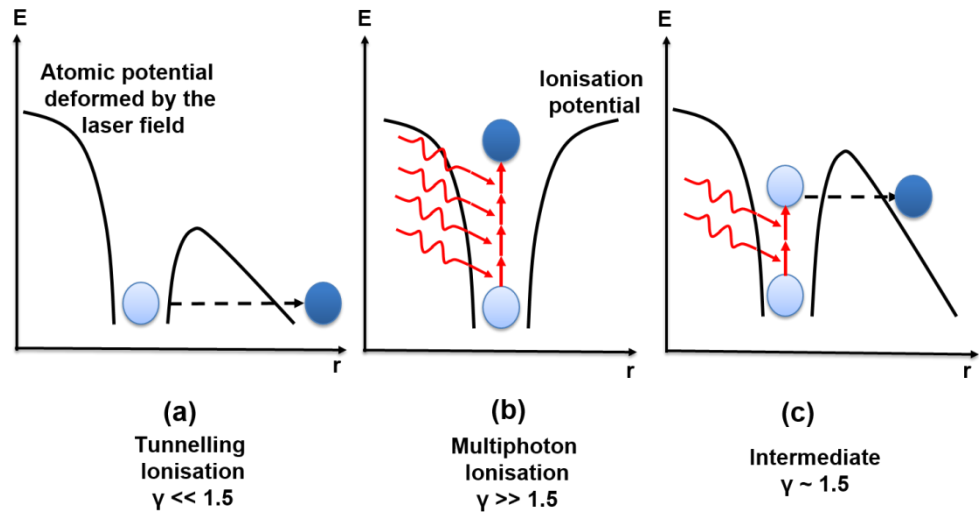
Figure 2. 2. Potential energy (E) versus distance (r) graphs for the various nonlinear photoionisation routes within a femtosecond laser-irradiated material. (a) Tunnelling ionisation (b) Multiphoton ionisation (c) Combination of both tunnelling and multiphoton ionisation.

Thus, the probability of tunnelling ionisation and multiphoton ionisation can be described in terms of the laser field intensity and frequency. Both the processes occur at high laser intensities, typically achieved during fs laser interaction with dielectrics and in fact, compete with each other. For high field strengths and photon energies close to the bandgap, multiphoton ionisation dominates, whereas for moderate laser field strengths and when the photon energies are much lower than the material bandgap, tunnelling ionisation takes over. A theoretical framework put forward in 1965 by Keldysh [57] can be used to determine the predominant ionisation mechanism and the transition between them, on the basis of γ, the Keldysh parameter. γ is given by the expression,

$$\gamma = \frac{\omega}{e} \sqrt{\frac{mcn\varepsilon_0 E_g}{I}} \tag{2.9}$$

where ω is the laser frequency, I is the laser irradiance, E_g is the material bandgap, n is the refractive index, c is the speed of light, ε_0 is the permittivity of free space and, m and e are the reduced electron mass and charge. Tunnelling ionisation dominates when $\gamma < 1.5$. For $\gamma > 1.5$, multi-photon ionisation dominates. Finally, for $\gamma \approx 1.5$, the ionisation process is a combination of the two, as given in Figure 2.2 (c).

2.3.2 Avalanche Ionisation

Avalanche ionisation can be considered to be a sequence of two processes, namely, free-carrier absorption and impact ionisation [58]. The pre-requisite to this process is the presence of free electrons in the conduction band, which are also called 'seed electrons', since they 'seed' the avalanche process. Once the electron is in the conduction band it can linearly absorb incident laser photons in a sequential manner and promote itself to even higher energy levels within the conduction band. This process is accompanied by phonon-assisted transitions in order to conserve energy and momentum.

For situations where *m* photons have thus been sequentially absorbed, such that, the criterion, $\boldsymbol{m}h\upsilon \geq E_g$ is satisfied, then the conduction band electron possesses a final energy greater than the bandgap of the material. This electron can then ionise a bound electron in the valence band by collisions, resulting in two electrons in the conduction band minimum. This is illustrated in Figure 2.3. The two free electrons can then sequentially absorb *m* photons each, to attain energies greater than the material bandgap and further impact ionise two more valence band electrons resulting in four free electrons. This process can continue as long as the incident laser irradiation is present, resulting in an avalanche of electrons, and hence the name.
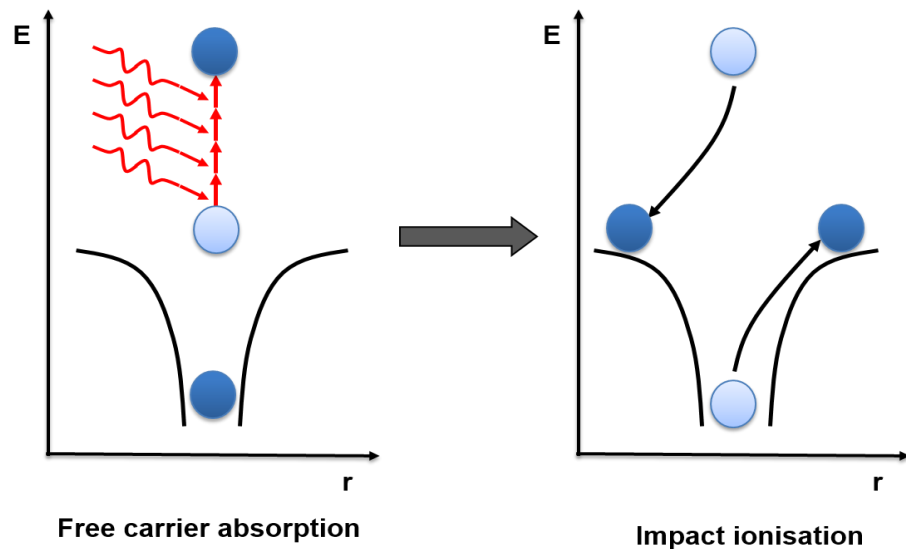
Figure 2. 3. Potential energy (E) versus distance (r) curves for avalanche photoionisation within a femtosecond laser-irradiated material.

The type of photoionisation process occurring in a laser-matter interaction depends indirectly on the pulse duration of the incident laser. For laser pulses with same average power, ps to ns durations have lower peak irradiances compared to fs pulses, thereby reducing the probability for multiphoton and tunnelling ionisation. The probable absorption mechanism is then avalanche ionisation. The initial seed electron required to feed the avalanche process depends on the presence of impurities in the materials. Impurities and defect sites in materials can introduce real energy levels within the material bandgap allowing linear absorption processes to promote a valence band electron into the conduction band. In the case of fs laser interaction, the high pulse irradiances initiate nonlinear photoionisation processes to generate free electrons in the material. Subsequent photoionisation occurs by avalanche ionisation.

There are distinct differences between material ionisation in the different pulsed laser regimes. In the case of ps to ns duration laser pulses, the ionisation process depends on the presence of impurities or defects, which are always present in arbitrary amounts in a given material. The resultant energy deposition is also random, allowing no repeatability to the process. For fs pulses however, the electrons in the conduction band are generated in a deterministic fashion by nonlinear photoionisation processes. This allows the monitoring of energy deposition within the material bulk in a reproducible way. In fact, this serves as the main reason for employing fs lasers for ULI.

22

2.4 Energy Transfer Mechanisms

The various nonlinear excitation processes thus result in the generation of a large number of free electrons in the conduction band, termed as free electron plasma. This free electron plasma possesses a characteristic resonant plasma frequency given by [59],

$$\omega_p = \sqrt{\frac{N e^2}{\varepsilon_0 m}} \qquad (2.10)$$

where ω_p is the plasma frequency, N is the number of free electrons, m and e are the reduced mass and charge of an electron, and ε_0 is the permittivity of free space. Incident light with angular frequency below the plasma frequency will be totally reflected, whereas, when its frequency matches the plasma frequency, the incident light energy is highly absorbed in the high density plasma by free-carrier absorption. Thus, in order for the incident laser energy to be absorbed by the substrate, the incident laser frequency must match the plasma frequency.

Following laser irradiation, the energy absorbed by the plasma is transferred to the lattice by thermal diffusion. In the case of fs laser pulses, the nonlinear absorption occurs on a time scale of the pulse duration, which is much shorter than the ps timescale required for thermal diffusion. Therefore, during laser irradiation, the material remains in a highly nonequilibrium state where, hot dense electrons with temperatures much higher than the surrounding ions are present within a cold lattice. The main energy transfer routes after this laser irradiation are electron-ion collisions on a ps timescale and recombination of electrons with ions on a ns timescale, finally leading to a thermal equilibrium. Most importantly, these processes manifest as different types of permanent material modifications in the irradiated volume, as discussed in the next section.

2.4.1 Material Modification Regimes

Energy transfer from the high density plasma to the surrounding lattice can be produces various forms of material modification. These can be broadly classified into three types: isotropic refractive index change, birefringent refractive index change, and void formation [49].

(a) *Isotropic Refractive Index Change*: At pulse energies just above the modification threshold of the material, an isotropic regime of modification is observed in the laser irradiated region, characterised by a refractive index variation which can be either positive, negative or a combination of both. This regime of laser exposure is typically used for ULI based waveguide fabrication. The physical processes governing this material modification are not fully understood. However, a number of theories have been proposed to explain this material modification, including colour centre formation, a thermal model and photostructural change [59]. The final refractive index change induced by ULI is considered to be due to contributions from all these mechanisms.

Colour centres refer to point defects in a crystal lattice that produces optical absorption bands in an otherwise transparent crystal and may be naturally occurring, or incorporated during growth. These can also be caused as a result of light absorption. In the case of ULI, the nonlinear absorption mechanisms leading to the generation of free electron plasma are considered responsible for the creation of colour centres. These laser-induced substrate defects can contribute to a refractive index variation through a Kramers-Kronig mechanism [60]. This mechanism is however considered to be only a contributing process to refractive index variation since removal of these defects by annealing does not recover the original index.

Another proposed theory for refractive index variation is a thermal model [60]. During ULI, fs laser irradiation is confined to the small focal volume, in turn, confining the region of thermal gradient. The rapid cooling of the lattice after the laser exposure can manifest a change in material density or refractive index. A third mechanism is laser-induced structural modification such as rearrangement of chemical bonds in glass structures leading to a density variation.

(b) *Birefringent Refractive Index Change*: In certain substrates such as fused silica and Foturan glass, structural change induced by ULI are in the form of nanogratings whose alignment depend on the incident laser polarisation [61]. These nanostructures are characterised by their periodic nature, resulting in a birefringent refractive index change, and are always oriented perpendicular to

the electric field vector of the linearly polarised inscription laser. This is illustrated in Figure 2.4.

A few mechanisms have been put forward to justify the formation of these periodic nanostructures. According to Shimotsuma *et al.*, an interference effect between the electric field of the incident laser beam and that of the free electron plasma can result in a periodic variation in the plasma concentration, and thereby result in such periodic nanostructures [62]. An alternate theory by Hnatovsky *et al.* suggests the growth of free electron plasma into disc-shaped nano-plasmas, with certain waveguiding effects within them providing them with their inherent periodicity [61].

The most important feature of these periodic nanostructures is their enhanced chemical etch rate in the presence of a suitable etchant such as hydrofluoric acid. This applicability is extremely valuable for microfluidic device fabrication [61, 63-65].

(c) *Void Formation*: At very high laser irradiances, an extremely large amount of energy is deposited in the small focal volume. The high pressure within the free electron plasma at the focus results in microexplosions, which are manifested as low density voids surrounded by a high density shell of material [66]. Such void formations find useful applications in optical memory devices [60].
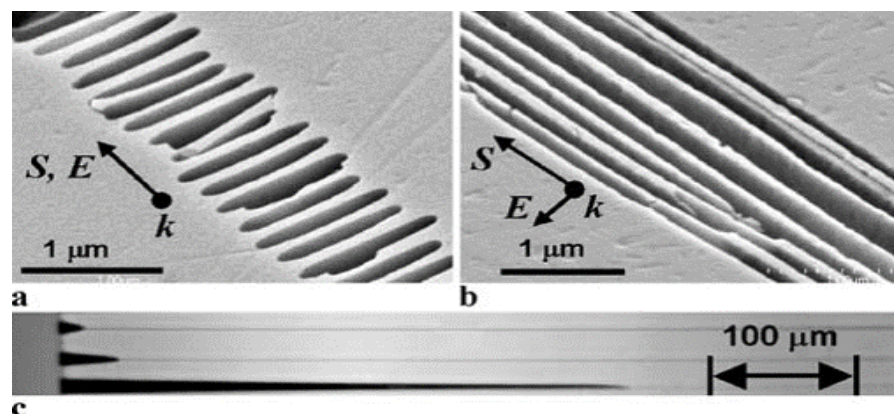
Figure 2. 4. Scanning electron microscope (SEM) images of nanogratings formed by ULI in fused silica. (a) The laser polarisation is parallel to the scan direction (b). The laser polarisation is perpendicular to the scan direction (c). Image demonstrating polarisation selective etching in the material with parallel (top), 45° (middle), and perpendicular laser polarisations. [61]

2.4.2   ULI- based Waveguide Classifications

As discussed in Section 2.4.1 (a), for certain laser irradiation conditions a refractive index change can be achieved within the substrate. These material modifications can be extended along any arbitrary 3-D path by means of a multi-axis translation stage used in the inscription setup, as shown in Figure 2.1.

If the fabrication conditions are optimised so that a refractive index increase is achieved at the focus, the laser processed region forms the core of a waveguide, as shown in Figure 2.5 (a). Such waveguides fabricated by virtue of a direct net refractive index change in the material are termed as Type I waveguides [47, 67], and commonly observed in glass materials. In materials where Type I modification is not feasible, such as most single crystal and polycrystalline substrates, optical waveguides are written by inscribing damage lines. The inscribed lines of catastrophic damage induce a strain field in the material confined between the lines, resulting in a refractive index change via the stress-optic effect. Such waveguides are referred to as Type II waveguides, as shown in Figure 2.5 (b). Materials for which this type of waveguide fabrication is used include LiNbO$_3$ [51] and YAG [52]. Type I waveguides have significantly lower propagation losses compared to Type II, especially since Type II modification essentially relies on the fabrication of highly scattering centres to create the waveguiding effect.
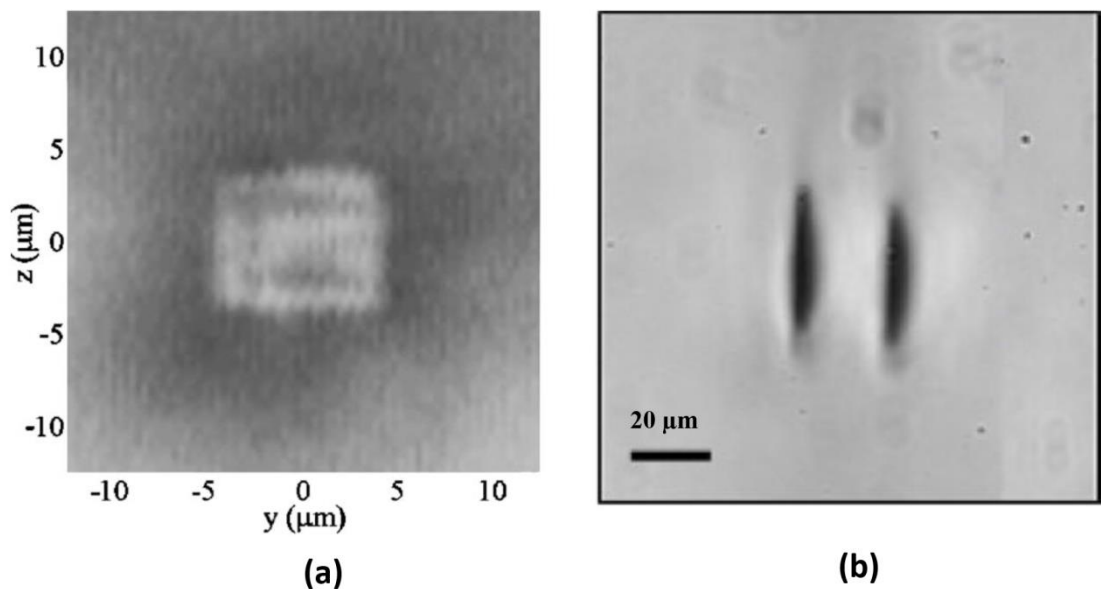
Figure 2. 5. End facet optical micrograph images of ULI waveguides. (a) Type I optical waveguide demonstrated in a silicate glass. Reproduced from [67] (b) Type II optical waveguide in YAG ceramic. Reproduced from Ref. [68].

In addition to Type I and Type II modifications, other novel inscription designs have allowed waveguide fabrication in materials that exhibit a negative refractive index change by ULI. These include double cladding [69] and depressed cladding structures [70], as shown in Figure 2.6. Based on the type of material modification, namely, laser-induced direct refractive index decrement, these structures can be classified as Type I. However, based on the core-cladding formation for light guiding, these structures are similar to Type II waveguides, with the laser-processed lower density regions forming the cladding.

The fabrication of low-loss guiding structures depends on the careful optimisation of the inscription parameters such as the laser wavelength, repetition rate, pulse energy, polarisation, sample translation speed and focusing optics. The following section details these deterministic parameters for ULI waveguide inscription.
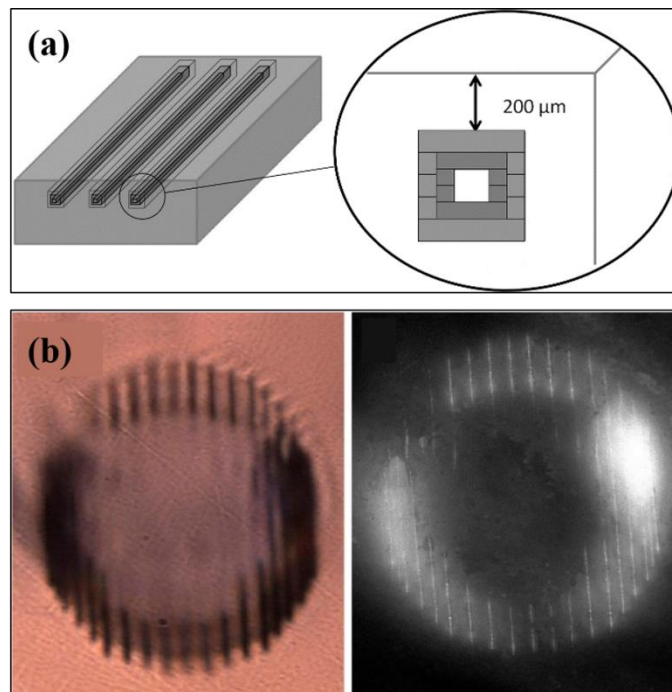
Figure 2. 6. (a) Double depressed cladding waveguide cross-section in Cr:ZnSe. The core of the waveguide is the non-irradiated Cr:ZnSe region. A negative refractive index change due to ULI forms the cladding. The secondary outer cladding is inscribed at higher pulse irradiances. Reproduced from Ref. [69]. (b) Optical micrograph and dark field images of depressed cladding waveguide structures in Cr:ZnSe with a circular cross-section. Reproduced from Ref. [70]. Field of view for the images is 100 × 150 μm.

2.5   Factors affecting ULI waveguide inscription

Optimal waveguide fabrication by ULI is achieved by a successful interplay of a variety of inscription parameters that depend on the inscription laser, steering and focusing optics, translational stage parameters, and ultimately, the material under study. The first step for any substrate involves waveguide inscription using a wide parameter range to estimate the ideal combination that provides low insertion loss waveguides. For certain substrates that are widely used for device applications, such as fused silica, the optimum parameters have been long established [59]. These working parameters serve as a platform for waveguide trials in new substrates. For a relatively new technology only just over 15 years old, optimal ULI waveguide parameters have been established for a wide number of substrates including glasses, crystals and polymers.

2.5.1   Material Parameters

The inherent properties of a material play an important role in the type of laser-induced material modification possible within it, and are discussed in this section. Since the material parameters for ULI inscription are fixed, the laser properties and other inscription parameters such as the focusing optics and translation speed have to be tailored according to each material in order to fabricate low loss waveguides.

Bandgap: Bandgap refers to the energy gap separating the valence band and the conduction band in the material. The important photoionisation processes, which drive the ULI technique, rely on the excitation of a valence band electron across this gap, and hence, the bandgap of the material is an important parameter. Specifically, the bandgap value along with the incident laser frequency determines the photoionisation mechanism achieved within the material. When the material bandgap is comparable to the single photon energy of the incident light, absorption occurs by multiphoton processes. The probability of multiphoton ionisation reduces with the number of photons required to bridge the gap. Thus, for incident photon energy lesser than the material bandgap, tunnelling ionisation dominates over multiphoton ionisation.

Nonlinearity: Material nonlinearity plays a vital role in laser-induced material modification. The high irradiances achieved at the focus of a laser pulse can drive other nonlinear processes instead of photoionisation. For example, self-focusing and

defocusing of the incident pulses leading to filamentation have been reported in highly nonlinear materials such as ZnSe [71]. Filamentation can be described thus; when self-focusing occurs for high irradiances of the incident pulse, it penetrates through the substrate until the irradiated material ionises leaving behind a column of plasma. This plasma contributes towards laser defocusing due to an interplay between laser-induced self-focusing and plasma-induced dispersion effects. These processes eventually lead to the formation of elongated structures of modified material, termed as filaments.

Impurities: The presence of impurities affects the type of photoionisation driving the ULI material modification. Impurities or defect sites in materials can introduce real energy levels within the material bandgap that can in turn facilitate linear absorption of photons. The resultant material ionisation process is avalanche ionisation. For precise laser micromachining, avalanche ionisation assisted by defect centres is not preferred since the ionisation rate depends on the randomly distributed impurities in the system. This makes the material modification highly erratic and non-repeatable.

Thermal Conductivity: For waveguide inscription at high laser repetition rates, where subsequent pulses are focused within the same volume even before the energy absorbed by the previous pulse has dissipated, heat accumulation effects occur. The accumulated heat eventually gets dissipated after the laser exposure is over. In such situations, the resultant material modification depends on its thermal conductivity. A material with high thermal conductivity allows faster heat dissipation and more uniform structures compared to a material with low thermal conductivity.

Symmetry: Certain crystals possess inherent asymmetries which affect ULI inscription. For instance, waveguide inscription at specific laser polarisation is favoured for certain crystals[72]. Another example is the non-reciprocal nature of ultrafast laser writing [73].

2.5.2   Laser Parameters

The properties of the inscription laser are extremely important for optimal waveguide fabrication. As we shall see in this section, the number of parameters, after excluding the material properties, which contribute to the laser-induced material modification, is about eight or more. A complete waveguide fabrication study by varying all these

parameters is not practical. Therefore, certain parameters are kept constant, such as the laser wavelength. The typically varied parameters include the laser pulse energy and the pulse repetition rate.

Pulse Energy: The material modification at the focal volume depends on the amount of energy deposited within it. This is dependent on the pulse energy of the laser, which is therefore a very important parameter. The size of the laser modified region is also affected by the pulse energy.

Laser Wavelength: Material processing of transparent materials by ULI requires the absence of linear absorption in the material. Therefore, the wavelength of the laser should be such that its single photon energy is incapable of exciting an electron from the valence band of the material to the conduction band. In other words, the energy of a single laser photon must be less than the bandgap of the material. In addition, ULI waveguides are found to exhibit unique wavelength-dependent properties. For example, waveguides in fused silica appear to have a lower loss for an inscription laser wavelength of 522 nm, compared to laser inscription at 1044 nm [74].

Laser Pulse Repetition Rate: In the case of multiple laser pulses falling in the same focal volume, thermal accumulation plays a very important role. The typical time scale for heat diffusion into the lattice is ~1 μs [75]. In the case of pulse repetition rates greater than ~ 1 MHz, a second pulse is incident before the absorbed heat from the first pulse diffuses away. As a result, the irradiated material experiences elevated temperatures. Once the series of pulses has left the focal volume, the heat diffuses out of the focal region in all directions. The resultant structural modification occupies a larger volume, causing a more isotropic structure and cross-sectional size. Figure 2.7 shows a systematic study of the waveguide cross-sections with respect to incident pulse fluence and pulse repetition rates. By varying the pulse fluence by four orders of magnitude, there is only a small increase in the size of the modified region, whereas, a massive increase in the structure size can be observed when changing the pulse repetition rate from 100 kHz to 1 MHz [76].

Polarisation: One of the factors affecting the efficiency of absorption of the incident laser is the polarisation of the beam. This is especially evident in crystal substrates,

where the laser absorption is related to the alignment of the crystallographic axis with respect to the incident laser polarisation [61, 77].

Pulse duration: The pulse duration of the inscription laser affects the nature of material modification and the resultant waveguide properties. For instance, as discussed previously, femtosecond laser inscription in highly nonlinear ZnSe material results in filamentation processes manifested as elongated modifications of ~ 80 µm length against the desired value of 9 µm. Since filamentation is dependent on the peak power of the pulse, the use of longer pulses of 1-2 ps was successful in eliminating the detrimental effects [69, 71].
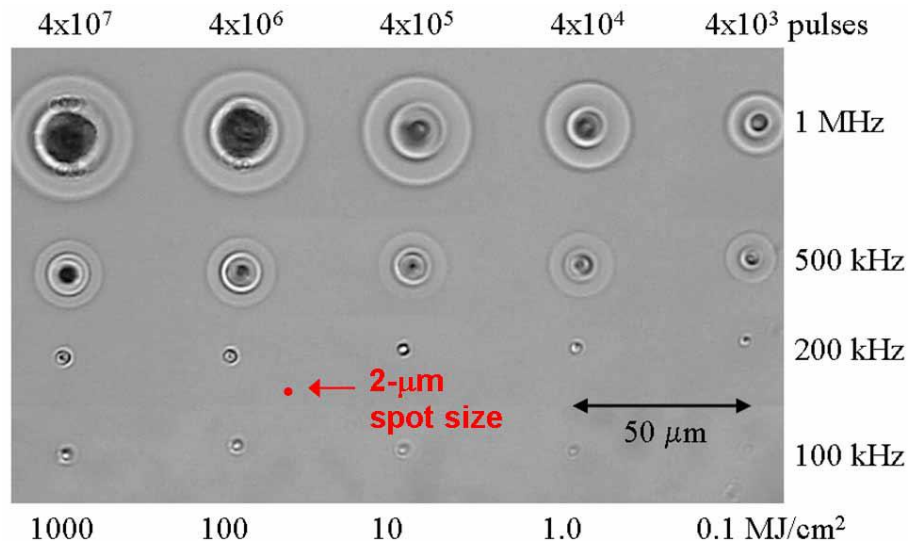
Figure 2. 7. Optical micrograph images of ULI inscribed structures with respect to increasing pulse fluences and laser repetition rates. Each row corresponds to waveguides written at a fixed repetition rate mentioned, but for different incident fluences. The material modification is found to increase rapidly with a change in the laser repetition rate over a change in the incident pulse fluence. Reproduced from Ref. [76].

2.5.3   Other Inscription Parameters

Inscription Geometry: ULI utilises two inscription geometries, namely, longitudinal writing geometry and transverse writing geometry; with their names being a good indication of the direction of laser inscription.

   (a) Longitudinal writing geometry: In this case, the substrate is translated along the same direction as that of the incident laser beam, as shown in Figure 2.8 (a). The

resultant waveguide has an inherently circular cross-section. In this case, the diameter of the inscribed waveguide is directly related to the focused beam waist. For 3-D inscription of waveguides requiring any bends in the inscription path, this writing configuration will alter cylindrical waveguides to induce an asymmetry in the structures, which is not desirable. Another disadvantage of this writing technique is its limited waveguide length, restricted by the working distance of the lens. Also, this writing technique is hampered by an increasing degree of spherical aberrations as a function of increasing depths [59].
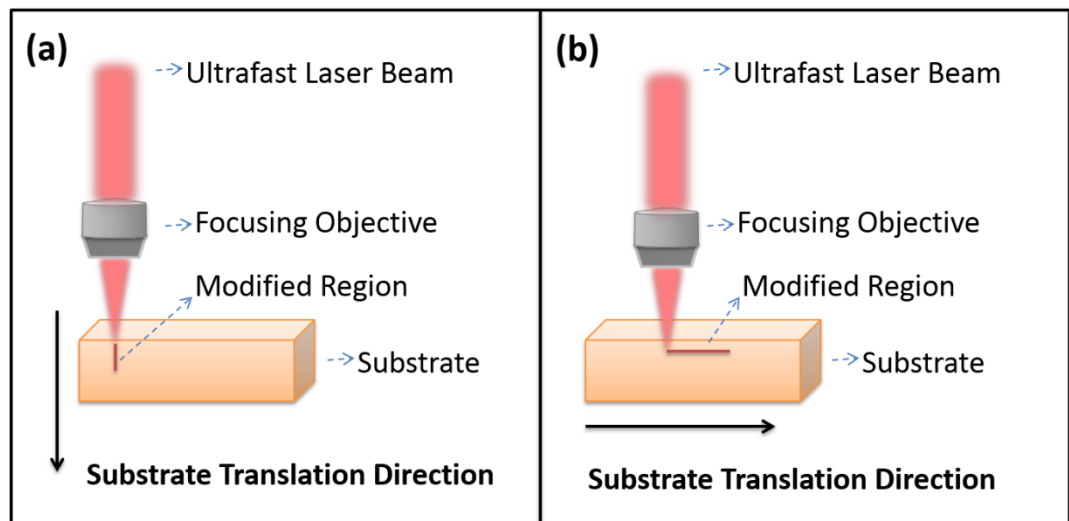
Figure 2. 8. Inscription geometries used for ULI. (a) Longitudinal inscription geometry, where the substrate is translated along the incident laser beam, and (b) Transverse inscription geometry, where, the sample translation is perpendicular to the incident laser beam.

(b) *Transverse writing geometry:* In this case, the substrate is translated in a direction perpendicular to the incident laser beam; see Figure 2.8 (b). This allows inscription of waveguides with arbitrary lengths and 3-D paths within the substrate. However, the cross-section of the inscribed region becomes highly asymmetric due to the contribution from both the confocal parameter and the beam waist diameter, as shown in Figure 2.9. In spite of this, the transverse writing geometry is preferred for ULI photonic device fabrication by virtue of its high flexibility. Also, a number of beam-shaping techniques have been introduced to resolve the limitation in terms of the waveguide asymmetry such as the use of a high NA objective, slit technique [78], cylindrical telescope [79], deformable mirror [80] and multiscan techniques [81].
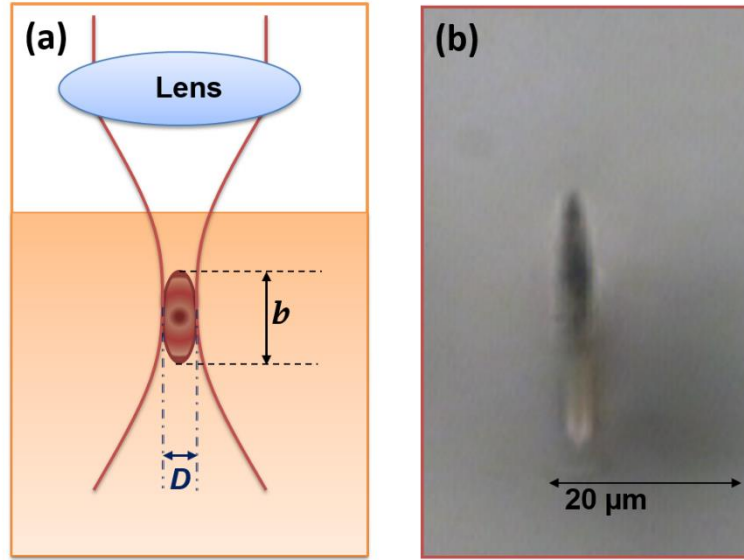
Figure 2.9. (a) The high degree of asymmetry in the waveguide cross-section for a transverse inscription geometry due to the unequal confocal parameter, b and beam waist diameter, D. (b) Single scan waveguide cross-sectional image obtained by the transverse writing geometry.

Focusing Optics: The focusing objective determines the spatial extent of the region modified by the incident laser beam, or, the focal volume. For longitudinal waveguide inscription geometry, the focal volume is solely dependent on the beam waist at the laser focus, resulting in inherently symmetric waveguides. The beam diameter at the focus is given as [59],

$$D = 2\,\omega_0 = \frac{2\,\lambda}{\pi \, . \, NA} \tag{2.11}$$

where *NA* is the numerical aperture of the focusing lens, λ is the incident laser wavelength, and ω_0 is the focused beam radius. In the case of transverse writing geometry, the laser irradiated region is dependent on two factors, namely, the confocal parameter and the beam waist at the laser focus, as illustrated in Figure 2.9. The confocal parameter (*b*) is given by the relation [59],

$$b = \frac{2\pi n \omega_0^2}{\lambda} \tag{2.12}$$

where n is the refractive index of the material under study at the incident laser wavelength λ, and ω_0 is the focused beam radius.

Sample Translation Speed: This is an important ULI parameter that allows control over the distribution of pulse fluence within the substrate. With increasing translational speeds, the amount of pulse energy deposited within the focal volume decreases thereby affecting the final material modification. This is an especially useful inscription parameter at high laser repetition rates, where faster translation speeds can be used to reduce heat accumulation effects.

2.6   Typical ULI Inscription Setups

This section describes the typical laser systems used for ULI waveguide inscription. While all the systems are effective in final material modification, there are distinct differences in the modification mechanisms induced using each laser system. The laser used for the work described in subsequent chapters is also given. Based on the repetition rates, inscription lasers can be classified into three types.

(a) *Low repetition rate lasers (1- 200 kHz):* The initial demonstrations of laser-induced waveguide fabrication employed regeneratively amplified Ti: Sapphire lasers working in the repetition rate regime of 1 – 200 kHz. This laser was chosen for ULI, mainly due to its ready availability in most research laboratories at the start of this technology in the late 1990s. The laser operated at a wavelength of 800 nm, with typical pulse energies of a few µJ and pulse durations of 50 – 200 fs. The lower repetition rates led to fabrication times for ULI devices that were extremely long, on the order of $20 - 100$ µm s^{-1}.

(b) *High repetition rate lasers (5 – 25 MHz)*: High repetition rate Ti: Sapphire systems with no amplifier stage have also been used for ULI. The typical pulse energies correspond to 20-100 nJ with pulse durations on the order of 10- 50 fs. While these lasers dramatically improved the material processing speeds from ~µm s^{-1} to ~cm s^{-1}, the laser setup was still complex.

(c) *Intermediate Repetition rate lasers (100 kHz – 5 MHz)*: Yb-doped fibre lasers and cavity-dumped Yb:KYW oscillators working at an intermediate repetition

rate regime of 100 kHz – 5 MHz, with pulse energies of the order of nJ to μJ have also been used for ULI [60]. These lasers have an operating wavelength around 1030 nm, close to the other laser systems, and have typical pulse durations of the order of few hundreds of fs. These systems provide a suitable balance between the laser repetition rate and the resultant material processing speeds. In addition, the lasers form a stand-alone unit with turn-key operation, favourable for industrial environments.

The laser system used for the work presented in subsequent chapters belongs to this category. The following section describes this laser system, as well as the other important components in the ULI inscription setup, as shown in Figure 2.10.
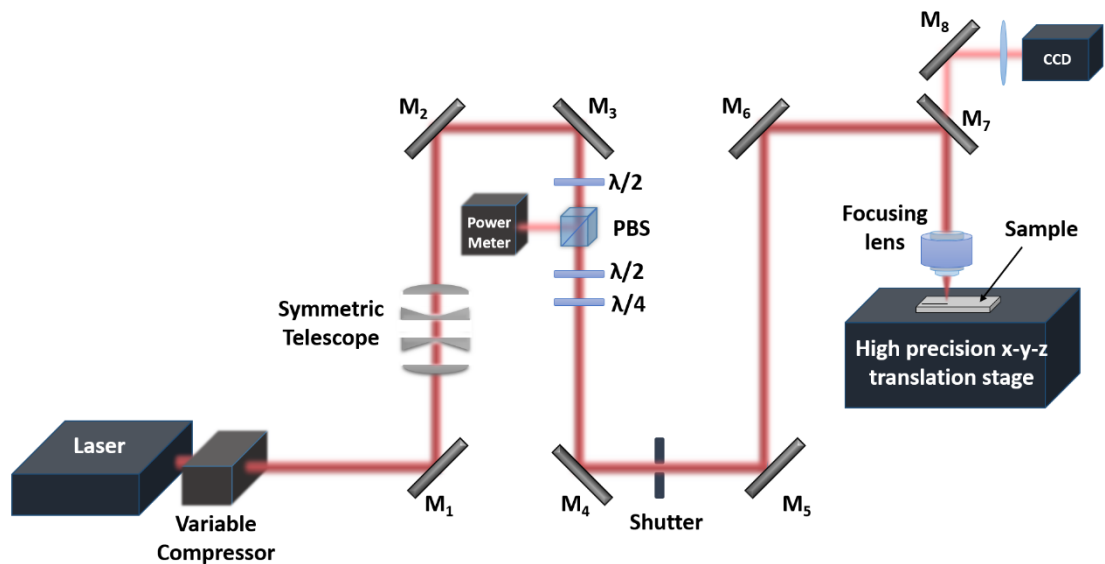
Figure 2. 10. Schematic diagram of the ULI inscription rig used for the work described in the thesis. The linearly polarised output from the laser is steered using mirrors M1 to M7 to be eventually focused within the bulk of a substrate using appropriate microscope objectives. A half-wave plate and polarisation beam splitter combination acts as the attenuator in the system. The polarisation state of the beam is controlled by the use of an additional half-wave plate, and a quarter-wave plate. The substrate is placed on a high precision translation stage system. The complete setup is computer controlled, including the translation stages, and the power and polarisation control.

Ultrafast Laser System: The laser system is a variable repetition rate Yb-doped fibre oscillator power amplifier system, IMRA FCPA μJewel D400. The repetition rate of the laser is adjustable from 100 kHz up to 5 MHz. The laser system also includes an adjustable compressor that can be used to change the pulse duration by varying the

linear chirp on the laser output, with the possible range varying from 350 fs to 3 ps. The laser produces linearly polarised pulses centred at an operating wavelength of 1047 nm, and is capable of producing an average power of ~350 mW at each repetition rate.

Steering and focusing optics: The linearly polarised laser output from the compressor stage is initially steered via various essential optics, indicated by the beam path from mirrors M1 to M7 in Figure 2.10, before it is incident on the focusing objective. A half-wave plate and polarisation beam splitter combination is utilised for a calibrated attenuation of the average power. This is followed by a second half-wave plate, which can be used to rotate the plane of polarisation of the laser, and a quarter-wave plate to obtain circularly polarised light. The rotation mounts for these optics are computer controlled, thereby allowing easy control of the power and polarisation of the inscription beam. The beam is subsequently steered using mirrors M4 to M7 to a vibration insensitive granite gantry and focused using the appropriate lens to a desired depth within the substrate. The substrate is placed on an automated high-precision, air-bearing x-y-z translation stage system, Aerotech ABL1000. An imaging system indicated by the beam path along M8 helps in precise positioning of the sample at the required depths.

As indicated in Figure 2.10, a transverse inscription geometry is employed for waveguide inscription. To compensate for the resultant asymmetric waveguide cross-section as shown in Figure 2.9, a multi-scan technique of waveguide shaping is used [81]. The schematic of this technique is given in Figure 2.11. In this technique, the sample is scanned through the laser focus multiple numbers of times, with each scan offset from the previous by a small distance. The scan offset is along the axis perpendicular to both the sample translation direction and the incident beam propagation axis. Thus, the inscription of multiple, slightly overlapping scans is used to build up a desired waveguide cross-section. To inscribe a single mode waveguide, typically 20 scans are used, laterally offset by 0.4 μm.

The multiscan technique is highly flexible, and convenient to implement. It allows fabrication of waveguides with close to square cross-sections, and almost step-index refractive index profile as previously shown in Figure 2.5(a). Also, since the waveguide cross-section is build up over many scans, the peak intensity used for laser inscription can be lowered. This, in turn, reduces the number of scattering and absorbing defects

within the modified focal volume. The resultant waveguides are characterised by low propagation losses in comparison with other ULI based waveguides [59].
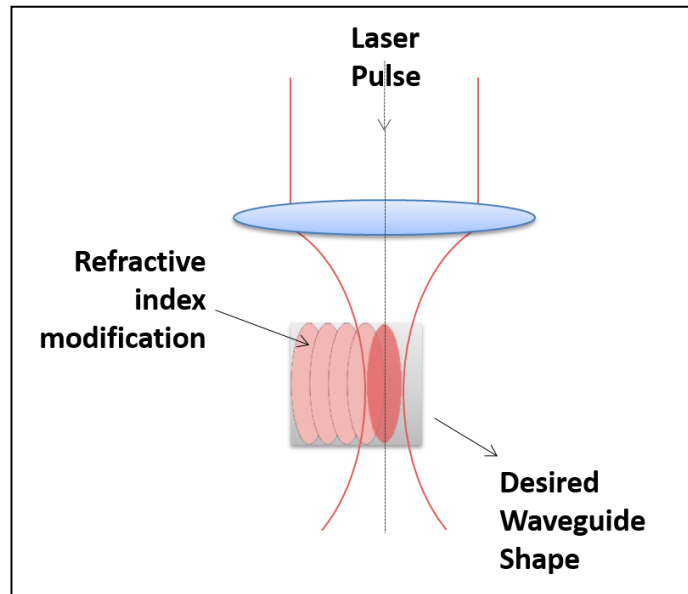
Figure 2. 11. Schematic of the multi-scan technique

2.7 Summary

This chapter introduced laser material processing by ULI technology. The underlying physical mechanisms of ULI leading to different structural modification regimes have been discussed. Each regime is characterised by its distinct properties and application potentials, the most widely used regimes being that of direct refractive index variation [47] and enhanced chemical etch rates [61]. The former has allowed a large number of waveguide based devices including passive splitters [49], couplers [82] and fan-outs [83] to active devices such as waveguide lasers [77] and amplifiers [67]. Enhanced chemical etch rates in certain materials have allowed the fabrication of microfluidic devices [61, 63-65], which additionally use ULI waveguides to process chips with enhanced functionalities. A few of these device applications, specifically active waveguide fabrication, will be discussed in the next chapter. The true 3-D capability of this technique suggests a high application potential for ULI, even leading to commercialisation of ULI based devices [84].

Chapter 3 – Review of ultrafast laser inscribed active photonic devices

3.1   Introduction

ULI has emerged as a versatile microfabrication tool for the development of novel photonic and microfluidic devices. In comparison with other waveguide fabrication technologies such as silicon-on-silicon, ion-exchange and sol-gel processes, ULI offers a maskless direct-write technique with true 3-D fabrication capability. These different features have resulted in a wide application regime for ULI including the fabrication of passive optical components, active waveguide devices and microfluidic channels [43].

ULI-based passive photonic circuits range from existing device architectures such as splitters, directional couplers and interferometers [49] to novel passive structures, for example, a photonic lantern [85]. A photonic lantern combines the output of 4×4 array of single-mode (SM) waveguides into a single multimodal (MM) output, or vice versa, as shown in Figure 3.1. This design can be scaled to accommodate many more SM waveguides. The waveguide design in such a case has extremely exacting tolerances as do the inscription parameters that allow low insertion loss waveguides <2 dB [49]. Since efficient functioning of these passive structures has a critical dependence on low-loss waveguide inscription by ULI, the typically used substrates are constrained to a few materials such as fused silica and borosilicate glass, that have been well-characterised over the years for ULI waveguide fabrication [49].
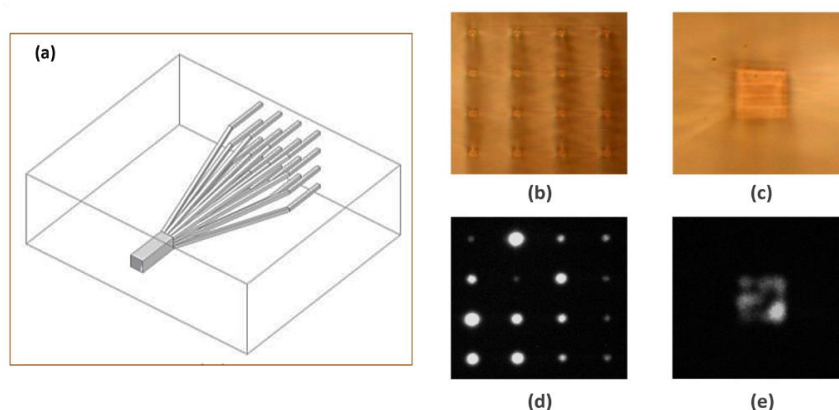
Figure 3. 1. (a) Design sketch of a MM to SM integrated photonic lantern transition, or vice versa. (b) White light transmission micrographs of the 4×4 SM array, (c) the MM output end. (d) The SM array end of the PL for an input light of 1539 nm at the MM end. (e) The MM end while adjusting the injection of 1539 nm light into the opposite end. Reproduced from Ref [85]. The field of view is 200×200 μm for (b) and (d), and 100×100 μm for (c) and (e).

Another ULI application regime, namely, active waveguide fabrication, arises from the versatility of the technology in terms of inscription substrates. ULI is applicable to a wide variety of materials, including active-ion doped glasses and crystals, by a suitable optimisation of irradiation parameters such as wavelength, pulse energy, repetition rate, focusing optics and sample translation speed. This has given rise to active research in the field of waveguide amplifiers and lasers. Waveguides based on Er and Er:Yb doped materials find useful applications as amplifier systems in the telecom C-band [86]. Lasers based on active ULI waveguides serve as compact sources for a broad spectral range from the visible [87] to the mid-IR [70] region of the electromagnetic spectra. The first fs-laser-written waveguide laser was demonstrated in 2004 in an Er:Yb doped phosphate glass, generating 1.7 mW laser output at 1534 nm, and having a low slope efficiency of 2% [88].

Subsequent developments in the field have been targeted at improving the laser performance in terms of slope efficiency, power scalability, operating wavelength and design architectures. Investigations of new gain materials play an important role in this. Consequently, ULI-based waveguide lasers have been demonstrated in a variety of glasses such as silicate, phosphate and bismuthate [49, 89, 90], as well as crystals, such as YAG [49] and double tungstates [91]. Such waveguide lasers find useful applications in areas requiring compact, high efficiency laser sources that are less susceptible to environmental disturbances, for example, compact laser radar and remote sensing [92]. Laser operation has been reported in a number of ULI waveguides, with the commonly used active dopant ions being Er [88, 93, 94], Nd [90] and Yb [95]. Pulsed laser operation has also been demonstrated from ULI waveguide lasers by the incorporation of SAs within the cavity [89, 96, 97].

A third application regime of ULI waveguides includes microfluidics. As discussed in the previous chapter in Section 2.4.1, fs laser processing can introduce a nanograting regime of material modification that results in an enhancement in chemical etching sensitivity. This unique property allows the fabrication of embedded microfluidic channels within substrates. Such structures can also be combined with ULI based optical waveguides to create monolithic devices well-suited for compact LOC devices [63]. Aqueous solutions of hydrofluoric acid or potassium hydroxide are typically employed to etch laser-inscribed structures in fused silica [98]. Recent studies have

shown selective etching of ULI tracks in a new substrate, namely, YAG, using an aqueous solution of orthophosphoric acid [99].

Within this wide range of applications of ULI, the work presented in this thesis focuses on the applicability of ULI for active photonic devices in glasses, specifically, waveguide lasers. In order to facilitate an understanding of the experimental work in subsequent sections, this chapter provides an overview of ULI waveguide laser development in transparent glass substrates. Section 3.2 describes the spectroscopic properties of the typically used rare-earth ions; Er, Nd, and Yb, along with their associated energy transfer processes. Section 3.3 introduces the mode-locking technologies for solid-state lasers, with emphasis on SA mode-locking. Finally, section 3.4 gives a brief review of ULI-based waveguide glass lasers.

3.2   The Rare-Earth Ion

Rare-earths constitute a set of seventeen elements in the periodic table including Scandium with the atomic number of Z= 21, Yttrium with Z =39 and the fifteen lanthanide elements. The lanthanides extend from Lanthanum with Z = 57, increasing progressively in atomic number to Lutetium with Z= 71. In their atomic shell, these lanthanide elements have an electronic configuration of [Xe] $6s^2$ $4f^n$, where [Xe] represents a stable Xenon core. The number of electrons n in the $4f$ orbital increases from 1 to 14 depending on the atomic number and oxidation state. In an ionic matrix, rare-earths predominantly exist in the +3 oxidation state, losing the two outer $6s$ and one of the $4f$ electrons to the surrounding matrix. The $4f$ electrons in rare-earths constitute the valence electrons; however they are strongly shielded from the surrounding environment by the fully occupied outer $5s$ and $5p$ orbitals. These electrons are therefore more analogous to core electrons that are tightly bound to the nucleus than to valence electrons.

In a doped matrix, the rare-earth ions replace host ions of similar size and same valency. The different energy transitions occur within the various states within the $4f$ orbital, which arise as a result of electron-electron and electron-host interaction. When a rare-earth is introduced in a host material, the local electric field around the rare-earth ion couples itself to the electrons of that ion. The coupling causes a splitting in the rare-earth energy levels. This splitting of spectral lines of atoms or molecules due to

presence of an external electric field is termed the Stark effect. In ordered solids such as crystals, the splitting of rare-earth spectral lines is uniform across the whole lattice, resulting in sharply defined pump and laser transitions with a small gain bandwidth of 1 nm or less [100].

A much broader bandwidth ~100 nm is typical of rare-earth doped glasses [101]. When a rare-earth ion is introduced in the disordered glass network, the splitting is unequal for each dopant across the substrate since the electric field varies from site to site. This results in the broadening of the emission spectrum of the embedded rare-earths [102]. The broad bandwidth thus achieved in glasses makes them suitable candidates for wavelength tuning and ultrashort pulse generation [100]. The random network structure of glasses also gives them the unique ability to dissolve a wide range of dopants in varied concentrations. Therefore, while the host plays a significant role in the *4f* energy level splitting, the subsequent transition features such as the wavelength of emission and transition cross-sections are largely insensitive to the environment by virtue of the optically passive *5f* orbital shield. This is especially significant for active device applications.

3.2.1 Energy transfer mechanisms in rare-earth ions

The performance of rare-earth doped glasses as effective laser materials is determined by the various interactions and energy transfer processes within the ions. The excitation of a rare-earth ion to higher lying energy levels in the *4f* orbital can occur either by direct radiative absorption or via energy transfer. The subsequent relaxation to the ground state can occur in the following different ways:

(a) *Radiative decay:* This corresponds to the relaxation of an excited ion to the ground state by the emission of photons. The emitted photon typically constitutes the useful transition for laser and amplifier applications.

(b) *Non-radiative decay:* This refers to the process where the ions relax to the ground state by transferring the absorbed energy to the surroundings, as vibrational quanta or phonons.

(c) ***Non-radiative energy transfer:*** This process refers to the transfer of energy between adjacent rare-earth ions resulting in degradation in excitation or radiative emission.

Rare-earth doped media exhibit characteristic ion-ion interactions based on these three basic relaxation transitions. The interaction can be between ions of the same rare-earth species or different ions. The former usually result in detrimental loss mechanisms in the system such as increased non-radiative decay routes, or undesired luminescence effects. Between ions of different rare-earths, the corresponding energy transfer mechanisms can be useful, such as novel pumping schemes. These will be described in the following section.

(1) ***Multi-phonon transitions***: This process refers to the relaxation of an excited state rare-earth ion by a non-radiative transition involving simultaneous emission of multiple phonons. The process is illustrated in Figure 3.2(a). Being quantised packets of vibrational energy, the phonon energy varies with different lattice configurations. Subsequently, the rate of multi-phonon transition decreases exponentially with an increase in the number of phonons required for the transition. It occurs only when a small number of phonons are required to close the energy gap between the transition states of the rare-earth ion. This process is a major factor that is responsible for depopulating upper excited states in rare-earth ions.

(2) ***Resonant Radiative transfer***: This type of energy transfer refers to situations where a photon emitted by one ion is reabsorbed by another ion of the same or different species, as shown in Figure 3.2 (b). The process is termed as 'resonant' as the two transitions, namely, emission and absorption, have equivalent photon energies. This process therefore occurs in identical ions or in ions with similar energy levels. The process represents a possible loss mechanism in useful photoluminescence pathways.

(3) ***Resonant non-radiative transfer***: The schematic of this energy-transfer process is given in Figure 3.2 (c). In this process, a rare-earth ion in an excited sate decays to the ground state by non-radiative energy transfer. Thus, the energy of

the excited rare-earth ion is transferred to an adjacent ion, resulting in the relaxation of the first ion meanwhile promoting the second to an excited state. Again, the process is termed as 'resonant' since the energies involved are equivalent for the two rare-earth ions.
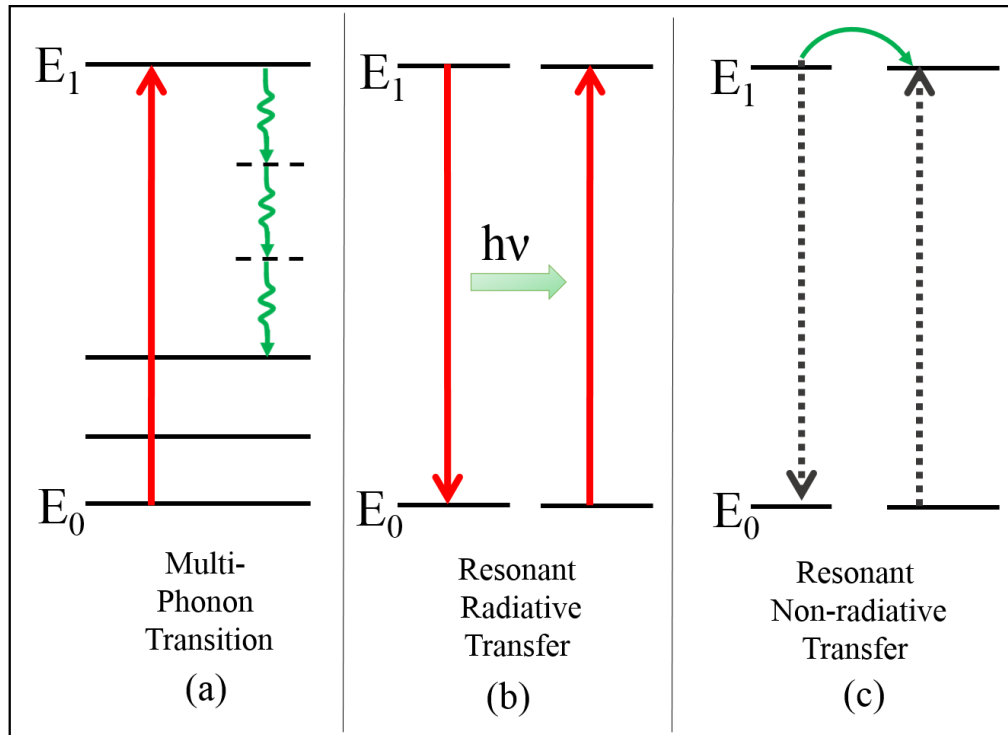
Figure 3. 2. The various energy transfer mechanisms in rare-earth ions. (a) Multi-phonon transitions (b) Resonant radiative transfer (c) Resonant non-radiative transfer.

Non-radiative energy transfer between identical rare-earths is detrimental, resulting in degradation in rare-earth luminescence. Between ions of different rare-earths, the process can however be useful. An example includes sensitised luminescence, whereby the excitation provided to one rare-earth species is transferred to another, resulting in efficient luminescence from the latter. This is prevalent in Yb: codoped Er systems, as shown in Figure 3.3 [88]. Er ions have a weaker absorption cross-section at the pump wavelength compared to Yb. Yb ions therefore act as a sensitiser to increase the pump efficiency at ~980 nm. The absorbed energy is transferred to the nearby $^4I_{11/2}$ state in Erbium ion by non-radiative energy transfer, resulting in a higher absorption cross-section than direct excitation of Er ions at that wavelength. When the concentration of Yb ions is high, the absorbed energy initially migrates between the different Yb^{3+}

ions by non-radiative energy transfer, until it finally reaches an Er^{3+} ion in close proximity for energy transfer.
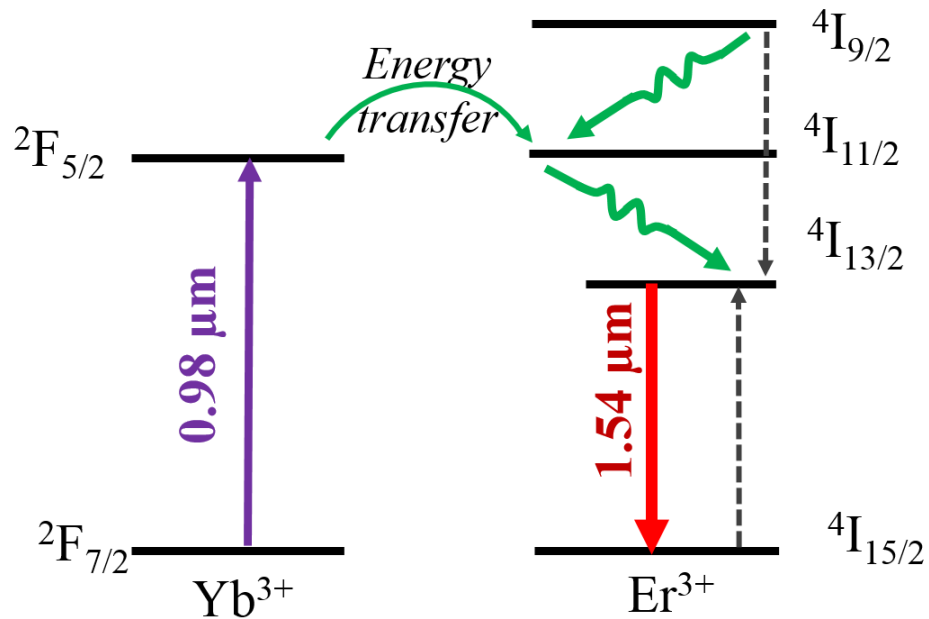
Figure 3. 3. Sensitised energy transfer mechanism in Er:Yb systems. Indicated electronic transitions include pump and laser emission (solid line), fast non-radiative decay (wavy lines) and cross-relaxation (dashed lines). Adapted from Ref. [103].

(4) ***Cross-relaxation***: In a cross-relaxation process, the energy of a rare-earth ion that is decaying from an upper excited state is absorbed by an adjacent ground state ion to promote it to a metastable level. This is illustrated in Figure 3.4(a), where the energy of the ion A decaying from an upper level E_2 to an intermediate level E_1 is transferred to a neighbouring ion B to excite it to the same level E_1.

When the energy gap between the intermediate and ground state levels has an efficient phonon generation route, both ions decay non-radiatively to the ground state (E_1- E_0). This process is detrimental to laser action, and can be observed in laser glasses doped with Nd^{3+} ions, where the original absorbed energy gets effectively converted into heat [104].

If the E_1- E_0 transition is radiative, this results in laser action with an increased efficiency, for example, in Er-doped systems. In Er ions, as shown in Figure 3.3,

the energy difference between $^4I_{9/2}$ and $^4I_{13/2}$ is close to that between $^4I_{13/2}$ and $^4I_{15/2}$. The population in the metastable state $^4I_{13/2}$ can be increased as a result of cross-relaxation; by the decay of an ion from the $^4I_{9/2}$ state and the following excitation of a ground state ion to the $^4I_{13/2}$ state.
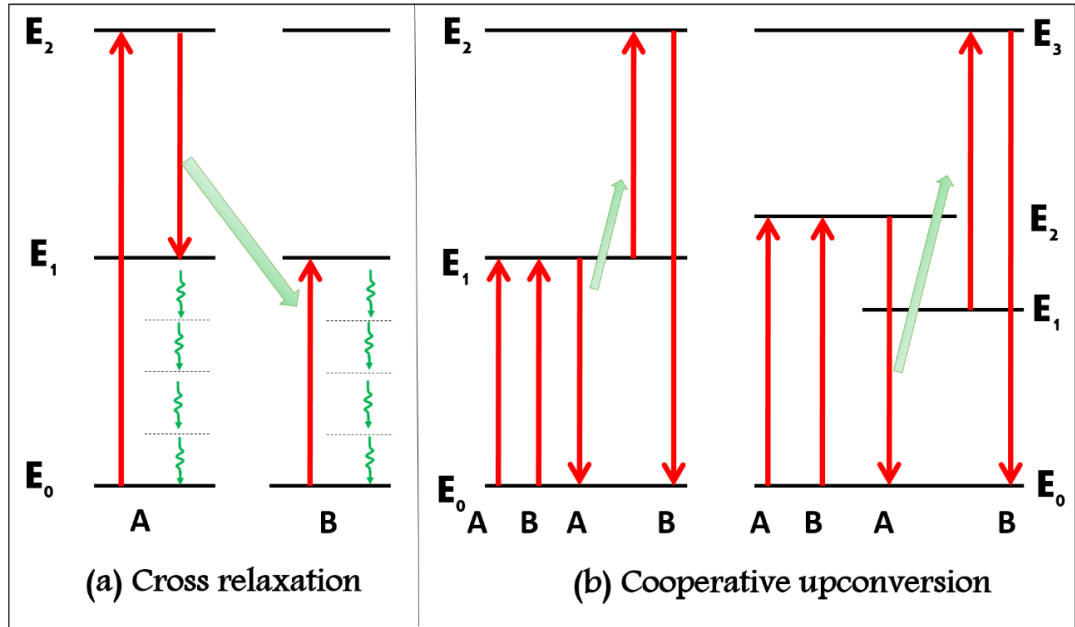
Figure 3. 4. (a) Cross-relaxation process (b) Cooperative upconversion. A,B are two different rare earth ions of the same species.

(5) ***Cooperative upconversion***: Cooperative upconversion occurs by the interaction of rare-earth ions present in the excited state, where, the excitation energy of one ion decaying to a lower energy level is absorbed by the other to promote it to an even higher energy level. This is shown in Figure 3.4(b), where A and B represent two ions in an intermediate state E_1. The energy of the ion A decaying from this level is transferred to the neighbouring ion B to excite it to higher lying level, E_2 (or E_3, as shown in Figure 3.4(b) on the right). The ion in the upper excited state can decay either by multi-phonon emission or by the emission of photons. The latter is used in upconversion lasers [105], where a pump of a lower frequency is used to generate a large laser photon energy. Examples include visible lasers pumped with infrared light, for example, a Tm:YLiF$_4$ blue upconversion laser emitting at 450.2 nm, achieved using CW pumping with Ti: Sapphire laser at 784.5 nm [105].

(6) **Excited state absorption:** In this process, an ion excited to a metastable state can absorb another pump photon to move to even higher lying levels. This can sometimes result in an excited metastable level, which provides an alternate laser path at a different wavelength. Usually, the electrons undergoing this process decay non-radiatively to the ground state.

(7) **Concentration Quenching**: This refers to a reduction in fluorescence intensity from the sample with increasing rare-earth concentrations. For rare-earth concentrations beyond a critical amount, the ions tend to interact with each other to form clusters or new rare-earth compounds that are optically inactive. This results in a decrease in fluorescence intensity, adversely affecting the efficiency of radiative transitions in the material.

The laser action of a rare-earth doped glass is also influenced by the properties of the host material. The glass host compositions can be controlled during the glass formation by varying either the concentration of glass network formers such as silicates and phosphates, or the concentration of network modifiers such as alkali and alkaline earth ions, or by varying both [106]. High power glass lasers based on rare-earth dopants require the corresponding glass hosts to possess a number of characteristics. Glass hosts ideally require a high thermal conductivity and a good thermal shock resistance [107], so that the laser action is not affected by any drastic change in temperature, and so that, the glass can withstand radiation capable of producing heat-induced stress fracture [108]. For high power laser applications, glasses are also ideally required to have a low nonlinear refractive index change, to avoid any undesirable nonlinear effects.

The first glass laser was demonstrated in 1961 by E. Snitzer in Nd-doped glass [109]. The rare-earth ions that have since been more commonly used include neodymium, erbium, ytterbium, holmium and thulium. The following section discusses the spectroscopic properties of three of these, namely, Nd, Yb, and Er ions.

3.2.2 Neodymium

Neodymium, with its atomic number of 60, has an electronic configuration of $4f^3$. Figure 3.5 shows the energy level scheme of Nd^{3+}, with four possible pump transitions, at 520, 580, 730 and 800 nm. The electrons excited from the ground state $^4I_{9/2}$ to these

energy levels relax non-radiatively to the metastable $^4F_{3/2}$ energy level. The primary laser transition occurs for $^4F_{3/2}$ to $^4I_{11/2}$ transition resulting in an emission wavelength around 1.05 μm. Nd has a 4-level energy scheme since the lower laser level $^4I_{11/2}$ is coupled to the ground state $^4I_{9/2}$ by fast non-radiative decay.

The most significant feature of Nd-doped systems is their inherently efficient operation with low pump thresholds, facilitated by the 4-level scheme. The emission properties depend on the host material, as discussed before. The peak emission wavelength for instance, changes from 1.049 μm in the case of ZBLAN to 1.064 μm in YAG, for a pump wavelength of 808 nm [100].
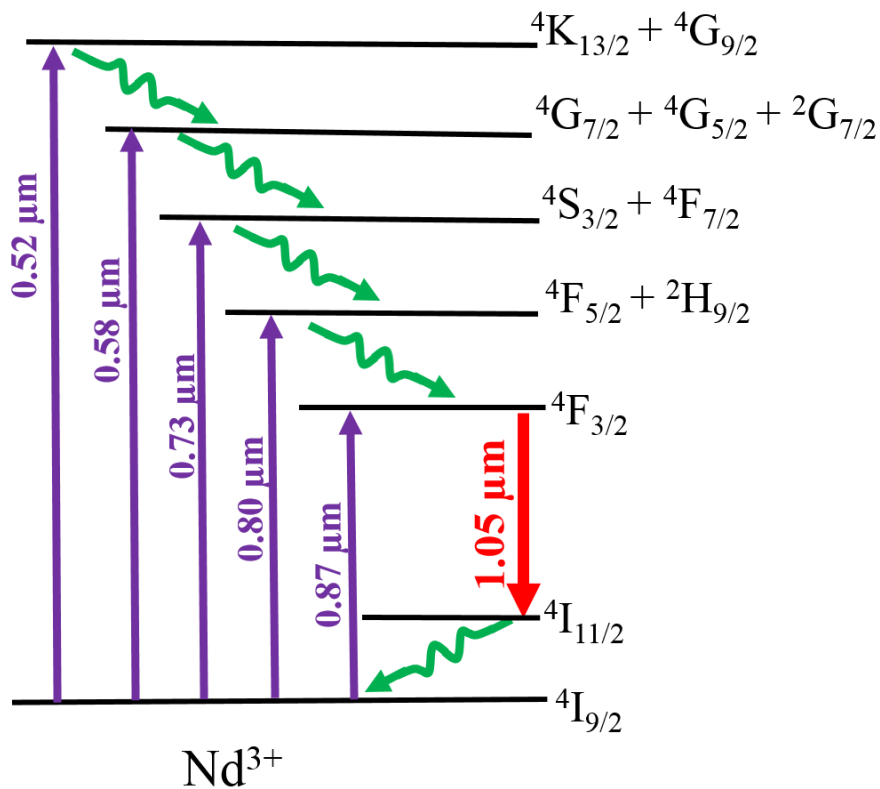
Figure 3. 5. Typical energy levels for Nd^{3+}. The indicated electronic transitions include: pump and laser transitions (solid lines), and fast non-radiative decay (wavy lines). Adapted from Ref.[103].

3.2.3 Ytterbium

Ytterbium, with an atomic number of 70, is a strong contender with Neodymium as an activeion for laser development in the NIR. Ytterbium has an energy level scheme

comprising of two electronic states, namely, $^2F_{5/2}$ excited state manifold, and $^2F_{7/2}$ ground state manifold. Pumping and laser transitions occur between the various Stark levels of each manifold. The highest energy sub-level of the ground state functions as the lower laser level, thereby making Yb-doped systems work as a quasi-three level laser, as shown in Figure 3.6. The pump wavelength in Yb^{3+} doped systems can be varied from 0.9 µm to 1 µm, with the main laser transition centred at 1.03 µm.
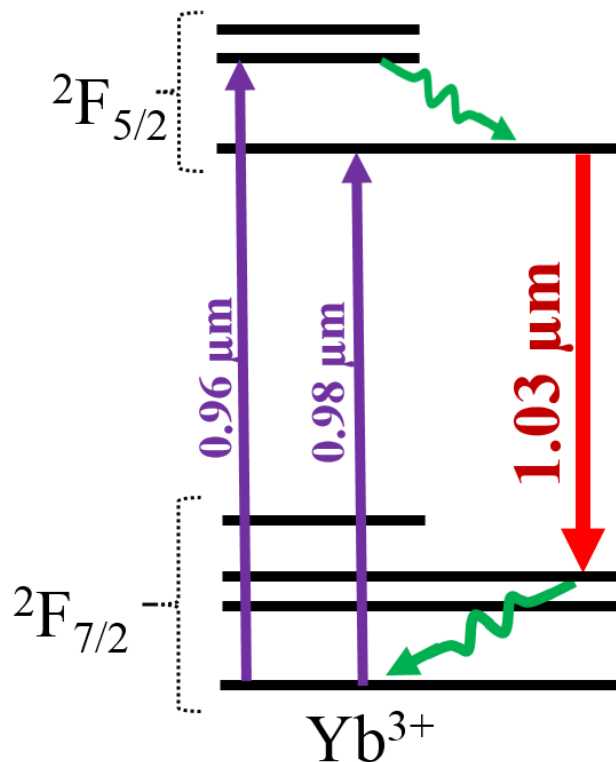
Figure 3. 6. Energy level diagram of Yb-doped systems. The solid lines indicate the pump and laser transitions, and the wavy lines indicate fast non-radiative decays. Adapted from Ref.[103]

As a result of the quasi-three level scheme, implies that Yb-doped systems typically exhibit higher thresholds for population inversion than Nd-doped four-level lasers. However, this limitation has been overcome due to advances in high power laser diodes that serve as pump sources. The presence of only 2 energy levels in Yb, $^2F_{5/2}$ and $^2F_{7/2,}$ ensures the absence of various detrimental effects such as excited state absorption and cross-relaxation [110]; making them attractive for high power laser development. This is re-enforced by the high efficiency inherently attainable from Yb-lasers by virtue of the small quantum defect, which is the difference in energies between a pump and a

signal photon. When doped in glass matrices, the inhomogeneous broadening in the system results in a broad bandwidth of ~100 nm, making Yb-doped glasses attractive for ultrafast laser applications as well as wavelength tuneability.

Yb-doped laser systems typically use a fibre laser architecture to allow efficient heat dissipation that in turn reduces the pump-induced thermal loading that occurs at high pump intensities. High power fibre lasers with output powers ~1 kW have been demonstrated using Yb-systems [111]. The same advantage is applicable in ULI-waveguide lasers.

3.2.4 Erbium

In Er^{3+} doped glasses, the laser and amplifier operation occurs at 1.5 μm, which corresponds to the C-band of the telecom window. Figure 3.7 shows the energy level diagram of an Er^{3+} doped laser system, with the main laser transition occurring between $^4I_{13/2}$ and $^4I_{15/2}$ energy levels. In the three-level laser system, erbium ions are excited to the $^4I_{11/2}$ band by a 980 nm pump. This is followed by multi-phonon decay to the metastable state $^4I_{13/2}$. Er^{3+} ions can also be excited to higher lying levels using other pump wavelengths, from which, they decay non-radiatively to the $^4I_{13/2}$ metastable level. Erbium can also function as a quasi-two-level laser system, since the absorption cross-section of the metastable state $^4I_{13/2}$ is higher than the emission cross-section of the ground state $^4I_{15/2}$. In this case, electrons are excited to the upper state of the $^4I_{13/2}$ band using a 1480 nm pump, from where they decay non-radiatively to the metastable level.

Often, Er systems are co-doped with Yb dopants. Yb ions have a higher absorption cross-section at 980 nm compared to Er, and thus, in Er:Yb systems, inversion of Yb ions by the pump results in an indirect pumping of the Er system by resonant energy-transfer mechanisms, as shown previously in Figure 3.3.

The laser action in Er^{3+} doped media is affected by a number of factors. Excited state absorption takes place in the three-level system, where, an electron pumped to the $^4I_{11/2}$ level absorbs another pump or signal photon to enter one of the higher lying energy levels of Er. The decay process is also determined by the properties of the host glass. In oxide glass, the ion excited from the upper laser level of $^4I_{13/2}$ to $^4 I_{9/2}$ decays non-radiatively back to the metastable state, whereas for fluoride glasses, non-radiative

decay from $^4I_{9/2}$ to the ground state occurs, thereby further reducing the laser efficiency [112]. There is also the possibility of cooperative upconversion; see Figure 3.4(b). In this case, two excited ions interact such that one ion de-excites to the ground state while the other gets excited to even higher energy states. The decay of electrons from the excited states occurs by multiphonon emission.
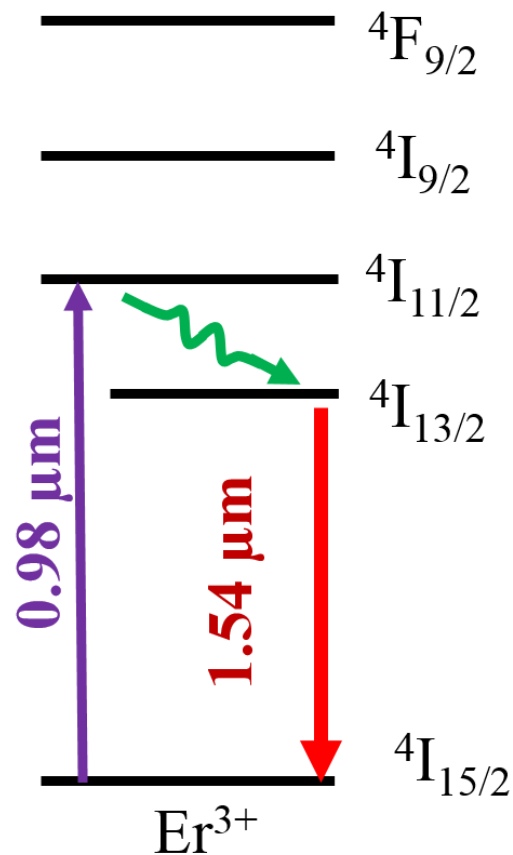
Figure 3. 7. Energy level diagram of an Er-doped laser system. The solid lines indicate the pump and laser transitions, and the wavy lines indicate fast non-radiative decay.

3.3 Passive mode-locking techniques for ultrafast lasers

Rare-earth doped lasers generating ultrashort pulses present a well-developed field, driven by their wide application realm. The applications of ultrafast lasers range from supercontinuum generation [113, 114], material processing [115], telecommunications [116] to life sciences [117]. In this regard, ultrafast waveguide lasers also have a broad application potential, along with the inherent advantages of their waveguide configuration. Short pulse generation is typically achieved by mode-locking techniques, either active or passive. While active mode-locking generates short pulses by means of

a sinusoidal loss modulation created by either acousto-optic or electro-optic modulators inserted in the laser cavity, passive mode-locking produces short pulses by self-amplitude modulation using a real or artificial SA. The latter includes KLM, already discussed in Chapter 1.

Generally, passive mode-locking techniques allow much shorter pulses of fs duration compared to the ps pulse duration achieved in active mode-locking. This is attributed to the inherently fast recovery time of the SA, which can modulate the resonator losses much faster than an electronic modulator. Most passive mode-locking techniques are also self-starting, an exception being KLM. In addition, SAs can be incorporated in laser cavities while preserving their compact and integrated cavity designs. This feature is frequently exploited in fibre laser development where CNT-SAs and graphene-SAs are integrated within fibre connectors to preserve an all-fibre format. This applicability is very important in waveguide laser systems as well, making passive mode-locking more favoured compared to active mode-locking.

The principle of mode-locking by an SA involves intensity-dependent absorption. At low intensities, SAs absorb all of the resonant light pulse, or exhibit high losses of the circulating radiation. At high intensities, the absorption is saturated due to the depletion of all the electrons in the ground state, which in turn allows increased transmission of the incident pulse. In a laser cavity, low intensity CW radiation is typically absorbed by the SA. The SA however favours any high intensity spikes in the cavity that arise due to noise fluctuations, initiating pulsed operation. Thereafter, when an intense pulse propagates through the SA, the central part of the pulse with its higher intensity gets transmitted while the edges of the pulse with lower intensities get absorbed. This results in a shortened pulse [118].

The SAs used for the initial studies in passive mode-locking include organic dyes [119] and SA-crystals such as Cr^{4+}:YAG [120]. Presently, the most important type of SA in use is SESAMs [118]. Relatively recently, novel SAs based on carbon nanostructures [35] have also emerged, namely CNT, and graphene. Typically, SAs are incorporated into mirror structures for ease of introducing them into laser cavities. The corresponding structures are termed as saturable absorber mirrors (SAM), a typical example being SESAMs. They can also be incorporated into the output coupler mirror in a laser cavity

(SA-OC); the output coupler being the semi-transparent mirror used to extract useful laser output. The characteristic properties of a SAM are detailed below.
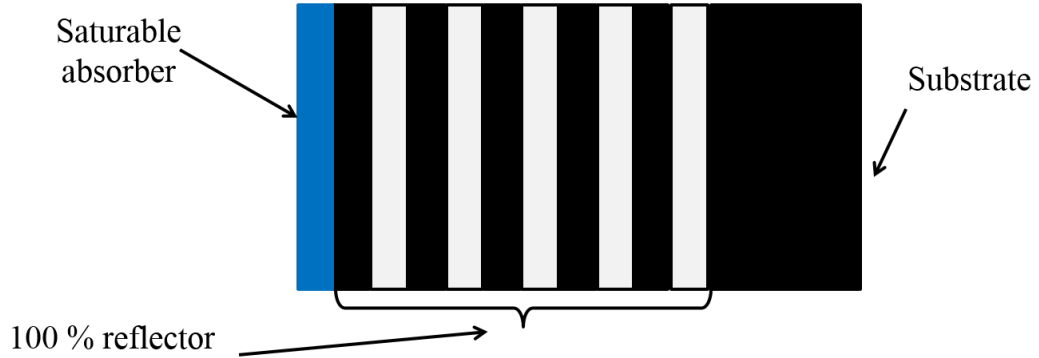
Figure 3. 8. Typical structure of a saturable absorber mirror. The SA is deposited on a mirror structure, which is often a Bragg mirror. A typical saturable absorber consists of a quantum well or layer of quantum dots in the case of SESAM, or, graphene- or CNT-SA, otherwise.

A SAM typically constitutes a ~100% reflectivity mirror structure with the SA forming the top layer or top coating, as shown in Figure 3.8. An SA-OC differs from a SAM by the partial reflectivity feature in the mirror structure. In the case of SESAMs, the semiconductor SA is typically a quantum well or layer of quantum dots. CNT and graphene SAs can also be incorporated as top coats in the mirror structures.

The important parameters that define a SA include modulation depth ΔR, relaxation time τ and saturation fluence F_{sat}. By varying these properties, SAMs can be custom designed according to specific application requirements. The following section defines these parameters based on the example of a SESAM.

A typical fluence dependent reflectivity curve of a SESAM is shown in Figure 3.9. The modulation depth, ΔR is defined as the amount of saturable absorption offered by the SA. In Figure 3.9, R_{lin} corresponds to the linear reflectivity and R_{ns} is the reflectivity of the SAM at the pulse energy fluence where the absorption is saturated. The modulation depth, ΔR, is then given as,

$$\Delta R = R_{ns} - R_{lin} \tag{3.1}$$
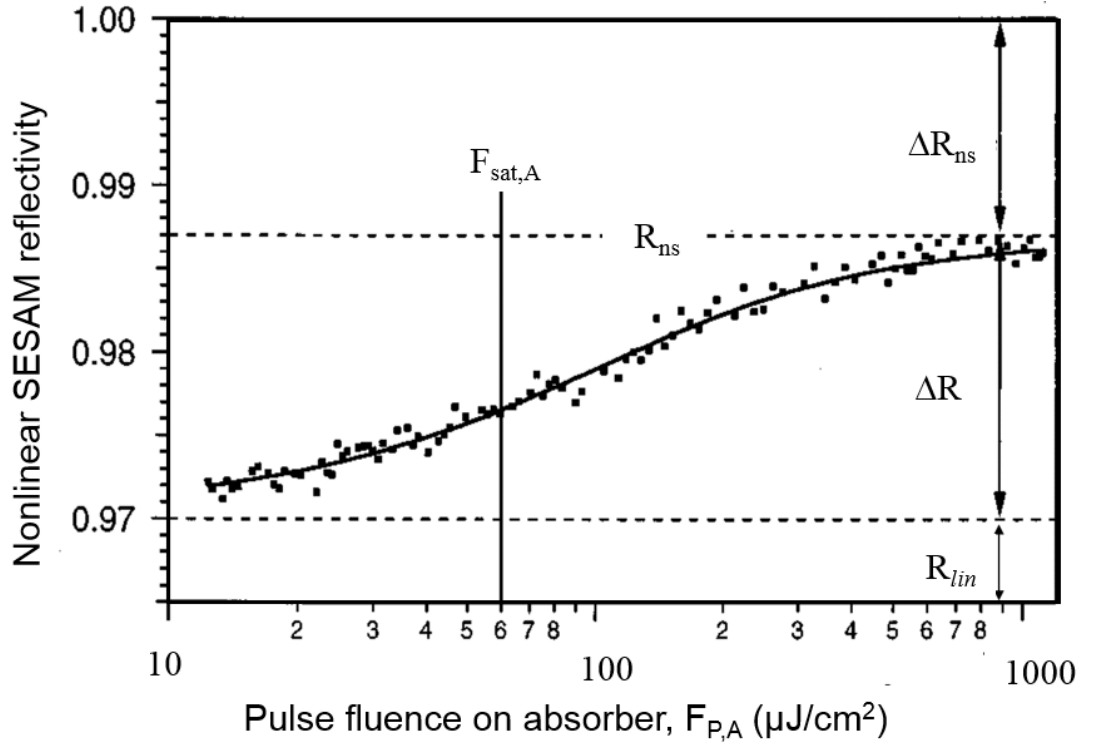
Figure 3. 9. The characteristic curve of nonlinear reflectivity R versus incident pulse fluence Fp. R_{lin}: linear reflectivity, R_{ns} : reflectivity for saturated absorption, ΔR: modulation depth, ΔR_{ns}: non saturable losses. F_{sat} : saturation fluence. Reproduced from Ref. [121].

In addition to linear and nonlinear absorption, there can also be some unwanted losses in the SAM due to scattering and non-saturable absorption, referred to as non-saturable losses ΔR_{ns}. It is given by the expression,

$$\Delta R_{ns} = 1 - R_{ns} \tag{3.2}$$

The saturation fluence, F_{sat}, is defined as the input pulse energy fluence required in order to change the reflectivity of the SAM by $1/e$ of its modulation depth. The other important SAM parameter is the recovery time τ, which is defined as the time taken for the SA to recover after being bleached. Successful passive mode-locking of lasers depends on the contribution from each of these SAM parameters.

SA mode-locking was initially demonstrated in a ruby laser using a colour-filter glass SA, and simultaneously, in a Nd-doped glass laser using a dye SA [24, 122]. These initial studies reported mode-locked pulses within a Q-switched envelope; the regime of

laser operation termed as Q-switched mode-locking (QML). The mode-locked pulses have a repetition rate determined by the laser cavity length, given as,

$$f_{rep} = \frac{c}{2nL} \tag{3.3}$$

where f_{rep} is the laser repetition rate, c is the speed of light, n is the refractive index and L is the length of the cavity. These pulses are modulated by a lower repetition rate Q-switch envelope, with the modulation occurring at a frequency defined by the upper state lifetime of the gain material. For rare-earth doped materials, the lifetime is of the order of ~1 ms, resulting in typical QML repetition rates of ~ kHz. Figure 3.10 provides a schematic representation of continuous-wave mode-locking (CW-ML) and QML, where CW-ML refers to mode-locked pulses generated with constant pulse energy. While QML lasers have the disadvantage of strong fluctuations by the Q-switched envelope, the increased pulse energy still concentrated in the ultrashort mode-locked pulses can be useful for application such as micromachining or surgery [121].
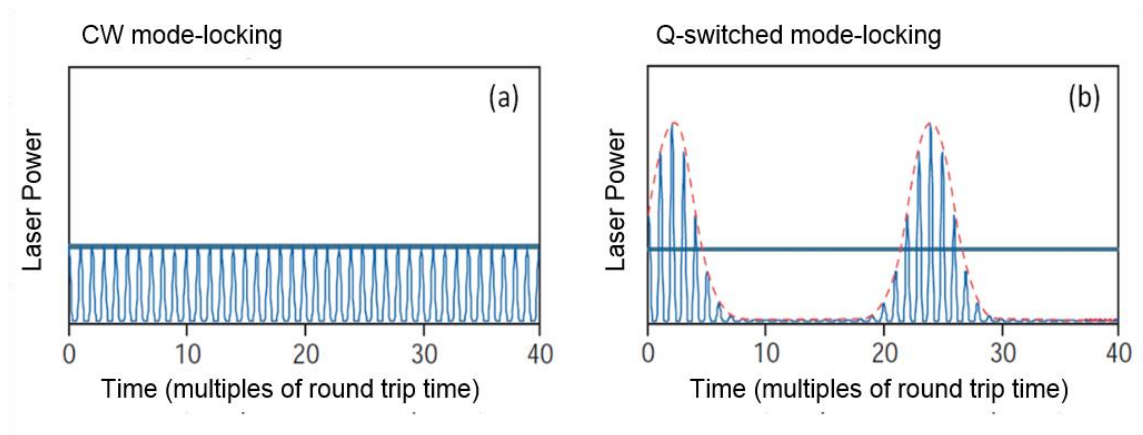
Figure 3. 10. Schematic of (a) CW mode-locking and, (b) Q-switched mode-locking. Reproduced from Ref. [118].

The stability limit of passively mode-locked solid-state lasers were studied by Kartner *et al.* [123] and augmented by Honninger *et.al.* [121] to derive a threshold condition for the transition from QML to CW-ML based on experimentally accessible parameters. This is given as,

$$E_p^2 > E_{sat,L}E_{sat,A}\Delta R \tag{3.4}$$

where E_p is the intracavity pulse energy, $E_{sat,L}$ is the saturation energy of the laser medium, $E_{sat,A}$ is the saturation energy of the SA, and ΔR is the modulation depth of the SA. These parameters are defined below.

(a) $\boldsymbol{E_p}$: The energy of a mode-locked pulse is given as,

$$E_p = PT_R \tag{3.5}$$

where P is the average intracavity power and T_R is the cavity round trip time.

(b) $\boldsymbol{E_{sat,L}}$: The saturation energy of the gain medium, $E_{sat,L}$, is defined as the product of the saturation fluence $F_{sat,L}$ and the effective laser mode area inside the gain medium $A_{eff,L}$, and given by,

$$E_{sat,L} = F_{sat,L} \times A_{eff,L} = \left(\frac{h\upsilon}{m\sigma_L}\right) \times (\pi\omega^2) \tag{3.6}$$

where $h\upsilon$ is the single photon energy, m is the number of passes through the gain medium per cavity round trip, σ_L is the emission cross-section of the gain medium and ω is the $1/e^2$ Gaussian beam radius with respect to intensity.

(c) $\boldsymbol{E_{sat,A}}$: The absorber saturation energy $E_{sat,A}$ is defined as the product of absorber saturation fluence $F_{sat,A}$ and the effective laser mode area on the saturable absorber $A_{eff,A}$.

$$E_{sat,A} = F_{sat,A} \times A_{eff,A} \tag{3.7}$$

(d) $\boldsymbol{\Delta R}$: The modulation depth of the saturable absorber is defined as the maximum change in nonlinear reflectivity as indicated in Figure 3.7.

Figure 3.11 gives a typical trend in laser operation regimes in a passively mode-locked solid-state laser using a SESAM [97]. With an increase in the intracavity power, there is a transition from the QML regime to CW-ML. The reduction in QML threshold is

achieved by careful optimisation of many overlapping parameters of the SA and the laser design. The following section provides a brief description of the different types of SAs used for passive mode-locking of lasers.
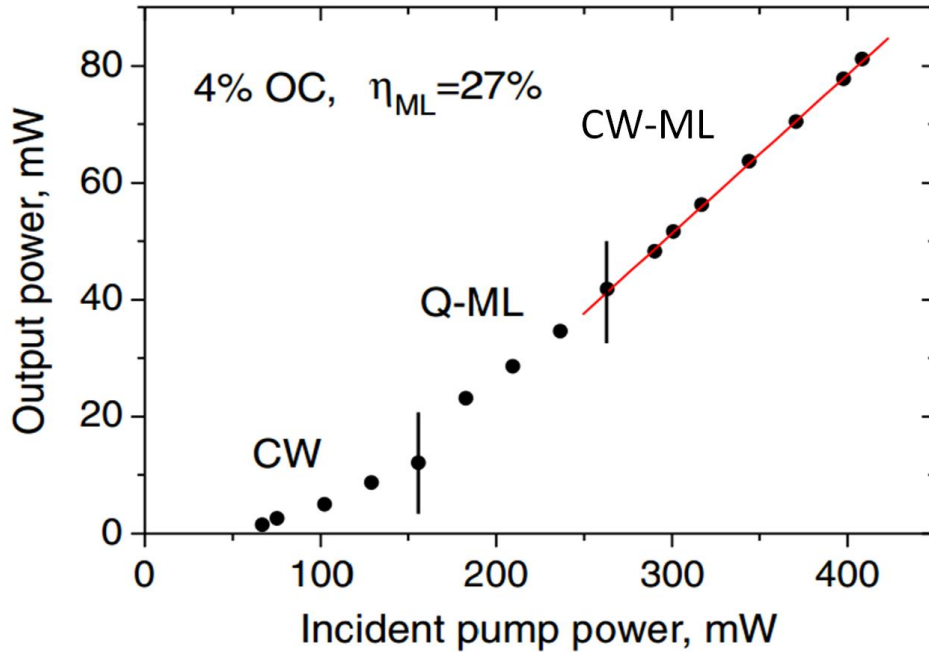
Figure 3. 11. The transition from CW operation to QML and CW-ML in a solid-state passively mode-locked Yb-doped glass waveguide laser [97].

3.3.1 Semiconductor Saturable Absorber Mirror (SESAM)

The conventionally used SAs before the advent of SESAMs includes organic dye and transition-ion doped crystals. While these are effective SAs, they have limited flexibility in saturable absorption parameters such as the operating wavelength and recovery times. In other words, the laser cavity has to be tailored around the SA parameters. Organic dye SAs also have the disadvantages of short lifetimes, high toxicity and complicated handling procedures [118]. In 1992, semiconductor SAs emerged as an alternate passive mode-locker with superior performance features [124]. Semiconductor materials can absorb over a broad range of wavelengths, from the visible to the mid-IR. Also, their recovery time and saturation fluences can be controlled during the device fabrication process, allowing exceptional flexibility in SA parameters.

Figure 3.12 illustrates the mechanism of saturable absorption in a semiconductor material, with a focus on the recovery times. As discussed before, at higher light

irradiances, the absorption of the material becomes saturated due to depletion of electrons in the valence band. The absorption partially recovers within 60 - 300 fs of excitation when the carriers in each band thermalise. Complete recombination occurs on a longer timescale, of the order of few ps-ns. The two different timescales contribute advantageously towards passive mode-locking. The longer recovery time ensures a low saturation intensity allowing self-starting mode-locking, whereas the shorter time constant is effective in short-pulse shaping [118].
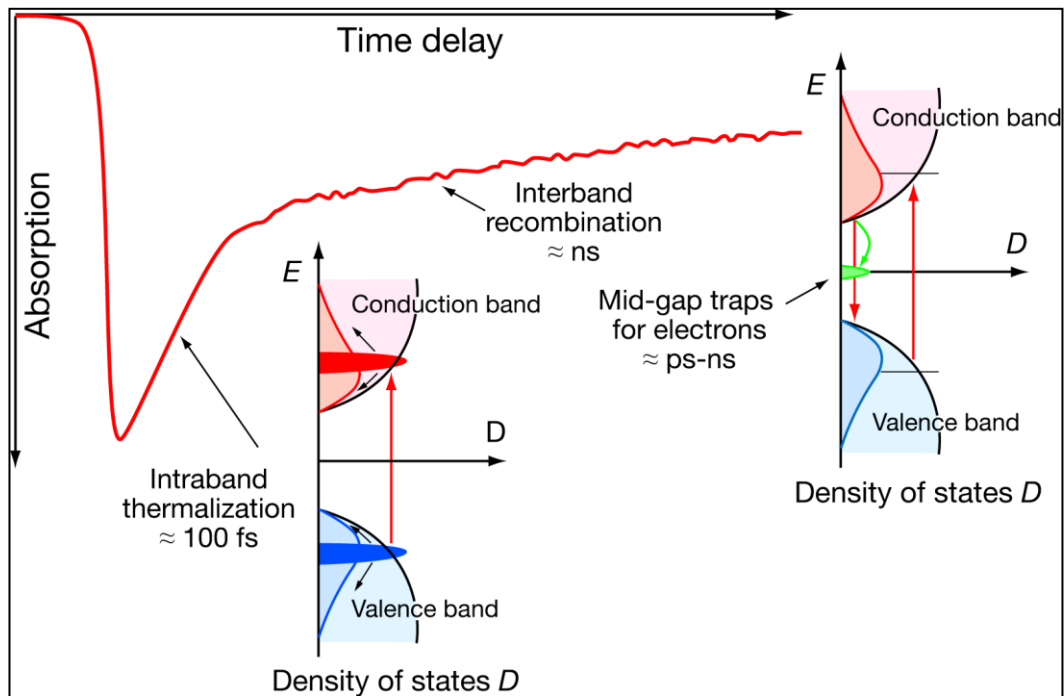
Figure 3. 12. The two different recovery time scales existent in SESAMs[118]

3.3.2 Carbon nanotubes and graphene

The 1-D and 2-D forms of carbon, namely CNT and graphene respectively, are a relatively recent addition as SAs for passive-mode-locking. CNTs have a cylindrical tube-like nanostructure as shown in Figure 3.13 (a). The carbon atoms are tightly packed in a honeycomb lattice by sp^2 hybridisation. The optical absorption in CNTs is related to the tube diameter and chirality; the latter defined as the twist angle along the tube axis. An unrolled CNT results in monolayer graphene, as shown in Figure 3.13 (b). Despite being only a single atom thick, graphene can absorb 2.3% of incident light. These carbon nanostructures are at the epitome of various research fields by the virtue of their unique electrical, optical, chemical and mechanical properties [125] .
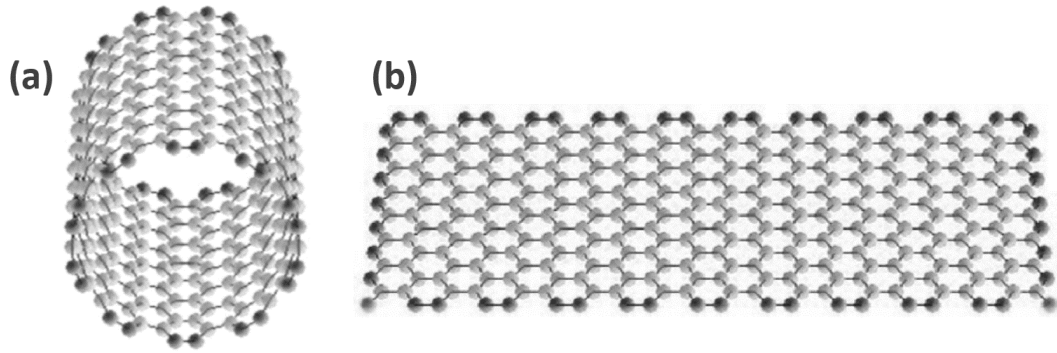
Figure 3. 13. (a) Cylindrical form of single-wall CNT (1-D), and (b) (2-D) graphene sheet [125].

Fast saturable absorption is possible in both CNTs and graphene. While CNTs have recovery times of the order of ps, ultrafast responses down to 100 fs have been observed in graphene. Absorption saturation was first demonstrated in CNT in 2006 [126], and used for passive mode-locking of fibre lasers [31, 32]. Saturable absorption in graphene was demonstrated more recently in 2009, and further applied for passive mode-locking [34, 35]. The unique features of these carbon nanostructures that make them distinct from SESAMs include their ease of fabrication, inherently fast recovery times and broadband operation [35]. The saturable absorption properties of CNT and graphene will be discussed in detail in subsequent chapters.

3.4   Brief Review of Ultrafast Laser Inscribed Waveguide Glass Lasers

Waveguide lasers, which by definition also include fibre lasers, possess certain unique properties. In waveguides, light is tightly confined to a small cross-sectional area ensuring high beam quality. Also, the large surface area to volume ratio allows good heat dissipation, consequently increasing the efficiency of operation and allowing the feature of power scalability in such lasers. They usually have a monolithic laser resonator, resulting in several advantages such as a stable and compact setup. A few of the limitations in such systems include undesirable nonlinear effects within the waveguide core and a limited gain per unit length. The latter can be attributed to concentration quenching in the sample, wherein a visible reduction in the fluorescence intensity occurs due to clustering of dopant ions at high concentrations.

ULI has emerged as a powerful microfabrication tool in recent years, allowing waveguide fabrication in rare-earth doped media, both crystals and glasses. The first ULI-based waveguide laser was demonstrated in 2004 [88] by Taccheo et al. in an Er:Yb-doped phosphate glass. The slope efficiency of the laser was only 2%, with an output power of 1.7 mW at 1533 nm. The result paved the way towards active research in ULI waveguide laser development, and is therefore an important milestone. The first waveguide laser was at the telecom wavelength, since both laser and fibre components optimised for this wavelength region were readily available. Subsequently, waveguide lasers have been demonstrated in a number of substrates, with their operating wavelengths ranging from the visible to the mid-IR [49]. This section provides a brief review of ULI-based waveguide glass lasers. While waveguide lasers have also been demonstrated in crystals and ceramics, the review is restricted to glass lasers since it has a direct consequence on the work presented in this thesis.

Table 3.1 gives relevant information about waveguide glass lasers fabricated by ULI. The progress in laser development over the years can be quantified in terms of the laser slope efficiency and output power, and also in terms of the laser cavity design. In the case of pulsed lasers, the important parameters include the pulse duration and repetition rate. These features are also included in the table. The first demonstration of a ULI waveguide laser in 2004 with a 2% slope efficiency was immediately followed by efforts to increase the laser performance from the same material, namely, Er:Yb-doped phosphate glass. The natural route for this in a waveguide cavity is the development of 'better' waveguides with lower propagation losses. This requires a systematic optimisation of waveguide inscription parameters such as the laser pulse energy and repetition rate. A lower propagation loss of 0.4 dB cm^{-1} against the previous value of 0.8 dB cm^{-1} in Er: Yb-doped phosphate glass resulted in a waveguide laser with a higher slope efficiency of 8.4% in 2006. The waveguide laser also had the additional capability of multiple laser wavelengths in the C-band [86].

Another milestone in ULI-waveguide lasers was based on the geometry of the laser cavity. In 2008, a monolithic waveguide laser was demonstrated by Marshall et al. in Er: Yb-doped phosphate glass. The true monolithic nature of the laser was obtained by incorporating laser inscribed distributed feedback Bragg gratings in the substrate [94]. The laser operated at a wavelength of 1537 nm, producing ~1 mW of output power. A similar waveguide laser, but for 1 μm wavelength was demonstrated soon after by the

same research group in Yb-doped phosphate glass. The laser generated 102 mW average output power with a 17% slope efficiency [95], marking an achievement in terms of output power, the previous best being 30 mW. Figure 3.14 gives a comparison of this waveguide laser with a fibre-based waveguide laser cavity [89]. The monolithic waveguide laser has the gain medium and cavity mirrors incorporated into a single substrate, whereas, the fibre ring cavity in Figure 3.14 (b) is similar to fibre lasers, with the gain fibre replaced by a buried channel waveguide. Other glass substrates used for ULI waveguide laser development include Nd-doped silicate glass operating at 1064 nm [90], integrated cavity waveguide lasers in Tm-doped fluorogermanate glass [127] and Ho:Tm-doped ZBLAN glass for an operating wavelength of 2 μm [128] .
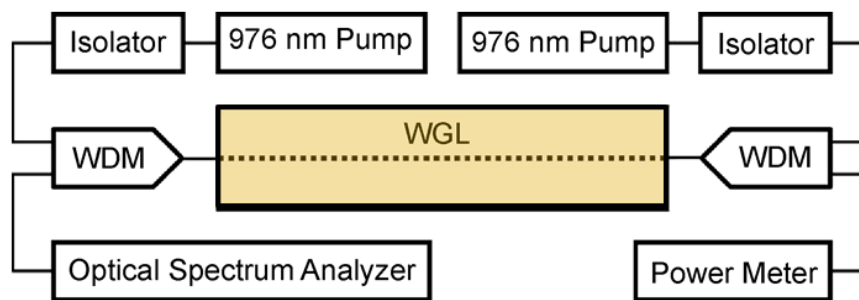
Figure 3. 14. Schematic of a waveguide laser with (a) a monolithic cavity [95], where the gain medium and the cavity mirrors are incorporated in a single substrate allowing a compact system and (b) fibre-coupled waveguide laser cavity [89], where the waveguide slab forms the gain medium and the remaining constituents in the cavity consists of fibre-based devices such as isolators and WDMs.

ULI waveguide lasers generating ultrashort pulses soon followed. The success of CNT and graphene-SA for passive mode-locking of fibre lasers proved an obvious route towards mode-locking in waveguide lasers as well. Since the majority of previously reported CW waveguide lasers used fibre-coupled cavities, a similar cavity configuration was used for pulsed operation, with a CNT-SA incorporated in the form of a free-standing film in fibre connectors. This first mode-locked waveguide laser generated 1.6 ps pulses at 16.7 MHz in an Er-Yb phosphate glass waveguide cavity [96]. Another important breakthrough in terms of achievable pulse duration from waveguide lasers was in 2010, in an Er-doped bismuthate glass waveguide-fibre ring laser generating 320 fs pulses [89]. This remains todate the shortest pulse duration achieved from ULI waveguide glass lasers. A SESAM mode-locked integrated waveguide laser with a pulse repetition rate of 4.9 GHz was reported in 2012, marking an important achievement in terms of repetition rates [97].

Laser action has also been reported in ULI-waveguides in laser crystals, such as YAG [49], and double-tungstates [91]. These materials are obvious gain materials of choice due to their prevalence in bulk laser development which also facilitated their improved material quality. Waveguide fabrication in these materials is possible by the inscription of Type II structures, discussed previously in Chapter 2. In comparison, glasses have the advantage of having a smooth refractive index change by ULI, which can be systematically studied. As summarised in Table 3.1, the study of active glasses for ULI has been limited to few materials. This naturally calls for further investigation of novel laser glasses for active waveguides by ULI; preferably glasses capable of high active-ion doping, and improved thermal conductivity. Consequent work based on glass laser development is detailed in subsequent chapters.

Table 3. 1. ULI-waveguide lasers demonstrated in glass materials.

	Laser Glass Materials	Wavelength (nm)	Slope efficiency (%)	Output power (mW)	Remarks	Reference/ Year of publication
1	Er:Yb-doped phosphate glass	1533.5	2	1.7	Fibre-waveguide cavity	[88], 2004
2	Er:Yb-doped phosphate glass	1560 1534	6.6 8.4	23 30	Fibre-waveguide cavity	[86], 2006
3	Er:Yb-doped phosphate glass	1537.62		0.37	Monolithic	[94], 2008
4	Yb-doped phosphate glass	1033	17	102	Monolithic	[95], 2009
5	Ho:Tm-doped ZBLAN glass	2052	20	76	Integrated cavity	[128], 2012
6	Tm-doped fluorogermanate glass	1091	6	32	Integrated cavity	[127], 2011
7	Nd-silicate glass	1064	15	7.5	Extended cavity	[90], 2010
8	Yb Bismuthate glass	1035	79	163	Quasi-monolithic	[129],2012
8	Er:Yb-doped phosphate glass	1534		5	Ring laser cavity	[130], 2013
9	Er:Yb-doped phosphate glass	1535	--	0.1	CNT passive mode-locking 1.6 ps, 16.7 MHz	[96], 2006
10	Er-Bismuthate glass	1560	-	1.25	CNT passive mode-locking- 320 fs, 40 MHz	[89], 2010
11	Yb-phosphate glass	1058	27	81	SESAM mode-locking, high repetition rate 800 fs, 4.9 GHz	[97], 2012
12	Yb bismuthate glass	1039	48	202	Quasi-monolithic cavity, Q-switched mode-locking 1.5 GHz, ~1 ps	[131], 2013

3.5 Summary

This chapter discussed the application potential of ULI for waveguide laser development in glass substrates. The typically preferred activeions include Nd, Yb, and Er. The important features of these rare-earth dopants including their radiative and non-radiative transitions have been detailed. A section introduced the various SAs used for passive mode-locking, in order to better understand ultrafast operation in rare-earth doped waveguide lasers. Finally, waveguide glass lasers fabricated by ULI have been reviewed. The developments in this field have been analysed based on deterministic laser performance features such as slope efficiency, average power output, pulse durations as well as laser cavity designs. ULI based waveguide laser development is still in its infancy and presents massive application potential, ranging from investigation of new gain materials to improvements in laser parameters in existing gain media.

Chapter 4 – Highly efficient compact waveguide laser in Yb doped bismuthate glass

4.1 Introduction

Waveguide laser development has emerged as one of the many applications of ULI, a tribute to the flexibility and versatility of the technique. By suitable optimisation of irradiation parameters, the nonlinear absorption mechanism that forms the basis of ULI facilitates waveguide fabrication in almost any transparent material, using the same laser source. This has led to waveguide inscription in a number of gain substrates for laser development, as discussed in Chapter 3. Initial research focused on active device development for the telecom wavelength using silica-based rare-earth doped substrates [48]; however, silicate glasses have limited amplifier bandwidth and doping concentration of rare-earths, impacting the performance of the active device.

To overcome the challenges posed by the host material on the active device, a variety of substrates have been studied. Phosphate glasses have been recognised as a suitable host for highly Er-doped waveguide lasers in view of their excellent spectroscopic properties, namely, a broadband emission spectrum around 1.5 μm and long lifetimes of the Er metastable state [48]. These glass hosts have also been used for high power (~100 mW) waveguide lasers at ~1 μm, using Yb-dopants [95]. Yb has a low quantum defect, reducing pump induced thermal load and resulting in high efficiencies. Other host glasses studied for ULI waveguide lasers include fluoro-germanate and ZBLAN glasses [127, 128]. The relatively low numbers of glass hosts analysed for active waveguide applications makes the investigation of new materials an important research area for ULI, while providing additional benefits.

New hosts investigated for active photonic device fabrication by ULI include Bismuthate (Bi_2O_3) based glass. These materials were initially demonstrated as promising hosts for waveguide amplifier applications in the telecom wavelength by virtue of their wide and flat gain spectrum and high Er-dopant solubility. Consequently, they were studied for ULI device fabrication by Robert Thomson and co-workers at the Nonlinear Optics group at Heriot-Watt University, resulting in a high gain Er-doped waveguide amplifier with a peak internal gain per unit length of 2.3 dB cm^{-1} at 1533 nm

[132]. The substrate was further studied to successfully develop an ultrafast waveguide laser at 1.56 μm, producing ~320 fs pulses from a CNT mode-locked ring laser cavity [89]. Thus, bismuthate glass was identified as an excellent glass host for ULI-based active devices at the telecom wavelength.

In recent years, bismuthate glass has also been studied as a potential host for Yb-dopants. Researchers at Asahi glass Company demonstrated thermally stable, highly Yb-doped bismuthate glass with a maximum dopant concentration of ~ 3 mol% of Yb_2O_3 [101]. A fibre laser doped with 0.5 mol% of Yb_2O_3 dopant was reported, producing a slope efficiency of 36%. The unique spectroscopic properties of Yb-doped bismuthate glass, namely, the absence of detrimental defect zones in the system and the high Yb solubility further supported by the success in fibre laser development, makes the glass an important candidate for ULI device applications at 1 μm.

Accordingly, the potential of Yb-doped bismuthate glass for ULI has been studied. This chapter provides a systematic study of this material for ULI-waveguide laser development. Section 4.2 introduces the gain medium. Sections 4.3 – 4.6 discussthe waveguide inscription details, with the main variables being the laser repetition rate, pulse energy and translation speed. The waveguides are characterised based on their structural morphology and insertion loss. Section 4.6 details the microluminescence studies performed in order to analyse the ULI-induced material change. The final section 4.7 features the work towards building an integrated cavity laser.

4.2   Yb-doped Bismuthate Glass

The ytterbium doped bismuthate glass (Yb-BG), developed by Asahi Glass Company in Japan, has a Yb dopant concentration of 6600 wt-ppm and a refractive index of 2.03. Figure 4.1 shows the linear absorption spectrum of the substrate measured by a Shimadzu UV-3100 spectrophotometer, with a peak absorption at 976 nm.
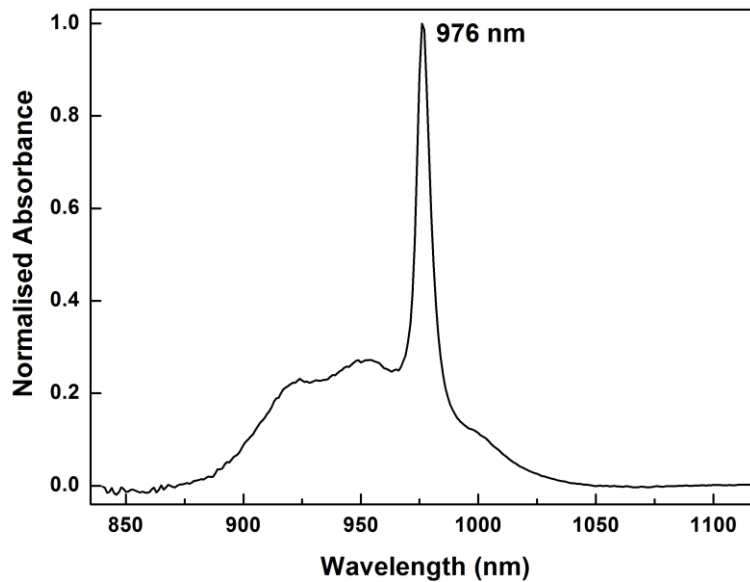
Figure 4. 1. Absorption spectrum of Yb doped Bi_2O_3 based glass, with the peak absorption wavelength corresponding to 976 nm.

Figure 4.2 shows the emission spectrum of Yb-BG as given in Ref. [101], with the possible transitions from the energy level designated *e* in the inset in the figure to *a*, *b*, *c*, and *d*, corresponding to the emission wavelengths of 977 nm, 1005 nm, 1029 nm, and 1060 nm, respectively.
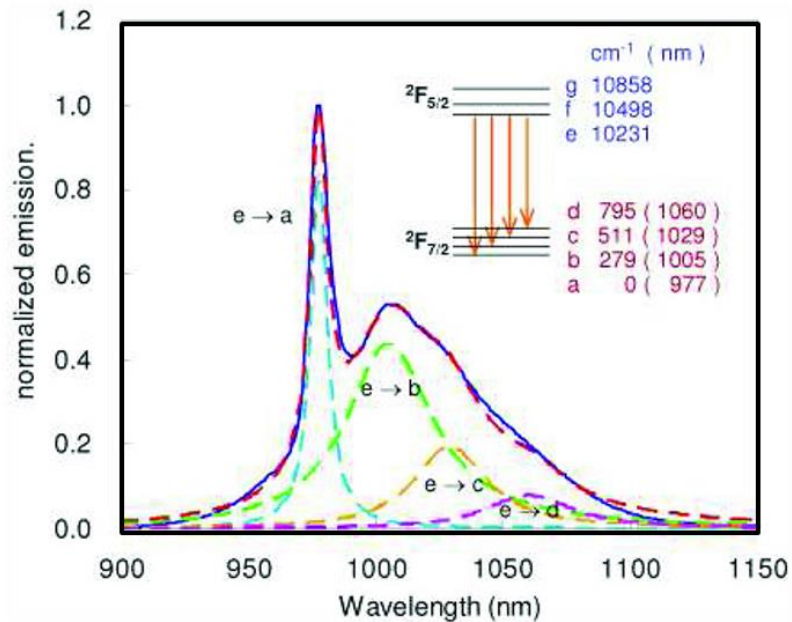
Figure 4. 2. Emission spectrum of Yb^{3+} doped Bi_2O_3-based glass pumped by a laser diode at 975nm. [101].

66

4.3   Preliminary Waveguide Fabrication Experiments

Waveguide fabrication in any new substrate by ULI first requires the identification of suitable irradiation parameters. This optimal processing window is achieved by performing a wide ULI parameter scan. For Yb-BG, Type I waveguides were inscribed in 15 mm × 10 mm × 2 mm samples using a master-oscillator power-amplifier fibre (MOPA) laser supplied by IMRA. The details of the inscription setup are given in Chapter 2, Section 2.6. The laser emits transform-limited pulses of ~340 fs duration centered at a wavelength of 1047 nm. The polarisation of the beam was set to be circular. A 0.4 NA aspheric lens was used to focus the laser beam to a depth of ~ 200 μm within the substrate, which was placed on a high precision Aerotech air-bearing translation stage system. A transverse writing configuration was employed for the inscription, where the sample was translated through the laser focus in a direction perpendicular to the incident laser beam. A single scan inscription results in a material modification measuring ~1.6 μm × 8.3 μm in dimension. This waveguide asymmetry was corrected by using the well-established multiscan technique [81]. Therefore, waveguides were inscribed by translating the sample through the laser focus 20 times, with each scan offset from the previous one by 400 nm, in a direction perpendicular to both the incident laser beam and the sample translation axis.

The wide parameter-scan in order to identify the optimal waveguide fabrication window in Yb-BG was obtained by varying the pulse repetition rate, pulse energy and sample translation speed. The inscription laser repetition rate was varied from 0.5, 1, 2, 4 up to 5 MHz, providing a systematic investigation of material modification with repetition rate. For each repetition rate, the laser pulse energy was varied between $30 - 200$ nJ. Sample translation speeds of 1, 2, 4, and 8 mm s^{-1} were used for each set of parameters.

4.4   Waveguide Characterisation

Initial characterisation of femtosecond-laser-written waveguides is performed by a number of sequential techniques. Microscope observation of the inscribed structures provides an estimate of the physical dimensions of the waveguide, along with a first indication of the guiding properties. The waveguiding in the structures is then analysed by viewing their mode profiles at the wavelength of interest. The most significant parameter is the insertion loss (IL), which determines the quality of the waveguide. Total IL consists of coupling loss at the input and output waveguide facets and the

propagation loss within the waveguide. The propagation loss or how low the IL value is, estimates the usefulness of a waveguide for device applications.

In the Yb-BG sample, after waveguide inscription, the substrate end facets were ground and polished. This was followed by waveguide characterisation, as discussed in the next section.

4.4.1 Waveguide Morphology

For initial characterisation, the waveguide cross-sections were analysed using a white light microscope working in the transmission mode. As mentioned previously, this simple microscope observation provides an estimate of the physical dimensions of the waveguide, and most importantly, the type of laser-induced modification. Laser induced material damage is identified as dark, non-guiding regions under the microscope, whereas a positive refractive index change results in an inscribed region that has a brighter contrast relative to the surrounding bulk. The latter configuration is analogous to an optical fibre with its denser core surrounded by a lower-index cladding and it also represents typical waveguiding in Type I inscription.

In Yb-BG, for high laser irradiances ~ 190 nJ material damage was observed, characterised by a dark waveguide core surrounded by the unmodified substrate. This is shown in Figure 4.3(a). With a decrease in laser irradiance, the type of material modification was found to change to a refractive index increment, characterised by a bright central core relative to the surrounding unmodified region. Figure 4.3 (b) shows this modification regime observed at ~166 nJ, a pulse energy just below the material damage threshold for Yb-BG, which ranges from 175-185 nJ at 500 kHz repetition rate.
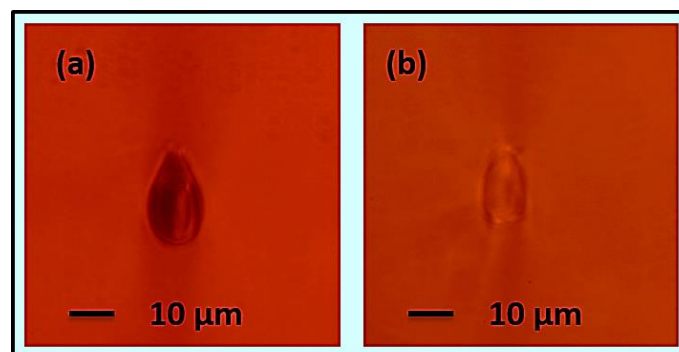
Figure 4. 3. Cross-sectional view of waveguides written at 500 kHz laser repetition rate in the Yb-BG substrate. (a) Damaged core inscribed at a laser pulse energy of 192 nJ (b) Guiding structures inscribed at a laser pulse energy of 166 nJ.

The regions of laser-induced positive refractive index change in Yb-BG were then mapped with respect to laser repetition rate, to estimate any change in waveguide morphology due to this particular inscription parameter. Figure 4.4 shows the variation in morphology for waveguides inscribed at repetition rates of 5 and 1 MHz, for similar pulse energies. At a lower laser repetition rate of 1 MHz, close to square cross-sections are obtained. These waveguides have a physical width of ~ 8 μm, in good agreement with the multiscan parameters of 20 scans offset by 400 nm.

For a high repetition rate of 5 MHz however, relatively large structures with almost 3 × multiscan-width are obtained. These waveguides have a characteristic tear-drop shape, consisting of a central elongated region flanked by an outer ring. This change in waveguide cross-section can be attributed to thermal accumulation effects typical at these repetition rates. At 5 MHz, the time interval between subsequent pulses falling on the substrate becomes much lesser than the thermal diffusion time of ~ 1 μs, resulting in an accumulation of heat at the focus. Following laser exposure, the accumulated heat gets transferred to the surrounding, extending the laser-heated region far beyond the focal volume. These tear-drop structures achieved in Yb-BG are similar to those observed in EAGLE 2000 borosilicate glass by Eaton et al.[133] and, in chalcogenide glass by Psaila et al. [113]. The central elongated region can be attributed to the high temperatures accompanying pulse absorption, and the surrounding ring due to thermal diffusion that occurs at an erratic rate due to the incomplete cooling between pulses [133].
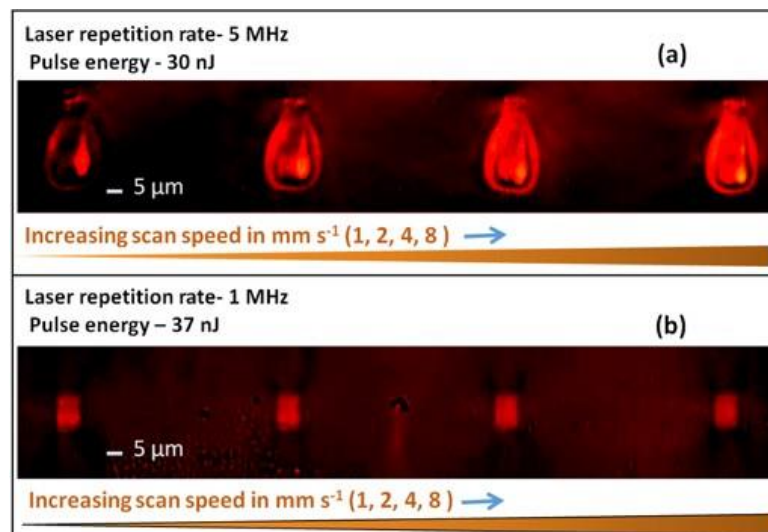
Figure 4. 4. Microscope images of the waveguide cross-sections in Yb-BG substrate for inscription laser repetition rates of (a) 5 MHz and (b) 1 MHz. The pulse energies are similar, within 10% of each other.

To determine the effect of pulse energy for laser inscription in Yb-BG, the waveguide cross-sections with respect to pulse energy were analysed for each laser repetition rate. Figure 4.5 gives the microscope images of waveguides inscribed at 1 MHz, in the order of decreasing pulse energies, from (a) 65 nJ to (d) 38 nJ. A trend from tear-drop structures to square cross-sections can be observed following this pulse energy decrease, similar to the cross-sectional trend noticed with laser repetition rates. This tear-drop morphology at high pulse energies ~65 nJ but a lower repetition rate ~ 1 MHz can be explained by the large laser absorption from a single high energy pulse, which becomes equivalent to the accumulated heat typical at ~5 MHz. This results in an increased diffusion scale length extending the modified region beyond the focal volume.
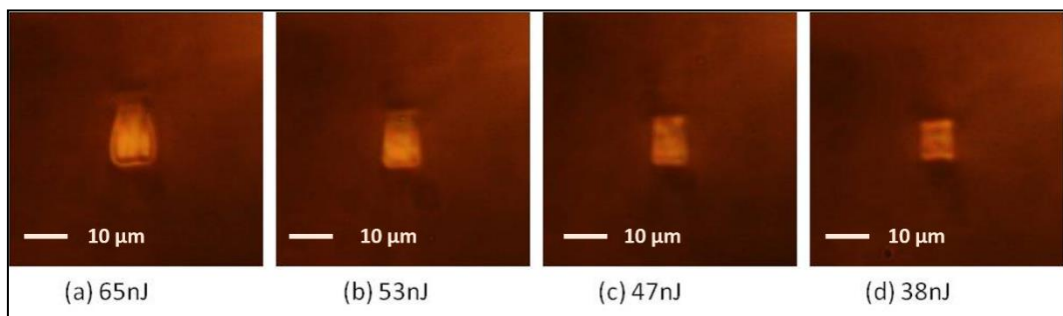
Figure 4. 5. Transmission mode optical micrographs of selected waveguide end-facets. Each structure was inscribed using a laser repetition rate of 1MHz and sample translation speed of 2 mm.s^{-1}. The pulse energy used to inscribe each structure is given below each image.

Another parameter that influences the ULI waveguide cross-section is the translation speeds used for the device inscription. The scan speed defines the number of pulses incident per spot. Hence, for a lower scan speed, there is a higher dwell time per spot, resulting in a more intense modification, and vice versa. For the scan speeds of 1, 2, 4, and 8 mm s^{-1}, employed for ULI in Yb-BG, a variation in material modification was not as evident as with other inscription parameters of laser repetition rate and pulse energy. Similar waveguide cross-sections are obtained for all scan speeds, as shown in Figure 4.4. However, a difference in waveguide morphology with scan speed is noticeable by a careful analysis of structures inscribed at 5 MHz. In Figure 4.4(a), for 1 mm s^{-1} scan speed, the modification tends towards material damage characterised by a weak guiding of light. This is a clear distinction with the waveguide inscribed at 8 mm s^{-1} that has a brighter contrast compared with the unmodified sample.

Thus, the initial characterisation of Yb-BG waveguides based on structural morphology alone gives an insight about the inscription parameters which provide a positive

refractive index change and close-to square cross-sections. Square cross-sections are desired since the geometry ensures a symmetric waveguide and thus a well-guided mode. For Yb-BG these are achieved for waveguides inscribed at lower pulse energies and repetition rates. This inscription regime is associated with uniform modification and lower scattering centres leading to low propagation losses in comparison to the uneven heating effects at higher laser absorption at the focus.

4.4.1 Insertion Loss Characterisation

The insertion loss (IL) of the waveguide is the most important parameter in determining the quality of the inscribed waveguide. It provides an upper limit to the loss attributed to the waveguide, which in turn determines the effective guiding within the structure. IL is usually measured using a fibre-optic test bed, and defined as the loss incurred in the signal power when a waveguide is inserted into the system. IL comprises propagation loss (PL) within the medium and coupling losses (CL) at the input and output ends of the waveguide. This can be expressed as,

$$IL = PL + 2CL \tag{4.1}$$

The PL is typically made up of the absorption in the sample, plus scattering and radiation losses. The CL includes the Fresnel reflections at the waveguide facets. The Fresnel loss can be determined from the refractive indices of the materials involved. For normal incidence, the Fresnel loss R_F is given by,

$$R_F = \left(\frac{n_1 - n_2}{n_1 + n_2}\right)^2 \tag{4.2}$$

where n_1 and n_2 are the refractive indices of the two interacting media.

Figure 4.6 shows the schematic of the experimental setup used to measure the IL of Yb-BG waveguides. An Nd: YAG laser operating at 1064 nm was chosen for the measurement, since the substrate has minimal absorption at this wavelength. Thus, any loss contribution due to absorption is eliminated from the system. As shown in Figure 4.6, the free-space input laser is coupled into a fibre using a ×30 aspheric lens. The fibre is connected to the main line of a tap coupler, with both its outputs connected to a

switch, which is in turn connected to a calibrated detector, KD Optics DATS 01 HP. The 1.1% tap line is used for monitoring the coupling of the laser output into the coupler fibre. Initially, the 98.9% arm of the coupler is directly connected to the detector as shown in Figure 4.6 (a) and the corresponding reading is recorded as the signal reference value, S_{ref}. Then the fibre along the 98.9% arm is broken, cleaved and butt coupled using index matching gel onto either side of the inserted waveguide; see Figure 4.6 (b) .The power transmitted now is recorded as signal S_t. If the powers are recorded in dBm, then the insertion loss in decibels is given as:

$$IL(dB) = S_{ref} - S_t \qquad (4.3)$$

The sample and the aligned fibres are mounted on an xyz translational stage system with pitch and yaw adjustments. The index matching gel with a refractive index n ~1.45 reduces the Fresnel reflections at the interfaces. The measured loss value gives an upper bound of the IL of the waveguides. In other words, any change in terms of coupling will contribute only towards an increase in the IL value.
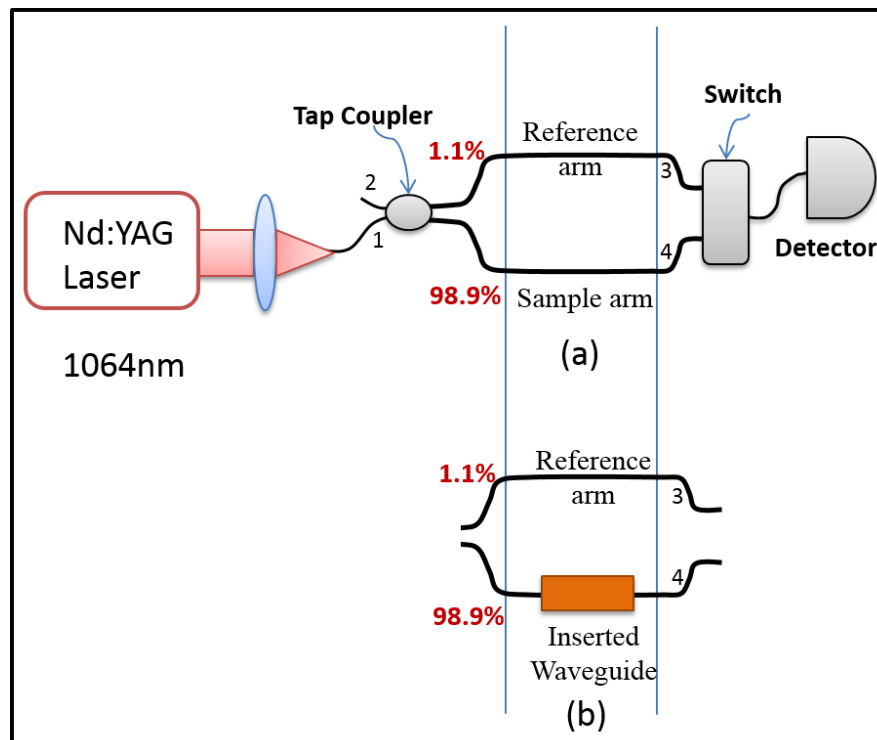
Figure 4. 6. Experimental setup used for the insertion loss measurements.

Figures 4.7 - 4.10 gives the IL with respect to laser pulse energy for waveguides written in Yb-BG substrate at laser repetition rates of 1, 2, 4 and 5 MHz respectively. Waveguides are written for 4 translation speeds: 1, 2, 4, and 8 mm s^{-1}. The experimental error in the insertion loss measurements as estimated from the fluctuations at the detector is ~0.4 dB, as indicated by the error bars.
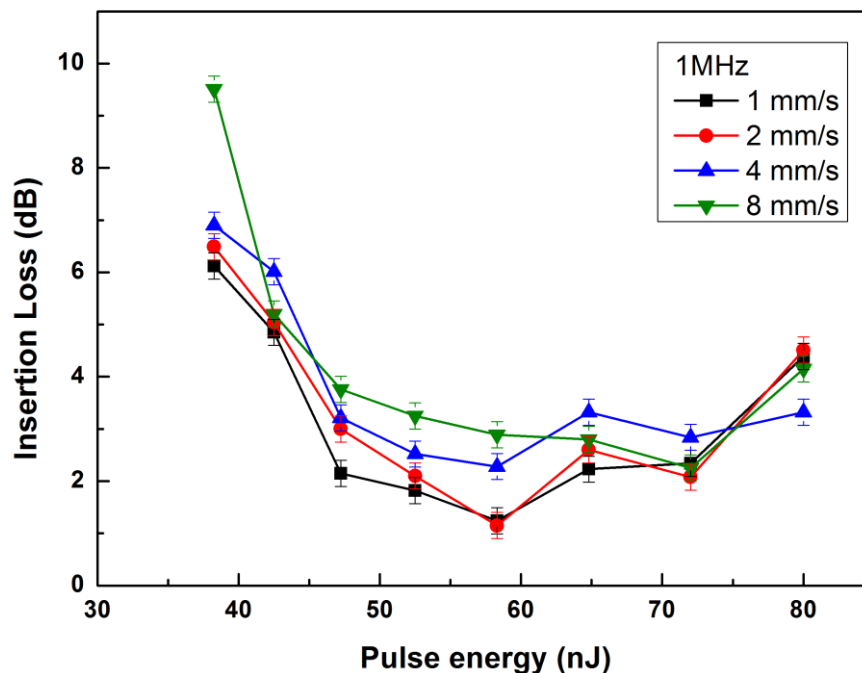
Figure 4. 7. IL measurements in Yb-BG waveguides with increasing laser pulse energies for 1 MHz. Waveguides are inscribed at translation speeds of 1, 2, 4 and 8 mm s^{-1}.

The waveguides written at 1 MHz follow a gradual decline in IL values with decreasing pulse energies, as shown in Figure 4.7. At high pulse energies ~ 80 J, the material modification experiences strong thermal effects. The resultant structures are a combination of possible material damage or uneven cooling at the focus. The higher occurrence of scattering and absorption centres at these pulse energies results in a higher IL for the waveguides. As the pulse energy is lowered, the material modification occurs solely by a well-defined refractive index modification that results in IL values < 2 dB. At even lower laser pulse energy, <45 nJ, the modification becomes weaker, characterised by weak guiding at 1064 nm and resulting in higher IL values. Waveguides with insertion loss ≤ 2 dB for the 15 mm long samples were obtained for laser pulse energies between 45 - 65 nJ, indicating a favourable window for waveguide fabrication.

73
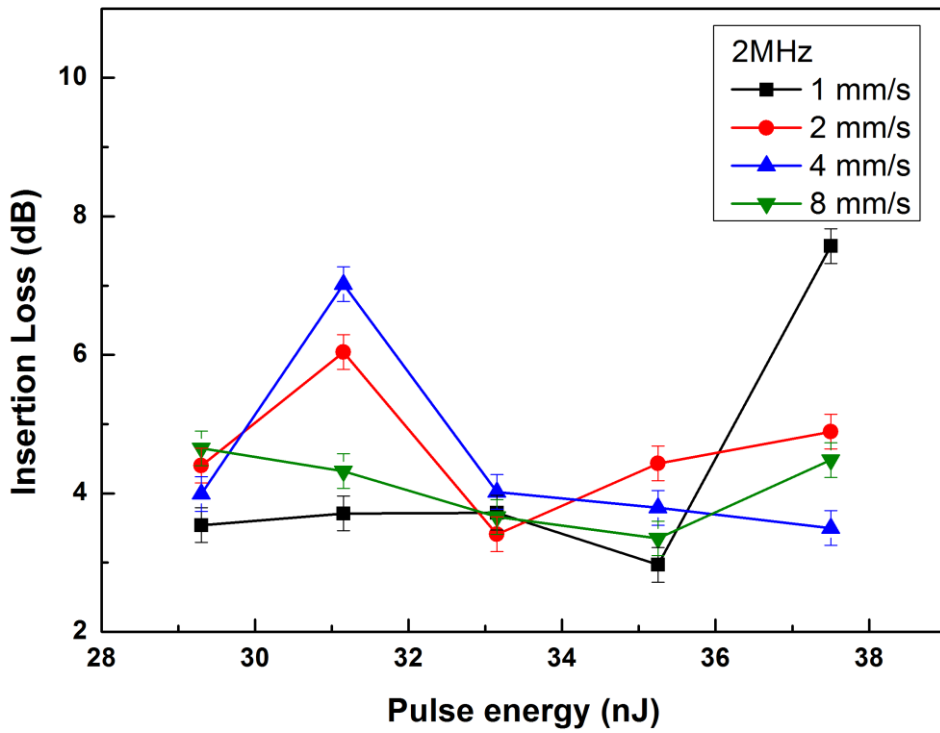
Figure 4. 8. IL measurements in Yb-BG waveguides with increasing laser pulse energies for 2 MHz. Waveguides are inscribed at translation speeds of 1, 2, 4 and 8 mm s^{-1}.
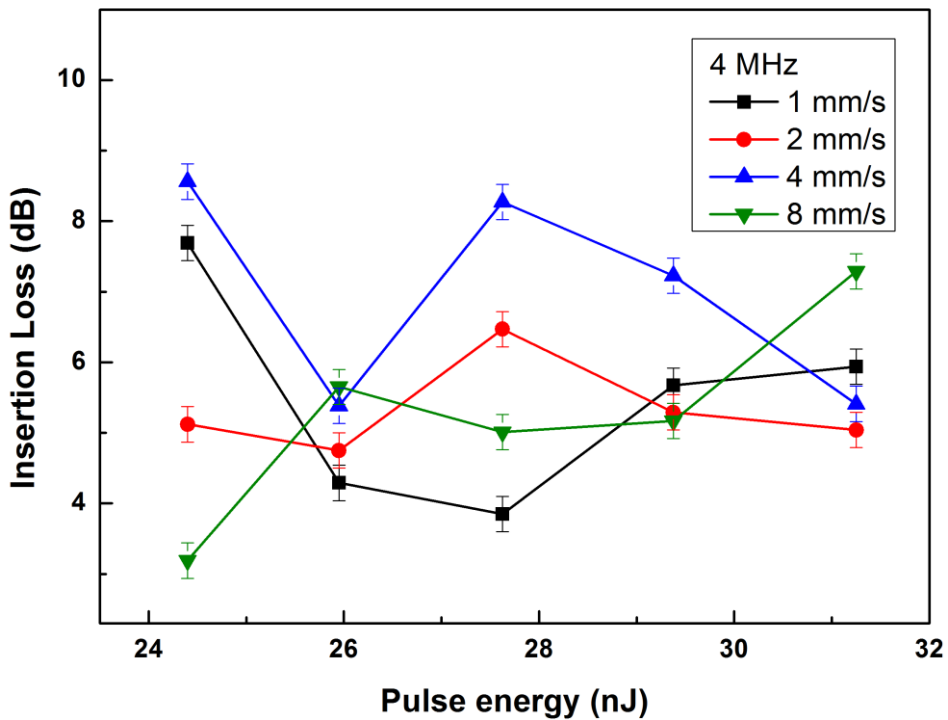
Figure 4. 9. IL measurements in Yb-BG waveguides with increasing laser pulse energies for 4 MHz. Waveguides are inscribed at translation speeds of 1, 2, 4 and 8 mm s^{-1}.
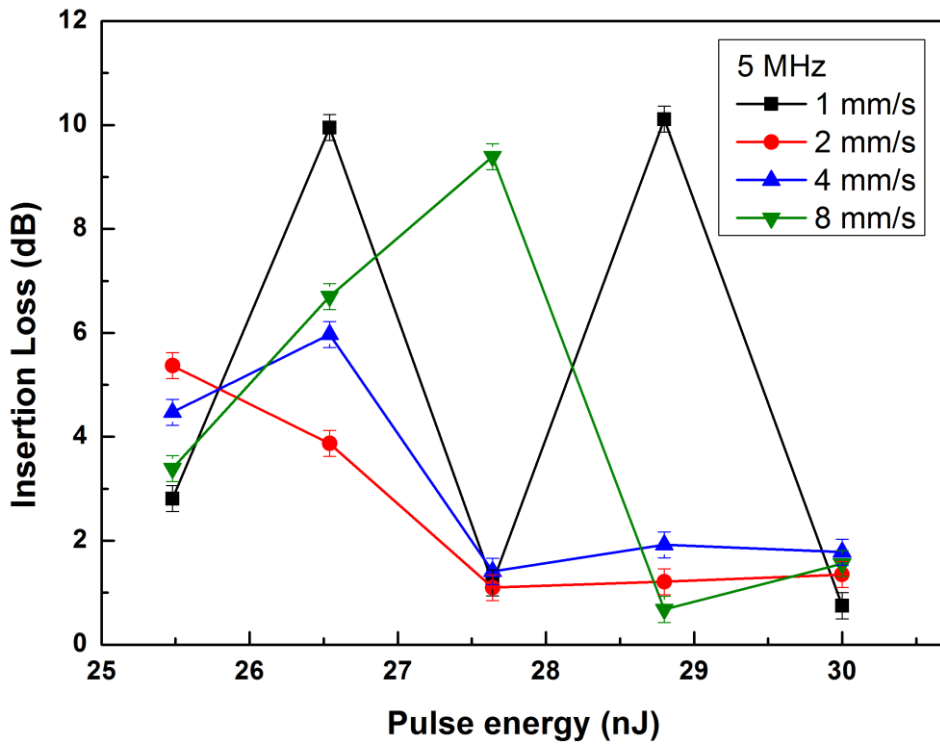
Figure 4. 10. IL measurements in Yb-BG waveguides with increasing laser pulse energies for 5 MHz. Waveguides are inscribed at translation speeds of 1, 2, 4 and 8 mm s^{-1}.

At higher repetition rates of 2-5 MHz as shown in Figures 4.8 to 4.10, the IL values are higher, > 3 dB. This can be attributed to the unpredictable nature of refractive index modification that accompanies cumulative heating effects. Notably, few waveguides inscribed at 5 MHz at sample translation speeds of 1, 2, and 8 mm s^{-1} exhibited low losses < 1.5 dB, as shown in Figure 4.10. However, the losses could not be replicated for further waveguide inscription at the same parameters, indicating the erratic nature of material modification at these repetition rates.

4.5   Optimal Waveguide Fabrication

Optimal waveguides are ideally characterised by low propagation losses. One method to measure the PL is the cut-back technique, where the IL is measured for various lengths of the sample by cutting it back. By assuming identical coupling for each measurement, the PL can therefore be estimated. Since Yb-BG samples are unique and far from dispensable, cutting back samples is not practical. However, inscription of identical waveguides in two samples of different lengths can help estimate an upper bound for the PL. This experimental technique include a number of assumptions, including

uniform polishing of the end facets after waveguide inscription and identical coupling losses.

Accordingly, waveguides were inscribed in a 50 mm long sample at a laser repetition rate of 1 MHz and pulse energies between 45 – 65 nJ. The longer length of the sample is additionally suitable for improved gain for laser experiments. After waveguide inscription and post-polishing, the IL value obtained for the ~ 48 mm long sample were compared with that of the 15 mm substrate, resulting in a PL of ~ 0.2 dBcm^{-1}. As a first estimate, this upper limit for the PL value is quite low.

For the laser experiments, waveguides with close-to square cross-sections in the ~ 48 mm sample were used. Figure 4.11 shows the IL values of these waveguides measured using the same experimental setup given in Figure 4.6. The loss values are found to be consistent with those obtained for the initial fabrication experiments, confirming the repeatability of ULI. IL < 3 dB was obtained for most of the waveguides inscribed at pulse energies between 40 and 65 nJ. The optimal processing window for Yb-BG sample which was further used for active waveguide characterisation is given in Table 4.1. The waveguide inscribed at a pulse energy of 52 nJ and sample scan speed of 8 mm s^{-1}, having an IL of 2.4 dB was used for subsequent laser experiments.
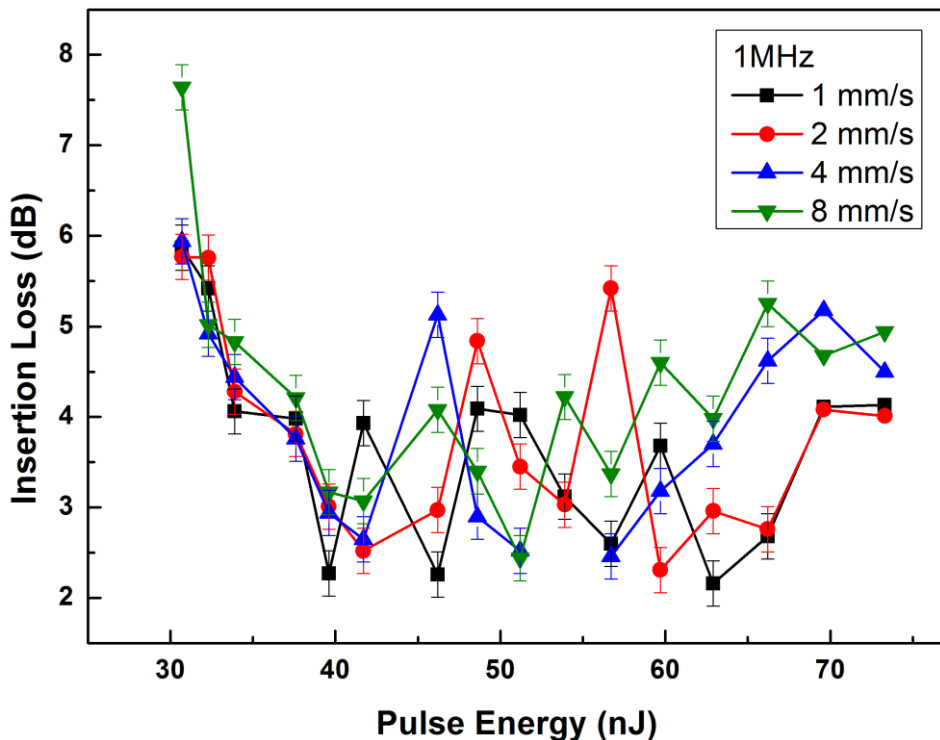
Figure 4. 11. Insertion loss versus inscription laser pulse energy at 1 MHz. The waveguides are inscribed in ~48.5 mm sample at scan speeds 1, 2, 4 and 8 mm s^{-1}.

Table 4. 1. Processing window for ULI in Yb-BG substrate which provides low-insertion loss waveguides.

ULI parameters used for Yb-BG substrate	
Wavelength	1047 nm
Pulse repetition rate	1 MHz
Pulse duration	~350 fs
Focusing objective	0.4 NA
Laser Polarisation	Circular
Pulse energy	40- 65 nJ
Sample Translation Speed	1, 2, 4, 8 mm s^{-1}

4.6 Microluminescence Studies

Spectroscopic analysis of waveguides is an important step in terms of optimisation of the ULI process for any particular substrate. It allows investigation into the nature of material modification occuring due to ULI. One powerful spectroscopic tool is confocal microluminescence; a non-destructive method that can characterise structures at the micron scale. Thus, it provides information about the modified material as well as the surrounding unmodified region. Waveguide spectroscopy in Yb-BG was therefore investigated using microluminescence studies, to analyse the laser induced structural changes in the glass responsible for the formation of optical waveguides in Yb-BG. This part of the work was done using the setup at the Universidad Autonoma de Madrid through collaboration with Professor Daniel Jaque.

The experimental setup consists of a fibre-coupled scanning confocal microscope, as shown in Figure 4.12. A 0.55 NA IR objective was used to focus a 920 nm excitation laser beam onto the sample. The excitation wavelength was so chosen in order to analyse the emission spectrum of Yb at the zero phonon line, which corresponds to the sharp Yb emission peak around ~ 976 nm as shown in Figure 4.2. This zero phonon line is very sensitive to perturbations within the material, and any change in this parameter for the ULI structures with respect to the unmodified region, will in turn reflect the nature of material modification.
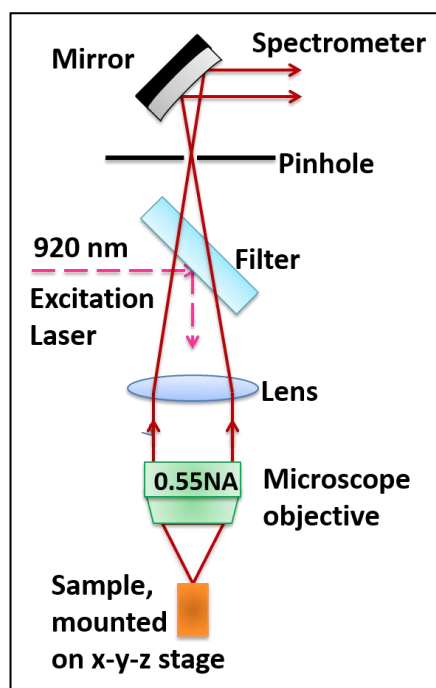
Figure 4. 12. A fibre coupled scanning confocal microscopy setup used for the microluminescence studies for Yb-BG waveguide.

The laser spot was linearly scanned across the waveguide cross-section, the scan line being shown in Figure 4.13 (a). The resulting back-emitted fluorescence along this scan, in the wavelength range of 960-1100 nm, was collected by the same IR objective and spectrally analysed by a high resolution spectrometer. In particular, the nature of the zero phonon line ~ 976 nm is studied. This is performed by the analysis of two important parameters, namely the Yb emission intensity at ~976 nm and the linewidth of the zero phonon line.
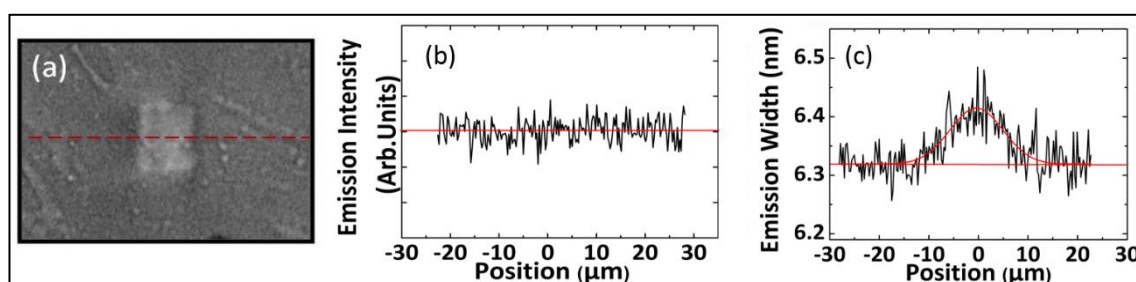
Figure 4. 13. (a) Facet image of the waveguide used for microluminescence studies, (b) Yb emission intensity across waveguide, (c) Yb emission linewidth of the zero phonon line across waveguide.

Figure 4.13 (b) shows the Yb emission intensity obtained along the linear scan. Typically, a decrease in fluorescence emission, termed fluorescence quenching, occurs when there are defects within the matrix or with a change in the Yb-dopant density. For

Yb-BG, as can be observed in Figure 4.13 (b), the emission intensity has a flat response with no observable change in fluorescence within the waveguide volume. This therefore indicates the absence of defect induced fluorescence quenching. Also, the fluorescence properties of the Yb ions are maintained even after waveguide inscription. Based on previous results, we attribute this to the presence of thermal assisted defect recombination during the ULI processes, which is favored by the high repetition rate used in this work that provides rapid annealing [68]. Thus, the ULI process does not change the Yb distribution, nor does it create a significant density of defects.

Although the fluorescence efficiency is not affected by the ULI process, ULI does affect the fluorescence linewidth of the zero phonon line. This is illustrated in Figure 4.13 (c), which gives a variation in the emission linewidth within the waveguide with respect to the surrounding unmodified material. A small increase in the emission linewidth of ~1.6% is observed in the irradiated area. This indicates a slight distortion of the glass matrix, which could account for the local refractive index increase.

Thus, the microluminescence studies establish that the ULI waveguides in Yb-BG are produced with a minimum perturbation of the original glass network. The process has not created any defects nor caused a Yb migration as indicated by the emission intensity profile. These results show the exceptional suitability of Yb-BG substrate for ULI based active device experiments, which are discussed in the next section.

4.7   Yb-BG Waveguide Laser

The main advantage of a waveguide geometry is the possibility of developing compact monolithic laser systems. In order to test this, a linear, compact laser cavity was designed and built, incorporating the active waveguide. The cavity consists of the laser end mirrors sandwiching the Yb-BG waveguide gain medium. The length of the cavity is therefore the length of the waveguide, being ~ 48 mm. The schematic of the laser cavity is given in Figure 4.14 (a), with a photograph of the cavity in Figure 4.14 (b). The pump source was a 975 nm fibre-coupled diode laser (Lumics LU0975M330-1002F10D) with a maximum output power of 265 mW. The diverging output at the fibre end of the pump was collimated and then focused into the waveguide using $\times$ 30 aspheric lenses, L_1 and L_2. The plane mirrors that form the laser cavity mirrors were butt-coupled to the waveguide end facets using an index matching gel. The pump mirror

M$_1$ is a dielectric mirror with high transmission at the pump wavelength and a reflectivity > 99.9% in the 1010 − 1200 nm wavelength range (Layertec 104965). To optimise the cavity, 8 - 10 output coupler mirrors (CVI Melles Griot), represented as M$_2$ in Figure 4.14 (a), with transmissions ranging from 3% to 89% were used. The laser emission from the waveguide was collected using a ×10 aspheric lens L$_3$. After eliminating any residual pump laser using a dichroic mirror DM, the laser output was measured using a thermal power meter (Coherent FM/GS). The following section details the laser performance features, quantified in terms of the input-output power measurements, laser spectral characteristics, and mode-profiles.
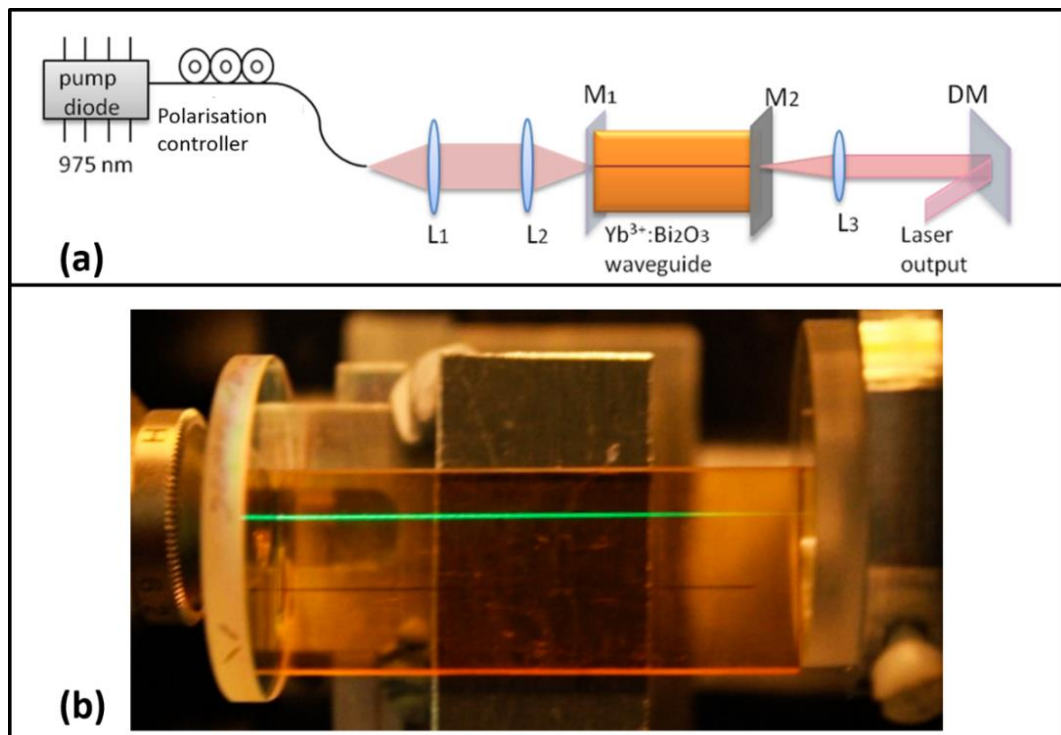
Figure 4. 14. (a) Schematic of the laser cavity. M1: Pump mirror, M2: Output coupler, DM: dichoric mirror to separate the pump and laser signal, L1, L2 and L3 : lenses. (b) Photograph of the linear integrated cavity. Green upconversion at the pump wavelength can be observed along the waveguide length.

4.7.1 Laser Performance

The performance of any laser system is quantified in terms of certain characteristic parameters including the laser threshold, slope efficiency and operating wavelength. Laser threshold refers to the input pump power where laser emission starts to occur. The slope efficiency is defined as the slope of a plot of output laser power versus pump power. The ultimate limit on the efficiency of a laser is determined by the quantum

defect (Qd) of the system, which is defined as the difference in pump and laser photon energies. As a percentage, the quantum defect (Qd) can be expressed:

$$Qd = \left(1 - \frac{h\nu_{LASER}}{h\nu_{PUMP}}\right) \times 100 = \left(1 - \frac{\lambda_{PUMP}}{\lambda_{LASER}}\right) \times 100 \qquad (4.4)$$

For typical Yb-doped systems, with a pump transition at 975 nm and the laser output at 1030 nm, the quantum defect is:

$$Qd = \left(1 - \frac{\lambda_{PUMP}}{\lambda_{LASER}}\right) \times 100 = \left(1 - \frac{975}{1030}\right) \times 100 = 5\% \qquad (4.5)$$

Thus, 5% of the pump power is wasted as heat or as photon re-absorption. The remaining ~95% of the pump energy can be converted into laser photons.

For the Yb-BG waveguide cavity, stable CW laser operation was obtained with all output couplers. Laser oscillation was also obtained without using an output coupler, due to the Fresnel reflection at the waveguide facet. For the Yb-BG – air interface, with their refractive indices of 2.03 and 1 respectively, the Fresnel loss is given as

$$R_F = \left(\frac{n_1 - n_2}{n_1 + n_2}\right)^2 = \left(\frac{2.03 - 1}{2.03 + 1}\right)^2 = 11.5\ \% \qquad (4.6)$$

Table 4.2 gives the CW laser performance for each output coupler. The output power as a function of pump power for selected output couplers is given in Figure 4.15.

Table 4. 2. The output couplers used to characterise the Yb-BG waveguide laser performance, and the corresponding results. A 975 nm pump laser with a maximum power of 265 mW was used for each measurement.

Output Coupler Transmission at 1060nm (%)	Output Power (mW)	Pump Threshold (mW)	Slope Efficiency (%)	Laser Wavelength (nm)
5.5	112.7	56	31	1042, 1049
10	101.5	38	44	1040
19	130.6	60	62	1006,1029,1037
30	163.3	62	79	1030,1035
41	117.3	89	65	1036
42	146.8	74	75	1037,1044
63	118.1	106	72	1023
70	104.8	112	66	1038
83	88.6	146	72	1025
89.5	45.4	202	76	1028
88.5/ Fresnel	46.1	201	81	1025
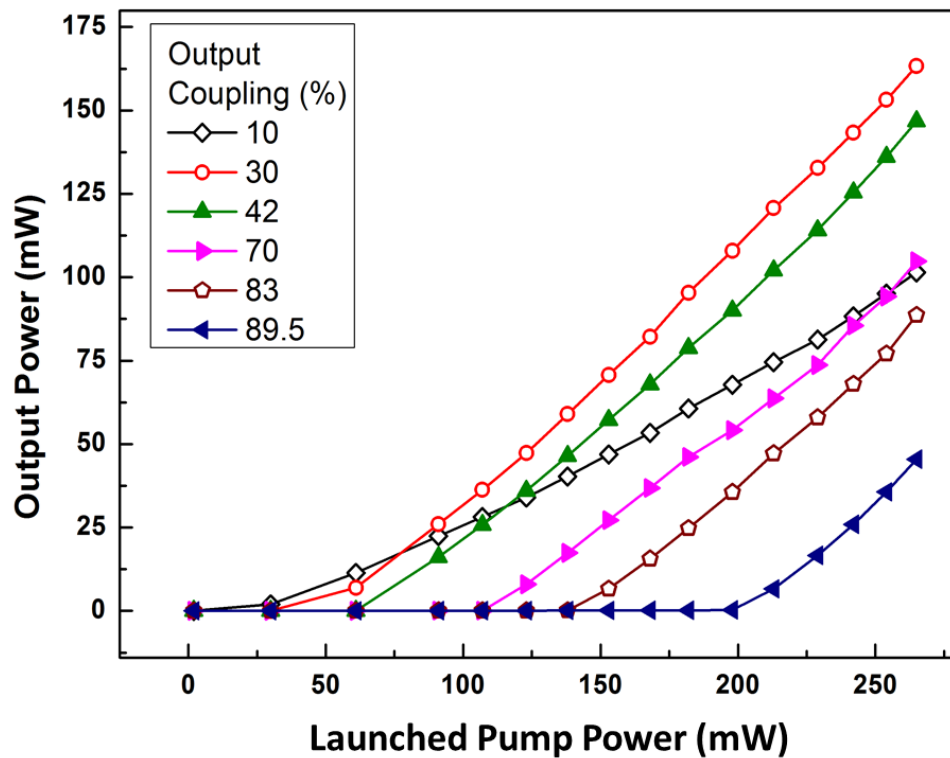
Figure 4. 15. Laser power as a function of absorbed pump power for different output couplers.

The waveguide laser shows efficient lasing for all output couplers, with the lowest slope efficiency of 30% attained with a mirror having 5.5% transmission at 1064 nm. The maximum slope efficiency is obtained for a cavity configuration with no output coupler. The end mirror is then formed by the 11.5% Fresnel reflection at the output end-facet, resulting in a slope efficiency of ~81%, which is close to the quantum defect limited value. A maximum output power of 163 mW is generated for an output coupling of 30%, with a corresponding slope efficiency of 79%.

4.7.2 Waveguide Loss Estimation based on Laser Performance

The propagation loss constitutes an important parameter that governs the performance of a waveguide laser. The waveguide PL can be estimated from the laser parameters by a number of methods based on the type of laser system. For four-level lasers, the loss can be estimated using a Findlay-Clay analysis whereas Caird Plots provide an estimate of loss in quasi three-level lasers. The Yb-BG waveguide laser forms a quasi three-level system. The PL in the cavity can therefore be estimated directly by a Caird plot analysis. A Findlay-Clay analysis can also be used, by accounting for additional loss due to re-absorption. The following section details both the Findlay-Clay analysis and Caird plots for Yb-BG system to provide a comparative analysis for the loss in the system.

The Findlay-Clay method [134] is used for waveguide loss estimation in four-level lasers, by an analysis of laser threshold values for different output couplers. At the laser threshold value, the cavity round trip gain exactly matches the cavity round trip loss, and can be expressed as [134],

$$2g_T l = 2\alpha l - \ln(R_1 R_2) \tag{4.7}$$

where g_T is the gain at threshold, α is the loss in the cavity per unit length and l is the length of the cavity. R_1 and R_2 are the reflectivity values of the cavity mirrors. We assume $R_1 \sim 1$, since it corresponds to the highly reflective pump input mirror. For an unsaturated gain medium, the gain is directly proportional to the pump power, and thus equation 4.7 can be expressed as:

$$P_T = K(L - \ln(R_{OC})) \tag{4.8}$$

where all the physical constants are grouped as K. P_T corresponds to the pump power at the laser threshold, $L \sim 2\alpha l$ is the cavity round trip loss and R_{OC} is the reflectivity of the output coupler. By plotting laser threshold versus $-\ln(R_{OC})$, the cavity round trip loss can be determined from the x-intercept of the linear fit. This method can be used for a quasi-three level system such as Yb-BG, for which the cavity round trip loss L also contains loss due to re-absorption.

Figure 4.16 shows the Findlay-Clay analysis for the Yb-BG waveguide laser, with the pump threshold plotted versus $-\ln(R_{OC})$. The cavity round trip losses were estimated by evaluating the x-intercept value of the linear fit to the experimental data, as 0.52 ± 0.084 dB. The length of the waveguide being 48 mm, the corresponding waveguide propagation loss is therefore 0.054 ± 0.008 dB cm^{-1}. This value includes re-absorption losses.
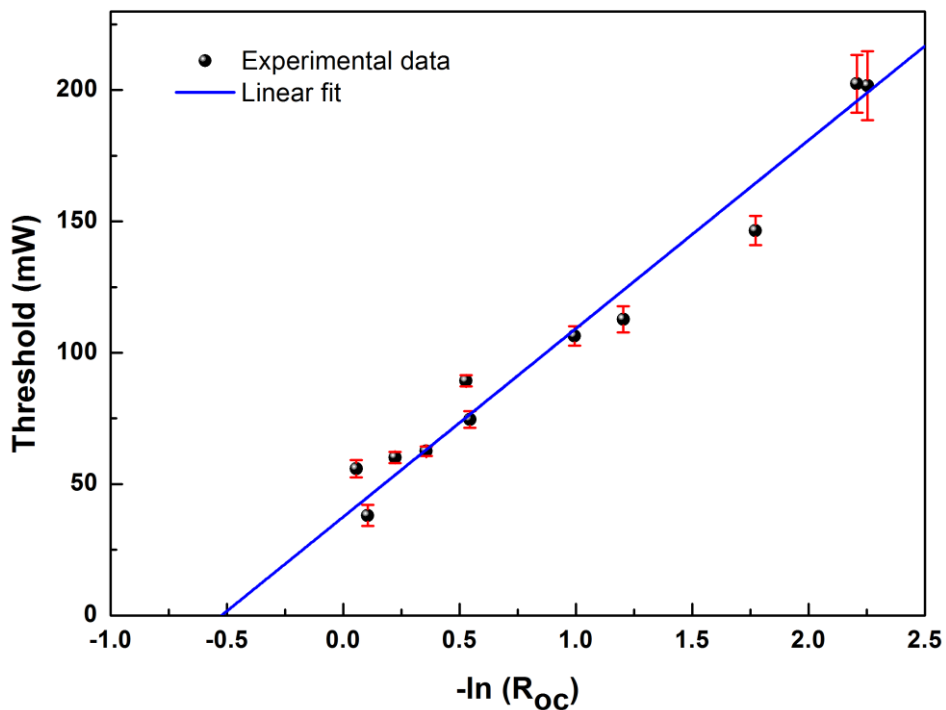
Figure 4. 16. Findlay-Clay analysis for the Yb-BG waveguide laser. The round trip cavity loss as given by the x-intercept is 0.52.

A more accurate method to estimate losses in quasi-three level lasers is by the Caird Plot method [135], which has little dependence on re-absorption losses. This method is based on the dependence of laser slope efficiencies on the cavity round trip loss, including the transmission at the output coupler. The Caird plot uses the relation,

$$\frac{1}{\eta} = \frac{1}{\eta_0} + \frac{L}{\eta_0}\frac{1}{T_{OC}} \qquad\qquad (4.9)$$

where η is the slope efficiency of the laser, η_0 is the intrinsic slope efficiency or the theoretical maximum value, L is the round trip propagation loss, and T_{OC} is the transmission of the output coupler. By plotting a straight line for $\frac{1}{\eta}$ versus $\frac{1}{T_{OC}}$, the intrinsic slope efficiency η_0 can be calculated from the intercept, and the propagation loss L can be estimated from the slope. For the Caird plot method of waveguide loss estimation, a plot of $\frac{1}{\eta}$ versus $\frac{1}{T_{OC}}$ was performed for the Yb-BG waveguide laser as shown in Figure 4. 17.
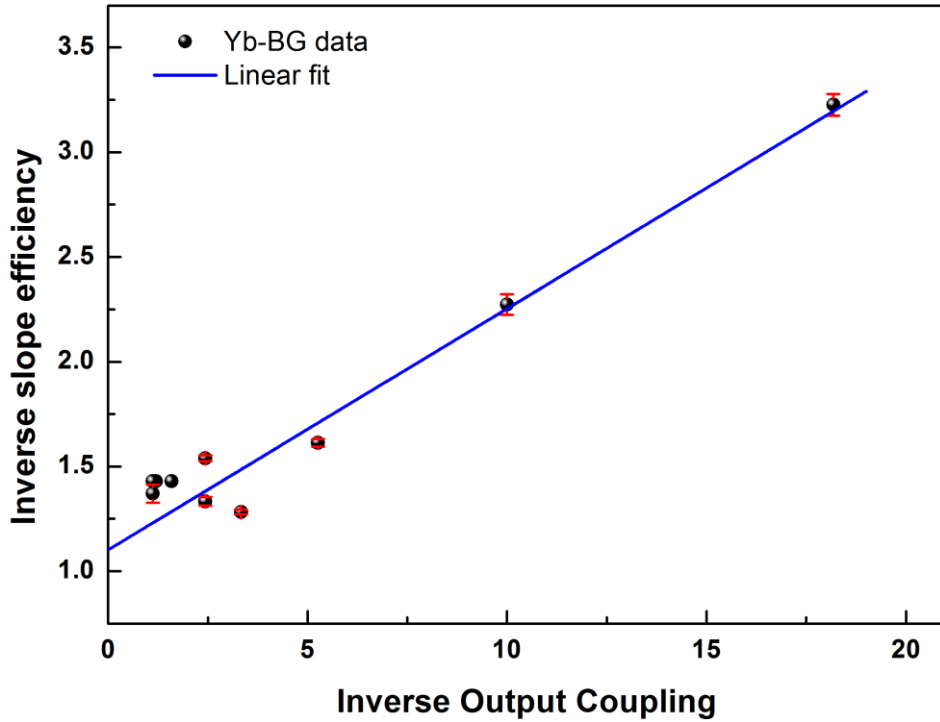
Figure 4. 17. The Caird plot for the Yb-BG waveguide laser. The intrinsic slope efficiency is the inverse value of the y-intercept of the linear fit.

The intrinsic slope efficiency is obtained from the linear fit to the data as the inverse of the y-intercept. η_0 is ~ 90.8% ± 6%, close to the quantum defect limited slope efficiency of ~95% typical of Yb-doped systems. The cavity propagation loss is then calculated from the slope of linear fit, and obtained as L= 10.44% ± 1.1%. For a cavity length of 48 mm, the loss is then 0.011 ± 0.001 cm^{-1}.The propagation loss of the waveguide can be calculated as, 0.047± 0.004 dB cm^{-1}.

For the Yb-BG substrate, both Findlay-Clay and Caird plots provide comparable values of PL. Both methods were compared to estimate the re-absorption losses in the system as ~ 0.007 dB cm^{-1}. The low propagation loss of the waveguides can account for the excellent laser performance in the Yb-BG linear cavity. This is supported by the microluminescence studies.

4.7.3 Modelling the Laser Performance: Rigrod Analysis

The optimal operating conditions for the waveguide laser, which involve a trade-off between low threshold pump power and high slope efficiency can be estimated by modeling the laser performance using a Rigrod type analysis [136, 137]. The Rigrod model provides information about the useful power output from a laser based on the small signal gain g_0, saturation intensity I_{sat}, and parasitic losses within the cavity.

Small signal gain g_0 is defined as the single pass gain experienced by an infinitely small signal when no amplifier saturation occurs. Saturation intensity I_{sat}, is that intensity at which the small signal gain drops to 1/e of its value, and parasitic loss corresponds to the total loss in the system excluding the useful output coupling.
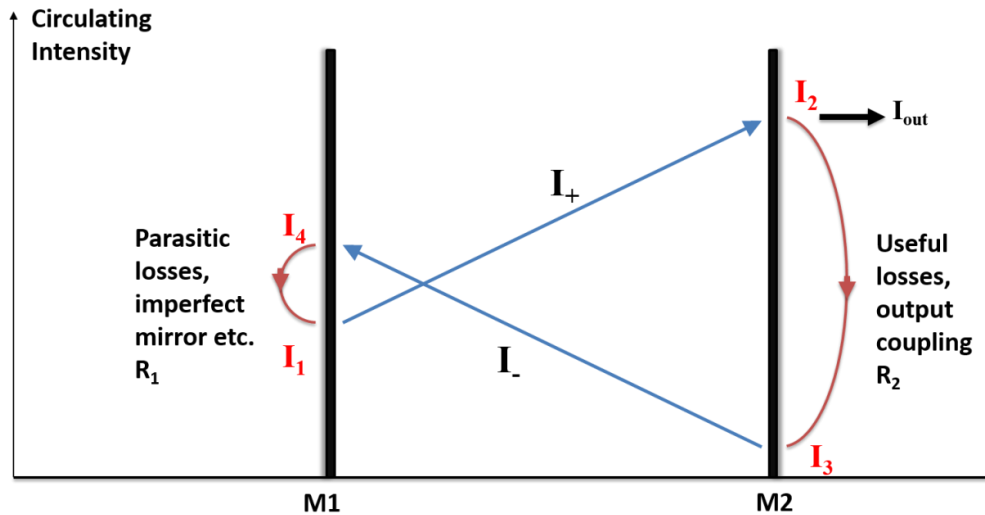
Figure 4. 18. The representation of gain and loss elements in a standing wave cavity, for Rigrod analysis. The possible loss in the system is accounted at both cavity mirrors. The input mirror introduces parasitic losses due to the mirror imperfections, whereas the output coupling constitutes useful losses. The counter propagating waves contribute towards the saturation of gain.

The Rigrod approach is based on a model of two counter propagating beams I$_+$ and I$_-$ within a standing wave laser cavity, similar to the waveguide laser. Figure 4.18 gives a

representation of the circulating intensities in a standing wave laser cavity that comprises a gain medium between cavity mirrors M_1 and M_2. M_1 is the HR mirror with a typical R~ 100%. M_2 corresponds to the output coupler. According to the model, the forward propagating beam in the cavity I_+ begins with an intensity I_1 at the mirror M_1, and ends with an intensity I_2 at mirror M_2. A portion of this beam is transmitted by the output coupler M_2 as useful laser output. The remaining quantity constitutes I_-, which travels in the reverse direction compared to I_+. Thus, I_- begins with intensity I_3 at mirror M_2, and gets amplified within the gain medium to reach a value I_4 at M_1. This cycle gets repeated in the laser cavity.

For this model, it is assumed that the intensity of both the counter propagating waves contribute to the gain saturation at a position within the cavity. Also, the parasitic losses within the cavity are concentrated at one point in the cavity, here, M_1. The intracavity intensity I_2 for the standing wave cavity can then be expressed as [136, 137],

$$I_2 = \frac{I_{sat}\left(g_0 L + \ln\sqrt{R_1 R_2}\right)}{1 + \sqrt{\dfrac{R_2}{R_1}} - R_2 - \sqrt{R_1 R_2}} \tag{4.10}$$

where, I_{sat} is the saturation intensity, g_0 is the small signal gain, L is the length of the cavity, R_1 is the parasitic loss in the cavity and R_2 is the useful output coupling at M_2. The useful laser output from the standing wave cavity is then given as,

$$I_{oc} = (1 - R_2)I_2 \tag{4.11}$$

For the Yb-BG waveguide laser, the experimental values of the laser output power I_{oc} for each output coupler value R_2 can be fit to the above equation 4.11 to estimate the saturation intensity , I_{sat}, the small signal gain, g_0, and the parasitic losses in the cavity, R_1 . Figure 4.19(a) shows the experimental data and the theoretical fit obtained by Rigrod analysis. The best fit of the Equation 4.11 to the experimental data yielded an optimum output coupling of ~30%, parasitic losses of 0.96% and a saturated power of 147 mW.
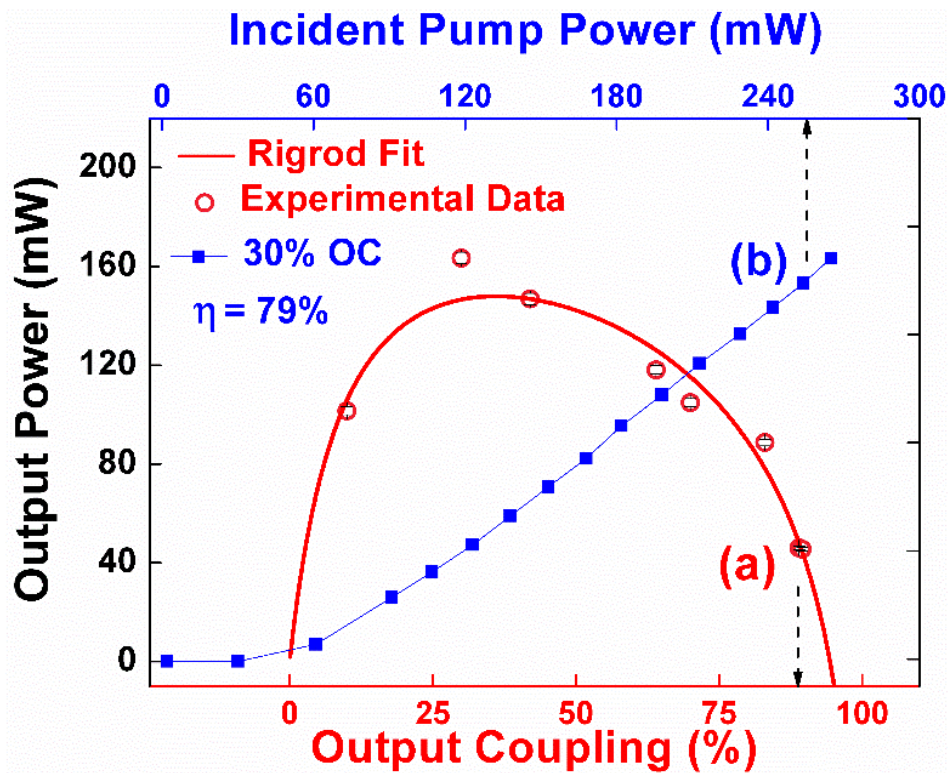
Figure 4. 19. (a) Output power vs. output coupling for a pump power of 265 mW. The fit was obtained using Rigrod analysis. (b) Slope efficiency and threshold measurements for 30% optimal output coupling.

For the optimum output coupling of 30% for the waveguide laser, a maximum output power of 163 mW for 265 mW incident pump power was obtained resulting in an optical conversion efficiency of 62%. The laser has a low threshold of 35 mW. The corresponding slope efficiency (η) was 79%, as shown in Figure 4.19(b); this value being the highest for a ULI-based waveguide laser at the time. The maximum output power was limited only by the available pump power.

The laser emission spectrum for the 30% optimum output coupling, measured using Advantest Q8384 Optical Spectrum Analyzer set at 0.5 nm resolution, is shown in Figure 4.20(a). It consists of two peaks separated by a few nanometers. The guided laser mode, shown in Figure 4.20(b), has a Gaussian intensity profile with a mode field diameter of 8.88 μm in the horizontal axis, and 8.75 μm in the vertical axis.

The laser beam quality was analysed using M^2 measurements using a knife edge and presented in Figure 4.21. An M^2 value of 1.3 was obtained along the axis defined by the number of ULI scans and a value of 2.4 was obtained along the confocal parameter axis.

The variation from the ideal $M^2 \sim 1$ along the latter is attributed to the multi-modal nature of the waveguide. These results were published in Optics Letters [138].
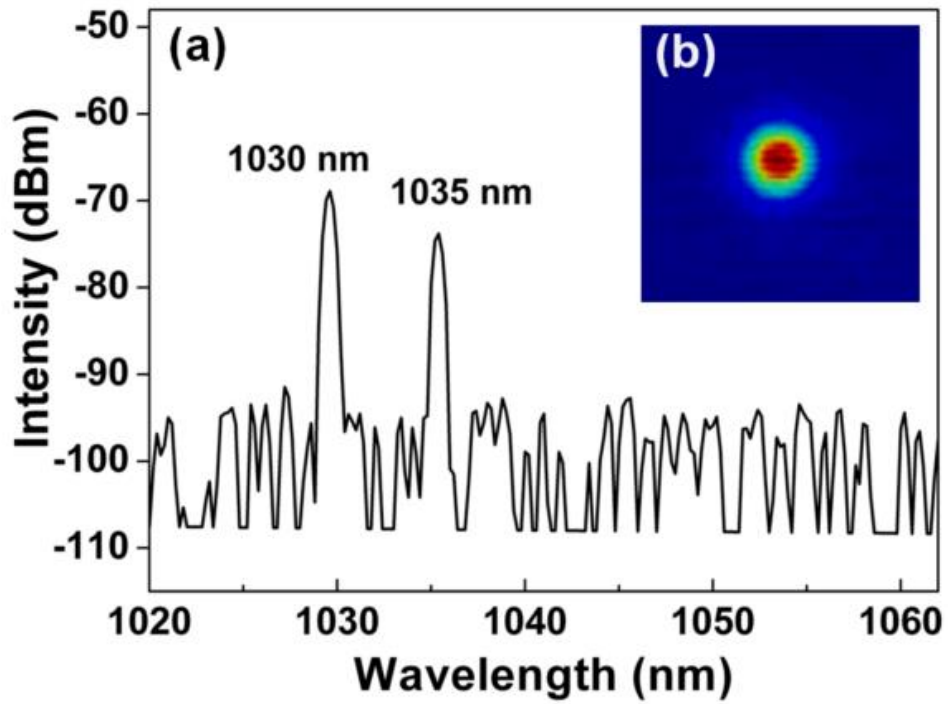
Figure 4. 20. (a) Emission spectrum of the Yb Bismuthate waveguide laser. (b) Near field distribution of the output beam.
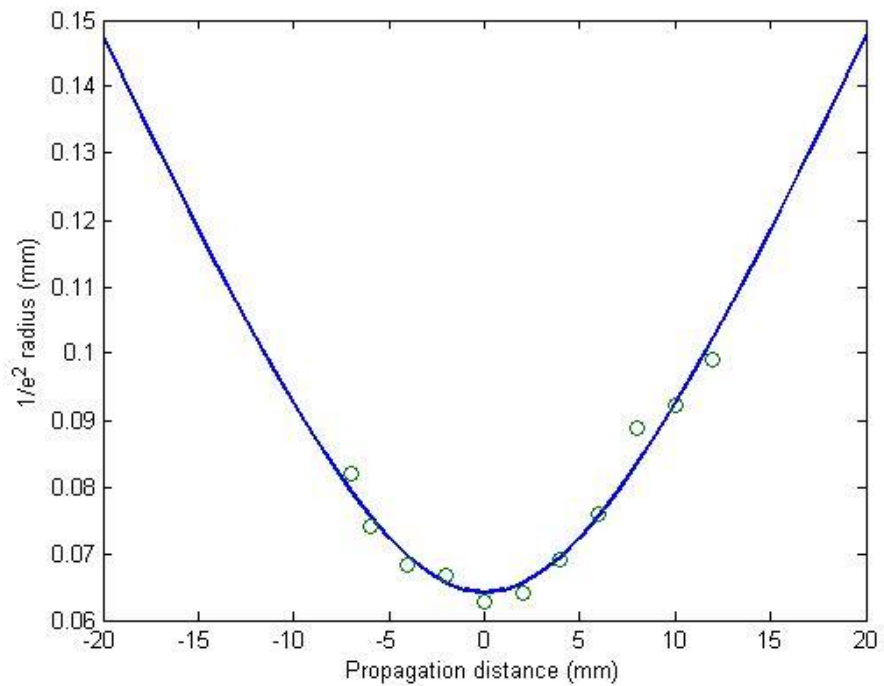
Figure 4. 21. M^2 measurement data of the Yb-BG waveguide laser

4.8 Conclusions

In this chapter, the applicability of Yb-BG substrate for ULI active device fabrication has been investigated. Low-loss waveguides were achieved in the substrate by the optimisation of the inscription parameters. This was followed by the demonstration of a highly efficient CW laser from the low-loss waveguide. Optimum output coupling of 30% resulted in a high laser slope efficiency of 79% that is close to the quantum defect limit and, a high optical conversion efficiency of 62%. The outstanding laser performance can be understood to arise from the high quality of the laser glass. This is confirmed by the micro-luminescence studies that indicate well-preserved properties of Yb ions in the bismuthate glass even after waveguide fabrication.

Chapter 5 – Nonlinear optical characterisation of graphene

5.1   Introduction

Graphene is the 2-D allotrope of carbon, with the carbon atoms tightly packed into a hexagonal lattice. Just one-atom thick, graphene has been studied theoretically as early as 1947 [139] as it forms the basic building block for other carbon allotropes with different dimensionalities. As shown in Figure 5.1, graphene can be wrapped to form zero-dimensional (0-D) fullerenes, rolled to form 1-D CNTs and stacked to form 3-D graphite. 2-D graphene was isolated only recently, in 2004, by Andre Geim and Konstantin Novoselov [140]. This achievement was followed by increased research into this material due to its exceptional properties in terms of tensile strength, electrical and thermal conductivity, flexibility and optical transparency [125] with the huge impact leading to a Nobel prize merely 6 years after its first production.

The property of graphene of relevance here is its saturation in optical absorption that makes it ideal for passive mode-locking of lasers. In graphene, for any excitation, there is always an electron-hole pair in resonance. Despite being only one atom thick, the material absorbs 2.3% of incident light for wavelengths spanning UV to THz [141]. The property of absorption saturation for a broad spectral range along with ultrafast recovery times in graphene has been widely utilised for passive mode-locking of lasers, including solid-state bulk, fibre, semiconductor and waveguide lasers [142, 143]. Fast saturable absorption is also exhibited by the 1-D allotrope of carbon, namely, CNT [142, 143]. Unlike the broadband absorption in graphene, the wavelength of operation in CNTs is determined by their chirality or diameter of the tubes. Tuneability is possible by using a wide diameter distribution, but with the risk of an increased loss in the system [142].
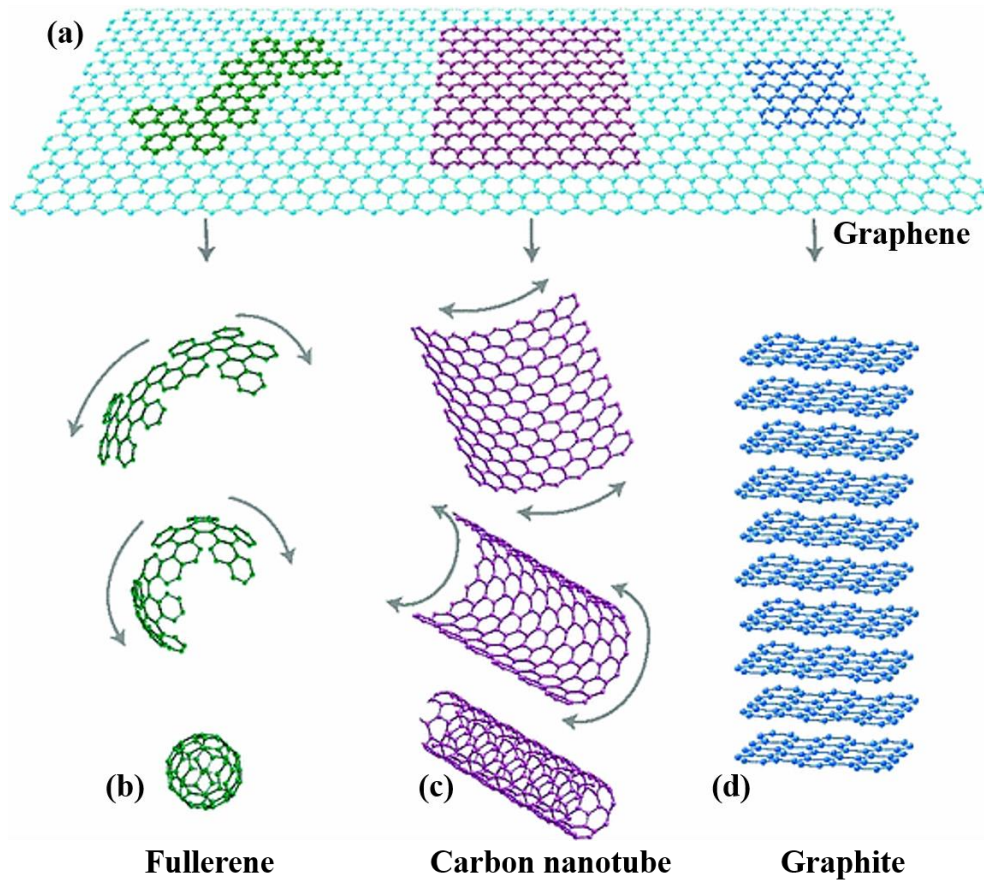
Figure 5. 1. (a) Graphene is the 2-D allotrope of carbon consisting of a planar honeycomb lattice. It forms the basis for other allotropes of carbon. Graphene can be wrapped to form (b) 0-D fullerenes, rolled to form (c) 1-D carbon nanotubes, and stacked to form (d) 3-D graphite. Reproduced from Ref [125].

This chapter discusses the unique properties of graphene which makes it ideal as a passive mode-locking element. Section 5.2 describes the optical properties of graphene and its ultrafast SA performance based on its bandstructure. The optical properties of CNTs are also discussed for completeness. Section 5.3 introduces the nonlinear optical characterisation techniques used to quantify a SA. Saturable absorption in graphene is then investigated at different wavelengths, and with respect to the number of graphene layers.

5.2   Saturable Absorption in Carbon Nanostructures

In any solid, the valence electrons of the atoms making up the material experience a periodic potential within the lattice due to the influence of other electrons and ions. According to quantum mechanics, these electrons are restricted to discrete energy states. In macroscopic structures, however, with a large number of atoms, the allowed discrete states of each electron combine to form continuous manifolds called energy bands.

Theoretically, every material has a large number of bands which may overlap or be separated by a bandgap; which is the range of energies where there are no allowed energy states. Of these manifolds, the most important bands and bandgaps in a material occur in the vicinity of the Fermi level, which is defined as the energy state which has a 50% probability of being occupied by an electron. The nature of the material, as a metal, semiconductor or an insulator is then based on the nature of the bands near this Fermi level, namely, the valence band and the conduction band.

The range of allowed energies for an electron within a solid is determined by the electronic bandstructure. It is represented as a plot of electron energies E(k) versus the wavevector k. This expression is also termed as the dispersion relation, and is derived using different theoretical models in a reciprocal lattice, depending upon the type of material. A reciprocal lattice, obtained by taking the Fourier transform of the original lattice wavefunction, is chosen, since the wavevector k can be represented as a point in this space. The reciprocal lattice does not describe a physical object. Rather, it is a geometrical tool for dealing with problems in the theory of diffraction and electronic structure of solids. A primitive cell in this reciprocal lattice is termed the Brillouin zone.

For covalent compounds such as graphene, the band structure is based on a tight binding model or tight binding approximation (TBA) which treats the final wave function as a linear combination of atomic orbitals. The dispersion relation is obtained by considering the solutions to the Schrödinger equation in a periodic potential. The following section describes the electronic band structure in graphene and CNT based on TBA and the resultant unique physical properties.

(a) Graphene

Monolayer graphene comprises of a hexagonal lattice of carbon atoms as shown in Figure 5.2(a). Each of the carbon atoms has 4 valence electrons, three of which form in-plane σ bonds with three neighbouring carbon atoms via sp^2 hybridisation. The 4th valence electron occupies the p_z orbital. The overlap between neighbouring p_z orbitals perpendicular to the plane results in the formation of π and π^* bonds, which are weakly bound to the carbon atoms and have higher energies than the σ bonds. The dispersion relation in graphene is obtained from the TBA model with these π and π^* bonds, and was first calculated by Phillip Russell Wallace in 1947 [139].

The hexagonal lattice in graphene can be considered as two interpenetrating sublattices, with lattice vectors $\mathbf{a_1}$ and $\mathbf{a_2}$, as shown in Figure 5.2(a). In the figure, the two sublattices are distinguished as red and blue atoms, namely, A and B. Transformation of the real atomic lattice of graphene into the reciprocal lattice yields a hexagonal first Brillouin zone, with the lattice vectors represented as $\mathbf{b_1}$ and $\mathbf{b_2}$; see Figure 5.2(b). A single hexagonal unit cell in the real lattice contains 2 atoms.

(a) Real space atomic lattice   (b) Reciprocal space lattice
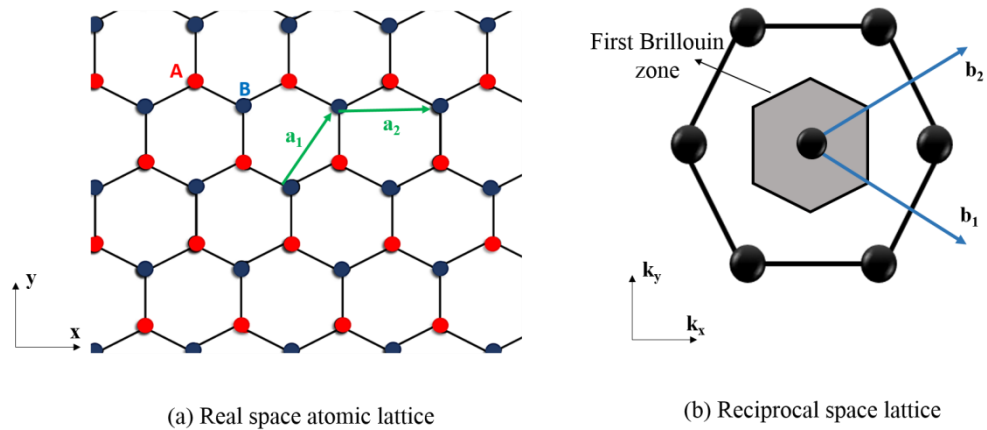
Figure 5. 2. (a) Real space hexagonal atomic lattice of graphene consisting of two sublattices, represented by atoms in red and blue. a_1 and a_2 are the lattice unit vectors. (b) The reciprocal lattice space representation of graphene. The lattice points in k-space are denoted by the black dots. The shaded region denotes the first Brillouin zone or the Wigner-Seitz unit cell in k-space. Adapted from [144].

Applying TBA to the reciprocal lattice of graphene shown in Figure 5.2 (b) yields the energy dispersion of graphene, which is given in Figure 5.3. The bandstructure of graphene consists of two bands, the π or valence band, and the $\pi*$ or conduction band. Both bands touch at 6 points termed K points or Dirac points situated at the edges of the first Brillouin zone in the reciprocal lattice [143]. Each carbon atom in graphene contributes one π electron and being fermions that are governed by Pauli's exclusion principle the electron may occupy either a spin-up or a spin-down state. As a result, the lower band in graphene is completely full and the conduction band is completely empty. The Fermi level is situated at the K point where the π and $\pi*$ band touches. Since the valence and conduction bands of graphene touch but do not overlap, graphene is termed as a zero bandgap semiconductor. This implies that irrespective of its energy, an incident photon can be absorbed by graphene.
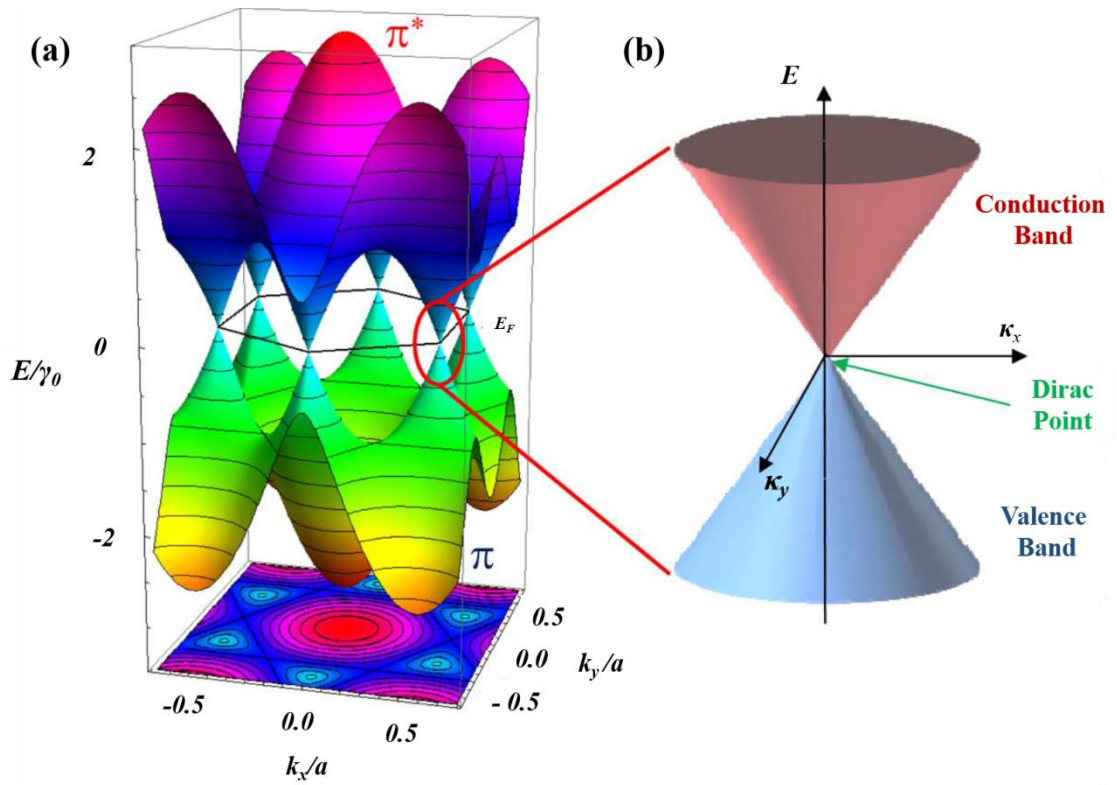
Figure 5. 3. Bandstructure of graphene. (a) Dispersion relation under TBA model. The valence and conduction bands meet at 6 points in the K-space called as K-point or Dirac point. These 6 points corresponds to the edges of the hexagonal Brillouin zone. (b) Near the Dirac point, the dispersion relation is linear. Reproduced from Ref [143].

Near the K-point, the band structure of graphene is approximately linear [143]. While conventional solids are described by the Schrödinger equation, low energy electrons in graphene are described by the Dirac equation that is typically used to describe relativistic massless electrons. This leads to a situation where, for low energy excitations < 4 eV [143], the electrons in graphene behave like massless particles. The high conductivity in graphene is a consequence of this massless property of the electrons, which can then travel at speeds close to the speed of light.

The linear dispersion relation also ensures a 2.3% linear absorption per layer for low energy excitations < 4 eV. In graphene, there is an electron-hole pair in resonance for a broad spectral range, which occurs as a result of the linear scaling in the size of the gap between the bands (not the bandgap) with respect to the Dirac point. This is illustrated in Figure 5.4(a).
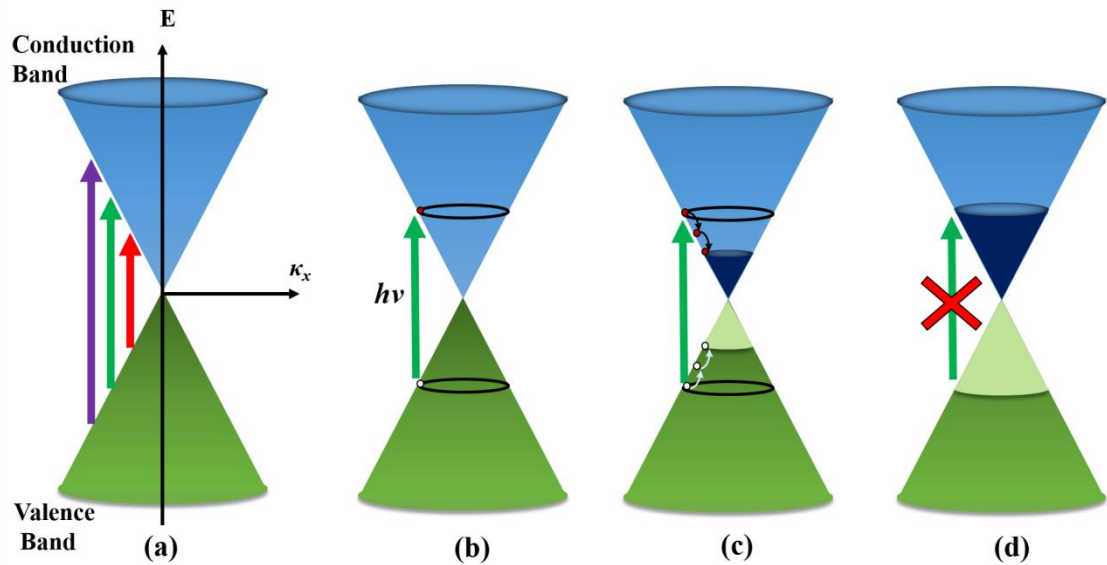
Figure 5. 4. The saturable absorption in graphene. (a) The linear dispersion relation in graphene. The blue and green cones represent the conduction band and valence band respectively. The solid arrows indicate excitation processes leading to linear optical absorption. The different colour coding indicates different frequencies of incident light (b) Absorption of an incident photon of energy hv, resulting in the excitation of an electron from the valence to the conduction band. (c) Intraband decay within the valence and conduction bands. This leads to a loss in carrier energy leaving room for further absorption of incident light into the same energy levels. (d) Absorption saturation in graphene at high irradiances that occurs as a result of completely filled lower energy levels.

The saturable absorption property in graphene arises from its band structure. For an incident photon of energy hv, there is always an electron-hole pair in resonance leading to absorption, as shown in Figure 5.4(b). No further absorption takes place, since by Pauli's exclusion principle, no two identical fermions or carriers in this case, can occupy the same quantum state. The absorbed electron in the conduction band loses energy by intraband collisions or intraband decay and migrates to lower energy levels within the same band. A similar process occurs within the valence bands for holes. The carriers (electrons and holes) first lose energy by collisions with other carriers, which occur in few fs time scale [145]. This is followed by collisions with the lattice, resulting in decay to lower energy levels. This intraband decay process, depicted in Figure 5.4(c), prevents the decay of the excited electrons back into the valence band but meanwhile allows the absorption of more electrons to the same initial level in the conduction band. When all the lower energy states in the conduction band and valence band become full by the intraband decay of carriers, the absorption of the incident light saturates, as shown in Figure 5.4(d). The material thereafter is transparent.

Graphene exhibits fast saturable absorption, with two recovery time scales associated with carrier relaxation [145]. The initial fast relaxation, of the order of ~100 fs is due to carrier-carrier and carrier-phonon transitions within the valence and conduction bands [143, 145], the process illustrated in Figure 5.4(c). The slower relaxation time ~ 1-2 ps occurs as a result of interband scattering between carriers and phonons, leading to the recombination of electrons and holes.

5.2.1.2   CNT

Single walled CNTs were discovered in 1993 by S. Iijima [146]. A CNT comprise of rolled up monolayer graphene with a typical tube diameter ~ 1 nm and length ~ 1 μm [143]. The type of cylindrical tube depends on how the graphene sheet is rolled and is expressed in terms of a parameter called chirality or the Chiral vector $\mathbf{C_h}$. The Chiral vector denotes two connecting points in a graphene layer whilst rolling to form a CNT and is described in multiples n and m of the in-plane lattice vectors $\mathbf{a_1}$ and $\mathbf{a_2}$, as,

$$\mathbf{C_h} = n\mathbf{a_1} + m\mathbf{a_2} \equiv (n, m) \tag{5.1}$$

Figure 5.5 shows a monolayer graphene sheet with lattice vectors $\mathbf{a_1}$ and $\mathbf{a_2}$. The shaded section in the layer indicates the portion that is rolled to form the CNT. A and B denote the connecting points in the graphene layer, which after rolling become a single point on the CNT tube surface. The Chiral vector connects these points A and B in the graphene sheet, and by vector addition, is represented by 5 units of $\mathbf{a_1}$ (n=5), and 2 units of $\mathbf{a_2}$ (m=2). The Chiral vector is therefore, $\mathbf{C_h} = 5\ \mathbf{a_1} + 2\ \mathbf{a_2} = (5,2)$ and provides a definite description of the structure of the CNT. Depending on the chiral vector, there can be different tubular structures for the CNT, as shown in Table 5.1.

The transition from 2-D graphene to 1-D CNT is associated with an electron confinement or boundary condition occurring at the circumference of the tube. The electronic band structure of CNT is obtained by considering a graphene plane folded into the Brillouin zone in the reciprocal lattice and applying the TBA model. While graphene is a zero gap semiconductor, with the occupied π and unoccupied π^* bands meeting at the K points in the Brillouin zone, CNTs can be metallic or semiconducting depending on the cylinder type and the zone folding. If the K point in the graphene
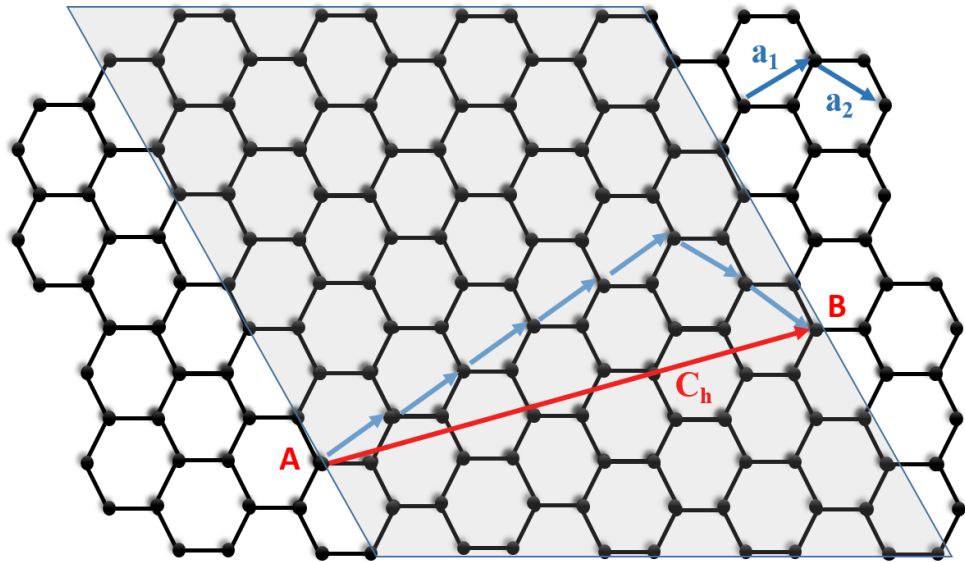
Figure 5. 5. The 2-D graphene sheet with lattice vectors denoted as a_1 and a_2. C_h, represented by line segment AB is the chiral vector. The tubes are formed by matching the end-points A and B of the chiral vector. The CNT structure is obtained by folding the graphene sheet through the connecting points represented by C_h. In this case $C_h = 5\,a_1 + 2\,a_2 = (5,2)$. Reproduced from Ref [143].

Table 5. 1. The tubular structure of CNT and the corresponding Chiral vectors.

CNT Tubular Structure	Chiral Vector
Zig-Zag	$m = 0$ (or $n = 0$)
Arm-chair	$n = m$
Chiral	$n \neq m$

bandstructure is mapped into the first Brillouin zone in the CNTs, then it results in metallic properties for the tube [143]. The nature of the CNT depends on the chirality of the tube and is governed by the following criterion, which is satisfied for metallic CNTs [143],

$$n - m = 3k \qquad (5.2)$$

where *k* is an integer. Semiconducting CNTs do not satisfy this criterion.

Figure 5.6 shows the band structure of metallic and semiconducting CNTs obtained by a superposition of graphene energy bands under a boundary condition, using the TBA model. Corresponding to the graphene Dirac points or K-points included in the superposition, many sharp peaks appear in the valence band (V_1, V_2...) and the conduction band (C_1, C_2,…), of the resultant CNT. These peaks are called van Hove singularities [143], and are illustrated in Figure 5.7 (a) and (b), which shows the energy level structure or density of states of metallic and semiconducting CNTS. The optical properties in CNTs occur as a result of electronic transitions between the V_1-C_1, V_2-C_2 states of CNTs, represented as transitions E_{11} and E_{22}. The energy gap corresponding to each van Hove singularity depends on the CNT structure. For semiconducting CNTs the bandgap depends on the tube diameter [143]. Thus by having nanotubes with a proper diameter distribution, the peak absorption can be tuned over a broad spectral range.
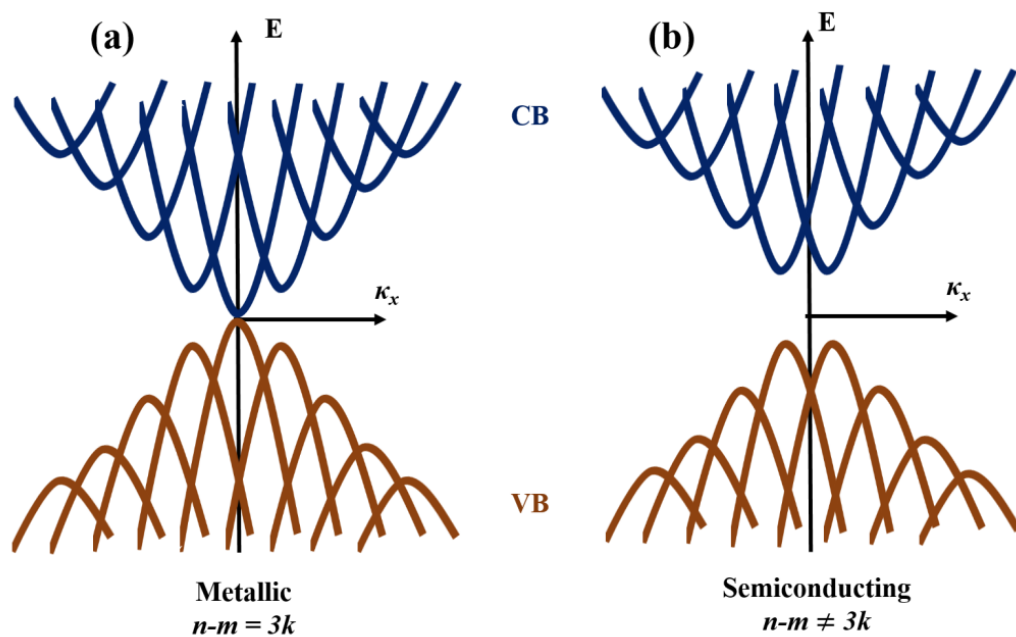
Figure 5. 6. Bandstructure of (a) metallic CNT and (b) semiconducting CNT. Reproduced from Ref [143].
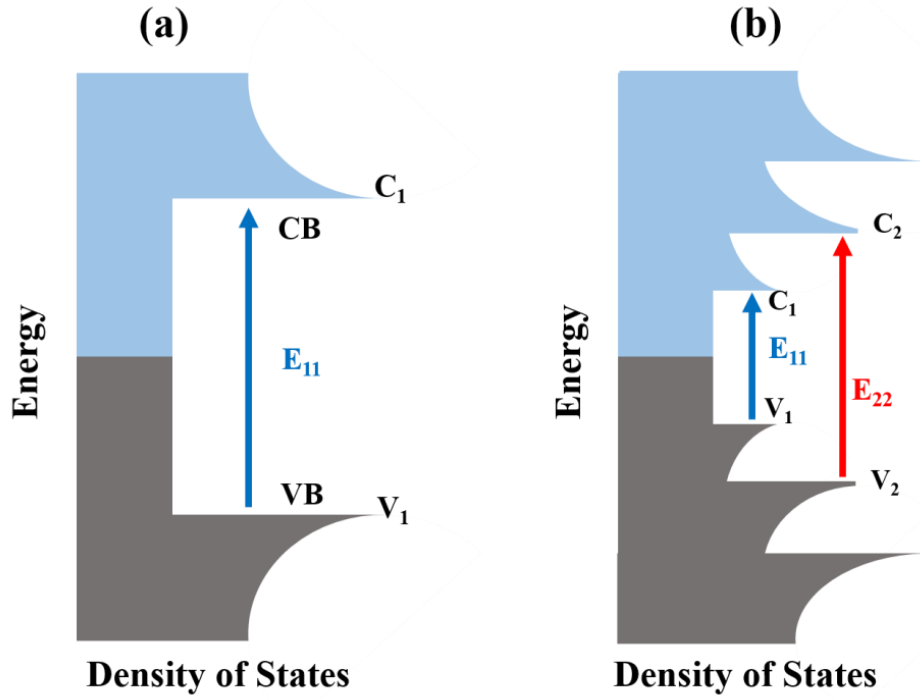
Figure 5. 7. Density of states of (a) metallic CNT and (b) semiconducting CNT. Adapted from Ref [143].

Similar to graphene, the absorption between two energy levels in CNTs also saturates at high irradiances [143]. The subsequent recovery time is inherently fast. For semiconducting CNTs, the E_{11} transition has a recovery time of ~1 ps, and for E_{22} transition, corresponds to ~ 100 fs [143]. These properties make them ideal for passive mode-locking. The property of fast saturable absorption was first demonstrated in CNT in 2003 [147], before it was observed in graphene. The first CNT mode-locked laser was demonstrated in 2004 by Set *et al.*[148], the same year as the first isolation of pure 2-D graphene by Novoselov *et al.* [140]. While the SA property in CNT has contributed significantly for ultrafast laser development [142], research around the world is currently focused on graphene mode-locking due to its superior properties, most importantly, broadband operation. Following a similar trend, the next section is focused on graphene, and describes the nonlinear absorption measurements in the material.

5.3 Nonlinear Optical Characterisation

The nonlinear optical properties of a SA provide the defining parameters of the absorber such as the modulation depth, ΔR, non-saturable loss, ΔR_{nr}, and saturation fluence, F_{sat}. The modulation depth refers to the maximum change in optical absorption and is typically expressed in percentage of transmission or reflectivity, depending on the type

of SA device. The non-saturable loss is the amount of loss in the system even after the absorber is bleached. The saturation fluence parameter refers to the fluence required to cause significant absorption saturation. These parameters for a SA are deduced from nonlinear absorption measurements, where the absorption or transmission of a SA is plotted with respect to incident laser pulse fluence [149]. The laser fluence can be derived from known values of the laser repetition rate and pulse duration.

In the case of mirror based SAs such as a SESAM, where transmission studies are not possible, the device is characterised based on its reflectivity [149]. Figure 5.8, reproduced from Haiml *et al.* [149] shows the theoretical curve for the saturation of a SESAM as a function of pulse fluence, in both the linear and log scale where, R_{lin} corresponds to the linear reflectivity and R_{ns}, the reflectivity of the SAM at absorption saturation.
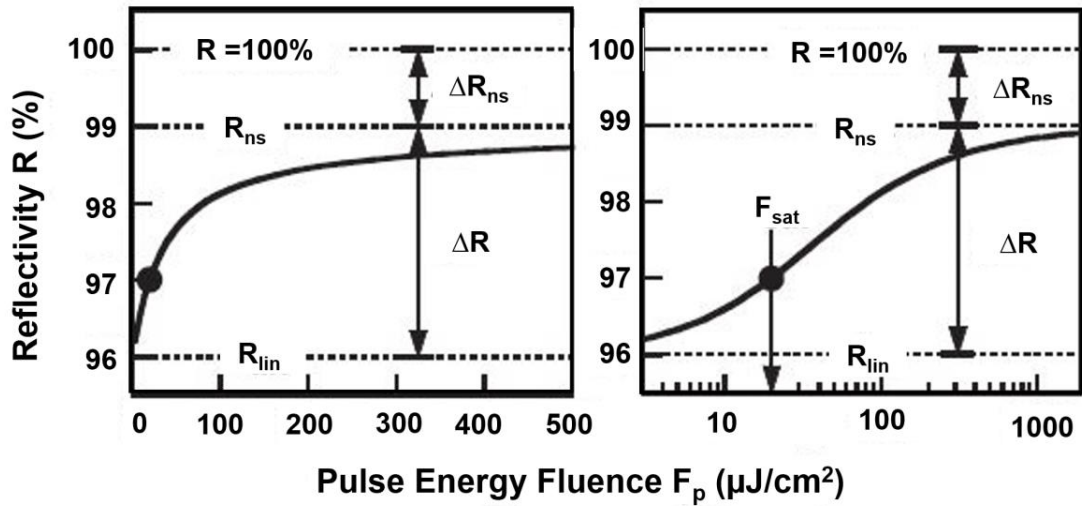
Figure 5. 8. Theoretical plot for nonlinear reflectivity R versus incident pulse energy fluence F_p. Left: linear scale. Right: logarithmic scale. R_{lin}: linear reflectivity; R_{ns}: reflectivity at absorption saturation; ΔR: modulation depth; ΔR_{ns}: nonsaturable losses in reflectivity; F_{sat}: saturation fluence. Reproduced from Ref [149].

The characteristic parameters of the device can be deduced from the plot based on a model function, which provides a relation for the reflectivity R of the SAM with respect to the input pulse fluence, F_p. The function is based on a travelling wave model that uses the rate equations for a two-level system, and is given as [149],

$$R(F_p) = R_{ns} \frac{\ln\left[1 + \frac{R_{lin}}{R_{ns}}(e^S - 1)\right]}{S} \qquad (5.3)$$

where S is the saturation parameter defined as $S = F_p/F_{sat}$. The modulation depth of the SA is then derived as $\Delta R = R_{ns} - R_{lin}$, and the non-saturable loss as, $\Delta R_{ns} = 1 - R_{ns}$, as previously introduced in Chapter 3.

Figure 5.9 shows the schematic of the measurement system used for nonlinear reflectivity studies, adapted from Haiml *et al.* [149]. The setup is used for nonlinear optical characterisation of graphene at 1064 nm, as discussed in the next section. The laser source is a Fianium fibre laser at a central wavelength of 1064 nm, repetition rate of 1 MHz and pulse duration of 1 ps. The collimated laser output has a beam diameter of 3 mm. The power of the laser is varied by using a variable attenuator system comprising of a half-wave plate and a polarising beam splitter (PBS). The half-wave plate rotates the polarisation of the incident beam, which is then split by the PBS into two beams of orthogonal linear polarisations.

By varying the relative angle between the half-wave plate and the PBS, the average laser power introduced into the system can be varied. At the point A in Figure 5.9, after the attenuator system, the average power output of the Fianium laser can be varied from 0 - 140 mW. At the focus of a 200 mm focal length lens, this corresponds to a maximum pulse fluence of 2230 μJ cm^{-2}. The attenuator system in combination with additional neutral density filters provides an input fluence range for the experiment that can be varied by up to three orders of magnitude.

The linearly polarised laser beam is then split into two paths, indicated as 'calibration arm' and 'sample arm', as shown in Figure 5.9. The laser beam along the calibration arm is sent to detector D_{IN}. The other beam is passed through the device under test (DUT). The DUT is placed on a mirror mount and xy translation stage at the focus of a 200 mm lens to achieve the required pulse fluence at the SA. The reflected light at the SA is collected at detector D_{OUT}. This method using two detection arms allows the elimination of the laser noise by subtracting the outputs from the two detectors. The reflectivity of the device is measured as the ratio of reflected intensity at D_{OUT} to the incident intensity at D_{IN}.

Lock-in detection is used in order to eliminate other noise sources such as the background light and the photodetector dark currents. Using a lock-in amplifier,

selective amplification is possible, where the signal that is oscillating in phase with a reference signal at a specific frequency is amplified and all other signals are rejected. A chopper is therefore inserted into the laser beam path to modulate the signal.
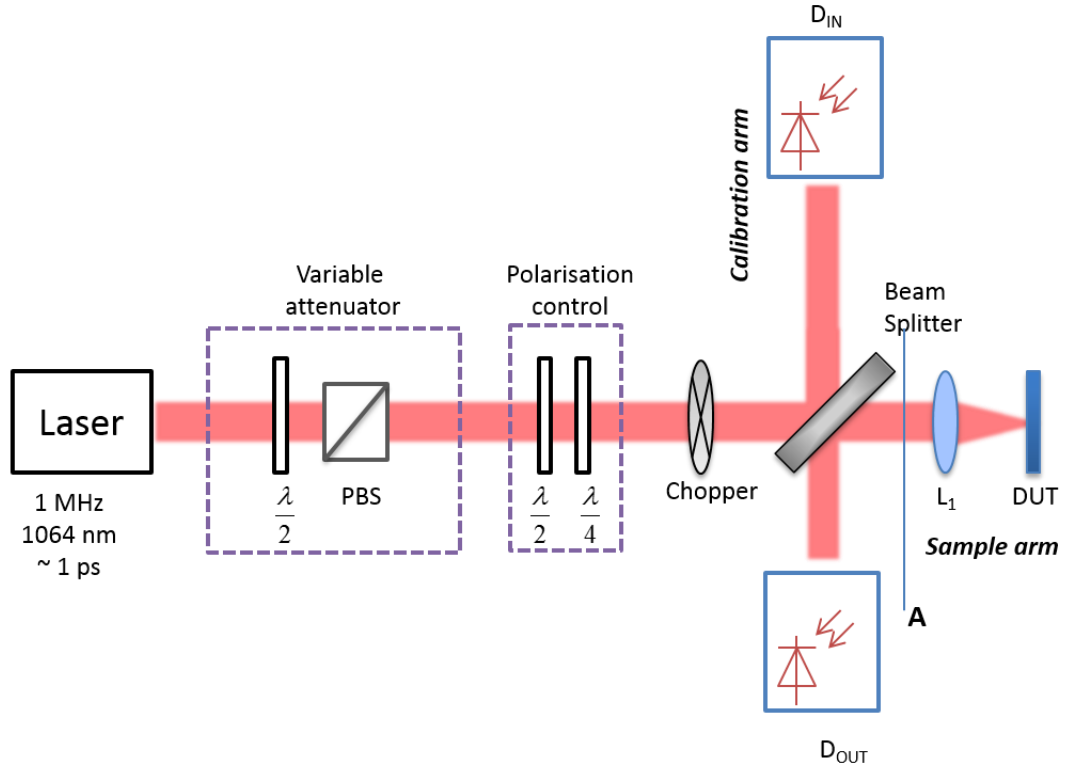
Figure 5. 9. Schematic of the experimental setup to measure the nonlinear optical properties of graphene. The pulsed laser after appropriate attenuation is incident on the beam splitter which splits the laser along two arms. The beam along the 'calibration arm' is measured by Detector D_{IN}. The beam along the 'sample arm' is focused by lens L_1 onto the device under test (DUT). The reflected beam from the DUT is measured by detector D_{OUT}. The chopper allows a lock-in detection, used to reduce background noise in the measurement.

5.3.1 Graphene Saturable Absorption

The most important feature of graphene SA is the broadband tuneability of the absorber by virtue of its linear dispersion relation. This has led to a definite shift in research interests, from CNT-SA to graphene SA, to study the application potential of the latter. The following section investigates the dependence of graphene absorption saturation on (a) operating wavelength and (b) number of graphene layers in the SA.

5.3.1.1 Wavelength Independent Absorption

The nonlinear absorption of graphene SA at 1 µm and 2 µm was studied. The graphene samples were obtained through a collaboration with the Cambridge Graphene Centre, University of Cambridge, UK. The graphene SA was prepared by Liquid Phase Exfoliation (LPE), a process where, graphite flakes are dispersed in a solvent which undergo ultrasonication and centrifugation to obtain a final dispersion containing small flakes of few layer and single layer graphene. This process is well-suited for mass production and is economical compared to other fabrication techniques such as chemical vapour deposition. The sample used for the experiments was prepared by LPE, yielding a graphene dispersion in deionised water with added sodium deoxycholate, which is a surfactant or a dispersant used to prevent clumping of the graphene flakes. The dispersion then undergoes vacuum filtration via 25 nm pore-size filters. This blocks the flakes while allowing the water to pass through resulting in a graphene film. For the optical absorption experiment, the film was placed on a partial reflector at 1 µm, and on a quartz plate. Pressure and heat were applied for two hours, followed by dissolution of the filter in acetone [131]. The partial reflector has a reflectivity of 90% at 1064 nm making the graphene film coated mirror ideal for characterisation measurements in the reflection mode.

The experimental setup used for the optical characterisation of the graphene is given in Figure 5.9. Initially, a commercially available SESAM from Batop, designed for 1064 nm and with a high modulation depth was used to calibrate the setup. By varying the incident pulse fluence, the saturable absorption in the device was mapped out. Using the model fit given in Equation 5.3, the saturation fluence of the SESAM is calculated as 24 µJ cm^{-2} with a modulation depth of 42%. These values are in good agreement with the manufacturer's data of 19 µJ cm^{-2} saturation fluence, and a modulation depth of 40%, confirming the measurement accuracy of the experimental setup.

For the characterisation of the graphene film deposited on a 90% reflectivity mirror, referred to as GF-SAM, the device was placed at the DUT position as shown in Figure 5.9. The position of the GF-SAM was adjusted to be at the focus of the lens L_1 using the translational control in the xy sample stage. For an incident collimated laser beam of 3 mm diameter and focused down by a 200 mm focal length lens, the focal spot size is calculated to be ~0.09 mm. This corresponds to a maximum laser pulse fluence of 2230 µJ cm^{-2} at the SA. The pulse fluence was varied from zero to this maximum value to

determine the range of the nonlinear reflectivity of the GF-SAM, as shown in Figure 5.10. The parameters of the SA were derived by fitting the experimental curve to the model fit given in Equation 5.3. The SA has a saturation fluence of 10.1 μJ cm^{-2}, a modulation depth of 17.6% and a non-saturable loss ~ 30%. The sample was used for laser mode-locking of a Yb-BG waveguide laser, which will be discussed in the next chapter. These results including Figure 5.10 were published in Optics Express [131].
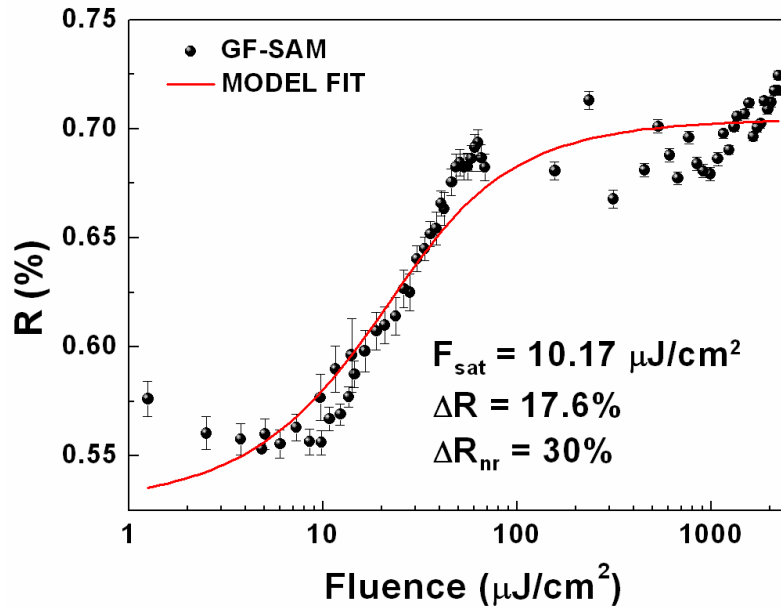
Figure 5. 10. Nonlinear reflectivity versus incident pulse fluence for graphene SA at 1064 nm. A model fit was used to derive the SA parameters: F_{sat} =10.17 μJ cm^{-2}, ΔR = 17.6 %, and ΔR_{ns} = 30%.

To measure the properties of graphene at a different wavelength of 2 μm, graphene film coated on a fused silica substrate was used. An experimental setup similar to that in Figure 5.9 was used, however in transmission mode due to the nature of the sample. The sample was placed at the DUT position along the focus of the lens, and the transmitted laser beam was collected by the detector D_{OUT} at the far side of the sample. The laser used was a Spectra-Physics optical parametric amplifier generating ~100 fs pulses at a repetition rate of 1 kHz, and centred at 2 μm. The input pulse fluence is varied in incremental steps to investigate the saturable absorption property of the sample. Figure 5.11 gives the evolution of device transmittance with respect to the incident pulse fluence. Fitting the data to the model function yields a saturation fluence ~59 μJ cm^{-2}, a modulation depth ~8.4% and non-saturable losses ~ 28% for graphene at 2 μm. This part of the work was done in collaboration with Giorgos Demetriou, also in the Nonlinear Optics Group at Heriot-Watt University. The results are used to characterise a

graphene based Tm:YAG laser at 2 μm and the corresponding paper submitted to the Journal of selected topics in Quantum Electronics.
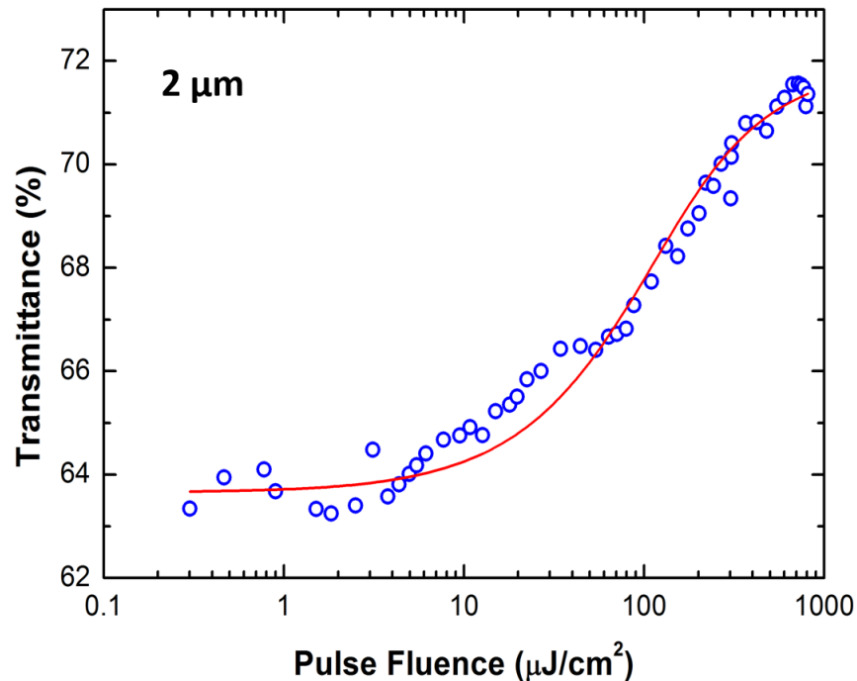
Figure 5. 11. Nonlinear transmittance versus incident pulse fluence for graphene SA at 2 μm. A model fit was used to derive the SA parameters: F_{sat} *=59 μJ cm^{-2},* ΔR *= 8.4 %, and* ΔR_{ns} *= 28%.*

The SA parameters of graphene at 1 μm and 2 μm wavelengths are summarised in Table 5.2. Both the graphene samples are fabricated by the LPE method. The saturation fluence of the GF at 2 μm is 59 μJ cm^{-2}. While the value is higher than that at 1 μm, both the values are of the same order of magnitude. The samples have identical non-saturable losses loss values ~30%. In terms of modulation depths, the values for the two samples differ by < 10%. The experimentally obtained SA parameters are therefore consistent with theoretical wavelength independent nature of saturable absorption in graphene [150]. While the wavelength dependent nature of absorption saturation in graphene has been studied previously [29], the saturable absorber parameters such as the modulation depth and saturation fluence vary depending on the type of graphene sample and the number of layers. In that regard, this study focused on LPE graphene samples contributes to the already vast literature, as experimental evidence for wavelength independence.

Table 5. 2. Nonlinear optical properties of graphene SA at different wavelengths.

	Graphene SA at 1μm	Graphene SA at 2 μm
Saturation fluence (μJ cm^{-2})	10	59
Modulation Depth (%)	17.6	8.4
Non-saturable Loss (%)	30	28

5.3.1.2   *Number of Graphene Layers*

Monolayer graphene, despite being only one-atom thick, absorbs ~2.3% of the incident light in a wavelength independent manner. Also, the absorption in graphene scales linearly with the number of graphene layers [143]. This property makes it important to study the nonlinear absorption behaviour of graphene with respect to the number of layers. An increase in the graphene layers is found to increase the non-saturable loss in the system due to additional loss per layer, and consequently decrease the modulation depth [151]. This section investigates the absorption saturation in graphene based on the number of layers. Since controlling the number of layers of graphene is essential for the experiment, graphene grown by chemical vapour deposition (CVD) was selected over the LPE technique. In the CVD method, a chemical reaction between a combination of gas molecules within a reaction chamber and a substrate surface produces uniform layers of graphene. While LPE produces few layer graphene, it does not provide the precise control of layers that CVD can afford. The samples were obtained through a collaboration with Graphene Research Centre, National University of Singapore, and are listed in table 5.3.

Table 5. 3. List of CVD graphene samples used for nonlinear optical characterisation of graphene. The change in SA properties with respect to the number of graphene layers is investigated. FLG- Few layer graphene with 5-7 layers. MLG – monolayer graphene.

	Sample Name	Description
1	MLG-1	Monolayer graphene (MLG) coated on a quartz substrate
2	MLG -2	Monolayer graphene (MLG) coated on a quartz substrate
3	FLG -1	Few layer graphene, with 5-7 layers coated on a quartz substrate
4	FLG -2	Few layer graphene, with 5-7 layers coated on a quartz substrate
5	FLG- MirrorT10	Few Layer Graphene (FLG) with 5-7 layers, coated on mirror with 10% transmission at 1064 nm
6	FLG – MirrorT40	FLG, with 5-7 layers coated on mirror with 40% transmission at 1064 nm

In order to obtain a clear distinction about the variation of SA properties with the number of graphene layers, monolayer graphene (MLG) absorption was compared with multi-layer graphene that comprises of 5-7 layers. In this section, the 5-7 layer graphene sample is referred to as few layer graphene (FLG). The availability of duplicate samples, namely 2 MLG samples and 2 substrates with FLG, ensures additional accuracy in the SA parameter estimation. FLG was also coated on partial reflectors with a transmission of 10% and 40% at 1064 nm, named FLG-MirrorT10 and FLG-MirrorT40 respectively. These samples are practical SA devices or SAMs that can be used for passive mode-locking of solid-state bulk or waveguide lasers.

The absorption saturation measurements for the graphene substrates were performed at a laser wavelength of 1064 nm using the experimental setup given in Figure 5.12. Since the majority of samples constitute graphene samples on quartz substrates, not suited for reflectivity measurements, the setup is designed for nonlinear transmission measurements. The setup is obtained by modifying that in Figure 5.9 from nonlinear

reflection to transmission mode. The laser, with 1 MHz repetition rate at 1 ps pulse duration was operated at 140 mW average laser output to provide a maximum pulse fluence of 2230 μJ cm^{-2} at the focus of the 200 mm focal length lens (L$_1$) along the sample arm. The graphene sample was placed at the DUT position, and the transmission through the sample with increasing pulse fluence is mapped out. The corresponding plots are given in Figures 5.13- 5.18. The measured transmittance of each sample is referenced using an identical non-coated substrate, such that the response of only the graphene film is obtained.
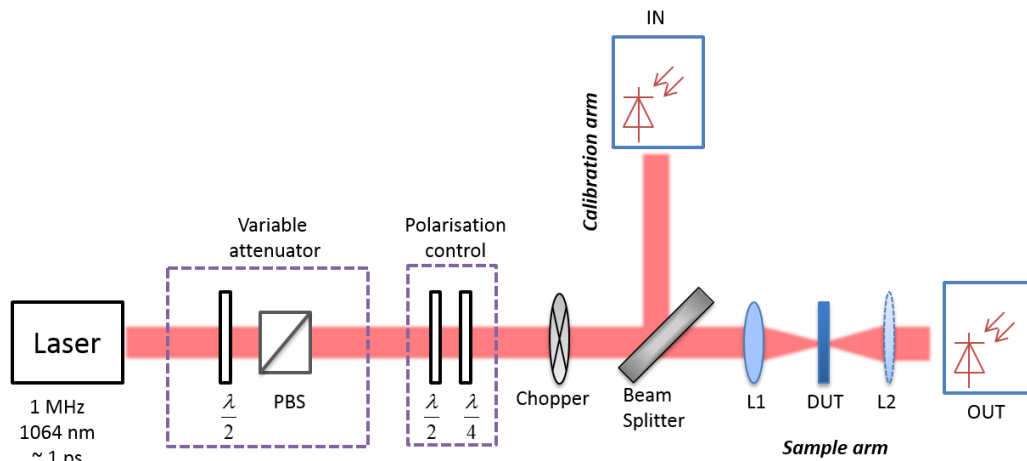
Figure 5. 12. The experimental setup for nonlinear transmission measurements of graphene.
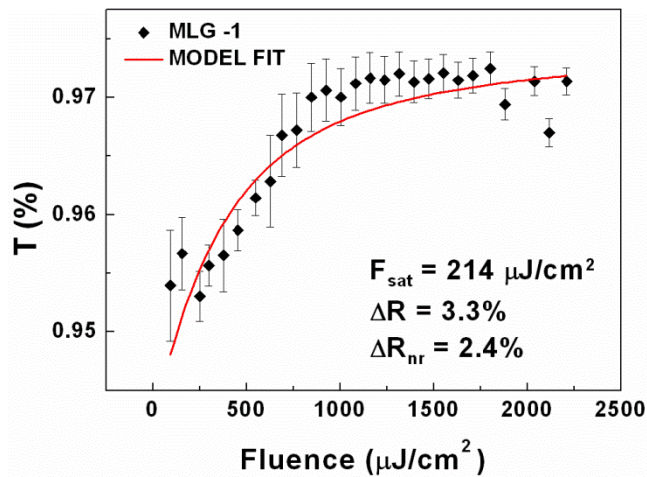
Figure 5. 13. Nonlinear transmittance versus pulse fluence for monolayer graphene (MLG) coated on a fused silica substrate. MLG Sample-1
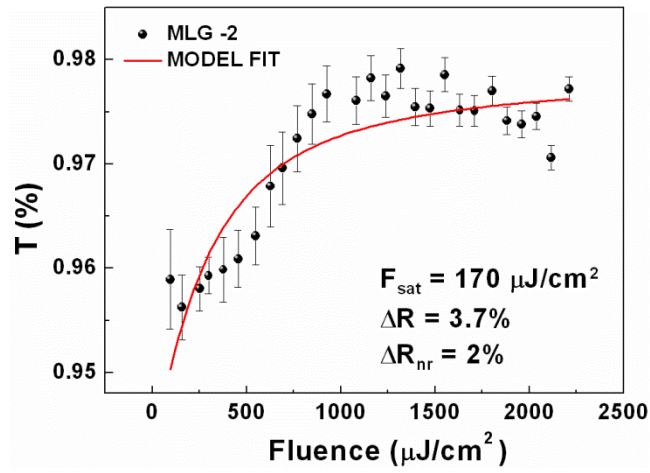
Figure 5. 14. Nonlinear transmittance versus pulse fluence for monolayer graphene (MLG) coated on a fused silica substrate. MLG Sample-2.
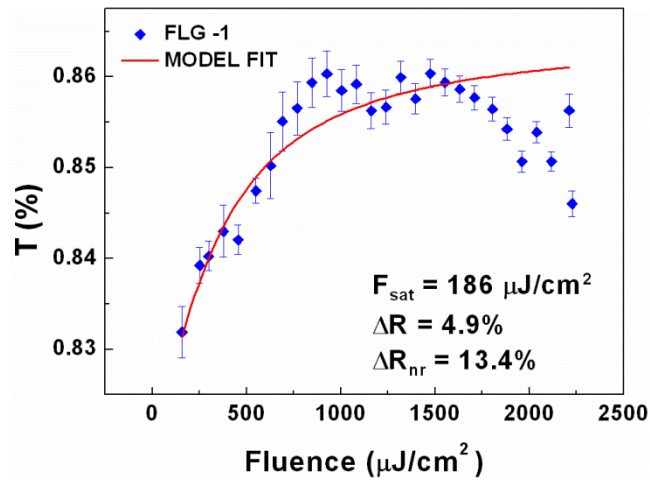
Figure 5. 15. Nonlinear transmittance versus pulse fluence for few layer graphene (FLG) coated on a fused silica substrate. FLG Sample-1
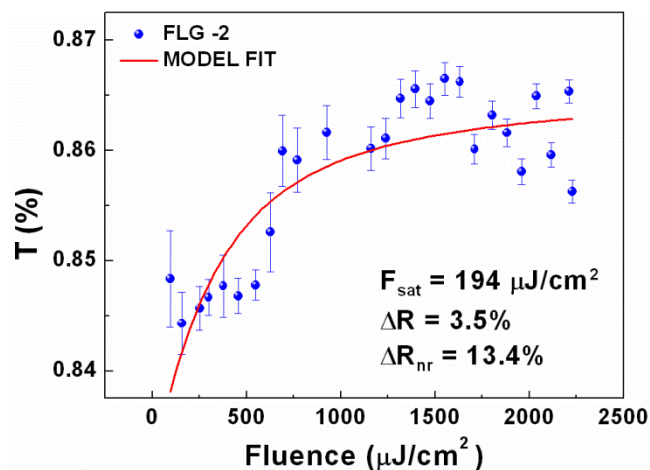
Figure 5. 16. Nonlinear transmittance versus pulse fluence for few layer graphene (FLG) coated on a fused silica substrate. FLG Sample-2.
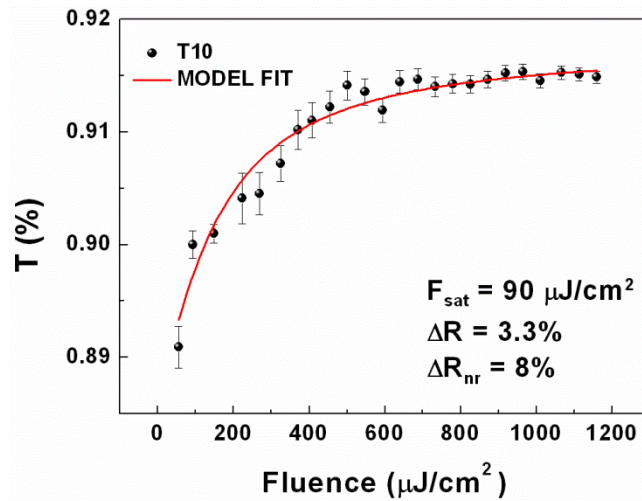
Figure 5. 17. Nonlinear transmittance versus pulse fluence for graphene coated on output coupler for 1064 nm. The mirror has a 10%T at 1064 nm.
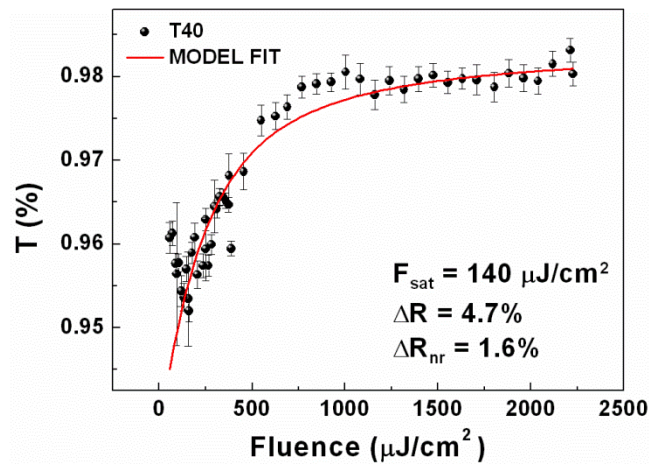
Figure 5. 18. Nonlinear transmittance versus pulse fluence for graphene coated on output coupler for 1064 nm. The mirror has a 40% T at 1064 nm.

The SA parameters for the graphene samples derived using the model fit given in Equation 5.3 are tabulated in Table 5.4. The graphene samples are found to have a small modulation depth <5%, making them ideal for passive continuous wave mode-locking. The SA parameters for single graphene layers are comparable, with ΔR values of 3.3 % amd 3.7%, and ΔR_{nr} values of 2.4% and 2% for MLG-1 and MLG-2 samples respectively. Similarly, the FLG samples have comparable SA parameters, thereby confirming the accuracy in the measurement system. The non-saturable loss in MLG system is ~ 2% whereas for FLG samples, ΔR_{nr} ~ 13.4%. This provides an experimental confirmation for the increased non-saturable loss with graphene layers due to additional loss contribution per layer. The graphene film on output couplers with 10% and 40% transmission has a modulation depth of 3.3% and 4.7% respectively. These values are

111

comparable to the ΔR values of FLG samples. The saturation fluences for the samples range from 90 – 214 μJ cm^{-2}, with the value almost half for the high reflectivity mirror. This could be explained by the 90% reflectivity in the mirror structure which leads to a higher amount of average light absorption by graphene due to a double pass within the film, in comparison with the 60% reflectivity mirror. The non-saturable loss in the FLG-MirrorT10 was 8%, comparable to ~13.4% in the other FLG samples. However, for the output coupler with a 40% transmission at the laser wavelength, the non-saturable loss was found to be low ~1.6%. One explanation for this anomaly could be the use of the difference substrates with varied transparencies at the laser wavelength. As the non-saturable loss value corresponds to that of mono-layer graphene, a defect in the sample could also be a possible factor, especially since the graphene film tended to detach easily from the substrate.

Table 5. 4. Saturable absorber parameters for the different graphene samples

Sample	Modulation Depth (%)	Saturation Fluence (μJ/cm^2)	Non-saturable losses (%)
MLG-1	3.3	214	2.4
MLG -2	3.7	170	2.0
FLG -1	4.9	186	13.4
FLG -2	3.5	194	13.4
FLG- MirrorT10	3.3	90	8
FLG – MirrorT40	4.7	140	1.6

5.4   Conclusion

The saturable absorber properties of graphene have been investigated. A variation of nonlinear reflectivity (or transmittance, depending upon the samples) with respect to incident pulse fluence has been studied. A model function based on travelling waves in a two-level system has been used to derive the key parameters of saturation fluence, modulation depth and non-saturable losses of the SA. Firstly, a nonlinear reflectivity study has been performed at two distinct wavelengths, at 1 μm and 2 μm. The study

yielded similar SA parameters confirming the wavelength independent absorption saturation in graphene. Secondly, the dependence of the number of graphene layers for saturable absorption was investigated. With an increase in graphene layers, the non-saturable loss of the SA is found to increase. The use of these SAs for laser mode-locking is investigated in the next chapter.

Chapter 6– Ultrafast pulse generation in an integrated cavity Yb-doped bismuthate glass waveguide laser

6.1   Introduction

The emerging interest for miniaturisation of optical devices based on on-chip integration has resulted in an increased interest in the development of compact ultrafast laser sources. A waveguide laser inherently satisfies this criterion, while maintaining a laser performance comparable to other systems. In Chapter 4, a compact high efficiency CW laser was demonstrated in a Yb-BG waveguide. In this chapter, ultrafast operation from this laser is investigated using the predominant SA technologies, namely, SESAM, CNT and graphene. Section 6.2 provides an introduction to ultrashort pulse generation and the measurement techniques used for quantifying them. In Section 6.3, passive mode-locking using semiconductor SAs is discussed. The laser performance using CNT-SA and graphene SA are described in Sections 6.4 and 6.5, respectively.

6.2   Characteristics of Ultrashort pulses

Ultrashort pulses, by definition, have pulse durations less than few tens of ps, and are achieved by various mode-locking technologies, previously outlined in Chapter 3. Mode-locking refers to the locking in phase of the longitudinal modes in a laser cavity. In a standing wave laser cavity such as the Yb-BG waveguide laser, with light bouncing between two parallel mirrors, only discrete frequencies of light are supported by constructive interference. This is governed by the relation,

$$\frac{m\lambda}{2} = L \tag{6.1}$$

where m represents the mode order, λ is the wavelength of light and L is the length of the cavity. These allowed set of frequencies are called the longitudinal modes of the cavity. All other frequencies interfere destructively. According to Equation 6.1, the modes oscillate at different wavelengths corresponding to different allowed values of the integer m. However, the allowed frequencies are also restricted by the gain bandwidth of the laser medium. Thus, only those values of λ that correspond to the gain

bandwidth, and that satisfy Equation 6.1 will be amplified. The frequency difference Δv between the longitudinal modes in a standing wave cavity is defined as:

$$\Delta v = \frac{c}{2L} \tag{6.2}$$

where L is the optical path length of the cavity. In the case of an integrated waveguide laser, the size of the gain medium determines the length of the cavity. Thus, Equation (6.2) can be modified to:

$$\Delta v = \frac{c}{2nL} \tag{6.3}$$

where n is the refractive index of the gain medium. As the number of superimposed longitudinal modes increases, the pulses become shorter. The pulse duration and spectral width of the laser are related by the time-energy uncertainty principle as:

$$\Delta t . \Delta E \geq \frac{\hbar}{2} \tag{6.4}$$

Or,

$$\Delta t . \Delta \omega \geq \frac{1}{2} \tag{6.5}$$

According to this equation, the generation of ultrashort pulses dictates broad spectral bandwidth for the laser. For example, a NIR pulse with 100 fs pulse duration utilises ~10 nm bandwidth. Equation 6.5 corresponds to the product of the pulse duration and the spectral bandwidth and is known as the time-bandwidth product (TBP) of the pulse. Since experimental quantities are measured based on the full-width at half-maximum (FWHM) values, the relation between the pulse duration and spectral bandwidth is modified to,

$$\Delta t . \Delta v \geq K \tag{6.6}$$

where Δt is the FWHM pulse duration, $\Delta \nu$ is the FWHM frequency bandwidth and K is the TBP value, dependent on the shape of the pulse. Table 6.1 lists the TBP values corresponding to different pulse shapes, including Gaussian and hyperbolic secant (sech^2). When the equality in Equation 6.5 is reached, the pulses are called transform-limited, and their instantaneous frequency is time-independent. The pulses then have the lowest duration for a particular spectral bandwidth. Conversely, for a given pulse duration, transform-limited pulses are those with the minimum possible spectral width. A pulse which is longer than its transform-limited duration is termed chirped. A chirped pulse is characterised by a variation in the instantaneous frequency that occurs as a result of dispersion.

Table 6. 1. The different values of TBP or K, depending on the pulse shape.

Pulse Shape	K
Gaussian function	0.441
Exponential function	0.140
Hyperbolic secant	0.315
Lorentian function	0.142

The design for a linear cavity laser generating ultrashort pulses consists of the gain medium, cavity mirrors and most importantly, a SA, as shown in Figure 6.1. The role of an SA for short pulse generation was previously discussed in Chapters 3 and 5. Following pulse formation in the standing wave cavity by locking of the modes in phase, the pulse is extracted from the cavity at the output coupler, a partial mirror that allows a small percentage of the beam to pass through, to form the output of the laser. The laser output is then quantified based on the following parameters.
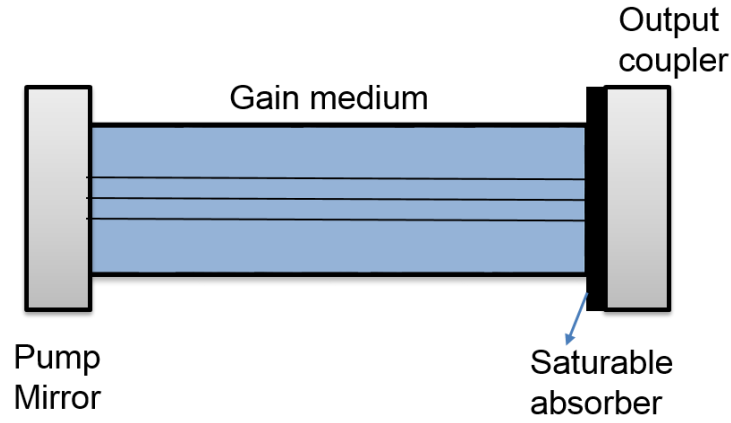
Figure 6. 1. Schematic of a linear cavity laser. The gain medium consists of a waveguide inscribed in an active glass. Ultrafast laser operation is achieved by fast saturable absorption provided by the SA.

(1) Pulse duration: The most characteristic property of an ultrashort pulse is its duration. For ultrashort pulses with durations of the order of ps-fs, an autocorrelation measurement is performed, where the ultrashort pulse itself is used as a reference to measure its duration. In an autocorrelator, the laser pulse is split into two using a beam splitter and, the two beams have a varying delay with respect to each other. The two pulses are then recombined within a nonlinear material. Based on the mode of interaction of light within the nonlinear material, the measurement is classified as intensity autocorrelation or interferometric autocorrelation.

In an intensity autocorrelation, the two laser beams with a delay between them are overlapped in a second harmonic crystal. A resultant signal is generated at twice the frequency of the incident beam, and available for an intensity measurement at the detector. The schematic of the experimental setup for an intensity autocorrelation is shown in Figure 6.2. The autocorrelation measurement is obtained as a plot of signal intensity versus the pulse delay. The laser pulse duration $\Delta\tau_p$ is determined from the FWHM value, $\Delta\tau_{ac}$, of the pulse intensity. The actual pulse duration $\Delta\tau_p$ is inferred based on the shape of the pulse. For Gaussian pulses, $\Delta\tau_p = \frac{\Delta\tau_{ac}}{1.414}$, and for sech^2 pulses, $\Delta\tau_p = \frac{\Delta\tau_{ac}}{1.543}$.
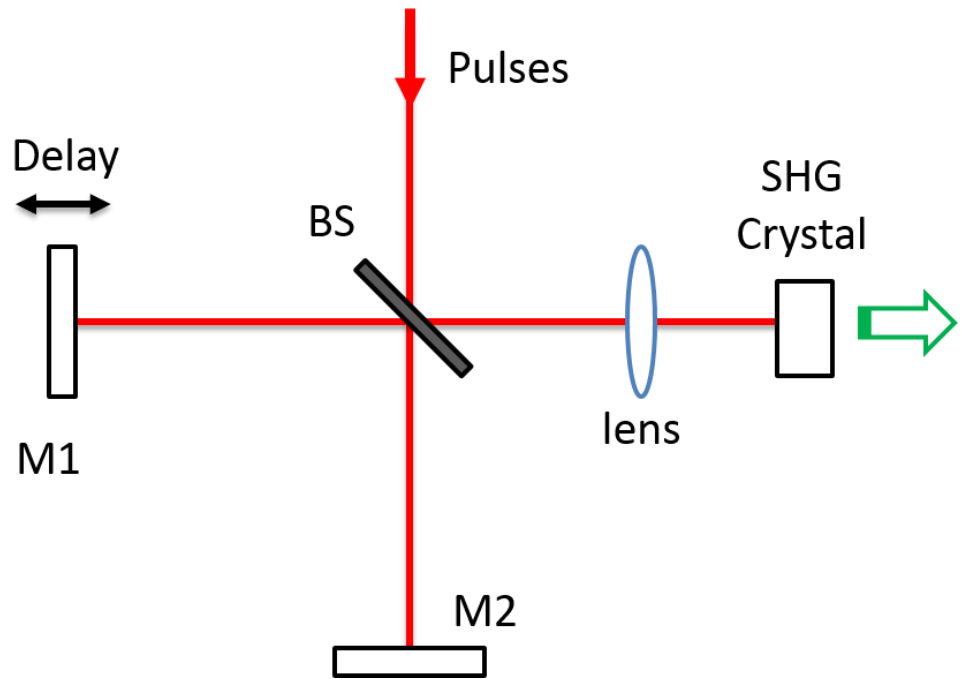
Figure 6. 2. Experimental setup for an intensity autocorrelator using an SHG crystal. The SHG pulse is measured with respect to the delay to yield an autocorrelation trace.

In the case of interferometric autocorrelation measurements, the two laser beams are overlapped in the detector to measure the two-photon absorption (TPA) signal. The input laser is initially split into two paths using a beam splitter. One of the beams is reflected by a mirror placed on a translation stage, whereas the other beam is reflected by a high reflector that is positioned on a speaker. The speaker system allows the mirror to oscillate at the required frequency such that the two pulses scan across each other as they overlap at the detector. The detector, which gives a nonlinear response to the incoming beam, measures the TPA signal as a function of the interferometric optical delay between the interacting pulses to give an interferometric autocorrelation.

(2) Optical Spectrum: The optical spectrum of an ultrafast laser provides information about the wavelength of operation as well as the spectral bandwidth. With the FWHM bandwidth and the pulse duration, the TBP of the laser pulse can be determined, as mentioned previously.

(3) Laser power: The average power output of the laser can be measured with respect to the input pump power, using appropriate detectors. The slope efficiency of the laser can be determined from this characteristic curve. The pulse energy of the laser is also inferred from the average power measurements.

(4) Radio frequency (RF) spectrum: The laser output detected by a photodiode and fed to a RF spectrum analyser provides direct information about the repetition rate of the laser, since the spectral region of radio waves spans the frequencies typical of laser pulses. In addition to the fundamental frequency, the RF spectrum also provides information about the harmonics, and most importantly, the mode-locking stability of the pulsed laser.

The following sections detail the passive mode-locking experiments for the Yb-BG linear cavity laser using a number of SAs.

6.3   Semiconductor Saturable Absorber based Laser Cavity

6.3.1 Semiconductor Saturable Absorber Mirror (SESAM)

SESAMs constitute the predominant SA used for passive mode-locking of lasers. Considering the widespread use of SESAMs for laser mode-locking, even including commercial systems, these devices serve as the first choice for mode-locking the Yb-BG laser. The linear cavity design used previously for the CW operation was maintained for the mode-locking studies, thus preserving the compactness of the cavity. The schematic of the waveguide laser is shown in Figure 6.3. A 976 nm fibre pigtailed laser diode was used as the pump source. A fibre optic isolator was spliced onto the end of this to avoid any back reflections to the pump. The output from the isolator was collimated and then focused on to the waveguide using two identical ×30 aspheric lenses L_1 and L_2. A half-wave plate was used to adjust the pump polarisation.

A linear integrated cavity was used, with the pump mirror and the output coupler attached to the waveguide facets using an index matching gel. The SESAM forms the back end of the laser cavity. The ~100% reflectivity of the SESAM implies that the useful laser output has to be extracted from the pump side. Thus, a dichroic mirror OC with an output coupling of 4% at 1 μm and high transmission ~80% at the pump wavelength was butt-coupled to the input waveguide facet as shown in Figure 6.3. The laser radiation from the cavity was collected at this side of the cavity. This is in distinct contrast from the laser cavity described in Chapter 4, for which the output coupler forms the rear end of the cavity. A second dichroic mirror DM was used to separate the pump and laser emission. The maximum launched pump power was measured to be 388 mW at the position immediately following the half-wave plate in the cavity.
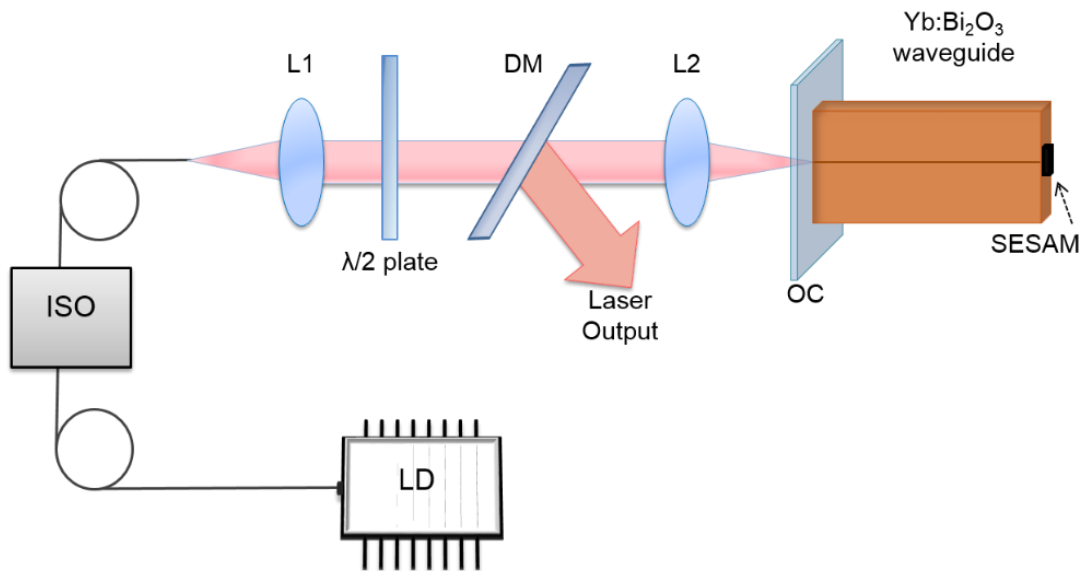
Figure 6. 3. The schematic of the laser setup incorporating a SESAM for passive mode-locking. The laser radiation is monitored at the input side of the cavity.

Initially, the CW performance of the laser was characterised using a high-reflectivity (HR) mirror instead of the SESAM. Lasing was obtained at a wavelength of 1060.6 nm at threshold pump power of 100 mW; see Figure 6.4(a). The evolution of the average laser output as a function of incident pump power is given in Figure 6.4 (b). An output power of 44 mW was obtained for the maximum pump power, resulting in a slope efficiency of 16%.
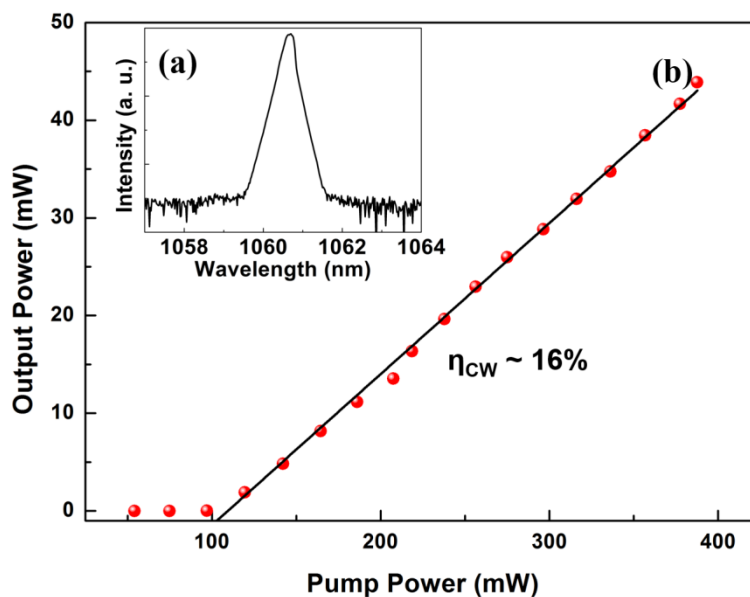
Figure 6. 4. (a) Optical spectrum of CW laser operation in Yb-BG waveguide laser. (b) Plot of average laser output power versus incident pump power for the CW operation. The laser has a slope efficiency of ~16%.

To analyse the pulsed laser characteristics of the cavity, the HR mirror was replaced with a commercial SESAM from Batop GmbH. The SESAM was selected based on the fast recovery of the SA. Designed for 1040 nm, the SESAM has a relaxation time of 500 fs, modulation depth of 2.6% and saturation fluence of 50 µJ cm^{-2}. Self-starting QML operation was observed from the cavity at a pump power of 75 mW. The QML pulse was analysed using a fast photodiode (Thorlabs SIR5-FC) and measured using an Agilent Infiniium DCA 86100A Wide-Bandwidth Oscilloscope combination. The mode-locked pulses observed beneath the Q-switch envelope measured a pulse repetition frequency of 1.51 GHz. This is in agreement with the cavity length, evaluated using Equation 6.3. The fast oscilloscope trace indicating the high repetition rate is shown in Figure 6.5. The Q-switched envelope has a lower repetition rate of the order of 100 kHz. With an increase in pump power, the repetition rate of the Q-switched pulses was found to increase, with a 450 KHz pulse repetition rate measured at the maximum pump.
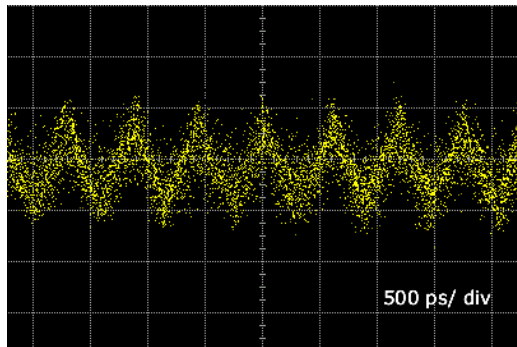
Figure 6. 5. Mode-locked pulse train

The laser was found to operate at a different centre wavelength of 1033.7 nm compared to the CW operation. This transition to a lower laser wavelength can be explained by the SESAM design, whose operating wavelength is at 1040 nm.; . The optical spectrum for the QML operation is given in Figure 6.6 (a). A plot of the output power from the pulsed laser as a function of the pump power is given in Figure 6.6 (b). The laser has a slope efficiency of 16%, comparable to its CW performance, and an optical conversion efficiency of 13%. These results were presented at the CLEO-PR 2013 conference [152].

In comparison to the CW waveguide laser demonstrated in Chapter 4 with a slope efficiency ~79%, the above laser has a low efficiency ~ 16%. This can be attributed to the difference in output coupling in the two cavity configurations. In the high efficiency Yb-BG laser, the pump was launched at one end of the waveguide and collected at the other end. The use of such independent ports for pump launch and laser output eliminates any loss in the pump by using suitable pump mirrors as well as allowing the optimisation of the cavity using a range of output couplers. In the reflective-cavity using SESAMs, both the pump launch and laser output are at the input waveguide facet. The incorporation of the characteristic features of both the pump mirror and output coupler in a single optic presents an expensive and complicated arrangement, and limits the final efficiency of the laser. A linear cavity laser similar to that in Chapter 4 for pulsed operation, is investigated in the following sections.
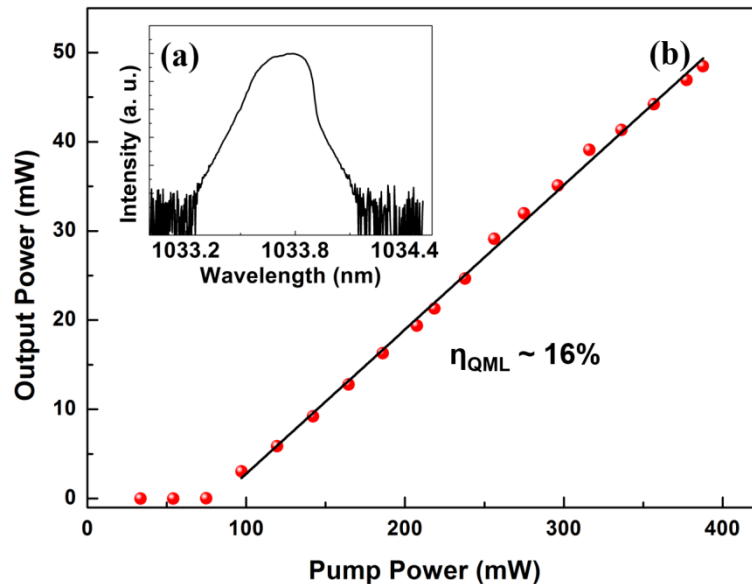
Figure 6. 6. (a) The optical spectra for the pulsed operation in the Yb-BG waveguide laser incorporating a SESAM. (b) The evolution of the output power with the launch pump. The laser has a slope efficiency of 16%.

6.3.2 Semiconductor Saturable Output Coupler (SESOC)

A SESOC combines the principles of the well-known SESAM and an output coupler. The difference between a SESAM and a SESOC is the partial reflectivity in the latter. The use of a SESOC in a Fabry-Perot laser cavity allows the extraction of useful laser output at the far end of the cavity, instead of at the pump input side of the waveguide. The subsequent laser cavity is depicted in Figure 6.7.
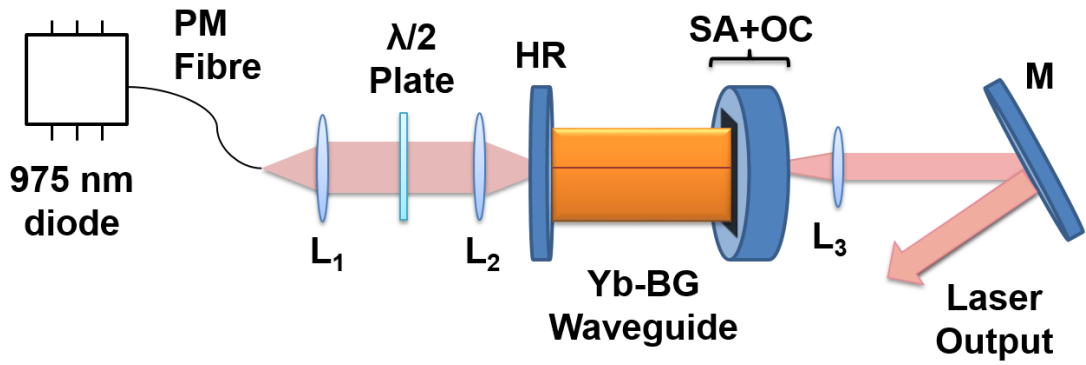
Figure 6. 7. Schematic of the laser cavity. The laser output is extracted from the far end of the cavity.

Commercially available SESOCs from BATOP GmbH were used for the experiments. The maximum available output coupling was limited to ~3%. This value is well away from the optimal output coupling value of 30% of the Yb-BG laser as previously determined in Chapter 4. These devices were however used as an initial SA device for the pulsed operation. Table 6.2 lists the parameters of the SESOCs used.

Table 6. 2. The specifications of the commercial SESOCs used for the pulsed laser operation. Obtained from Batop GmbH.

	SOC 1040	**SOC 1064**
Laser Wavelength (nm)	1040	1064
Transmittance (%)	3	3.2
Modulation Depth (%)	6	1.7
Non Saturable Loss (%)	5	1
Saturation Fluence (μJ cm^{-2})	80	90
Relaxation Time Constant (ps)	1	<3
Absorbance (%)	11	2.7

Two SESOCs were used, namely, SOC 1040 and SOC 1064, distinguished based on their wavelength of operation. Figure 6.8 shows a photograph of the laser cavity using the SESOC. Initially, SOC 1040, with an absorbance of 11%, and 6% modulation depth

was used. The evolution of the output spectra of the waveguide laser with an increase in pump power for the SOC 1040 is shown in Figure 6.9. The abrupt change from narrow linewidth CW operation to broadband operation is noticeable and is indicative of pulsed operation. This transition occurs for a pump power of ~ 50 mW. The working of the laser was hampered by thermal drifts as a result of the high absorbance value ~ 11% of the SOC 1040. This is indicated by the different slopes for the evolution of average output power versus input pump power, shown in Figure 6.10. The laser has a slope efficiency of 2%, a maximum average power of 9 mW for an input pump of 530 mW.
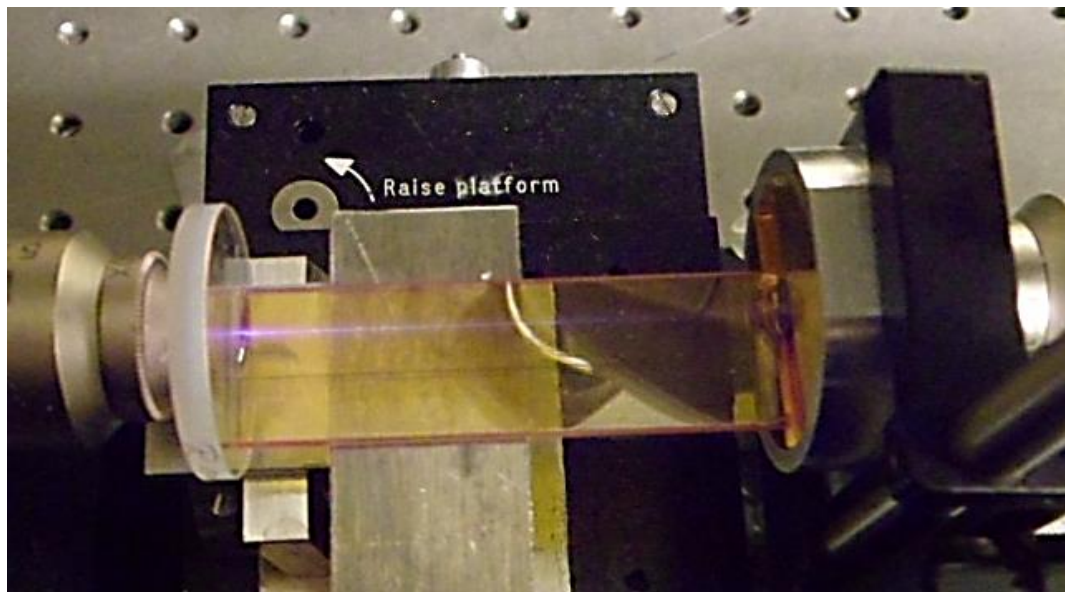
Figure 6. 8. The linear cavity waveguide laser using a SESOC.

Using SOC 1064 nm, which has a comparatively lower absorbance ~2.7%, an improved laser performance was achieved. Self-starting QML was observed at the threshold pump of 53 mW. Figure 6.11 gives the pulse characteristics, namely, the QML pulse train, the Q-switched envelope, and the mode-locked pulse train. The mode-locked pulses are separated in time by ~660 ps, corresponding to 1.5 GHz repetition rate. The laser produces an average power of ~26 mW for 530 mW pump power, resulting in an optical conversion efficiency of 5%. The laser has a slope efficiency of ~6%, as shown in Figure 6.12.
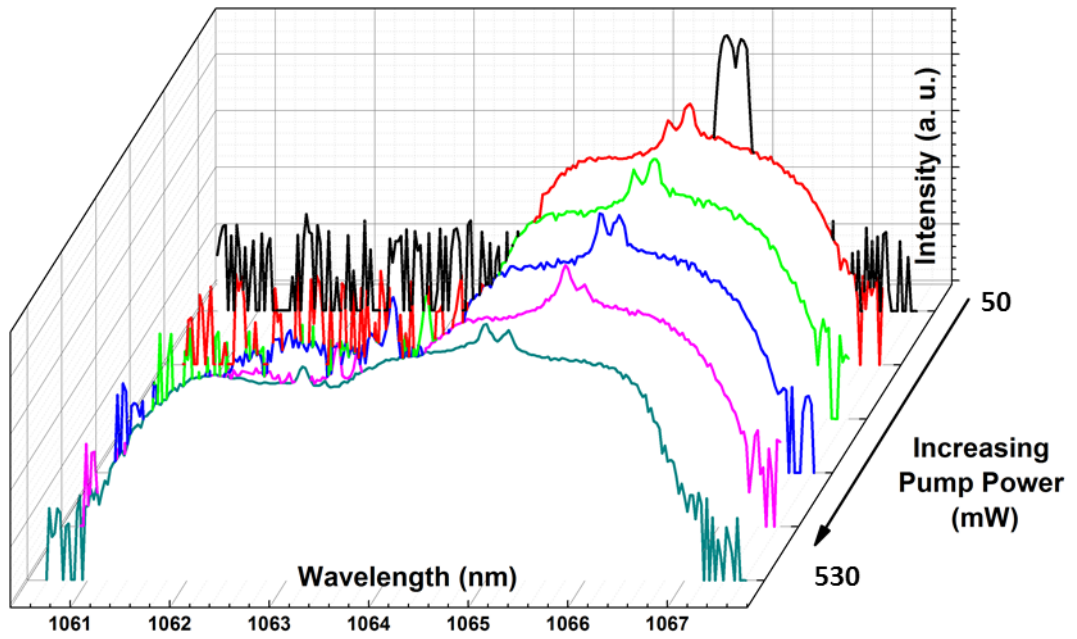
Figure 6. 9. The evolution of the optical spectra with respect to the pump power. The pump power for the transition corresponds to ~50 mW.
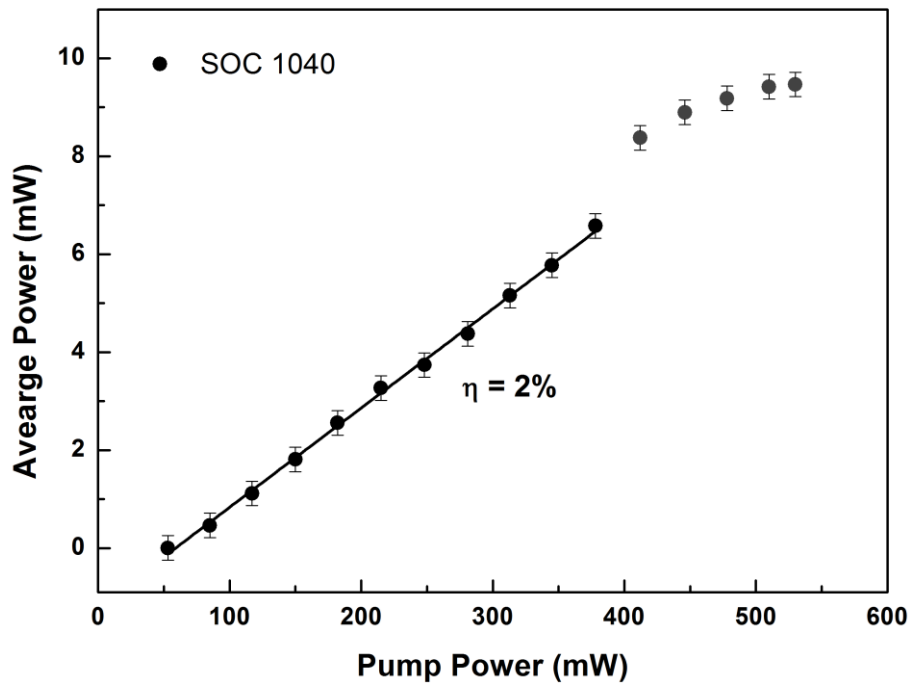
Figure 6. 10. Evolution of the average output power versus input pump for SOC 1040. The laser produces an average output power of 9 mW.
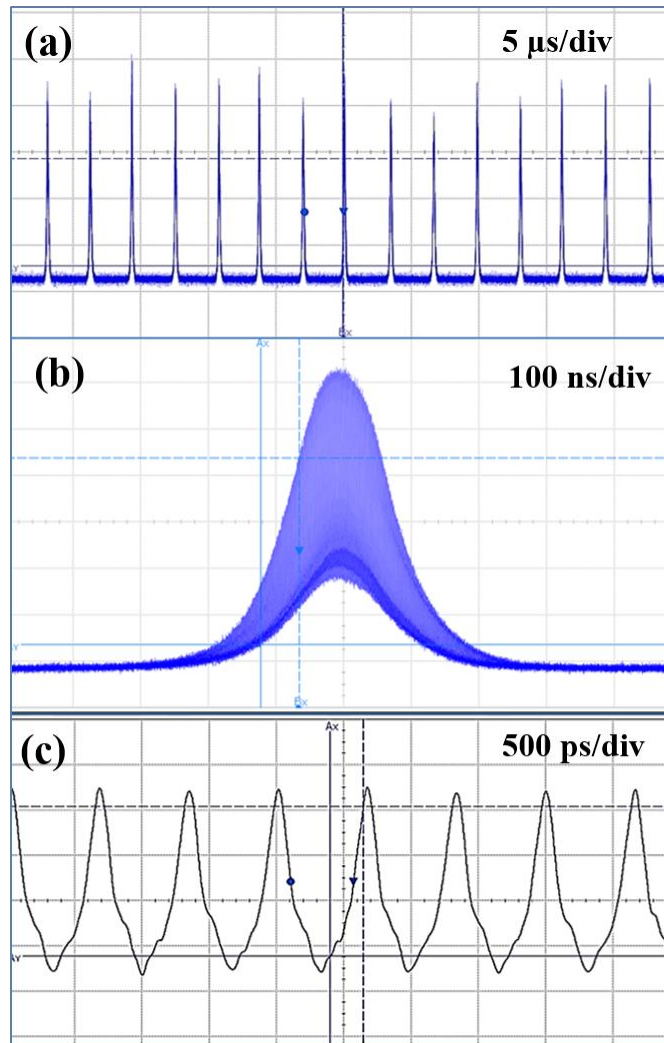
Figure 6. 11. The QML laser characteristics observed for a pump power of 150 mW using SOC 1064. (a) QML pulses which have a repetition rate of ~0.3 MHz, (b) Q-switched envelope (c) Mode-locked pulse train.
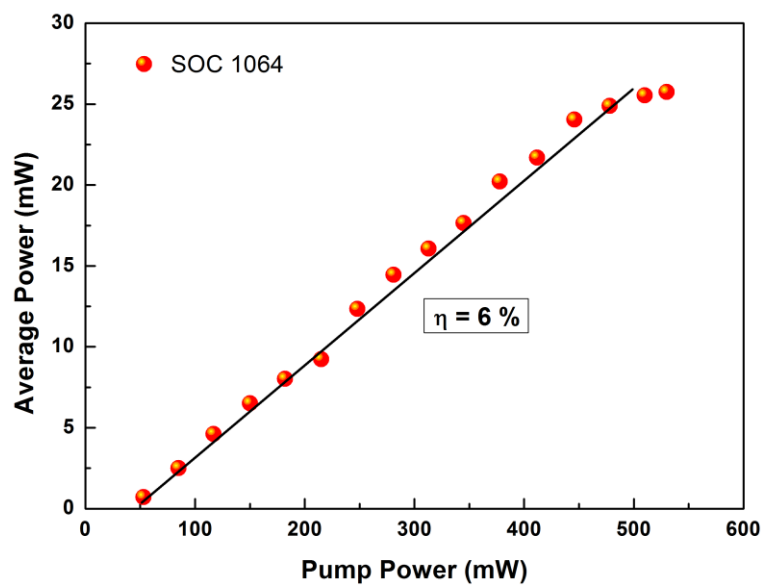
Figure 6. 12. Output power versus pump power characteristics for SOC 1064. The laser generated 26 mW average output power. The laser has a slope efficiency of 6%.

126

6.4   CNT Saturable Absorber based Laser Cavity

Passive mode-locking was further investigated using the relatively novel SAs based on carbon nanostructures, namely, CNT and graphene. One of the advantages of these SAs is their easy integration within a cavity. Different approaches have been used to incorporate CNT and graphene SAs within solid-state lasers, including free-standing SA-polymer composite and a SA coating on a suitable optical component. For our investigation using CNT-SA, the latter was chosen. CNT film was coated on a 40% output coupler. The 40% transmission for the output coupler was chosen since the value is close to the optimal coupling of ~30%, as established in Chapter 4. The laser cavity scheme is identical to that in Figure 6.7.

The cavity was optimised by adjusting the pump coupling efficiency, pump beam polarisation, and by changing the position of the CNT-SA. The beam spot size on the SA corresponded to the mode size of the waveguide, ~8.8 µm. Self-starting QML was initiated at an input pump power of ~130 mW. The Q-switched pulse train recorded at an input pump power of 150 mW is plotted in Figure 6.13 (a). Figure 6.13(b) and (c) shows the Q-switch envelope and the mode-locked pulses observed beneath the Q-switch envelope, respectively. The mode-locked pulses have a spacing of ~660 ps, corresponding to a repetition frequency of 1.51 GHz, in agreement with the cavity length. The laser repetition rate was also measured using a Rigol DSA 1030 RF spectrum analyser. Figure 6.14(a) shows the RF spectrum with a fundamental repetition rate of 1.51 GHz. The magnitude spectrum showing the fundamental repetition rate and the harmonics of the pulsed laser, measured using a wide-bandwidth oscilloscope is shown in Figure 6.14(b).
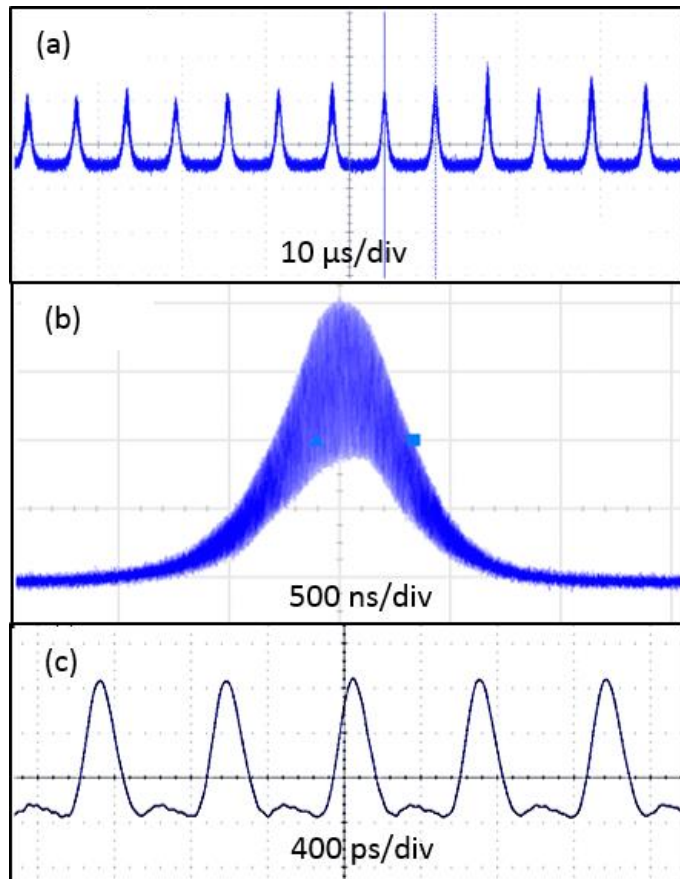
Figure 6. 13. The QML laser characteristics observed for a pump power of 150 mW using CNT-SA in the cavity. (a) QML pulses which have a repetition rate of ~0.3 MHz, (b) Q-switched envelope (c) Mode-locked pulse train.
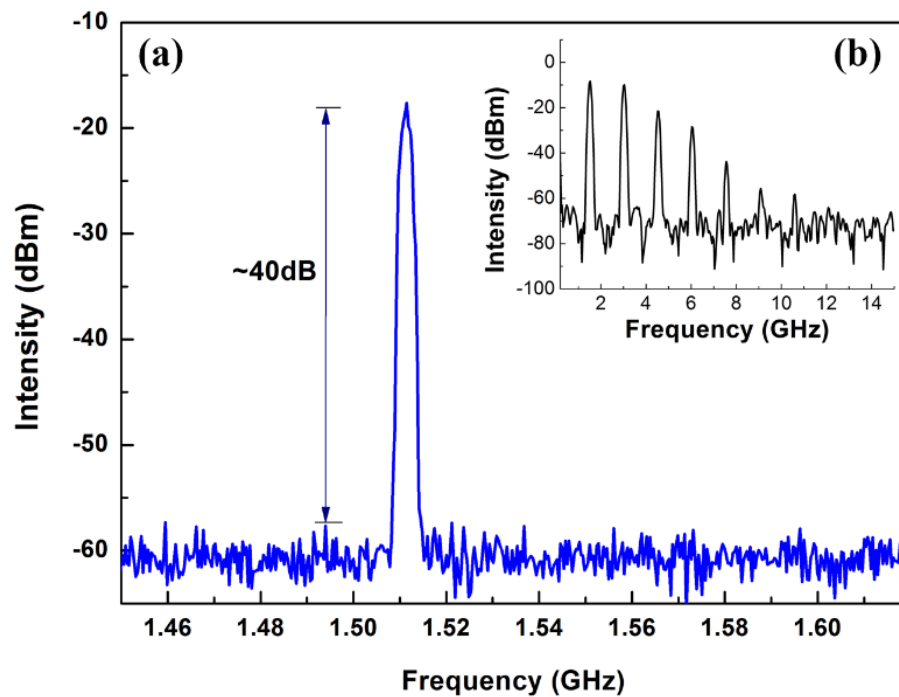
Figure 6. 14. (a) RF spectrum of the Yb-BG laser showing a fundamental repetition rate of 1.51GHz. (b) The fundamental repetition rate and the higher order harmonics of the laser pulse.

With an increase in pump power, the repetition rate of the Q-switched pulses was found to increase. This is indicative of potential transition from QML to CW mode-locking. At a pump power of 320 mW, the Q-switched pulses were found to coalesce, as shown in Figure 6.15(a), while maintaining the mode-locked pulses observed at a time scale of 1 ns/div; see Figure 6.15(b). The overlapping sinusoidal characteristics observed within the waveform shown in Figure 6.15 (a) suggest a regime of CW-mode-locking, although it is unstable.
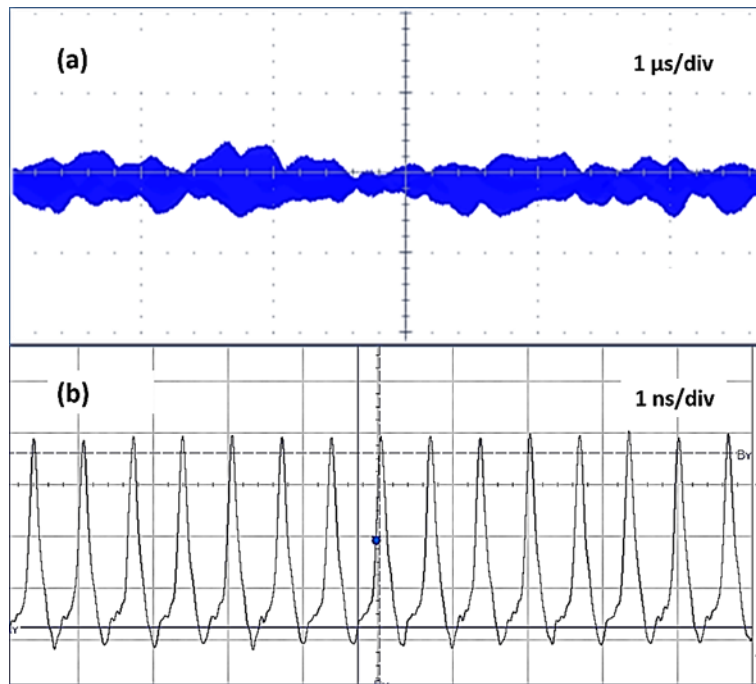
Figure 6. 15. (a) The coalesced QML pulses, indicative of CW-mode-locking. The presence of sinusoidal variations within these pulses indicate the instability in the laser.(b) The mode-locked pulse train.

The optical spectra for this CW-mode-locking regime shown in Figure 6.16 (a)-(b) show the existence of 2 peaks at the wavelengths of ~1033.1 nm and ~1037.5 nm. This could be explained by the multi-modal nature of the waveguide in conjunction with the broad emission cross-section of the gain medium with the different modes being supported by the cavity simultaneously at differing emission wavelengths.
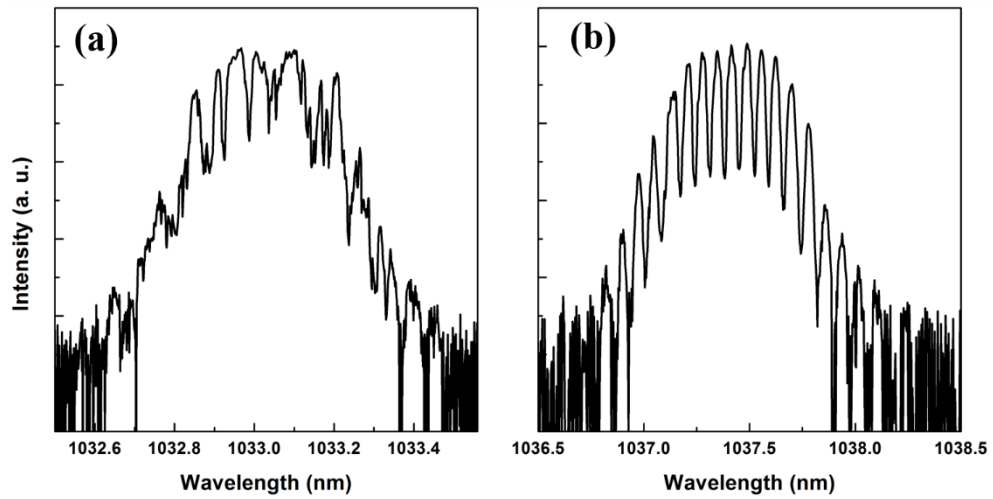
Figure 6. 16. The optical spectra for Yb-BG mode-locked with CNT-SA.

The evolution of the average power output from the Fabry-Perot cavity waveguide laser with respect to pump power is given in Fig. 6.17. A maximum output power of 112 mW is obtained for a launched pump power of 530 mW, resulting in an optical conversion efficiency of 21%. The laser has a slope efficiency of 27%.
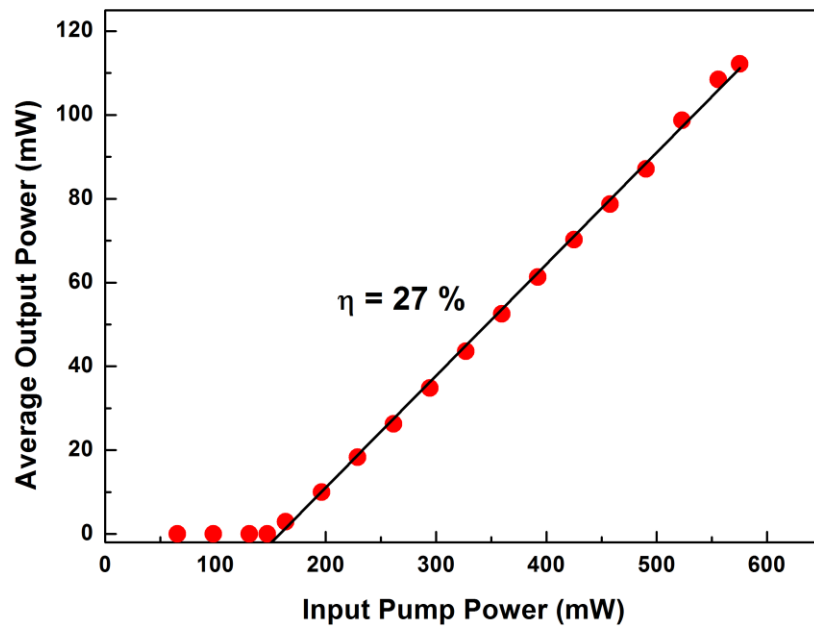
Figure 6. 17. Laser output characteristics for the CNT-SA.

The intensity autocorrelation obtained for the waveguide laser is given in Figure 6.18, fitted to a $sech^2$ function. The pulse duration was inferred to be ~714 fs, confirming the generation of 'ultrashort' pulses from the laser cavity. These results were presented at the '2012 International Conference on Fibre Optics and Photonics' [153].
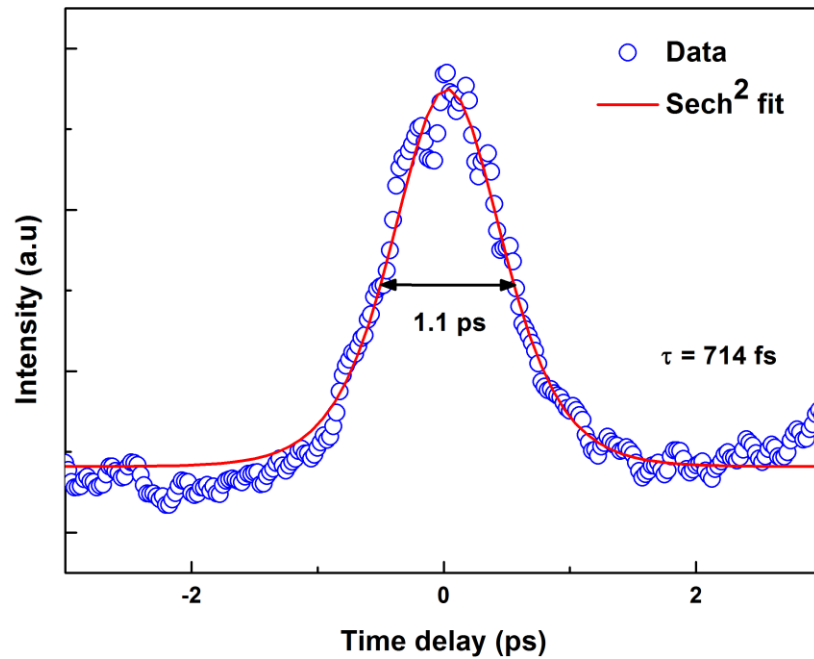
Figure 6. 18. The intensity autocorrelation trace for the Yb-BG laser passively mode-locked with CNT-SA. The FWHM pulse width is 1.1 ps. Deconvolution with a sech^2 fit yields a laser pulse width of 714 fs.

6.5 Graphene Saturable Absorber based Laser Cavity

In the Yb-BG cavity, graphene SA was introduced by two different approaches: as a free standing graphene-polymer composite, and graphene film on a 40% output coupler. The former was used following its prevalence for fibre laser mode-locking. The SA samples were obtained as part of a collaboration with the Cambridge Graphene Centre, University of Cambridge.

Graphene–Polymer Composite: For the integrated cavity, a graphene-polyvinyl alcohol (PVA) flake was incorporated between the waveguide end facet and a 10% output coupler mirror using index matching gel, as shown in Figure 6.19.
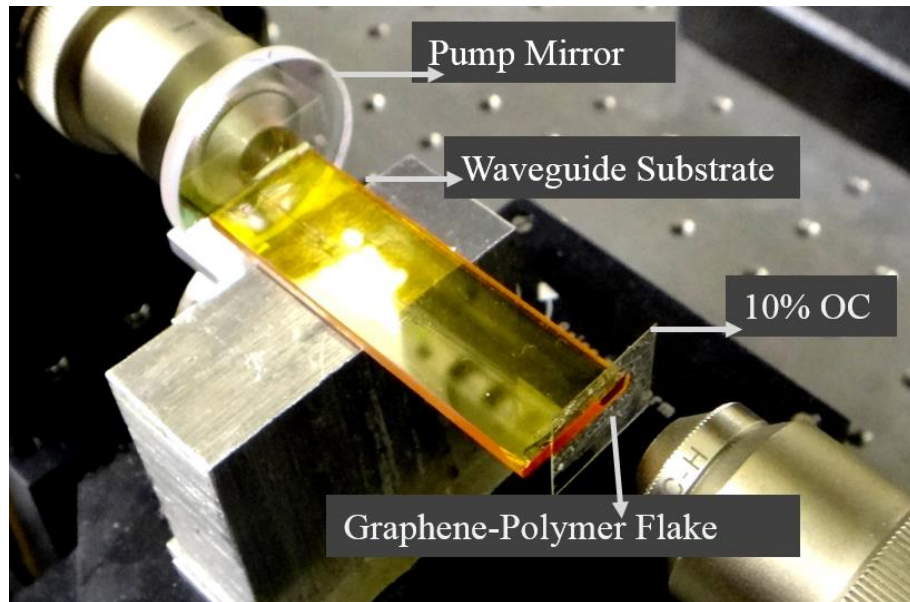
Figure 6. 19. Integrated Yb-BG laser cavity, mode-locked using a free standing graphene-polymer flake. The flake can be identified as the black film against the waveguide output facet.

A similar self-starting QML operation was observed from the waveguide laser at a pump threshold of 100 mW. With an increase in pump power, the QML pulses were found to coalesce indicating a near CW mode-locking. The sinusoidal fluctuations at this operational regime however indicate an unstable regime at the threshold of CW modelocking. An average output of 42 mW was obtained for 530 mW input pump resulting in a slope efficiency of 11%; see Figure 6.20.
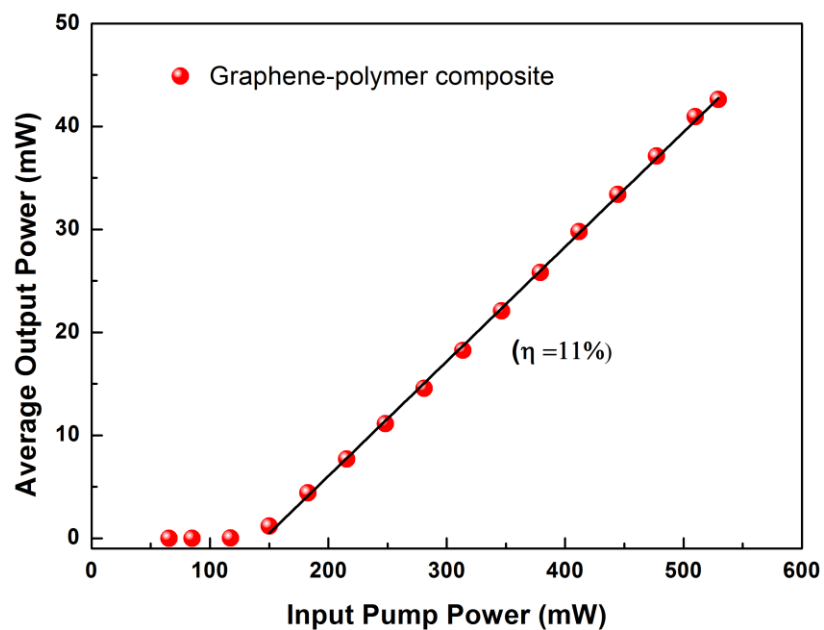
Figure 6. 20. Laser output characteristics using a graphene-PVA SA flake.

Since the graphene-PVA film has a random distribution of graphene flakes across the sample, obtaining QML operation from the cavity was challenging. When changing the position of the film, the polymer was found to get damaged, inducing damage to the waveguide facet as well. The microscope image of the damaged graphene-PVA film is given in Figure 6.21. The red circles indicate the film damage induced at the waveguide facet.
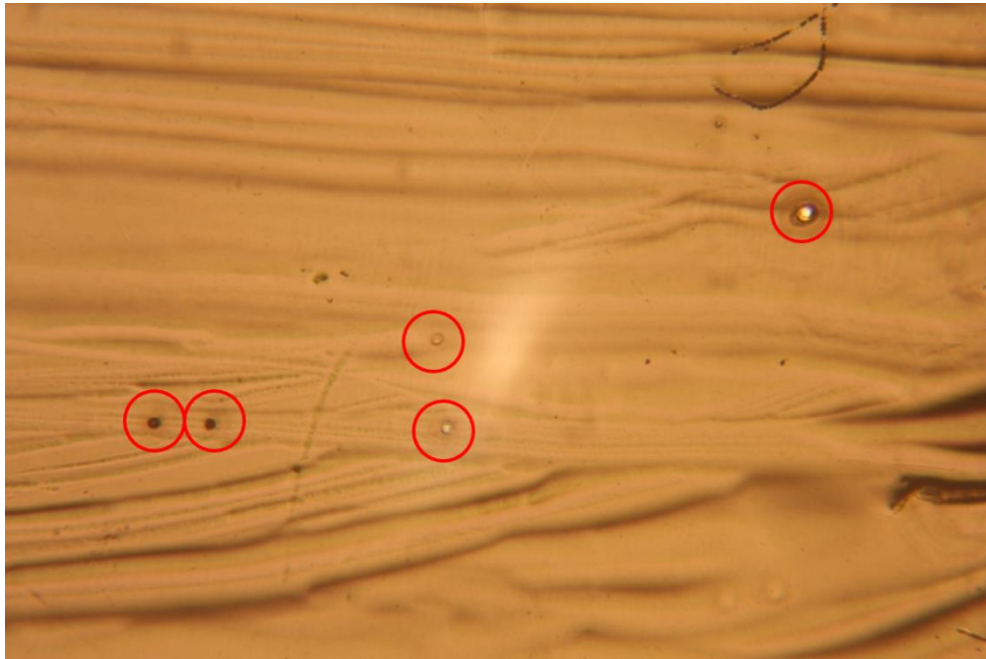
Figure 6. 21. Graphene-polymer composite used for passive mode-locking of the Yb-BG waveguide laser. The low damage threshold of the polymer film induced damage in the film, as shown by the red circles. The dimension of the circular damage region corresponds approximately to the waveguide dimension.

Graphene Film on a 40% Output Coupler: An output coupler mirror coated with graphene was also investigated for laser experiments. Laser operation was observed to initiate at a threshold pump power of 100 mW in a self-starting QML regime. At the threshold of operation, the Q-switched pulses were measured to have a repetition rate of 200 kHz, detected using a fast photodiode (Thorlabs SIR5-FC) and measured using an Agilent Infiniium DCA 86100A Wide-Bandwidth Oscilloscope. Mode-locked pulses at a fundamental repetition rate of 1.51 GHz corresponding to the free spectral range of the cavity were measured within the Q-switched envelope.

Figure 6.22 shows the evolution of QML pulse repetition rate with respect to the launched input power. As the launch pump power was increased, the time period between the Q-switched pulses was found to reduce indicating potential CW mode-

locking. At the highest pump power, the Q-switched pulses had a repetition rate of 0.95 MHz. The constant mode-locked pulse train behaviour measured at a time scale of 500 ps/div is given in Figure 6.23.
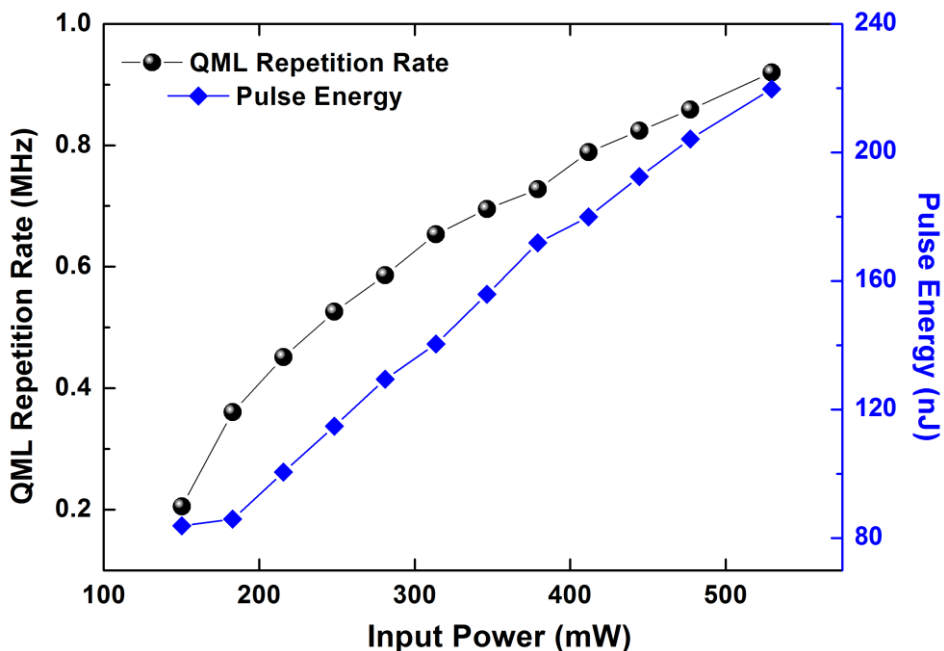
Figure 6. 22. Repetition rate and energy within the Q-switched envelope, as a function of input pump power.
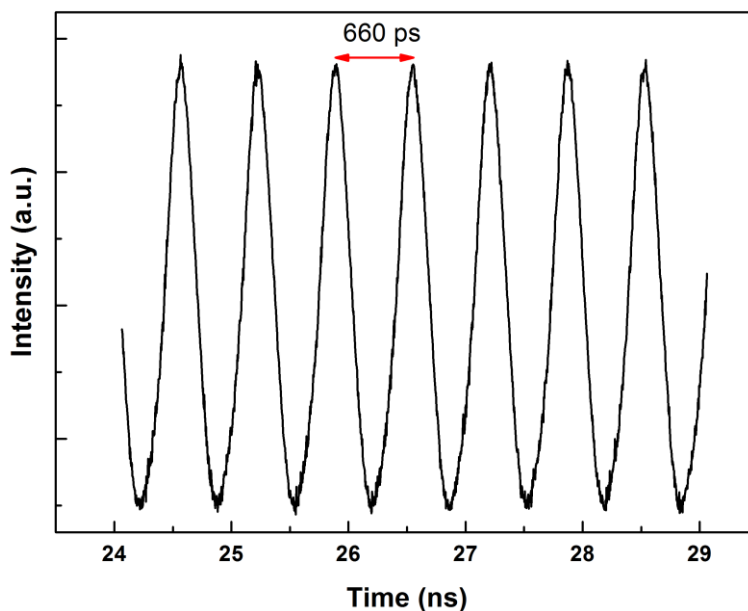
Figure 6. 23. Mode-locked pulse train

Mode-locking at the fundamental repetition rate is also verified by measuring the RF spectrum using a Rigol DSA 1030 spectrum analyser, as shown in Figure 6.24(a). The relatively broad RF spectrum shown in Figure 6.24 (b) indicates the absence of proper cw modelocking.
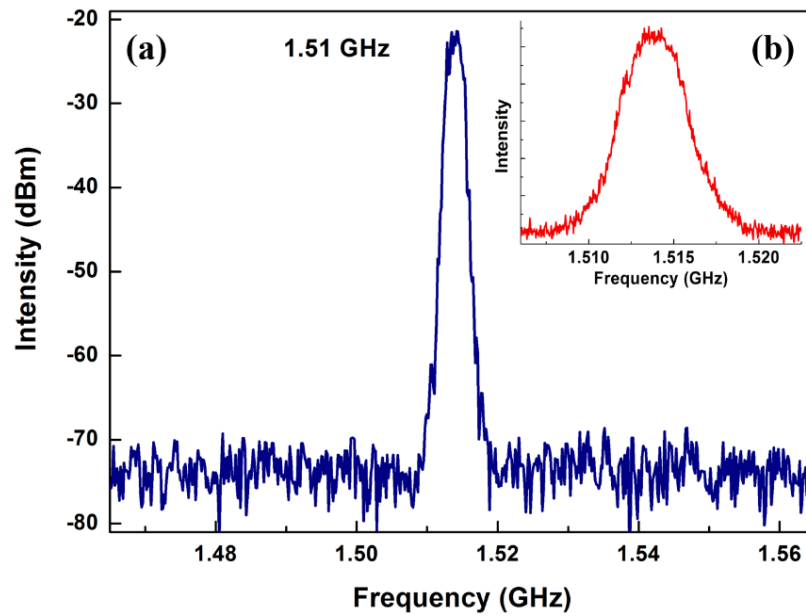
Figure 6. 24. (a) RF Spectrum measured at the maximum pump power (b) Magnified central region of the spectrum.

For the maximum input pump power of 530 mW, an average output power of 202 mW was measured using a Coherent FM/GS thermal power meter. The dependence of the output power on the pump for the graphene deposited output coupler based cavity is given in Figure 6.25. The QML waveguide laser has a high slope efficiency of 48%, and an optical-to-optical efficiency of 38%.
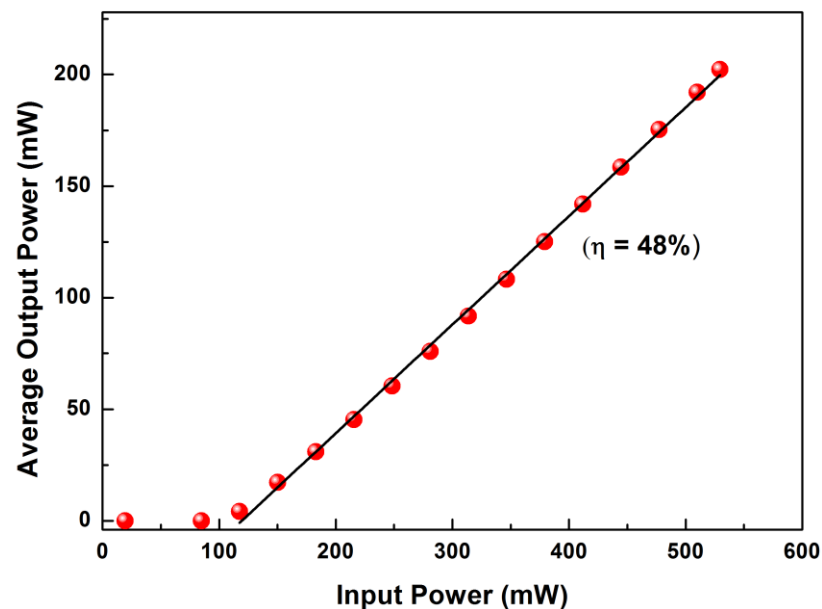
Figure 6. 25. Output power with launched pump power. The laser has a slope efficiency of ~48% and a maximum output power of 202 mW.

The optical spectrum was measured using an Advantest Q8384 Optical Spectrum Analyser set to 0.5 nm resolution. Figure 6.26 shows the spectrum obtained for the highest pump power. The spectral bandwidth, corresponding to a pump power of 530 mW, is 1.1 nm. The intensity autocorrelation trace of the output pulse is plotted in Figure 6.27. The temporal profile of the pulse is represented by a sech^2 fit, giving a 1.06 ps pulse duration after deconvolution. For the 1039 nm output wavelength, the calculated time-bandwidth product is ~0.324, indicating the pulses to be near-transform-limited. These results were published in Optics Express in 2013 [131].
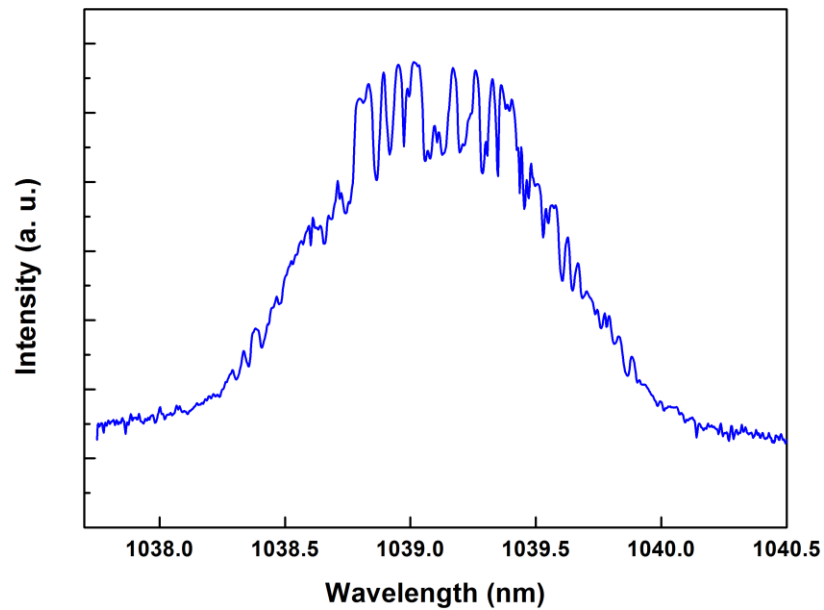
Figure 6. 26. Optical spectra of the laser
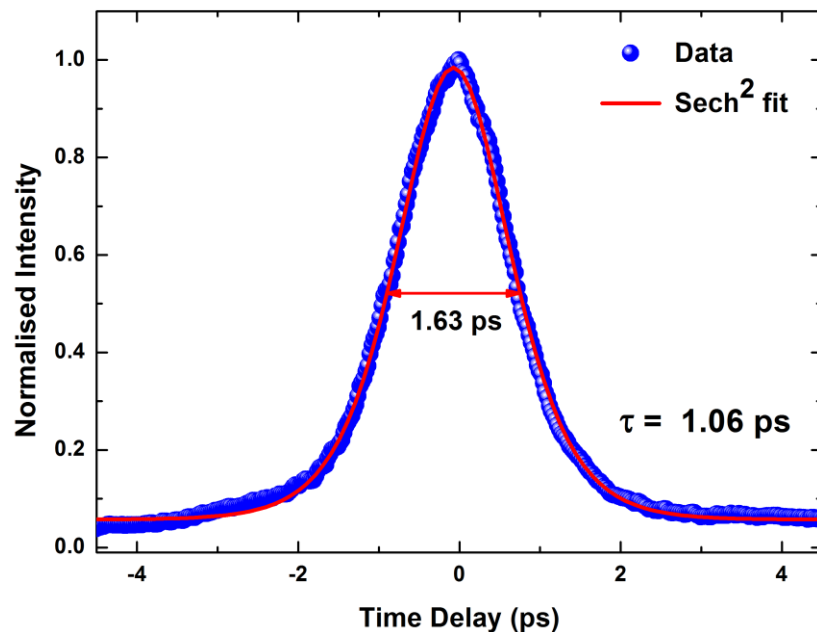
Figure 6. 27. Intensity autocorrelation trace

6.6   Power Scalability

With a view to scaling the achievable power from the system and investigating the possibility of attaining CW mode-locking, the pump power was scaled using two 976 nm fibre-coupled diode lasers. A total pump power of ~1 W was achieved by polarisation combining the two outputs into a single fibre. Self-starting QML operation was obtained at a pump threshold of 100 mW. A maximum output of 485 mW was achieved resulting in an optical conversion efficiency of 43%. The laser has a slope efficiency of 49%, as indicated in Figure 6.28.
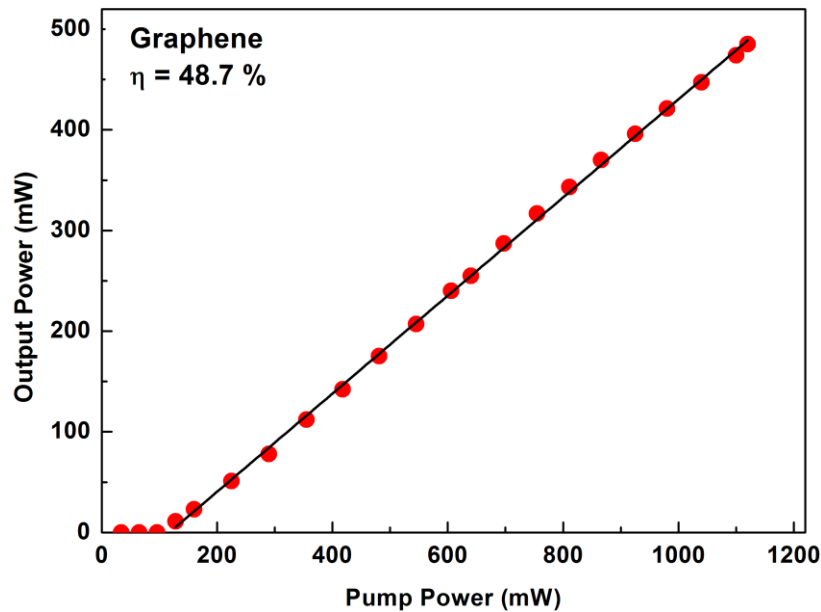
Figure 6. 28. Evolution of average output power with respect to pump power in the waveguide laser incorporating graphene SA. The available pump power is ~1W, resulting in a laser output power of 485 mW and slope efficiency of 49%.

For the complete characterisation of the high efficiency pulsed waveguide laser, an optical saturation experiment for the graphene SA film was performed at 1064 nm. The graphene SA was measured to have a saturation fluence of 10.2 µJ cm^{-2}, and modulation depth of 17.6%. The details of the corresponding experiment are given in Chapter 5. These values were used to analyse the possibility of obtaining mode-locked pulses with high amplitude stability from the integrated cavity. The criterion for stable continuous-wave mode-locking, discussed previously in Chapter 3, is given as :

$$E_p^2 > E_{L,sat}E_{A,sat}\Delta R \qquad\qquad (6.7)$$

where E_p is the intracavity pulse energy and $E_{L,sat}, E_{A,sat}$ are the saturation energies of the gain medium and the SA respectively, and ΔR is the modulation depth of the SA. The term on the right is called the QML parameter. For the Yb-BG glass waveguide laser at its peak performance, producing 485 mW, the square of the pulse energy in the cavity was found to be ~ 2.23×10^{-18} J^2; less than the QML parameter ~ 15.2×10^{-18}. Therefore, achievement of stable CW mode-locking using the waveguide requires further engineering of the SA, or a modification in the laser cavity design.

6.7 Discussion

The Yb-BG waveguide laser performance on the basis of the different types of SAs is tabulated in Table 6.3.

Table 6. 3. Yb-BG waveguide laser performance for various SAs.

SA	SOC 1040	SOC 1064	CNT on 40% OC	Graphene-PVA with 10% OC	Graphene on 40% OC	
Maximum available pump power (mW)	530	530	530	530	530	1120
Pump Power for QML threshold (mW)	50	53	130	100	100	95
Average Output Power (mW)	9	26	112	42	202	485
Slope Efficiency (%)	2	6	27	11	48	49
Optical Conversion Efficiency (%)	2	5	21	8	38	43

The key feature of the laser is the compactness of the cavity which additionally allows high repetition rate for the passively mode-locked pulses. While most ultrafast laser

applications use mode-locked pulses at a constant amplitude, by CW mode-locking the high pulse energy stored in the QML pulses cannot be overlooked. Moreover, the threshold condition (Equation 6.7) differentiating the various mode-locking regimes establishes that the laser works well within the QML regime. The best performance was achieved using a graphene-SA coated on a 40% OC, resulting in a slope efficiency of 49%.

Even higher efficiencies can be achieved by optimising the SAM. Recently, several research groups have investigated saturable absorption in graphene SAM [154-156]. For optimal functioning, the graphene layer should be positioned carefully with respect to the nodes and antinodes of the electric field of the incident light. In the case of graphene coated on bare mirrors, the layer lies very close to the field node resulting in low absorption and very high saturation fluence. This issue has been overcome by the use of a spacer layer between the mirror and graphene layer, as shown in Figure 6.29, to thus ensure an increased absorption at the SA.
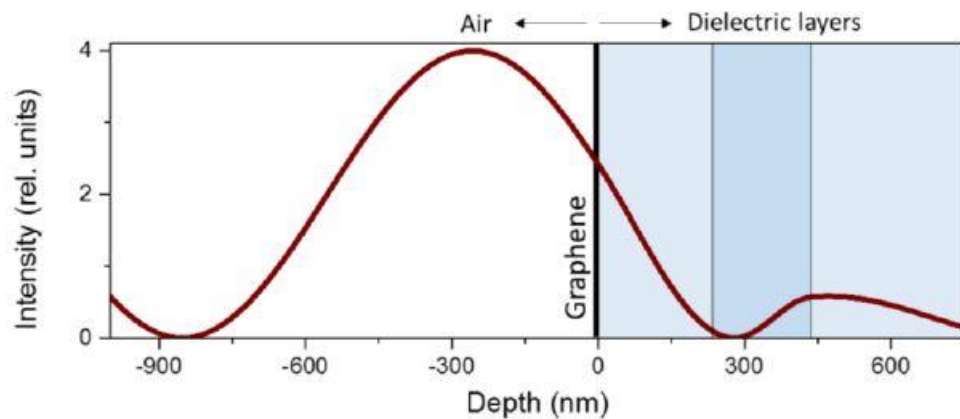
Figure 6. 29.. Effective light field distribution near the HR mirror surface and in the surface layers. The black thick line denotes position of graphene absorber at the top of the upper layer. Reproduced from Ref.[156].

The SA coated output couplers used in the experiments described in this Chapter were not designed for maximum light absorption at the SA surface. Further optimisation of the SA based on the positioning of the nodes and antinodes of the electric field provides an investigation route to better laser performances and even CW mode-locking.

6.8   Conclusions

This chapter discussed ultrashort pulse generation in a Yb-BG waveguide laser employing a quasi-monolithic cavity configuration. SAs based on semiconductor materials and novel carbon nanostructures, namely CNT and graphene were used for the investigation. The SA was integrated with the laser output coupler thereby preserving the compactness of the cavity. The laser operated in a self-starting Q-switched mode-locking regime with a mode-locked pulse repetition rate of 1.5 GHz. The high repetition rate of the laser constitutes one of the advantages of the system, with regard to applications such as frequency comb generation. The laser generated ultrashort pulses of ~ 1 ps duration at a maximum average output power of 485 mW and a slope efficiency of 49%. The laser presents the first result for ULI waveguide lasers employing graphene SA in an integrated cavity configuration and presents a significant step in the development of compact waveguide lasers.

Chapter 7 – Evanescent field mode-locking using an orthogonal waveguide geometry

7.1 Introduction

Recent advances in CNTs and graphene as SAs have resulted in their use for ultrashort pulse generation in a variety of laser configurations including solid-state bulk, fibre, semiconductor and waveguide lasers [35]. In fibre lasers, the SAs are typically sandwiched between two fibre connectors, deposited on fibre ends or within the cores, resulting in an alignment free format. For other laser configurations, the predominant SA-integration strategies include free-space coupling and deposition on high reflectivity cavity mirrors. The linear cavity Yb-BG waveguide laser discussed in Chapter 6 employed SAs deposited on an output coupler mirror.

While efficient mode-locking is possible using these formats, it comes with the risk of thermal damage due to the high intracavity powers as well as mechanical damage due to manual handling. Integration of SAs in specially designed geometries to facilitate evanescent-field interaction has emerged as an alternative to overcome these drawbacks [35]. Evanescent waves correspond to the exponentially decaying field generated when light undergoes total internal reflection (TIR) at the interface of two media. In fibre lasers, evanescent waves are generated at the core-cladding interface, and when in close proximity with a SA result in short pulse generation. Compared to the other techniques that are based on direct interaction of light with a SA, this scheme of passive mode-locking uses only a fraction of the circulating light to induce loss modulations within the cavity, much lower than the damage threshold of the SA. This allows higher power pulsed operation on account of the lower throughput utilised for mode-locking.

This chapter describes a novel evanescent wave mode-locking technique based on waveguides inscribed by ULI technology. Section 7.2 introduces the evanescent mode-locking schemes used in fibre lasers. The techniques for evanescent wave generation demonstrated in ULI-waveguides are also discussed, which are mainly used for sensing applications. Section 7.3 introduces the proposed waveguide device design, which consists of a right angle waveguide geometry to allow efficient evanescent wave

141

generation at the vertex. This design is thus distinct from the other lateral-interaction geometries. The fabricated waveguide substrate is converted into a mode-locker device by coating CNT-SA at the right angle which lies along the angled facet of the chip. Section 7.4 details the laser cavity incorporating this device and the subsequent laser performance.

7.2 Evanescent- field mode-locking

Light travelling from a denser medium of refractive index n_1 to a rarer medium of refractive index n_2 undergoes TIR at the interface, when the angle of incidence θ is greater than the critical angle θ_c. The critical angle is given by the expression,

$$\theta_c = sin^{-1}(n_2/n_1) \tag{7.1}$$

For the glass-air interface, with $n_1 \sim 1.5$ and $n_2 = 1$, the critical angle is calculated to be $\theta_c \sim 42°$. Thus, for an incident angle, $\theta > 42°$, light undergoes TIR at the glass-air boundary and all the incident energy at the interface is reflected back into the denser medium. Although no power is transferred to the rarer medium, an exponentially decaying field is generated in that medium, called the evanescent wave. Figure 7.1 shows a schematic of an evanescent wave generated by TIR. This wave is characterised by an exponentially decaying amplitude in the direction perpendicular to its surface of generation, represented by,

$$I(z) = I_0 e^{-z/d} \tag{7.2}$$

where z is the distance along the direction of decay, I is the intensity and d is the decay length or the penetration depth, as shown in Figure 7.1. The penetration depth is defined as the distance where the evanescent field decreases to 1/e of its maximum, and is given by the expression,

$$d = \frac{\lambda_0}{4\pi n_1} \frac{1}{\sqrt{sin^2(\theta_1) - n^2}} \tag{7.3}$$

Here, $n = \frac{n_2}{n_1} < 1$, and λ_0 is the wavelength of the incident light. For a glass-air interface, with $n_1 \sim 1.5$ and $n_2 = 1$, $n = 0.67$. At a wavelength of 1550 nm, the decay length then corresponds to $d = 1480$ nm for an incident angle of $45°$. Thus, the penetration depth of the evanescent waves is extremely small, of the order of the wavelength of the light used.

When another medium with an index $n_3 > n_2$ is placed close to the second medium such that the evanescent wave in the second medium does not decay completely but extends into the third medium, the TIR process becomes 'frustrated' and power is coupled across to the third medium. This process is termed as 'frustrated TIR' (FTIR) and is analogous to quantum mechanical tunnelling. The confined nature of the evanescent wave close to the interface is used to study various near-surface phenomena and is a key principle for various sensing technologies including infrared spectroscopy, TIR fluorescence microscopy, interference based chemical and bio-sensing applications and surface plasmon resonance (SPR) sensors.
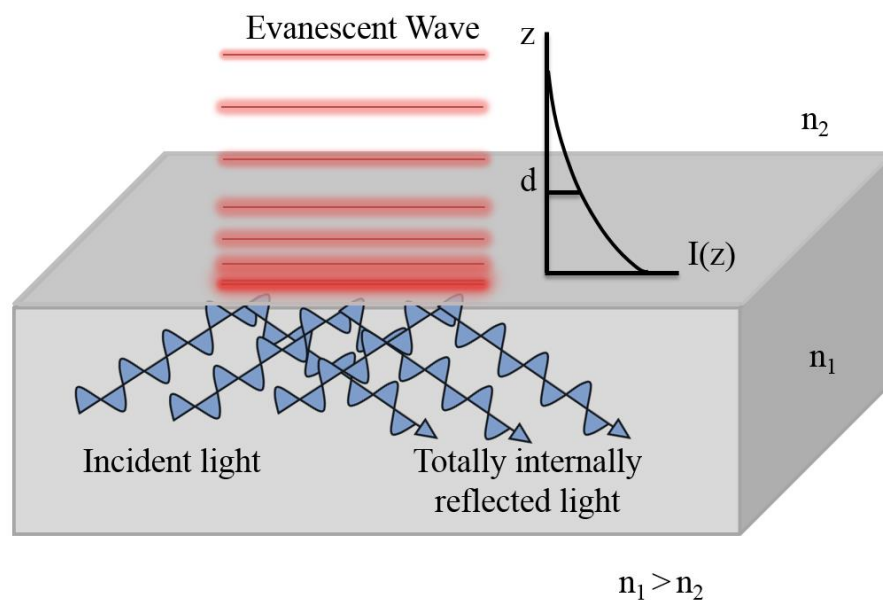
Figure 7. 1. Schematic representation of evanescent wave generation at an interface where the incident light undergoes TIR. n_1 and n_2 are the refractive indices of the two media, with $n_1 > n_2$; d is the penetration depth of the evanescent wave.

The conventional geometry for evanescent-wave sensing applications uses a prism coupling method. However, with the rapid advances in lasers and fibre optics, the field

has extended to fibre-optic and photonic circuit technologies. In optical fibres, the evanescent field generated at the core-cladding interface has been exploited for various sensing applications by using different geometries such as de-clad, tapered, U-shaped and tapered tip optical fibres. The sensors work via the monitoring of perturbations in the exponentially decaying field in the presence of an external medium, with the fibre acting as a modulator. The same principle can be used for passive mode-locking by evanescent-wave interaction of light with a SA. The fast modulation attained at the SA by the evanescent field is coupled into the cavity to introduce ultrashort pulse generation.

Evanescent wave mode-locking using CNT and graphene SAs has been demonstrated, mainly in fibre lasers, following the successful fibre geometries already in use for sensing applications. The following section discusses the predominant fibre geometries used for evanescent-wave mode-locking.

7.2.1 Fibre geometries for evanescent wave mode-locking

In optical fibres with light guided by TIR within the core, an evanescent field exists at the core-cladding interface. The interaction of the evanescent field with a suitable SA results in pulsed operation in fibre lasers without interrupting the optical path in the fibre. Different fibre geometries have been used for this purpose; all the techniques essentially involve the removal of the cladding layer or part of it such that the generated evanescent wave can interact with the surroundings, namely the SA.

(a) *Side-polished fibres or D-shaped fibres*: In this geometry, part of the cladding from a fibre is removed such that the resultant fibre cross-section denotes a D shape. For this, the fibre is mounted on a V-grooved quartz block, and part of the cladding portion is removed by polishing. Figure 7.2 shows the (a) cross-sectional and (b) 3-D view of a side polished fibre in a quartz block, coated with a CNT-PMMA composite SA. In the D-shaped region of the fibre, the guided mode is broadened as a result of effective index change resulting in efficient interaction of the light with the SA.
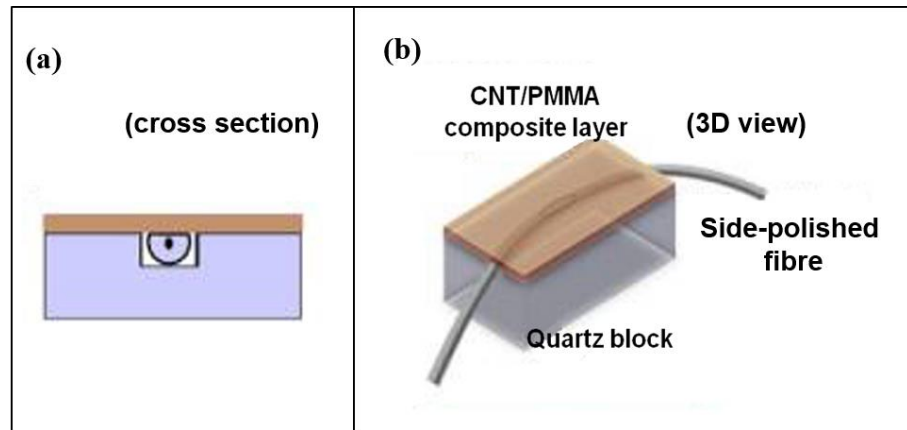
Figure 7. 2. (a) Cross-sectional view of a side-polished or D-shaped fibre geometry. (b) Corresponding evanescent-wave mode-locking scheme in a fibre laser. A CNT/PMMA composite layer is coated at the polished section of the D-shaped fibre to allow evanescent-field interaction. Adapted from Ref. [157].

The performance of such a fibre geometry depends on the quality of the polishing. The technique requires micron-scale precision and *in situ* monitoring of the IL in order to attain optimum fabrication results.

(b) **Tapered fibres:** A fibre taper is produced by heating a section of the fibre and pulling it as it melts. It consists of three sections: a convergent section of decreasing diameter, the taper waist and a diverging section of increasing diameter. This tapered profile supports a modal structure that spreads out into the medium surrounding the taper, allowing efficient evanescent-field interaction with a SA coated around the taper. Figure 7.3 shows a fibre taper with a SA coating at the taper waist. Post fibre-pulling, a standard single mode fibre with a core/cladding diameter of 8.2/125 µm has a typical taper waist diameter of 4.8 µm and a waist length of ~ 22 mm. The nature of the fabrication process ensures a long interaction length, however, the fibre pulling process requires critical *in situ* monitoring of the insertion loss to ensure good device performance. In addition, the tapered regions are delicate and require special packaging.
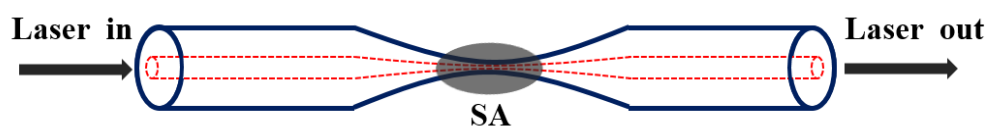
Figure 7. 3. A tapered fibre geometry with a SA coated around the taper. The taper waist constitutes the region of evanescent-wave interaction. Adapted from Ref. [158].

(a) ***Micro-machined slots in the fibre core***: In this technique, direct femtosecond laser writing is employed to induce material modifications within the fibre cladding, but in close proximity to the core. The modified region is typically rectangular shaped, and is then selectively removed by etching the fibre in HF bath. The resultant micro-slot is then filled with a suitable SA. Figure 7.4 shows the micro-slot fabricated for evanescent-field mode-locking. This fabrication technique allows control over the modified regions, including their dimension and location in the fibre. The process also does not require special fibres or splices since the SA is directly integrated within the fibre.
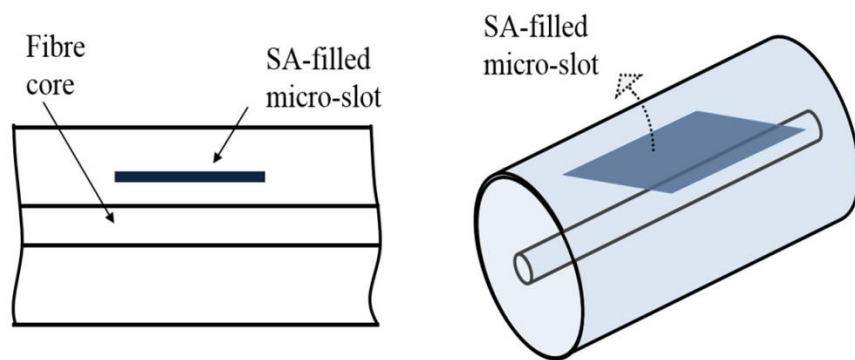
Figure 7. 4. Evanescent-wave mode-locking by integrating SA-filled micro-slots in the cladding. The micro-slot is fabricated by femtosecond laser irradiation followed by selective chemical etching. Adapted from Ref. [159].

Evanescent-field mode-locking in fibre lasers thus predominantly utilises a lateral interaction scheme that allows relatively long and stable nonlinear interaction between the optical field and the SA. Evanescent-field interaction has also been used in planar and channel waveguide devices for sensing applications and potential mode-locking.

Waveguides based on ULI have also been employed to fabricate evanescent wave sensors. A side-polished fibre-like ULI waveguide sensor was demonstrated by Beecher *et al.* in a fused silica substrate [160, 161]. The device consisted of ULI waveguides which start and terminate 75 μm below the sample surface but have a central section approaching the top surface of the chip via an s-bend. This central waveguide section which is ~6 μm away from the top surface forms the region of evanescent wave generation. The suitability of the device as a sensor was tested by coating the top surface with an index matching gel, resulting in leaky waveguide modes. The schematic of the waveguide sensor is shown in Figure 7.5.
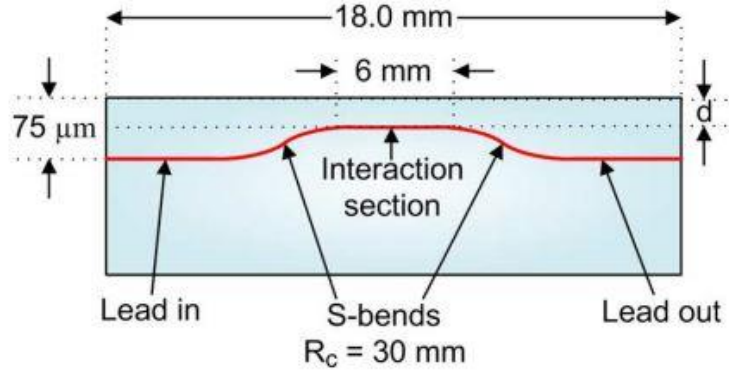
Figure 7. 5. Schematic of the ULI fabricated waveguide with a central elongated region that facilitates evanescent-field interaction. R_c is the radius of curvature and d is the distance from substrate surface to the interaction section. Reproduced from Ref. [161]

Similar ULI waveguide geometries have been utilised to develop pulsed lasers. Tan *et al.* [162] demonstrated Q-switched operation from an Nd:YAG waveguide laser using evanescent-wave interaction of light with a graphene SA in a lateral interaction scheme.

In the work discussed in this chapter, we change from a lateral evanescent-field interaction scheme to a right-angle waveguide geometry. This device is subsequently used as a passive mode-locker. The simplicity of design, effectiveness of the evanescent-field interaction, and lack of precision polishing makes this novel waveguide device a major contender for integrated photonic device applications such as compact waveguide laser sources and waveguide sensors.

7.3   Orthogonal Waveguide Geometry for Evanescent-wave generation

This section introduces an evanescent-field mode-locking approach using ULI based channel waveguides. The proposed device design is shown in Figure 7.6. It consists of a right angle waveguide, with its point of intersection lying along a polished angled facet of the chip. Light guided along one waveguide is incident at the angled dielectric-air facet at an accurately pre-defined angle greater than the critical angle, so that the totally internally reflected light is coupled into the second waveguide by the inherent nature of the design. The angle of incidence in this case is fixed at 45°, which is greater than the critical angle of $\theta_c = 42°$ for a glass-air interface, as calculated in Equation 7.1. The corresponding penetration depth of the evanescent wave is then ~1480 nm.
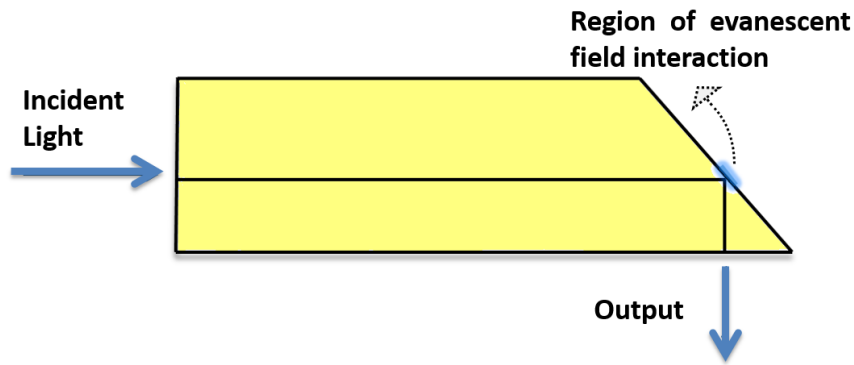
Figure 7. 6. Right-angle waveguide geometry for evanescent-field generation. Light undergoes TIR along the waveguide trajectory with the evanescent waves generated at the angled facet.

This device can become a passive mode-locker by the deposition of a suitable SA at the angled facet. The evanescent waves generated at the angled facet will interact with the SA to induce loss modulations by virtue of fast saturable absorption. These loss modulations must be coupled back into the orthogonal waveguide due to the waveguide design thereby facilitating pulse generation in a laser cavity. The design can be implemented in a passive substrate and then incorporated in a laser cavity, or inscribed in an active medium for compact laser development.

As a first step towards the realisation of such a device, the design was implemented in a passive substrate. The following section details the waveguide fabrication and optimisation processes for the orthogonal waveguide geometry in a glass substrate.

7.3.1 Inscription details

A $30\times10\times1$ mm^3 glass wafer (Corning EAGLE 2000) was chosen as the substrate for the waveguide device. Waveguides were inscribed using a master-oscillator power-amplifier fibre laser supplied by IMRA. The details of the inscription setup are given in Chapter 2, Section 2.6. The laser was set to a repetition rate of 500 kHz, producing ~400 fs pulses centered at 1047 nm. A 0.4 NA aspheric lens was used to focus the laser pulse train to a depth of 350 μm below the surface. Waveguides were inscribed by translating the sample through the focus in the desired trajectory using a high precision automated x-y-z translation stage from Aerotech. The multiscan technique, with 20 scans laterally offset by 0.4 μm, was used to define the waveguide cross-section. The optimal

parameters for waveguide inscription were identified to be 230 nJ laser pulse energy at 8.0 mm.s^{-1} sample translation speed.

To replicate the right-angled waveguide design in the substrate, 50 waveguides were inscribed along the length and width of the chip, as shown in Figure 7.7. The waveguides were inscribed with a vertical pitch of 100 μm, and a slightly offset horizontal pitch of 102.8 μm. The points of intersection of these waveguides therefore lie at an angle of 45.8° from the vertical, or 44.2° from the horizontal. Post-inscription, the substrate was diced at 45°, and polished along the dice line. The glass-air interface formed at this angled facet forms the basis of evanescent–field generation in the device. A close-up of two consecutive intersection points for the orthogonal waveguides is shown in Figure 7.8; the points of intersection indicated as 'A' and 'B'. The difference in the horizontal and vertical pitches, denoted by line segment BD ~ 2.8 μm implies that there is a ~0.8° difference in angles between the dice line and the line formed by the intersection points of the waveguides. This is chosen such that for an ideal pair of waveguides intersecting at the angled facet, shown as 'A' in the Figure 7.8, the next intersecting point 'B' is within 2 μm from the angled facet. This is calculated as,

$$BC = BD \sin 45° = 2.8 \sin 45° \sim 2 \text{ μm} \qquad (7.4)$$

In other words, the difference in the pitches ensures that there is always one waveguide vertex within 1 μm of the polished facet to allow efficient evanescent wave coupling by TIR. This eliminates the need for precision polishing of the angled facet and is one of the major advantages of this device geometry.
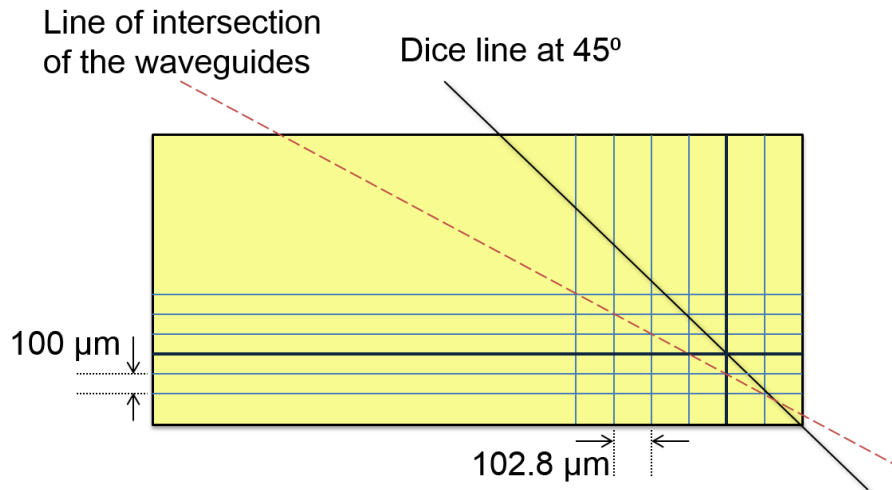
Figure 7. 7. Waveguide inscription specifications used to implement the orthogonal waveguide geometry. Straight waveguides are inscribed in the horizontal and vertical axes, with a pitch of 100 μm and 102.8 μm, respectively. The substrate is then diced along the dice line and polished back such that one optimum pair of perpendicular waveguides undergo TIR at the angled facet, to generate evanescent waves.
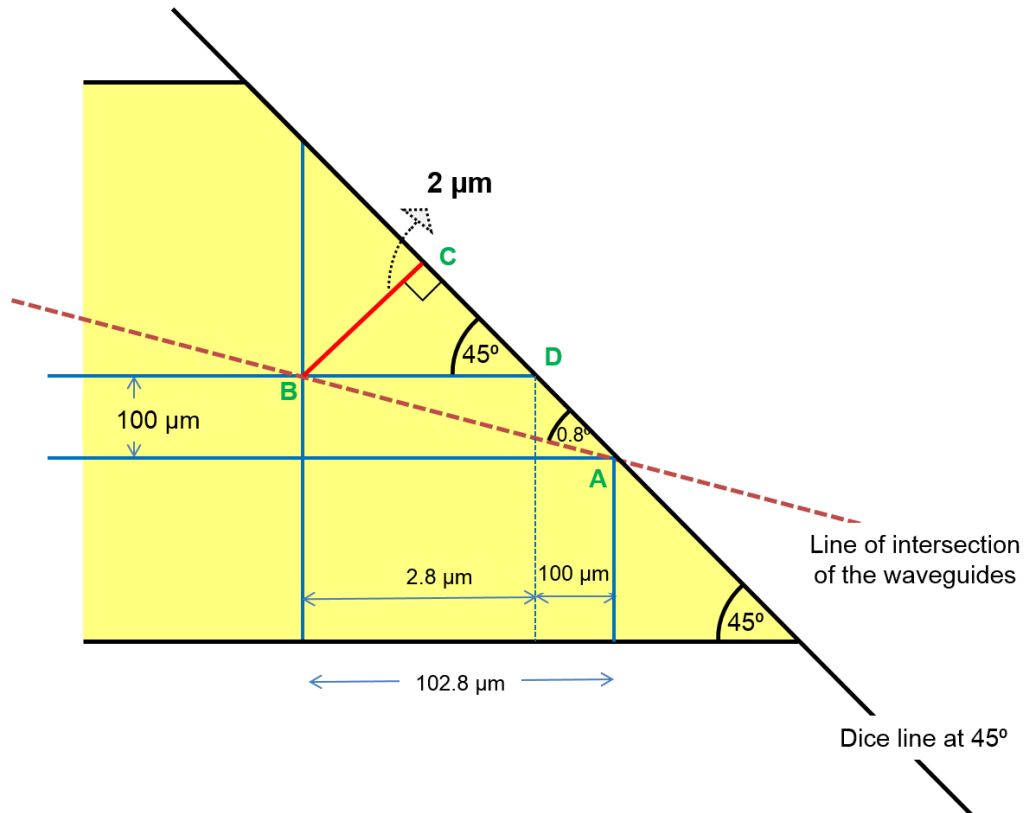
Figure 7. 8. Schematic of the angled facet of the substrate. Two adjacent intersection points of waveguide pairs are given, namely, A and B. A indicates the optimum waveguide pair which is totally internally reflected at the angled facet. The difference of ~2.8 μm in the horizontal versus vertical pich implies that the next intersecting point B is within ~ 1 μm of the polished angled facet. The figure is purposefully drawn out-of-scale in order to provide a clear distinction between adjacent points of intersection of waveguides, marked A and B.

Passive characterisation of the device was performed using a broadband ASE source. The light guided along an SMF-28 fibre was measured using a KD optics detector and recorded as the reference measurement. The fibre was then cleaved and butt-coupled onto the end facets of the waveguide chip, as shown in Figure 7.9, and the resultant signal measured. The difference in the two measurement values yielded a device insertion loss of ~ 1 dB.
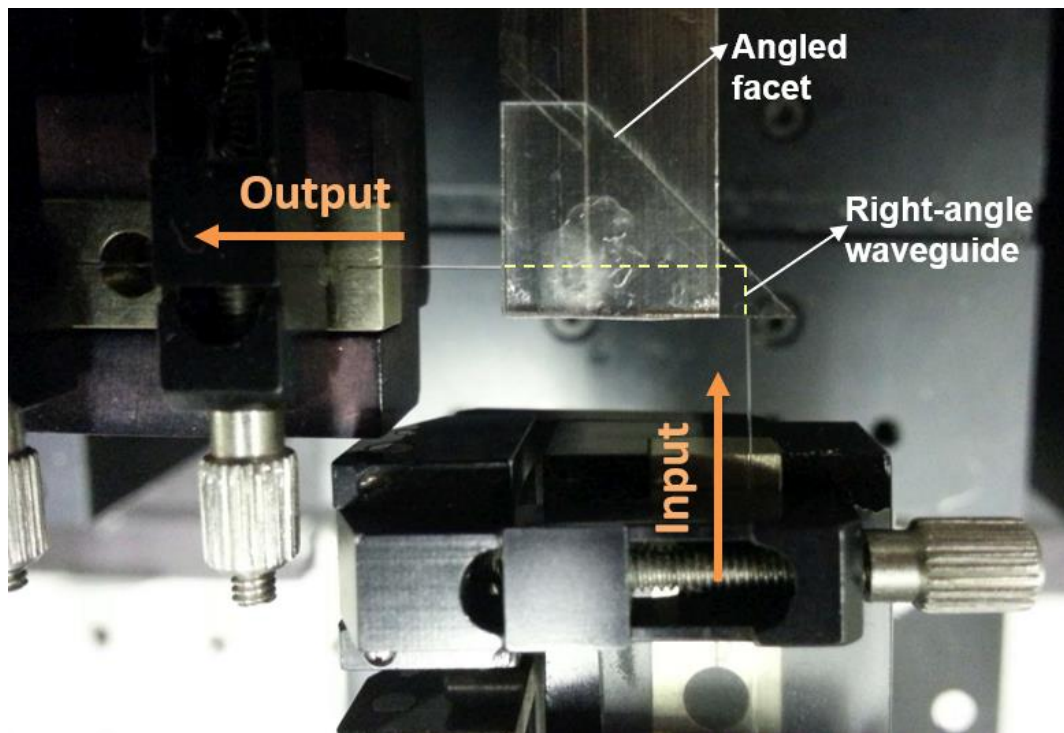
Figure 7. 9. The fibre-based alignment format used to measure the insertion loss in the waveguide chip.

7.3.2 Mode-locked laser experiments

The functionality of the device as a passive mode-locker requires the deposition of a suitable SA at the interface, based on the wavelength of the laser. For our experiments, we used an Erbium-doped fibre ring laser cavity with an operating wavelength of 1.5 μm to investigate the device performance.Accordingly, we used single walled CNT-SA with ~1 nm mean diameter, designed for optimal functioning at 1.5 μm. A high pressure carbon monoxide (HiPCo) CNT-dispersion was obtained as a collaborative input from Cambridge Graphene Centre, University of Cambrige, UK. The CNT-SA was drop cast along the dice line and dried over 24 hours to form a SA coating at the angled facet.

Figure 7.10 represents the evanescent wave coupling in the right-angle waveguide device. The optical saturable absorption of the CNT film at 1550 nm is measured using an optical parametric oscillator (Coherent, Chameleon) delivering 200 fs pulses at 80 MHz repetition rate. The CNT film has a linear transmittance of 33%, with saturation achieved at 50%. This results in a modulation depth of 17%. The saturation intensity is 12.4 MW cm^{-2}.
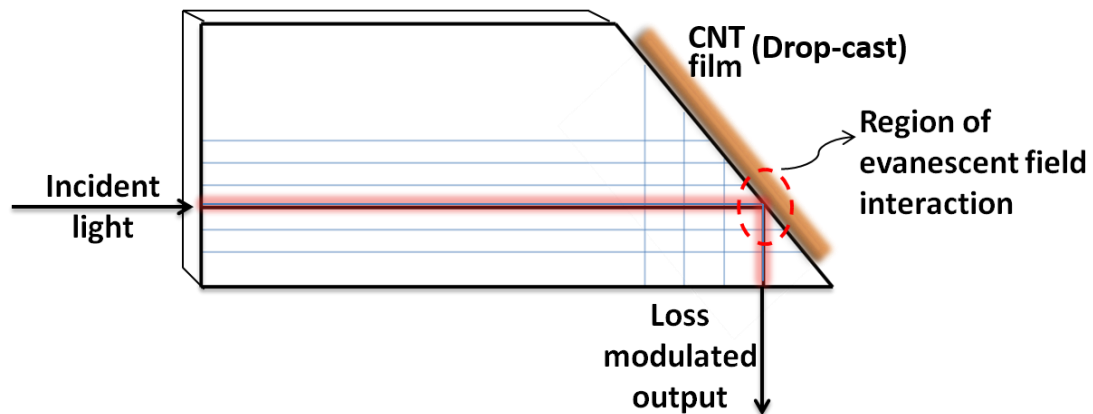
Figure 7. 10. Principle of evanescent-wave interaction in the right-angled waveguide geometry. Deposition of CNT-SA at the angled facet converts the device into a passive mode-locker.

The CNT-coated waveguide device was then inserted in an Erbium-doped fibre ring cavity as shown in Figure 7.11. The laser uses a 980 nm pump laser, which is introduced into the cavity using a fibre based wavelength division multiplexer (WDM). A fibre optic isolator ensures unidirectional operation, and a polarisation controller matches the round-trip polarisation state. A broadband fibre output coupler with 80:20 coupling ratio (JDS Uniphase) was used to extract the laser output. The CNT-based waveguide device with fibres butt-coupled to the orthogonal waveguide facets completes the ring cavity. An index matching fluid (Decane) is used to reduce reflections between the fibre and substrate facets.
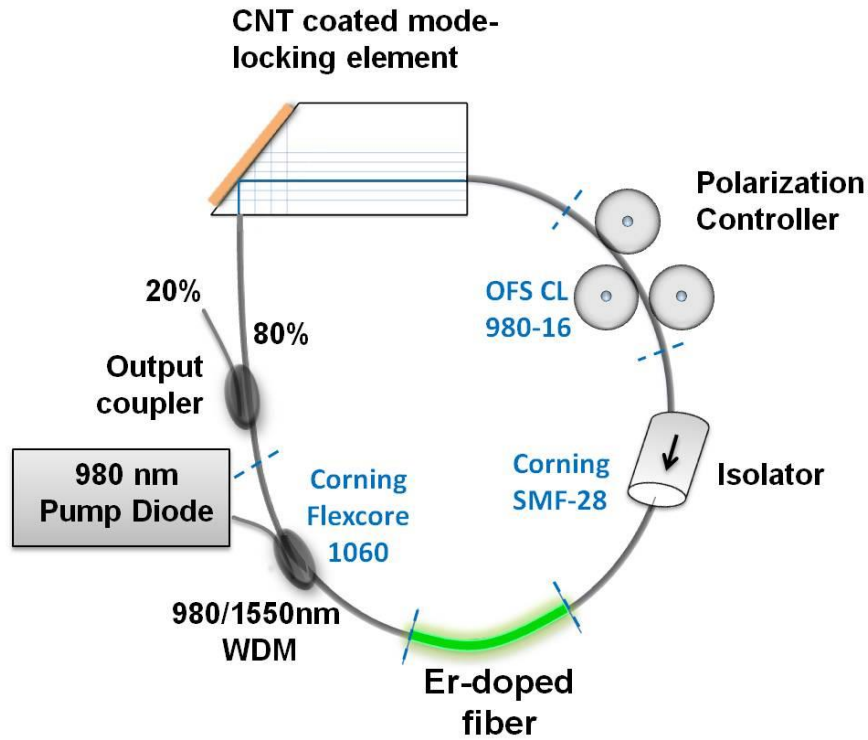
Figure 7. 11. Schematic of the Er-doped ring laser cavity.

The laser cavity is designed to work in a soliton mode-locking regime. A soliton refers to a stable ultrafast pulse which, in the absence of loss, can propagate indefinitely without changing shape. A soliton is generated when self-phase modulation effects balance out the effects due to linear dispersion in the cavity. In the Er-doped fibre laser, the total intracavity dispersion is maintained to be anomalous. The gain section of the fibre laser consists of a 46.8 cm Liekki Er80-8/125 Erbium-doped fibre with an anomalous dispersion of −20 fs^2/mm. The remaining cavity length comprises 533.8 cm of Corning SMF-28, 35.4 cm of Corning Flexcore 1060, and 155.4 cm of OFS Clearlight 980 16 fibres; with their corresponding linear dispersions estimated as 17.9 ps/nm.km, 8 ps/nm.km and -1 ps/nm.km. The dispersion values corresponding to the different cavity components and the net dispersion from each are listed in table 7.1. Assuming the dispersion contribution from the waveguide chip to be negligible, the measured net dispersion in the cavity is anomalous, with a value of -0.13 ps^2; thereby enabling soliton mode-locking.

Table 7. 1. The dispersion chart of the cavity components in the Er-doped fibre laser

Cavity Component	Length of the Component, L (mm)	Dispersion, $D(fs^2/mm)$	Net Dispersion $(L \times D) fs^2$
Corning SMF fibre	5338	-23.1	-123307
Corning Flexcore 1060	354	-10.3	-3646
OFS CL 980-16 (Coupler fibre)	1554	1.29	2004
Erbium-doped gain fibre	467.5	-20	-9350

Self-starting mode-locking is obtained as a result of evanescent field interaction with the CNT-SA at the right angled waveguide geometry, producing a 1.3 mW average output power. This corresponds to a pulse energy of 50 pJ, considering the 26 MHz repetition rate of the mode-locked pulses measured using a fast photodiode (Thorlabs SIR5-FC) and a Rigol DSA 1030 RF spectrum analyser. The measured RF spectrum is given in Figure 7.12, showing the fundamental repetition rate as well as the higher order harmonics of the mode-locked laser.

The optical spectrum measured using an Optical Spectrum Analyser set to 0.5 nm resolution is given in Figure 7.13. The spectrum of the mode-locked laser is centred at 1558 nm, with a FWHM spectral width of 3 nm. The spectrum shows Kelly sidebands [163] that are characteristic of soliton lasers. Kelly sidebands are narrow peaks superimposed on the optical spectrum and are related to periodic disturbances of soliton pulses in the laser cavity[163].
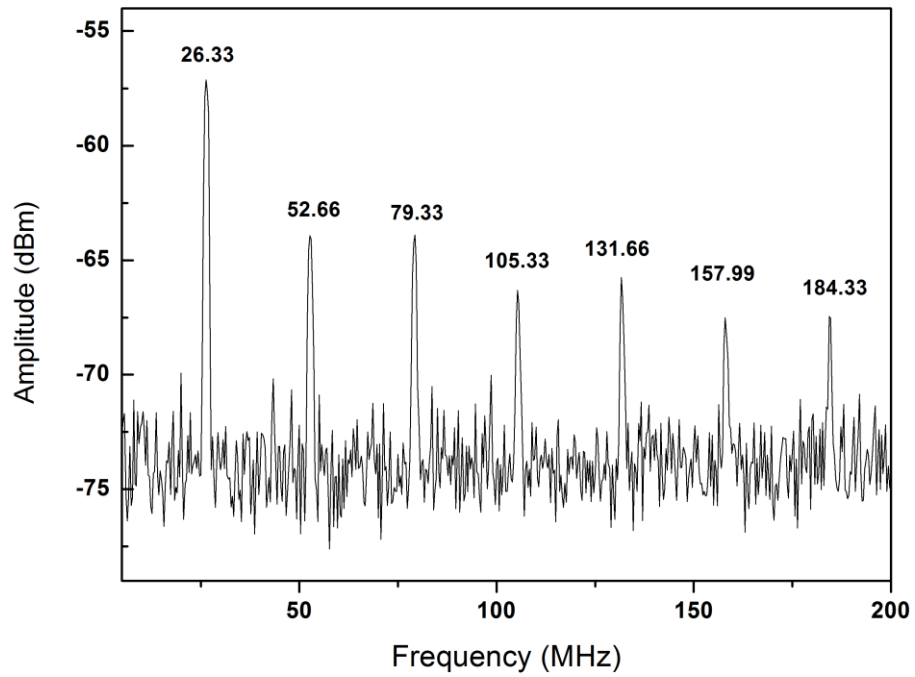
Figure 7. 12. RF spectrum of the Er-doped fibre ring laser, showing the fundamental repetition rate and the higher order harmonics of the laser pulse. The laser is mode-locked by evanescent wave interaction of the optical field with the CNT-SA at the angled facet of an orthogonal waveguide chip.
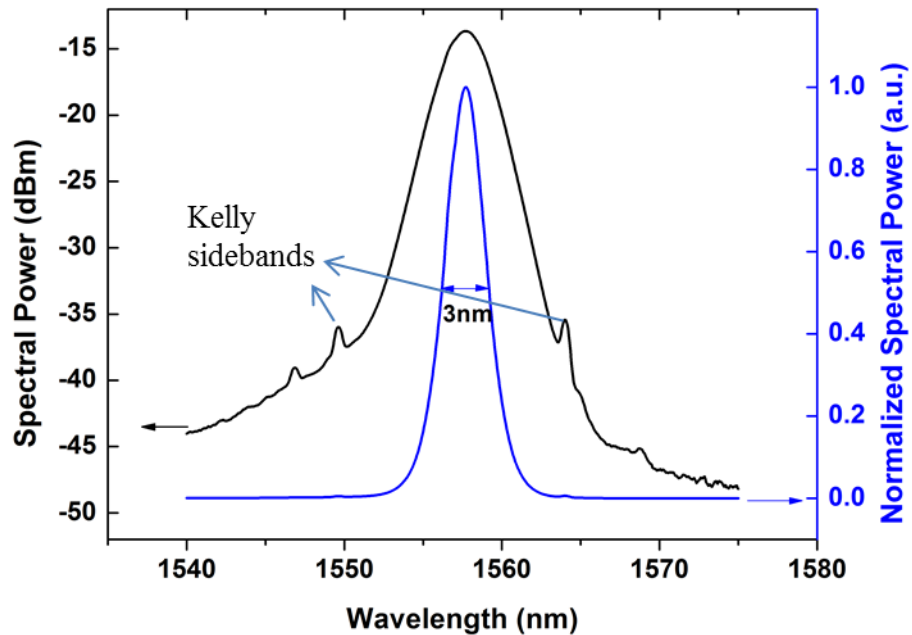
Figure 7. 13. Optical spectrum of the laser output on a logarithmic scale (black line) and linear scale (blue line).

The autocorrelation pulse profile derived from an interferometric autocorrelator measurement is given in Figure 7.14. Assuming a $sech^2$ pulse shape, the FWHM pulse width is estimated to be 800 fs. This yields a TBP of 0.30, close to 0.315, the value expected for bandwidth-limited $sech^2$-shaped pulses [164].
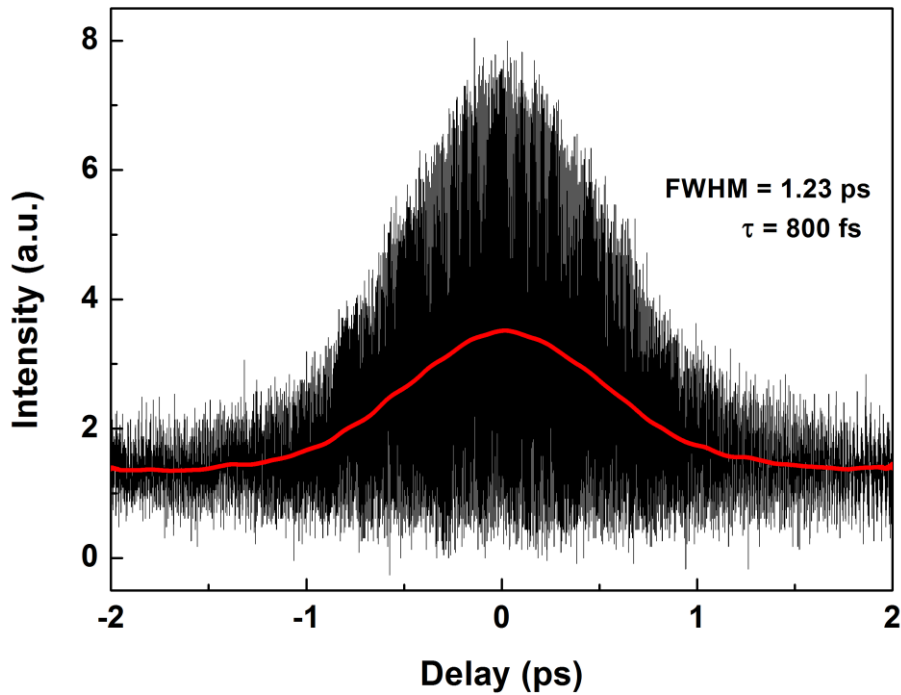
Figure 7. 14. The interferometric autocorrelation trace of the Er-fibre laser. The evanescent-wave mode-locked pulses have a pulse duration of 800 fs.

These results were published in Applied Physics Letters [165].

As an evanescent-field mode-locker, the right-angle waveguide device has a number of advantages over previously demonstrated fibre-based designs. In side-polished and fibre tapered devices, in order to expose a region close enough to the fibre core to achieve sufficient non-linear absorption, the polishing and fibre-pulling processes have to be extremely precise and carefully monitored. In contrast, the integrated waveguide device has no need for precision polishing or critical optical monitoring by virtue of the variation in the horizontal and vertical waveguide pitches in the waveguide design. In addition, the right-angle design reduces the required deposition surface area.

Even though the waveguide device based ring cavity laser deviates from the increased alignment-free format characteristic of fibre systems, it is an excellent demonstration of the scope of the novel waveguide device. The novelty of the device can be transferred to different gain media to develop monolithic waveguide laser sources, with important applications in integrated optics. The following section discusses the initial work towards implementing the orthogonal waveguide design in Yb-BG waveguides for compact laser development at 1µm.

7.4 Towards evanescent-wave passive mode-locking in an integrated cavity right-angle waveguide laser

ULI waveguides in Yb-BG substrate exhibit excellent laser performance, both CW and pulsed, as discussed in Chapters 4 and 6. Yb-BG was therefore chosen to implement the right-angle waveguide design in order to develop a monolithic laser to be mode-locked by evanescent-field interaction with a SA. The glass have a refractive index $n_1 \sim 2$. At the Yb-BG-air interface, with the refractive index of air being $n_2 \sim 1$, the critical angle for TIR is calculated as,

$$\theta_c = sin^{-1}\left(\frac{1}{2}\right) = 30° \tag{7.5}$$

Since the orthogonal waveguide geometry dictates an incident angle of $45°$, the corresponding penetration depth of the evanescent-wave at the angled facet is measured to be ~ 80 µm. The extremely small penetration depth of the evanescent-wave eliminates the option of CNT as a SA, since typical CNT diameter measure ~1 µm. In terms of the SA that can be used for evanescent-field mode-locking, the suitable SA is therefore few layer graphene.

The orthogonal waveguide geometry as given in Figure 7.7 was realised in the substrate using the optimum waveguide fabrication parameters previously identified. Waveguides were inscribed at a repetition rate of 1 MHz, pulse energy of 51 nJ and a sample translation speed of 8 mm s^{-1}. A multi-scan technique employing 20 scans laterally offset by 0.4 µm was used to define the waveguide geometry.

Orthogonal waveguides were inscribed with varied horizontal and vertical pitches, such that the line of intersection of the waveguides and the dice line have an angular separation of 0.8°. The substrate was diced along the 45° dice line, and polished back. The insertion loss in the optimal waveguide pair was measured to be ~4 dB at 1064 nm using a setup similar to that in Figure 7.9.

As an initial experiment towards laser operation, an integrated cavity waveguide laser was setup to operate in a CW mode. The schematic of the cavity is given in Figure 7.15. The pump mirror and the output coupler are butt-coupled to the waveguide edges using index-matching gel.
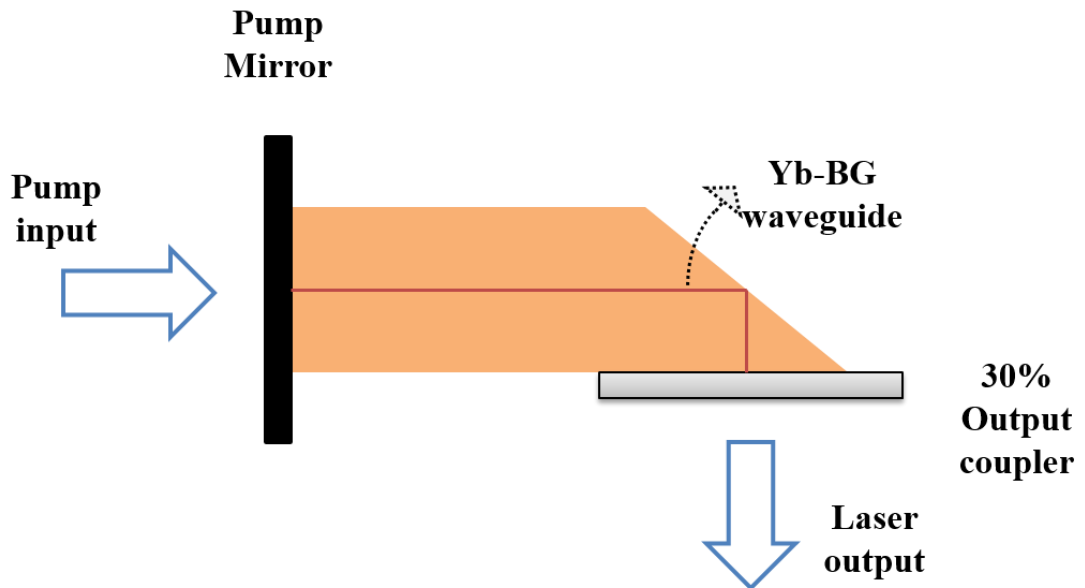
Figure 7. 15. Schematic of the laser setup for an integrated laser using a right angle waveguide.

In such a geometry, with a right-angled Yb-BG waveguide as the gain medium, no laser operation was observed. We attribute this to the multi-mode nature of the ULI waveguides which hampers efficient coupling of the incident light into an orthogonal waveguide. The future work for this research includes waveguide parameter study for single-mode waveguides in Yb-BG.

The orthogonal waveguide geometry with a fixed incident angle of 45° implies that corresponding penetration depth of the evanescent-wave at the angled facet is ~ 80 μm. To account for this extremely small penetration depth of the evanescent-wave, the dice line for the angled facet should be steeper such that the incident angle is just above 30°. This will result in an evanescent wave penetration depth of the order of the wavelength of light. Thus the design can be extended to any combination of refractive indices to achieve efficient evanescent-wave generation. This design criterion has to be taken into account in future works in this device.

7.5   Conclusion

This chapter introduced a novel evanescent-wave mode-locking scheme based on a right-angle waveguide geometry. The orthogonal waveguide geometry was realised in a passive EAGLE substrate with a device insertion loss of ~1 dB. The device was converted into a mode-locker by coating the angled facet with CNT-SA. The effectiveness of the device was tested by incorporating it in a Er-doped fibre ring laser. Subsequently, the laser produced mode-locked pulses at a repetition rate of 26 MHz and pulse duration of 800 fs. The right-angled waveguide device presents a novel approach for evanescent-wave mode-locking extending the application regime from fibre lasers to waveguide lasers. The device is inherently simple, robust and does not require critically monitored polishing procedures. In addition to mode-locking applications, the waveguide design with its reduced footprint for evanescent field interaction has huge implications for sensing applications. Initial work towards the use of the orthogonal design for the development of compact waveguide lasers have also been discussed based on waveguides inscribed in Yb-BG gain medium.

Chapter 8 – Conclusion and future work

8.1   Conclusion

ULI is a powerful technology for novel photonic device fabrication based on optical waveguides. Over a decade old, the technique has rapidly matured, meanwhile opening up new avenues for research. The work presented in this thesis focuses specifically on the application of ULI for the development of compact ultrafast lasers in the NIR region of the electromagnetic spectrum. The thesis features a novel gain medium for ULI based active devices at 1 μm, namely, ytterbium doped bismuthate glass. Chapter 4 presents waveguide fabrication and spectroscopic characterisation experiments in this novel gain medium. A compact CW waveguide laser in a Fabry-Perot cavity configuration is demonstrated with slope efficiencies close to the quantum defect limit. Ultrafast operation is achieved from the cavity by integrating the advantages of ULI waveguides with innovative mode-locking technologies based on carbon nanostructure saturable absorbers. Chapter 5 introduces graphene and its property of saturable absorption, suitable for passive mode-locking of lasers.   Chapter 6 presents ultrashort pulse generation in an integrated cavity waveguide laser using saturable absorbers based on semiconductor materials and carbon nanostructures. These results surpass previously reported ULI waveguide lasers in terms of maximum output powers and slope efficiencies, as well as being the first demonstration of a graphene mode-locked ULI waveguide system. Chapter 7 demonstrates a novel laser mode-locking technique by evanescent field interaction of the optical field with a saturable absorber in a right-angle waveguide chip. The summary of the work presented in each chapter is given below.

Chapter 4 presents waveguide fabrication in novel ytterbium doped bismuthate glass gain media. A multi-scan fabrication technique was utilised to inscribe waveguides with low-loss guiding and symmetric cross-sections. The optimal waveguides have an insertion loss of 2.4 dB for a 48 mm long sample. The propagation losses were estimated using a Caird plot analysis to be of the order of ~0.047 ± 0.004 dB cm^{-1}. In addition to the low-loss guiding, the Yb-dopants in the glass have well-preserved fluorescence properties even post-inscription, indicating the high quality of the glass for ULI. A quasi-monolithic linear cavity laser was constructed with the optimal waveguide as the gain medium. The threshold of operation was ~35 mW with a pump laser operating at 976 nm.   Slope efficiencies close to the quantum defect limit and in excess of 78% have been obtained from the laser [129]. For an optimal output coupling of

30%, the laser produced a maximum output power of 163 mW for a pump power of 275 mW, yielding an optical conversion efficiency of 62%. This laser presented a significant step in the field of ULI waveguide lasers, by virtue of its low lasing threshold, record high slope efficiency and average output powers. The simultaneous achievement of low propagation losses and preservation of the fluorescence properties of ytterbium ions is at the basis of the outstanding laser performance.

Chapter 5 presents the nonlinear optical characterisation of graphene saturable absorbers. The unique properties of graphene are applicable in a broad application range, including passive mode-locking of lasers. It also presents a novel route to pulsed operation for the Yb doped bismuthate waveguide laser discussed in Chapter 4. The nonlinear absorption in graphene was studied as a function of the pulse fluence incident at the sample to derive the defining parameters of a saturable absorber, namely, the modulation depth, saturation fluence and non-saturable losses. Two independent studies were performed. Firstly, the wavelength independent absorption saturation in graphene was investigated. The experiment was performed at two different wavelengths of 1 μm [131] and 2 μm using graphene samples fabricated by liquid phase exfoliation. The comparable values of the saturable absorber parameters at the different wavelengths provide a good contribution to the universal nature of saturable absorption in the material. Secondly, the absorption saturation in graphene was studied with respect to the number of graphene layers in the sample. CVD graphene samples with a single layer and 5-7 layers were used for the study. The samples have a modulation depth ~3.5%. The non-saturable loss in the sample was found to increase by a factor of 6 for a transition from single layer to multilayer graphene. This is justified by the additional loss contribution per layer.

Chapter 6 presents a passively mode-locked, 1.5 GHz repetition rate ytterbium doped bismuthate waveguide laser. The high quality of the substrate for ULI-based active photonic devices was previously established in Chapter 4, leading to this next definite step of pulsed operation. Graphene saturable absorbers, discussed in Chapter 5, presented the most novel and significant mode-locking technology to be pursued. Thus, a linear integrated cavity laser was constructed, with the saturable absorber sandwiched between the waveguide output facet and the output coupler mirror. The laser operated in a Q-switched mode-locking regime with the mode-locked pulses having a measured

repetition rate of 1.5 GHz, in agreement with the cavity length. A repetition rate of the order of few hundred kHz was measured for the Q-switched pulses.

For a first investigation, the well-established semiconductor saturable absorber technology was applied to the laser, resulting in low slope efficiencies ~16%[152]. A relatively new saturable absorber was then investigated, namely, CNT coated on a 40% output coupler. The laser generated ~714 fs pulses at a maximum output power of 112 mW for 530 mW input pump, resulting in a slope efficiency of 27% [153].

Most importantly, laser mode-locking was investigated using a novel graphene saturable absorber. Two different graphene compositions were used; graphene-PVA film and pure graphene film on a 40% output coupler. Graphene-PVA film incorporated in the cavity was found to provide a laser slope efficiency of 11% and a maximum output power of 42 mW for 530 mW launched pump. However, the direct interaction of the laser with the polymer was found to induce damage to the PVA film, thereby damaging the waveguide facet in contact with it. This presents an important demonstration of the unsuitable nature of graphene-polymer composites for high-power laser development. Considering the large publication record related to fibre lasers mode-locked using polymer composites embedded with CNT or graphene, this demonstration shows a critical limitation of free-standing carbon nanostructures and calls for a definite shift in the research focus towards improvement in carbon nanostructure saturable absorbers.

As an alternate solution, graphene-only film deposited on a 40% transmission output coupler was used in the cavity to realise highly efficient laser performance. The laser generated ~1.06 ps pulses with a maximum output power of 202 mW for 530 mW launched pump power, resulting in a 48% slope efficiency [131]. This was the first demonstration of graphene mode-locking in a ULI waveguide laser, with the key features being the high laser slope efficiency ~48% and the high repetition rate > 1 GHz of the mode-locked pulses.

The feature of power scalability was investigated in the same cavity by using a pump with a maximum output power of ~1.12 W. Self-starting Q-switched mode-locked operation with a maximum output power of 485 mW was realised, yielding a slope

efficiency of 49% [19]. The output power is a record in terms of ULI waveguide laser development and represents a significant step towards high-power operation in waveguide lasers. Revisiting the power graph in Chapter 1 that provides a comparison of solid state bulk, semiconductor and fibre lasers; the performance regime of the Yb-BG laser featured in this thesis is shown in Figure 8.3. The waveguide laser is found to exhibit a performance similar to that of fibre lasers. This is an expected result considering the identical operation principle in both. The possibility of higher average and peak power operation in the waveguide laser can be explored further by fabrication of even lower loss waveguides, optimisation of the saturable absorbers or use of even higher pump powers.
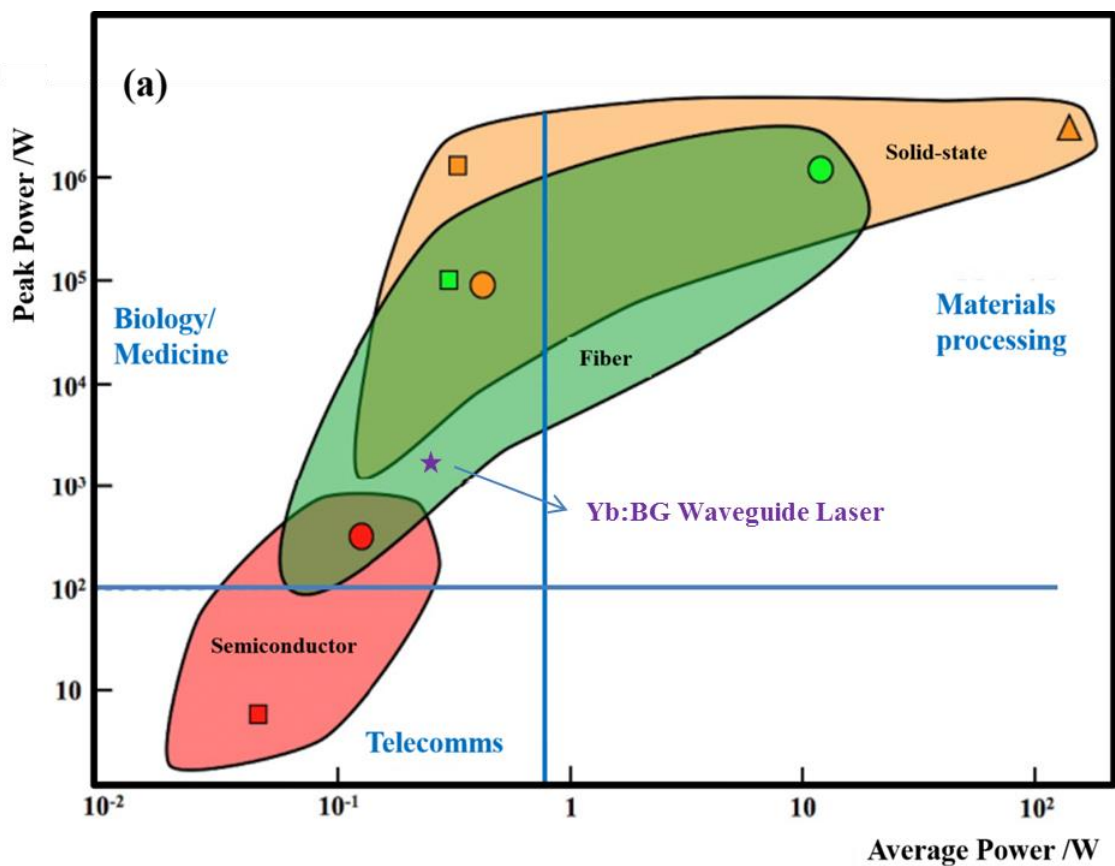
Figure 8. 1 A plot of peak power versus average power for different laser architectures in the NIR. The performance of the waveguide laser discussed in the thesis is also indicated.

Chapter 7 presents a novel evanescent mode-locking device based on a right-angle waveguide design. The device provides an exemplary example of the flexibility of ULI. The device consists of orthogonal waveguides, with their points of intersection lying along a polished angled facet of the chip. A small variation is introduced in the vertical

and horizontal pitches used for waveguide inscription so that the points of intersection of the waveguides vary by a small angle of ~ 8° with the dice line that defines the angled facet. Light guided along one waveguide is incident at the angled dielectric-air facet at a pre-defined angle greater than the critical angle, so that the totally internally reflected light is coupled into the second waveguide. The waveguide device, fabricated in fused silica substrate, was converted into a saturable absorber by depositing a single wall CNT film at the angled dielectric surface. This was used to mode-lock an Erbium doped fibre ring laser cavity at 1.55 μm, with a repetition rate of 26 MHz, and pulse duration of 800 fs [165, 166].

Considering the other evanescent-wave mode-locking wave schemes predominantly used for fibre lasers, the right-angle waveguide design has unique advantages. One is, it extends the mode-locking technology from fibres to other laser configurations. The extremely precise polishing or fibre pulling process required in the lateral interaction geometries in fibres is relaxed in the case of the right-angle waveguide design due to the variation in the horizontal and vertical waveguide pitches. Also, the design provides a nonlinear absorption interaction length of the order of the waveguide mode diameter, which, in turn reduces the required deposition surface area.

The novel design was applied to Yb doped Bismuthate laser gain media, as an initial step towards the development of monolithic waveguide laser sources that find important applications in integrated optics.

8.2   Future Work

Ytterbium doped glass substrates present an attractive gain media for ultrafast lasers in the NIR region. The large gain bandwidths associated with laser glasses are ideal for wavelength tuning and more importantly, the generation of ultrashort pulses. The application of ULI technology to these gain media facilitates highly efficient waveguide lasers by virtue of the guiding geometry. The work embodied in this thesis covers few significant features of ULI waveguides in ytterbium doped bismuthate glass for compact ultrafast laser development. ULI in ytterbium doped bismuthate glass facilitates low propagation loss waveguides, meanwhile preserving the fluorescence properties of the ytterbium ions. This glass therefore appears to be a novel gain medium with unprecedented potential for ultrafast laser inscribed 3-D waveguide devices. This

capability is reflected in the title of the thesis. While only 2-D waveguide devices have been demonstrated in this thesis, namely straight and right-angled waveguide geometries, the applicability of the gain media can be extended to the third dimension to fabricate novel and intricate waveguide designs.

8.2.1 Compact ultrafast waveguide lasers

(a) Monolithic waveguide laser

The quasi-monolithic nature of the compact CW waveguide laser discussed in Chapter 4 can be extended towards a truly monolithic laser cavity. This can be accomplished by having appropriate coatings at the waveguide facet to serve as the pump mirror and the output coupler. An alternate solution is the use of ULI technology to inscribe a Bragg grating output coupler in the waveguide path.

(b) High-repetition rate mode-locked lasers

The compact passively mode-locked waveguide illustrated in the thesis has a mode-locked pulse repetition rate of 1.5 GHz. The applications of such high repetition rate lasers, for example in frequency comb generation, call for certain pre-requisites for the laser, including highly stable CW mode-locking. A compact laser with the cavity mirrors butt-coupled to the waveguide gain media can be CW mode-locked by providing precise dispersion control. A. Choudhury *et al.* [97] demonstrated an intra-cavity dispersion control based on the Gires-Tournois Interferometer (GTI) effect by introducing a gap between the waveguide and the output coupler. This technique however was not effective for the ~50 mm ytterbium bismuthate glass waveguide laser, owing to the large value of normal dispersion associated with the long sample length. With shorter waveguide samples, multi-GHz repetition rate laser operation can be investigated, along with the use of this simple technique for dispersion control.

Another aspect for CW mode-locking in an integrated waveguide cavity is associated with the systematic optimisation of the SA. Graphene appears as the ideal SA for this purpose, considering the expertise achieved around the world in terms of graphene production and characterisation. Also, the field of graphene mode-locking is far from optimised, especially considering the very recent analysis of light

absorption in graphene coated dielectric mirrors [154, 156]. In SESAMs which have had decades of research leading to their optimisation, the absorbing quantum wells are positioned in the antinodes of the electric field incident at the mirror to ensure a low saturation fluence. This aspect has been neglected in the case of graphene-based mirrors until very recently where a spacer layer has been introduced between the graphene film and the dielectric mirror to facilitate maximum absorption [154, 156]. This discovery also means that the large number of publications to date of solid-state bulk and waveguide lasers based on graphene coated dielectric mirrors suffer from the same significant limitation.

An alternate method for CW mode-locking in a waveguide laser cavity at 1 µm is based on moving away from an integrated cavity system to an all-normal-dispersion (ANDi) ring laser. Mode-locking can be achieved by the technique of nonlinear polarisation evolution, where, the polarisation state of the circulating beam is dependent on the irradiance of the optical field. ANDi lasers can be designed to provide high repetition rate mode-locked pulses for similar applications as the integrated waveguide cavity.

8.2.2 Applications of evanescent-wave right-angle waveguide

(a) Universal saturable absorber device

Chapter 7 reported an orthogonal waveguide device in fused silica, used for laser mode-locking via evanescent-field interaction of light with a SA at the device right-angle. The device can be modified to incorporate graphene as a saturable absorber. The wavelength independent absorption saturation in graphene is one of the major conclusions of Chapter 5. This property of graphene can be utilised in the right angle fused silica chip to realise a "universal saturable absorber device". By replacing the CNT coating with graphene, and ensuring an optimal loss for the waveguide chip for a wide wavelength spectrum, the device can be used as a passive mode-locker for a broad spectral range. The evanescent-wave approach for mode-locking also ensures high power laser operation.

(b) Monolithic waveguide laser with a right-angled geometry

Work in the immediate future is focused on adapting the right-angle waveguide design in ytterbium doped bismuthate glass. Significant optimisation of the waveguide fabrication parameters is required to realise single-mode waveguides, a key criterion for effective evanescent-wave coupling at the right angle. A quasi-monolithic waveguide laser can be developed with bulk mirrors, both pump mirror and output coupler attached to the input and output facets of the right-angled waveguide. The use of custom made Bragg-coatings at the input and output facets can achieve a true monolithic laser cavity configuration.

(c) Integrated Master oscillator Power Amplifier (MOPA)

A MOPA consists of a mode-locked laser as a seed which is then fed into an amplifier system to provide multi-watt output powers. The output can be compressed after the amplifier stage to provide near-transform limited pulses. The technology of ULI can be utilised to fabricate a MOPA system in a selected gain medium, with significantly reduced footprint. Figure 8.2 shows a proposed MOPA system design incorporating straight waveguides. The master oscillator consists of a standing wave laser with ULI enabled Bragg grating as a spectral filter and output coupler on one end. The mode-locking element can be an SA-filled slot in the direct path of the waveguide. Evanescent wave mode-locking with a lateral interaction scheme using surface waveguides can also be used. The amplifier stage following the oscillator comprises a straight waveguide in the same gain medium.
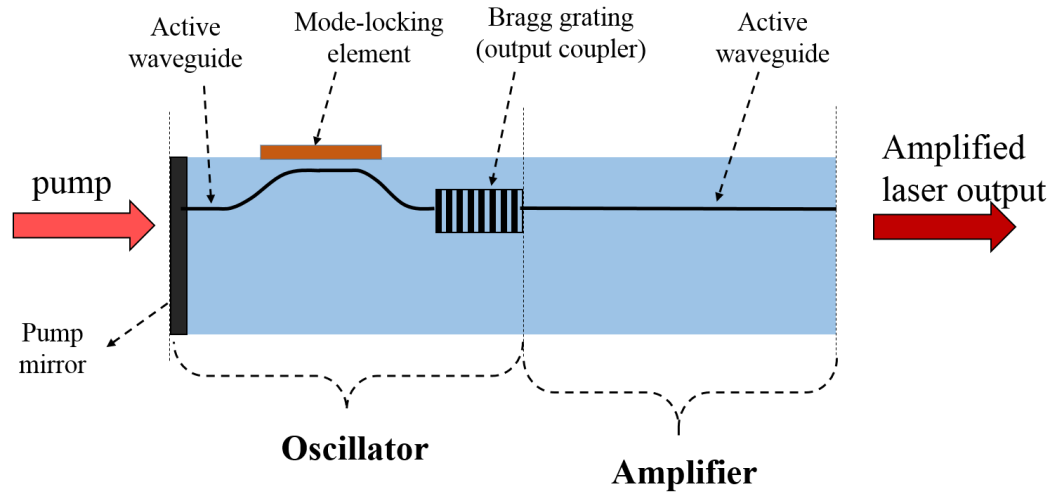
Figure 8. 2. Integrated MOPA configuration with straight waveguides (Side-view). The oscillator comprises a standing wave laser cavity. Mode-locking is achieved by the evanescent wave interaction of light with a SA coated on the surface of the substrate. A ULI based Bragg reflector allows wavelength selectivity as well as output coupling into the next stage of the MOPA. The amplifier stage comprises of a waveguide in the same gain medium.

An alternate integrated MOPA configuration is based on the right angled waveguide geometry discussed in Chapter 7. Figure 8.3 shows a schematic of the proposed design. The master oscillator comprises a right angled waveguide. A dielectric coating providing high transmission for the pump, and high reflectivity for the laser wavelength, can be deposited at the waveguide input facet. A ULI-based Bragg grating inscribed within the substrate constitutes the output coupler. The key feature of this geometry is the relatively simple means of mode-locking the system based on evanescent-wave interaction of light with a SA deposited at the right-angle facet. The design only requires prior knowledge of optimal waveguide parameters in the substrate. An optimisation step of the mode-locking element which forms an important step in the previous MOPA configuration is absent in this design. A subsequent waveguide in the same substrate can be used as the amplifier stage of the MOPA.

The amplifier in the proposed MOPA design can be pumped from either side or from both ends. In cases where the pump used for the oscillator is not appreciably depleted, the residual pump can be used to drive the amplifier by varying the output coupling ratio in the Bragg mirror. It is to be noted that, while the design presents a

simple route to a monolithic MOPA, a large number of critical factors have to be taken into account for its implementation, such as the suitable substrate choice and optimal ULI inscription parameters. The latter includes the refractive index contrast that is possible in the system, which in turn affects the effectiveness of the Bragg stack. The number of Bragg layers required to achieve a specific reflectivity decreases with a higher refractive index contrast.
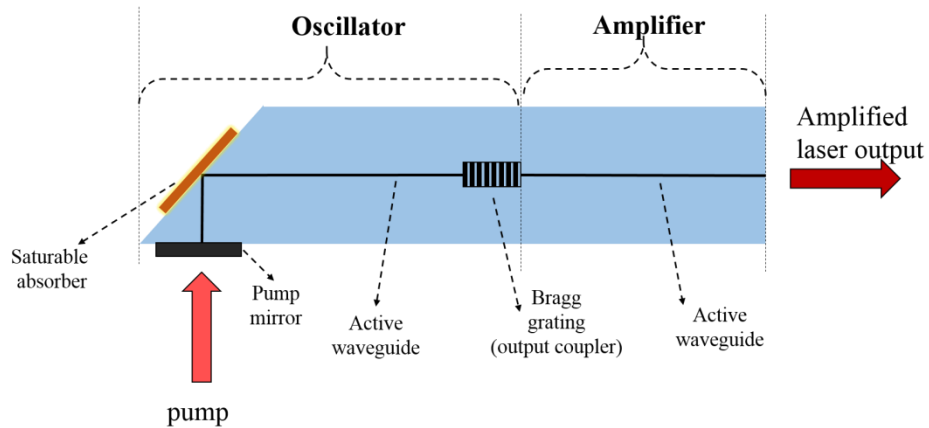
Figure 8. 3. MOPA configuration using the right-angle waveguide geometry (top-view). The oscillator comprises a right angled waveguide. The laser is mode-locked using the evanescent wave interaction of the optical field with a SA deposited at the angled facet of the substrate. This method of mode-locking is essentially simple compared to other techniques of SA integration in a waveguide cavity. The amplifier stage of the MOPA is an active waveguide in the same substrate.

8.2.3   Fibre-fuse effect

The power scaling feature of the waveguide laser, demonstrated in Chapter 6, is accompanied by other detrimental effects that become pronounced at high power laser operation. This includes the fibre-fuse effect [167], first observed in 1988 [168, 169]. A fibre-fuse is a continuous destruction of the optical fibre core, induced and fed by the propagating light. It is triggered by the local heating at some point within a waveguide structure through which an input beam is being delivered. At this defect point, the propagating radiation is strongly absorbed leading to a formation of an optical discharge. Once the heat induced high density plasma is captured in the core region, it travels backwards along the fibre toward the laser source, consuming the light energy and leaving a hollow damage train. This fibre fuse effect initiated by local defect points within a fibre, although a pretty sight, can lead to the destruction of kilometres of fibres.

For the high-power operation of the ytterbium doped bismuthate waveguide laser mode-locked by graphene, and emitting 485 mW output, a fibre-fuse effect was observed that resulted in complete damage of the waveguide core along the entire length. The effect was characterised by periodic voids and bubble formation, and initiated at the far end of
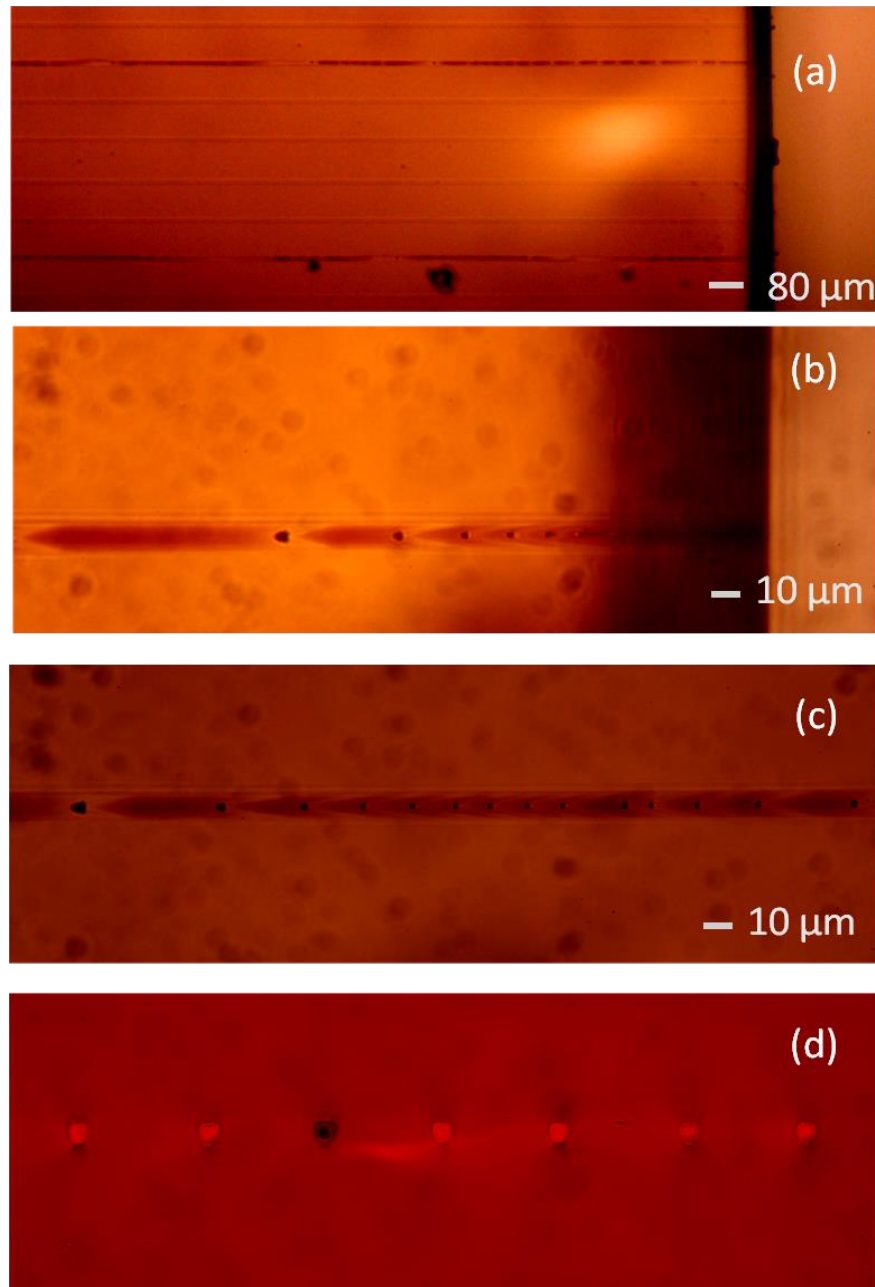
Figure 8. 4. Optical microscope images showing waveguide damaged by fibre-fuse effect. (a) Top surface view of the sample showing two damaged waveguides (b) A zoomed in top view of the fibre-fuse damage. The input facet of the waveguide is shown, with the pump light incident from the right. (c) This top surface view gives a clearer image of the observed bullet shaped damage centres in the waveguide core. (d) Comparison of guiding structures and the waveguide core damaged by fibre fuse.

the cavity. Figure 8.4 (a-c) shows the images as viewed from the top surface of the waveguide, with the periodic bullet shaped hollow damage centres. Figure 8.3 (d) shows the damaged waveguide facet in comparison with the neighbouring guiding structures. While this effect is highly undesirable, the demonstration, however accidental, is a clear indication of one other issue that needs to be resolved in the path of compact waveguide laser development, and require a systematic study. Significant work exists in a systematic study of this effect in waveguides, including the factors leading to local heating in the beam path and the threshold for plasma generation.

With its unique advantages in terms of design freedom, device integration and rapid prototyping, ULI is now an established field for novel device fabrication. The technology allows the investigation of material processing for a wide parameter range for a large number of substrates. The focus of this thesis, on a single gain medium but leading to numerous significant results, signifies the vast untapped potential of this technology. ULI has thus transformed the outlook of microfabrication and integrated optics even leading to its commercialisation [84].

References

1.	T. H. Maiman, "Stimulated optical radiation in Ruby," Nature **187**, 493-494 (1960).
2.	"The United Nations proclaims an International Year of Light in 2015" (European Physical Society Press Release: 20 December 2013), retrieved 17 Jan 2014,
	http://c.ymcdn.com/sites/www.eps.org/resource/resmgr/events/EPS_IYL2015Adopted.pdf.
3.	"Particle Acceleration by Lasers." retrieved 17 Jan 2014 http://www.eli-beams.eu/science/particle-acceleration-by-lasers/
4.	"NIF laser fusion experiments yields record energy", retrieved 17 Jan 2014, http://optics.org/news/4/8/37.
5.	"Scottish scientists to search for alien life" retrieved 17 Jan 2014, http://www.scotsman.com/news/scotland/top-stories/scottish-scientists-to-search-for-alien-life-1-3273612.
6.	D. Faccio, T. Arane, M. Lamperti, and U. Leonhardt, "Optical black hole lasers," Classical Quant Grav **29**(2012).
7.	A. Javan, D. R. Herriott, and W. R. Bennett, "Population Inversion and Continuous Optical Maser Oscillation in a Gas Discharge Containing a He-Ne Mixture," Phys. Rev. Lett. **6**, 106-110 (1961).
8.	A. K. Dubey and V. Yadava, "Laser beam machining - A review," Int. J. Mach. Tool Manu. **48**, 609-628 (2008).
9.	F. J. Mcclung and R. W. Hellwarth, "Giant Optical Pulsations from Ruby," J. Appl. Phys. **33**, 828-829 (1962).
10.	L. E. Hargrove, R. L. Fork, and M. A. Pollack, "Locking of He-Ne Laser Modes Induced by Synchronous Intracavity Modulation," Appl. Phys. Lett. **5**, 4 (1964).
11.	T. Popmintchev, M. C. Chen, P. Arpin, M. M. Murnane, and H. C. Kapteyn, "The attosecond nonlinear optics of bright coherent X-ray generation," Nat Photonics **4**, 822-832 (2010).
12.	M. A. Haase, J. Qiu, J. M. Depuydt, and H. Cheng, "Blue-Green Laser-Diodes," Appl. Phys. Lett. **59**, 1272-1274 (1991).
13.	S. Nakamura, "InGaN-based violet laser diodes," Semicond. Sci. Tech. **14**, R27-R40 (1999).
14.	R. L. Fork, B. I. Greene, and C. V. Shank, "Generation of Optical Pulses Shorter than 0.1 ps by Colliding Pulse Mode-Locking," Appl. Phys. Lett. **38**, 671-672 (1981).
15.	J. A. Valdmanis, R. L. Fork, and J. P. Gordon, "Generation of Optical Pulses as Short as 27 Femtoseconds Directly from a Laser Balancing Self-Phase Modulation, Group-Velocity Dispersion, Saturable Absorption, and Saturable Gain," Opt. Lett. **10**, 131-133 (1985).
16.	D. H. Sutter, G. Steinmeyer, L. Gallmann, N. Matuschek, F. Morier-Genoud, U. Keller, V. Scheuer, G. Angelow, and T. Tschudi, "Semiconductor saturable-absorber mirror-assisted Kerr-lens mode-locked Ti : sapphire laser producing pulses in the two-cycle regime," Opt. Lett. **24**, 631-633 (1999).
17.	M. R. Querry, D. M. Wieliczka, and D. J. Segelstein, "Water (H2O)," in *Handbook of Optical Constants of Solids*, E. D. Palik, ed. (Academic Press, Burlington, 1997), pp. 1059-1077.
18.	P. Keane, H. Ruiz-Garcia, and S. Sadda, "Clinical applications of long-wavelength (1,000-nm) optical coherence tomography," Ophthalmic Surg. Lasers Imaging Retina. **42**, S67-S74 (2011).

19.   R. Mary, D. Choudhury, and A. K. Kar, "Applications of fiber lasers for the development of compact photonic devices," IEEE J. Sel. Top. Quant. Electron. **20** 1-13 (2014 (doi: 10.1109/JSTQE.2014.2301136)).

20.   C. H. Li, A. J. Benedick, P. Fendel, A. G. Glenday, F. X. Kartner, D. F. Phillips, D. Sasselov, A. Szentgyorgyi, and R. L. Walsworth, "A laser frequency comb that enables radial velocity measurements with a precision of 1 cm. s-1," Nature **452**, 610-612 (2008).

21.   A. Bartels, R. Cerna, C. Kistner, A. Thoma, F. Hudert, C. Janke, and T. Dekorsy, "Ultrafast time-domain spectroscopy based on high-speed asynchronous optical sampling," Rev. Sci. Instrum. **78**, 035107 (2007).

22.   W. Sibbett, A. A. Lagatsky, and C. T. A. Brown, "The development and application of femtosecond laser systems," Opt. Express **20**, 6989-7001 (2012).

23.   E. Garmire, "Nonlinear optics in daily life," Opt. Express **21**, 30532-30544 (2013).

24.   A. J. Demaria, D. A. Stetser, and H. Heynau, "Self Mode-Locking of Lasers with Saturable Absorbers " Appl. Phys. Lett. **8**, 174 (1966).

25.   D. E. Spence, P. N. Kean, and W. Sibbett, "60-fsec Pulse Generation from a Self-Mode-Locked Ti-Sapphire Laser," Opt. Lett. **16**, 42-44 (1991).

26.   U. Morgner, F. X. Kartner, S. H. Cho, E. Chen, H. A. Haus, J. G. Fujimoto, E. P. Ippen, V. Scheuer, G. Angelow, and T. Tschudi, "Sub-two-cycle pulses from a Kerr-lens mode-locked Ti : sapphire laser (vol 24, pg 411, 1999)," Opt. Lett. **24**, 920-920 (1999).

27.   U. Keller, D. A. B. Miller, G. D. Boyd, T. H. Chiu, J. F. Ferguson, and M. T. Asom, "Solid-State Low-Loss Intracavity Saturable Absorber for Nd-Ylf Lasers - an Antiresonant Semiconductor Fabry-Perot Saturable Absorber," Opt. Lett. **17**, 505-507 (1992).

28.   C. R. E. Baer, O. H. Heckl, C. J. Saraceno, C. Schriber, C. Krankel, T. Sudmeyer, and U. Keller, "Frontiers in passively mode-locked high-power thin disk laser oscillators," Opt. Express **20**, 7054-7065 (2012).

29.   Z. W. Zheng, C. J. Zhao, S. B. Lu, Y. Chen, Y. Li, H. Zhang, and S. C. Wen, "Microwave and optical saturable absorption in graphene," Opt. Express **20**, 23201-23214 (2012).

30.   D. Jaque, J. C. Lagomacini, C. Jacinto, and T. Catunda, "Continuous-wave diode-pumped Yb : glass laser with near 90% slope efficiency," Appl. Phys. Lett. **89**, 121101 (2006).

31.   S. Y. Set, H. Yaguchi, Y. Tanaka, and M. Jablonski, "Laser mode locking using a saturable absorber incorporating carbon nanotubes," J. Lightwave Technol. **22**, 51-56 (2004).

32.   S. Y. Set, H. Yaguchi, Y. Tanaka, and M. Jablonski, "Ultrafast fiber pulsed lasers incorporating carbon nanotubes," IEEE J. Sel. Top. Quant. **10**, 137-146 (2004).

33.   Q. L. Bao, H. Zhang, Y. Wang, Z. H. Ni, Y. L. Yan, Z. X. Shen, K. P. Loh, and D. Y. Tang, "Atomic-Layer Graphene as a Saturable Absorber for Ultrafast Pulsed Lasers," Adv. Funct. Mater. **19**, 3077-3083 (2009).

34.   Z. P. Sun, T. Hasan, F. Torrisi, D. Popa, G. Privitera, F. Q. Wang, F. Bonaccorso, D. M. Basko, and A. C. Ferrari, "Graphene Mode-Locked Ultrafast Laser," Acs Nano **4**, 803-810 (2010).

35.   Z. Sun, T. Hasan, and A. C. Ferrari, "Ultrafast lasers mode-locked by nanotubes and graphene," Physica E-Low-Dimensional Systems & Nanostructures **44**, 1082-1091 (2012).

36.   S. Yamashita, "A Tutorial on Nonlinear Photonic Applications of Carbon Nanotube and Graphene," J. Lightwave Technol. **30**, 427-447 (2012).

37. J. Deile, R. Brockmann, and D. Havrilla, "Current Status and Most Recent Developments of Industrial High Power Disk Lasers," 2009 CLEO Conference (Cleo/Qels 2009), Paper CThA4, 834-835 (2009).

38. C. Jauregui, J. Limpert, and A. Tunnermann, "High-power fibre lasers," Nat. Photon. **7**, 861-867 (2013).

39. P. K. Tien, "Light Waves in Thin Films and Integrated Optics," Appl Optics **10**, 2395-& (1971).

40. C. J. Karlsson, F. A. A. Olsson, D. Letalick, and M. Harris, "All-fiber multifunction continuous-wave coherent laser radar at 1.55 mu m for range, speed, vibration, and wind measurements," Appl. Opt. **39**, 3716-3726 (2000).

41. R. R. Thomson, N. D. Psaila, H. T. Bookey, D. T. Reid, and K. A. K., "Controlling the Cross-section of Ultrafast Laser Inscribed Optical Waveguides," in *Femtosecond Laser Micromachining*, G. Della Valle and R. Osellame, eds. (Springer, 2012), p. 95.

42. R. G. Hunsperger, "Waeguide Fabrication Techniques," in *Integrated Optics : Theory and Technology* (Springer, New York, 2009).

43. D. Choudhury, J. R. Macdonald, and A. K. Kar, "Ultrafast laser inscription: perspectives on future integrated applications," Laser & Photon. Rev. (2014 (doi: 10.1002/lpor.201300195)).

44. R. R. Thomson, N. D. Psaila, H. T. Bookey, D. T. Reid, and K. A. K., "Controlling the Cross-section of Ultrafast Laser Inscribed Optical Waveguides," in *Femtosecond Laser Micromachining*, G. Della Valle and R. Osellame, eds. (Springer, 2012), p. 100.

45. J. M. Senior, "Optical fiber Waveguides," in *Optical fiber communications* (Prentice Hall, 1992).

46. S. M. Eaton and P. R. Herman, "Passive photonic devices in glass," in *Femtosecond Laser Micromachining*, G. Della Valle and R. Osellame, eds. (Springer, 2012), p. 157.

47. K. M. Davis, K. Miura, N. Sugimoto, and K. Hirao, "Writing waveguides in glass with a femtosecond laser," Opt. Lett. **21**, 1729-1731 (1996).

48. G. Della Valle, R. Osellame, and P. Laporta, "Micromachining of photonic devices by femtosecond laser pulses," J. Opt. A.- Pure Appl. Opt. **11**, 013001 (2009).

49. G. Della Valle, R. Osellame, and P. Laporta, "Micromachining of photonic devices by femtosecond laser pulses," J. Opt. A-Pure. Appl. Opt. **11**(2009).

50. F. Chen and J. R. V. de Aldana, "Optical waveguides in crystalline dielectric materials produced by femtosecond-laser micromachining," (2013).

51. J. Burghoff, C. Grebing, S. Nolte, and A. Tunnermann, "Efficient frequency doubling in femtosecond laser-written waveguides in lithium niobate," Appl. Phys. Lett. **89**(2006).

52. G. A. Torchia, A. Rodenas, A. Benayas, E. Cantelar, L. Roso, and D. Jaque, "Highly efficient laser action in femtosecond-written Nd : yttrium aluminum garnet ceramic waveguides," Appl. Phys. Lett. **92**(2008).

53. R. W. Boyd;, "The nonlinear optical susceptibility," in *Nonlinear optics,* 3rd ed. (Academic Press, 2008).

54. P. A. Franken, G. Weinreich, C. W. Peters, and A. E. Hill, "Generation of Optical harmonics," Phys. Rev. Lett. **7**, 118-119 (1961).

55. B. C. Stuart, M. D. Feit, S. Herman, A. M. Rubenchik, B. W. Shore, and M. D. Perry, "Nanosecond-to-femtosecond laser-induced breakdown in dielectrics," Phys. Rev. B. **53**, 1749-1761 (1996).

56. C. B. Schaffer, A. Brodeur, and E. Mazur, "Laser-induced breakdown and damage in bulk transparent materials induced by tightly focused femtosecond laser pulses," Meas. Sci. Technol. **12**, 1784-1794 (2001).

57. L. V. Keldysh, "Ionization in Field of a Strong Electromagnetic Wave," Sov. Phys. Jetp-USSR **20**, 1307-1314 (1965).

58. D. Du, X. Liu, G. Korn, J. Squier, and G. Mourou, "Laser-Induced Breakdown by Impact Ionization in SiO2 with Pulse Widths from 7 ns to 150 fs," Appl. Phys. Lett. **64**, 3071-3073 (1994).

59. R. Thomson and G. Cerullo, "Ultrafast Laser Inscription of Photonic Devices in Bulk Dielectrics," in *Ultrafast Nonlinear Optics*, R. Thomson, C. Leburn, and D. Reid, eds. (Springer, 2013).

60. M. Ams, G. D. Marshall, P. Dekker, M. Dubov, V. K. Mezentsev, I. Bennion, and M. J. Withford, "Investigation of Ultrafast Laser-Photonic Material Interactions: Challenges for Directly Written Glass Photonics," IEEE. J. Sel. Top. Quant. **14**, 1370-1381 (2008).

61. C. Hnatovsky, R. S. Taylor, E. Simova, P. P. Rajeev, D. M. Rayner, V. R. Bhardwaj, and P. B. Corkum, "Fabrication of microchannels in glass using focused femtosecond laser radiation and selective chemical etching," Appl. Phys. A. **84**, 47-61 (2006).

62. Y. Shimotsuma, P. G. Kazansky, J. R. Qiu, and K. Hirao, "Self-organized nanogratings in glass irradiated by ultrashort light pulses," Phys. Rev. Lett. **91**(2003).

63. D. Choudhury, W. T. Ramsay, R. Kiss, N. A. Willoughby, L. Paterson, and A. K. Kar, "A 3D mammalian cell separator biochip," Lab Chip **12**, 948-953 (2012).

64. Y. Bellouard, A. Said, M. Dugan, and P. Bado, "Fabrication of high-aspect ratio, micro-fluidic channels and tunnels using femtosecond laser pulses and chemical etching," Opt. Express **12**, 2120-2129 (2004).

65. A. Marcinkevicius, S. Juodkazis, M. Watanabe, M. Miwa, S. Matsuo, H. Misawa, and J. Nishii, "Femtosecond laser-assisted three-dimensional microfabrication in silica," Opt. Lett. **26**, 277-279 (2001).

66. E. N. Glezer and E. Mazur, "Ultrafast-laser driven micro-explosions in transparent materials," Appl. Phys. Lett. **71**, 882-884 (1997).

67. N. D. Psaila, R. R. Thomson, H. T. Bookey, A. K. Kar, N. Chiodo, R. Osellame, G. Cerullo, A. Jha, and S. Shen, "Er : Yb-doped oxyfluoride silicate glass waveguide amplifier fabricated using femtosecond laser inscription," Appl. Phys. Lett. **90**(2007).

68. A. Benayas, W. F. Silva, A. Rodenas, C. Jacinto, J. V. de Aldana, F. Chen, Y. Tan, R. R. Thomsom, N. D. Psaila, D. T. Reid, G. A. Torchia, A. K. Kar, and D. Jaque, "Ultrafast laser writing of optical waveguides in ceramic Yb:YAG: a study of thermal and non-thermal regimes," Appl. Phys. A-Mater. **104**, 301-309 (2011).

69. J. R. Macdonald, S. J. Beecher, P. A. Berry, K. L. Schepler, and A. K. Kar, "Compact mid-infrared Cr:ZnSe channel waveguide laser," Appl. Phys. Lett. **102**(2013).

70. J. R. Macdonald, S. J. Beecher, P. A. Berry, G. Brown, K. L. Schepler, and A. K. Kar, "Efficient mid-infrared Cr:ZnSe channel waveguide laser operating at 2486 nm," Opt. Lett. **38**, 2194-2196 (2013).

71. J. R. Macdonald, R. R. Thomson, S. J. Beecher, N. D. Psaila, H. T. Bookey, and A. K. Kar, "Ultrafast laser inscription of near-infrared waveguides in polycrystalline ZnSe," Opt. Lett. **35**, 4036-4038 (2010).

72.   F. M. Bain, A. A. Lagatsky, R. R. Thomson, N. D. Psaila, N. V. Kuleshov, A. K. Kar, W. Sibbett, and C. T. A. Brown, "Ultrafast laser inscribed Yb:KGd(WO4)(2) and Yb:KY(WO4)(2) channel waveguide lasers," Opt Express **17**, 22417-22422 (2009).

73.   W. J. Yang, P. G. Kazansky, and Y. P. Svirko, "Non-reciprocal ultrafast laser writing," Nat. Photonics **2**, 99-104 (2008).

74.   L. Shah, A. Arai, S. Eaton, and P. Herman, "Waveguide writing in fused silica with a femtosecond fiber laser at 522 nm and 1 MHz repetition rate," Opt. Express **13**, 1999-2006 (2005).

75.   C. B. Schaffer, A. Brodeur, J. F. Garcia, and E. Mazur, "Micromachining bulk glass by use of femtosecond laser pulses with nanojoule energy," Opt. Lett. **26**, 93-95 (2001).

76.   S. M. Eaton, H. B. Zhang, and P. R. Herman, "Heat accumulation effects in femtosecond laser-written waveguides with variable repetition rate," Opt. Express **13**, 4708-4716 (2005).

77.   F. M. Bain, A. A. Lagatsky, S. V. Kurilchick, V. E. Kisel, S. A. Guretsky, A. M. Luginets, N. A. Kalanda, I. M. Kolesova, N. V. Kuleshov, W. Sibbett, and C. T. A. Brown, "Continuous-wave and Q-switched operation of a compact, diode-pumped Yb3+:KY(WO4)(2) planar waveguide laser," Opt. Express **17**, 1666-1670 (2009).

78.   M. Ams, G. D. Marshall, D. J. Spence, and M. J. Withford, "Slit beam shaping method for femtosecond laser direct-write fabrication of symmetric waveguides in bulk glasses," Opt. Express **13**, 5676-5681 (2005).

79.   P. S. Salter, A. Jesacher, J. B. Spring, B. J. Metcalf, N. Thomas-Peter, R. D. Simmonds, N. K. Langford, I. A. Walmsley, and M. J. Booth, "Adaptive slit beam shaping for direct laser written waveguides," Opt. Lett. **37**, 470-472 (2012).

80.   R. R. Thomson, A. S. Bockelt, E. Ramsay, S. Beecher, A. H. Greenaway, A. K. Kar, and D. T. Reid, "Shaping ultrafast laser inscribed optical waveguides using a deformable mirror," Opt. Express **16**, 12786-12793 (2008).

81.   Y. Nasu, M. Kohtoku, and Y. Hibino, "Low-loss waveguides written with a femtosecond laser for flexible interconnection in a planar light-wave circuit," Opt. Lett. **30**, 723-725 (2005).

82.   A. M. Streltsov and N. F. Borrelli, "Fabrication and analysis of a directional coupler written in glass by nanojoule femtosecond laser pulses," Opt. Lett. **26**, 42-43 (2001).

83.   R. R. Thomson, H. T. Bookey, N. D. Psaila, A. Fender, S. Campbell, W. N. MacPherson, J. S. Barton, D. T. Reid, and A. K. Kar, "Ultrafast-laser inscription of a three dimensional fan-out device for multicore fiber coupling applications," Opt. Express **15**, 11691-11697 (2007).

84.   "Optoscribe", retrieved 18 Feb, 2014, http://optoscribe.com/.

85.   R. R. Thomson, T. A. Birks, S. G. Leon-Saval, A. K. Kar, and J. Bland-Hawthorn, "Ultrafast laser inscription of an integrated photonic lantern," Opt. Express **19**, 5698-5705 (2011).

86.   R. Osellame, N. Chiodo, G. Della Valle, G. Cerullo, R. Ramponi, P. Laporta, A. Killi, U. Morgner, and O. Svelto, "Waveguide lasers in the C-band fabricated by laser inscription with a compact femtosecond oscillator," IEEE J. Sel. Top. Quant. **12**, 277-285 (2006).

87.   F. Reichert, T. Calmano, S. Muller, D. T. Marzahl, P. W. Metz, and G. Huber, "Efficient visible laser operation of Pr,Mg: $SrAl_{12}O_{19}$ channel waveguides," Opt. Lett. **38**, 2698-2701 (2013).

88. S. Taccheo, G. Della Valle, R. Osellame, G. Cerullo, N. Chiodo, P. Laporta, O. Svelto, A. Killi, U. Morgner, M. Lederer, and D. Kopf, "Er : Yb-doped waveguide laser fabricated by femtosecond laser pulses," Opt. Lett. **29**, 2626-2628 (2004).

89. S. J. Beecher, R. R. Thomson, N. D. Psaila, Z. Sun, T. Hasan, A. G. Rozhin, A. C. Ferrari, and A. K. Kar, "320 fs pulse generation from an ultrafast laser inscribed waveguide laser mode-locked by a nanotube saturable absorber," Appl. Phys. Lett. **97**(2010).

90. E. Ramsay, R. R. Thomson, N. D. Psaila, A. K. Kar, and D. T. Reid, "Laser Action From an Ultrafast Laser Inscribed Nd-Doped Silicate Glass Waveguide," IEEE Photon. Tech. Lett. **22**, 742-744 (2010).

91. F. M. Bain, A. A. Lagatsky, R. R. Thomson, N. D. Psaila, N. V. Kuleshov, A. K. Kar, W. Sibbett, and C. T. A. Brown, "Ultrafast laser inscribed Yb:KGd(WO$_4$)$_2$ and Yb:KY(WO$_4$)$_2$ channel waveguide lasers," Opt. Express **17**, 22417-22422 (2009).

92. C. J. Karlsson, F. A. A. Olsson, D. Letalick, and M. Harris, "All-fiber multifunction continuous-wave coherent laser radar at 1.55 μm for range, speed, vibration, and wind measurements," Appl. Opt. **39**, 3716-3726 (2000).

93. N. D. Psaila, R. R. Thomson, H. T. Bookey, A. K. Kar, N. Chiodo, R. Osellame, G. Cerullo, S. Shen, and A. Jha, "Laser action from an Er : Yb-doped oxyfluoride silicate glass waveguide fabricated using femtosecond laser inscription," 2007 Pacific Rim Conference on Lasers and Electro-Optics, Vols 1-4, 808-809 (2007).

94. G. D. Marshall, P. Dekker, M. Ams, J. A. Piper, and M. J. Withford, "Directly written monolithic waveguide laser incorporating a distributed feedback waveguide-Bragg grating," Opt. Lett. **33**, 956-958 (2008).

95. M. Ams, P. Dekker, G. D. Marshall, and M. J. Withford, "Monolithic 100 mW Yb waveguide laser fabricated using the femtosecond-laser direct-write technique," Opt. Lett. **34**, 247-249 (2009).

96. G. Della Valle, R. Osellame, G. Galzerano, N. Chiodo, G. Cerullo, P. Laporta, O. Svelto, U. Morgner, A. G. Rozhin, V. Scardaci, and A. C. Ferrari, "Passive mode locking by carbon nanotubes in a femtosecond laser written waveguide laser," Appl. Phys. Lett. **89**(2006).

97. A. Choudhary, A. A. Lagatsky, P. Kannan, W. Sibbett, C. T. A. Brown, and D. P. Shepherd, "Diode-pumped femtosecond solid-state waveguide laser with a 4.9 GHz pulse repetition rate," Opt. Lett. **37**, 4416-4418 (2012).

98. C. Hnatovsky, R. S. Taylor, E. Simova, V. R. Bhardwaj, D. M. Rayner, and P. B. Corkum, "Polarization-selective etching in femtosecond laser-assisted microfluidic channel fabrication in fused silica," Opt. Lett. **30**, 1867-1869 (2005).

99. D. Choudhury, A. Rodenas, L. Paterson, F. Diaz, D. Jaque, and A. K. Kar, "Three-dimensional microstructuring of yttrium aluminum garnet crystals for laser active optofluidic applications," Appl. Phys. Lett. **103**(2013).

100. G. Della Valle and R. Osellame, "Active Photonic Devices," in *Femtosecond Laser Micromachining*, R. Osellame, G. Cerullo, and R. Ramponi, eds. (Springer, 2012), p. 267.

101. S. Ohara and Y. Kuroiwa, "Highly ytterbium-doped bismuth-oxide-based fiber," Opt. Express **17**, 14104-14108 (2009).

102. M. J. Miniscalco, "Optical and Electronic Properties of Rare Earth Ions in Glasses," in *Rare-Earth-doped fiber lasers and amplifiers*, M. J. F. Digonnet, ed. (Dekker, 2001), p. 33.

103. G. Della Valle and R. Osellame, "Active Photonic Devices," in *Femtosecond Laser Micromachining*, R. Osellame, G. Cerullo, and R. Ramponi, eds. (Springer, 2012), p. 268.

104. S. Guy, C. L. Bonner, D. P. Shepherd, D. C. Hanna, and A. C. Tropper, "High-inversion densities in Nd : YAG: Upconversion and bleaching," IEEE J. Quant. Elect. **34**, 900-909 (1998).

105. T. Hebert, R. Wannemacher, R. M. Macfarlane, and W. Lenth, "Blue Continuously Pumped up-Conversion Lasing in Tm: $YLiF_4$," Appl. Phys. Lett. **60**, 2592-2594 (1992).

106. M. J. Weber, "Handbook of Lasers," (CRC Press, 2001).

107. M. Yamane and Y. Asahara, "Glasses for Photonics," (Cambridge University Press, 2000).

108. S. Y. Feng, S. G. Li, L. Chen, W. Chen, and L. L. Hu, "Thermal loading in laser diode end-pumped Yb^{3+}/Er^{3+} codoped phosphate glass laser," Appl. Opt. **49**, 3357-3362 (2010).

109. E. Snitzer, F. Hoffman, and R. Crevier, "Neodymium-Glass-Fiber Laser," J. Opt. Soc. Am. **53**, 515 (1963).

110. D. Jaque, J. C. Lagomacini, C. Jacinto, and T. Catunda, "Continuous-wave diode-pumped Yb : glass laser with near 90% slope efficiency," Appl. Phys. Lett. **89**(2006).

111. Y. Jeong, J. K. Sahu, D. N. Payne, and J. Nilsson, "Ytterbium-doped large-core fibre laser with 1 kW of continuous-wave output power," Electron. Lett. **40**, 470-472 (2004).

112. M. J. Miniscalco, "Optical and Electronic Properties of Rare Earth Ions in Glasses," in *Rare-Earth-doped fiber lasers and amplifiers*, M. J. F. Digonnet, ed. (Dekker, 2001), p. 36.

113. N. D. Psaila, R. R. Thomson, H. T. Bookey, S. X. Shen, N. Chiodo, R. Osellame, G. Cerullo, A. Jha, and A. K. Kar, "Supercontinuum generation in an ultrafast laser inscribed chalcogenide glass waveguide," Opt. Express **15**, 15776-15781 (2007).

114. S. Nolte, M. Will, J. Burghoff, and A. Tuennermann, "Femtosecond waveguide writing: a new avenue to three-dimensional integrated optics," Appl Phys a-Mater **77**, 109-111 (2003).

115. S. Nolte, M. Will, J. Burghoff, and A. Tuennermann, "Femtosecond waveguide writing: a new avenue to three-dimensional integrated optics," Appl. Phys. A-Mater. **77**, 109-111 (2003).

116. S. Boscolo, S. K. Turitsyn, and K. J. Blow, "Nonlinear loop mirror-based all-optical signal processing in fiber-optic communications," Opt. Fiber Technol. **14**, 299-316 (2008).

117. D. L. Wokosin, V. Centonze, J. G. White, D. Armstrong, G. Robertson, and A. I. Ferguson, "All-solid-state ultrafast lasers facilitate multiphoton excitation fluorescence imaging," IEEE J. Sel. Top. Quant. **2**, 1051-1065 (1996).

118. U. Keller, "Recent developments in compact ultrafast lasers," Nature **424**, 831-838 (2003).

119. A. J. Demaria, D. A. Stetser, and H. Heynau, "Self Mode-Locking of Lasers with Saturable Absorbers - (Regenerative Pulse Oscillator Bleachable Dyes E)," Appl. Phys. Lett. **8**, 174 (1966).

120. H. Ridderbusch and T. Graf, "Saturation of 1047-and 1064-nm absorption in Cr^{4+}: YAG crystals," IEEE J. Quantum. Elect. **43**, 168-173 (2007).

121. C. Honninger, R. Paschotta, F. Morier-Genoud, M. Moser, and U. Keller, "Q-switching stability limits of continuous-wave passive mode locking," J. Opt. Soc. Am. B. **16**, 46-56 (1999).

122. H. W. Mocker and R. J. Collins, "Mode Competition and Self-Locking Effects in Q-Switched Ruby Laser " Appl. Phys. Lett. **7**, 270 (1965).

123. F. X. Kartner, L. R. Brovelli, D. Kopf, M. Kamp, I. Calasso, and U. Keller, "Control of Solid-State Laser Dynamics by Semiconductor-Devices," Opt. Eng. **34**, 2024-2036 (1995).

124. U. Keller, D. A. B. Miller, G. D. Boyd, T. H. Chiu, J. F. Ferguson, and M. T. Asom, "Solid-State Low-Loss Intracavity Saturable Absorber for NdYlF Lasers - an Antiresonant Semiconductor Fabry-Perot Saturable Absorber," Opt. Lett. **17**, 505-507 (1992).

125. A. K. Geim and K. S. Novoselov, "The rise of graphene," Nat. Mater. **6**, 183-191 (2007).

126. S. Y. Set, H. Yaguchi, M. Jablonski, Y. Tanaka, Y. Sakakibara, A. Rozhin, M. Tokumoto, H. Kataura, Y. Achiba, and K. Kikuchi, "A noise suppressing saturable absorber at 1550 nm based on carbon nanotube technology," Proc. Opt. Fiber Commun. Conf. **FL2.**(2003).

127. F. Fusari, R. R. Thomson, G. Jose, F. M. Bain, A. A. Lagatsky, N. D. Psaila, A. K. Kar, A. Jha, W. Sibbett, and C. T. A. Brown, "Lasing action at around 1.9 μm from an ultrafast laser inscribed Tm-doped glass waveguide," Opt. Lett. **36**, 1566-1568 (2011).

128. D. G. Lancaster, S. Gross, H. Ebendorff-Heidepriem, A. Fuerbach, M. J. Withford, and T. M. Monro, "2.1 μm waveguide laser fabricated by femtosecond laser direct-writing in Ho^{3+}, Tm^{3+} : ZBLAN glass," Opt. Lett. **37**, 996-998 (2012).

129. R. Mary, S. J. Beecher, G. Brown, R. R. Thomson, D. Jaque, S. Ohara, and A. K. Kar, "Compact, highly efficient ytterbium doped bismuthate glass waveguide laser," Opt. Lett. **37**, 1691-1693 (2012).

130. J. Hoyo, V. Berdejo, T. T. Fernandez, A. Ferrer, A. Ruiz, J. A. Valles, M. A. Rebolledo, I. Ortega-Feliu, and J. Solis, "Femtosecond laser written 16.5 mm long glass-waveguide amplifier and laser with 5.2 dB cm(-1) internal gain at 1534 nm," Laser Phys. Lett. **10**(2013).

131. R. Mary, G. Brown, S. J. Beecher, F. Torrisi, S. Milana, D. Popa, T. Hasan, Z. P. Sun, E. Lidorikis, S. Ohara, A. C. Ferrari, and A. K. Kar, "1.5 GHz picosecond pulse generation from a monolithic waveguide laser with a graphene-film saturable output coupler," Opt. Express **21**, 7943-7950 (2013).

132. R. R. Thomson, N. D. Psaila, S. J. Beecher, and A. K. Kar, "Ultrafast laser inscription of a high-gain Er-doped bismuthate glass waveguide amplifier," Opt.Express **18**, 13212-13219 (2010).

133. S. M. Eaton, H. Zhang, M. L. Ng, J. Z. Li, W. J. Chen, S. Ho, and P. R. Herman, "Transition from thermal diffusion to heat accumulation in high repetition rate femtosecond laser writing of buried optical waveguides," Opt. Express **16**, 9443-9458 (2008).

134. D. Findlay and R. A. Clay, "The measurement of internal losses in 4-level lasers," Physics Letters **20**, 277-278 (1966).

135. J. A. Caird, S. A. Payne, P. R. Staver, A. J. Ramponi, L. L. Chase, and W. F. Krupke, "Quantum Electronic-Properties of the $Na_3Ga_2Li_3F_{12}:Cr^{3+}$ Laser," IEEE J. Quant. Electron. **24**, 1077-1099 (1988).

136. W. W. Rigrod, "Saturation Effects in High-Gain Lasers," J. Appl. Phys. **36**, 2487 (1965).

137. A. E. Siegman, "Fundamentals of Laser Oscillation," in *Lasers* (University Science Books, 1986).

138. R. Mary, S. J. Beecher, G. Brown, R. R. Thomson, D. Jaque, S. Ohara, and A. K. Kar, "Compact, highly efficient ytterbium doped bismuthate glass waveguide laser," Opt Lett **37**, 1691-1693 (2012).
139. P. R. Wallace, "The Band Theory of Graphite," Phys. Rev. **71**, 622-634 (1947).
140. K. S. Novoselov, A. K. Geim, S. V. Morozov, D. Jiang, Y. Zhang, S. V. Dubonos, I. V. Grigorieva, and A. A. Firsov, "Electric field effect in atomically thin carbon films," Science **306**, 666-669 (2004).
141. J. M. Dawlaty, S. Shivaraman, J. Strait, P. George, M. Chandrashekhar, F. Rana, M. G. Spencer, D. Veksler, and Y. Q. Chen, "Measurement of the optical absorption spectra of epitaxial graphene from terahertz to visible," Appl. Phys. Lett. **93**(2008).
142. Z. Sun, T. Hasan, and A. C. Ferrari, "Ultrafast lasers mode-locked by nanotubes and graphene," Physica E. **44**, 1082-1091 (2012).
143. S. Yamashita, "A Tutorial on Nonlinear Photonic Applications of Carbon Nanotube and Graphene," J Lightwave Technol **30**, 427-447 (2012).
144. A. K. Geim and A. H. MacDonald, "Graphene: Exploring carbon flatland," Phys. Today **60**, 35-41 (2007).
145. F. T. Vasko, "Saturation of interband absorption in graphene," Phys. Rev. B. **82**(2010).
146. S. Iijima and T. Ichihashi, "Single-Shell Carbon Nanotubes of 1-nm Diameter," Nature **363**, 603-605 (1993).
147. S. Y. Set, H. Yaguchi, M. Jablonski, Y. Tanaka, Y. Sakakibara, A. Rozhin, M. Tokumoto, H. Kataura, Y. Achiba, and K. Kikuchi, " A noise suppressing saturable absorber at 1550 nm based on carbon nanotube technology.," Proc. Opt. FiberCommun. Conf. **no. FL2**(2003).
148. S. Y. Set, H. Yaguchi, Y. Tanaka, and M. Jablonski, "Laser modelocking using a saturable absorber incorporating carbon nanotubes," J. Lightw. Technol. **22**, 51–56 (2004).
149. M. Haiml, R. Grange, and U. Keller, "Optical characterization of semiconductor saturable absorbers," Appl. Phys. B. **79**, 331-339 (2004).
150. F. Bonaccorso, Z. Sun, T. Hasan, and A. C. Ferrari, "Graphene photonics and optoelectronics," Nat. Photon. **4**, 611-622 (2010).
151. Q. L. Bao, H. Zhang, Z. H. Ni, Y. Wang, L. Polavarapu, Z. X. Shen, Q. H. Xu, D. Y. Tang, and K. P. Loh, "Monolayer graphene as a saturable absorber in a mode-locked laser," Nano Res. **4**, 297-307 (2011).
152. R. Mary, G. Brown, S. J. Beecher, S. Ohara, and A. K. Kar, "Passive Mode-locking of a Monolithic Waveguide Laser with Simultaneous Q-Switching," 2013 Conference on Lasers and Electro-Optics Pacific Rim (Cleo-PR) (2013).
153. R. Mary, S. J. Beecher, G. Brown, Z. P. Sun, D. Popa, T. Hasan, A. C. Ferrari, S. Ohara, and A. K. Kar, "Q-switched modelocking using carbon nanotubes in an ultrafast laser inscribed ytterbium doped bismuthate glass waveguide laser," 2012 International Conference on Fiber Optics and Photonics (Photonics) (2012).
154. C. A. Zaugg, Z. Sun, V. J. Wittwer, D. Popa, S. Milana, T. S. Kulmala, R. S. Sundaram, M. Mangold, O. D. Sieber, M. Golling, Y. Lee, J. H. Ahn, A. C. Ferrari, and U. Keller, "Ultrafast and widely tuneable vertical-external-cavity surface-emitting laser, mode-locked by a graphene-integrated distributed Bragg reflector," Opt. Express **21**, 31548-31559 (2013).
155. S. Husaini and R. G. Bedford, "Graphene saturable absorber for high power semiconductor disk laser mode-locking," Appl. Phys. Lett. **104**(2014).
156. N. Tolstik, E. Sorokin, and I. T. Sorokina, "Graphene mode-locked Cr:ZnS laser with 41 fs pulse duration," Opt. Express **22**, 5564-5571 (2014).

157. C. S. Jun, J. H. Im, S. H. Yoo, S. Y. Choi, F. Rotermund, D. I. Yeom, and B. Y. Kim, "Low noise GHz passive harmonic mode-locking of soliton fiber laser using evanescent wave interaction with carbon nanotubes," Opt. Express **19**, 19775-19780 (2011).

158. Z. Q. Luo, J. Z. Wang, M. Zhou, H. Y. Xu, Z. P. Cai, and C. C. Ye, "Multiwavelength mode-locked erbium-doped fiber laser based on the interaction of graphene and fiber-taper evanescent field," Laser Phys. Lett. **9**, 229-233 (2012).

159. A. Martinez, K. M. Zhou, I. Bennion, and S. Yamashita, "Passive mode-locked lasing by injecting a carbon nanotube-solution in the core of an optical fiber," Opt. Express **18**, 11008-11014 (2010).

160. S. J. Beecher, R. R. Thomson, and A. K. Kar, "The Evanescent Interaction of an Ultrafast Laser Inscribed Optical Waveguide," 2011 Conference on Lasers and Electro-Optics (CLEO) (2011).

161. S. J. Beecher, R. R. Thomson, B. P. Pal, and A. K. Kar, "Single Stage Ultrafast Laser Inscription of a Side-Polished Fiber-Like Waveguide Sensor," IEEE Sens. J. **12**, 1263-1266 (2012).

162. Y. Tan, C. Cheng, S. Akhmadaliev, S. Zhou, and F. Chen, "Nd:YAG waveguide laser Q-switched by evanescent-field interaction with graphene," Opt. Express **22**, 9101-9106 (2014).

163. S. M. J. Kelly, "Characteristic sideband instability of periodically amplified average soliton," Electron. Lett. **28**, 806-807 (1992).

164. K. Tamura, E. P. Ippen, and H. A. Haus, "Optimization of filtering in soliton fiber lasers," IEEE Photonics Tech. L. **6**, 1433-1435 (1994).

165. R. Mary, G. Brown, S. J. Beecher, R. R. Thomson, D. Popa, Z. Sun, F. Torrisi, T. Hasan, S. Milana, F. Bonaccorso, A. C. Ferrari, and A. K. Kar, "Evanescent-wave coupled right angled buried waveguide: Applications in carbon nanotube mode-locking," Appl. Phys. Lett. **103**(2013).

166. G. Brown, R. R. Thomson, S. J. Beecher, R. Mary, D. Popa, Z. Sun, F. Torrisi, T. Hasan, S. Milana, F. Bonaccorso, A. C. Ferrari, and A. K. Kar, "Mode-locking Using Right-angle Waveguide, Based Nanotube Saturable Absorber," 2013 Conference on Lasers and Electro-Optics Pacific Rim (Cleo-PR) (2013).

167. R. Kashyap, "The Fiber Fuse - from a curious effect to a critical issue: A 25th year retrospective," Opt. Express **21**, 6422-6441 (2013).

168. D. P. Hand and P. S. Russell, "Solitary Thermal-Shock Waves and Optical-Damage in Optical Fibers - the Fiber Fuse," Opt. Lett. **13**, 767-769 (1988).

169. R. Kashyap and K. J. Blow, "Observation of Catastrophic Self-Propelled Self-Focusing in Optical Fibers," Electron. Lett. **24**, 47-49 (1988).